



Strengthening of Existing Inverted-T Bent Caps— Volume 2: Experimental Test Program

Technical Report 0-6893-R1-Vol2

Cooperative Research Program

TEXAS A&M TRANSPORTATION INSTITUTE
COLLEGE STATION, TEXAS

in cooperation with the
Federal Highway Administration and the
Texas Department of Transportation
<http://tti.tamu.edu/documents/0-6893-R1-Vol2.pdf>

1. Report No. FHWA/TX-18/0-6893-R1-Vol2	2. Government Accession No.	3. Recipient's Catalog No.	
4. Title and Subtitle STRENGTHENING OF EXISTING INVERTED-T BENT CAPS— VOLUME 2: EXPERIMENTAL TEST PROGRAM		5. Report Date Published: November 2018	
		6. Performing Organization Code	
7. Author(s) Stefan Hurlebaus, John B. Mander, Anna C. Birely, Tevfik Terzioglu, Jilong Cui, and Sun Hee Park		8. Performing Organization Report No. Report 0-6893-R1-Vol2	
9. Performing Organization Name and Address Texas A&M Transportation Institute The Texas A&M University System College Station, Texas 77843-3135		10. Work Unit No. (TRAIS)	
		11. Contract or Grant No. Project 0-6893	
12. Sponsoring Agency Name and Address Texas Department of Transportation Research and Technology Implementation Office 125 E. 11th Street Austin, Texas 78701-2483		13. Type of Report and Period Covered Technical Report: September 2015–August 2018	
		14. Sponsoring Agency Code	
15. Supplementary Notes Project performed in cooperation with the Texas Department of Transportation and the Federal Highway Administration. Project Title: Strengthening of Existing Inverted-T Bent Caps URL: http://tti.tamu.edu/documents/0-6893-R1-Vol2.pdf			
16. Abstract Inverted-T bent caps have been widely used in Texas to provide increased clearance underneath bridges while providing an aesthetically pleasing substructure alternative. The bottom flange (ledge) must have sufficient transverse and punching shear capacity to be able to transfer the applied loads to the web. In this study, retrofit solutions to strengthen the in-service inverted-T bent caps, which have deficiencies with an increased number of lanes, were identified and are discussed in the previous volume. An experimental test program consisting of eight half-scale specimens with hanger, ledge flexure, and punching shear deficiencies was then conducted, with each specimen consisting of external and internal girder locations. Thirty-three individual tests were conducted to investigate six strengthening solutions: end-region stiffener, clamped threadbar with channel, load-balancing post-tensioning, concrete infill with full- and partial-depth fiber-reinforced polymer anchored by steel waling, and large bearing pad. Based on the test results, all retrofit solutions except large bearing pad improved the capacities by 16 percent to 82 percent. The measured ultimate load for all retrofit solutions was greater than the calculated ultimate demands. A capacity analysis based on the 2014 American Association of State and Highway Transportation Officials (AASHTO) <i>LRFD Bridge Design Specifications</i> was also conducted for all tests. The estimated capacities were compared to the measured capacities and determined to be over-conservative in most cases, and rational modifications for the capacity estimations were proposed based on the observed test results. The modified calculations improved the accuracy of the capacity estimations by 8 percent to 28 percent, compared to 2014 AASHTO load and resistance factor design provisions.			
17. Key Words Inverted-T, Bent Cap, Bridge, Strengthening, Ledge Flexure, Ledge Shear Friction, Hanger, Punching Shear, Bearing, Half-Scale Test, FRP Sheet, FRP Wrap, External Post-Tensioning		18. Distribution Statement No restrictions. This document is available to the public through NTIS: National Technical Information Service Alexandria, Virginia http://www.ntis.gov	
19. Security Classif.(of this report) Unclassified	20. Security Classif.(of this page) Unclassified	21. No. of Pages 202	22. Price

**STRENGTHENING OF EXISTING INVERTED-T BENT CAPS—
VOLUME 2: EXPERIMENTAL TEST PROGRAM**

by

Stefan Hurlebaus, Ph.D.
Professor
Zachry Department of Civil Engineering
Research Scientist
Texas A&M Transportation Institute

John B. Mander, Ph.D.
Zachry Professor of Design and Construction Integration
Zachry Department of Civil Engineering
Research Scientist
Texas A&M Transportation Institute

Anna C. Birely, Ph.D.
Assistant Professor
Zachry Department of Civil Engineering
Assistant Research Scientist
Texas A&M Transportation Institute

Tevfik Terzioglu, Ph.D.
Postdoctoral Research Associate
Texas A&M Transportation Institute

and

Jilong Cui and Sun Hee Park
Graduate Assistant Researchers
Texas A&M Transportation Institute

Report 0-6893-R1-Vol2
Project 0-6893
Project Title: Strengthening of Existing Inverted-T Bent Caps

Performed in cooperation with the
Texas Department of Transportation
and the
Federal Highway Administration

Published: November 2018

TEXAS A&M TRANSPORTATION INSTITUTE
College Station, Texas 77843-3135

DISCLAIMER

This research was performed in cooperation with the Texas Department of Transportation (TxDOT) and the Federal Highway Administration (FHWA). The contents of this report reflect the views of the authors, who are responsible for the facts and the accuracy of the data presented herein. The contents do not necessarily reflect the official view or policies of the FHWA or TxDOT. This report does not constitute a standard, specification, or regulation.

This report is not intended for construction, bidding, or permit purposes. The researcher in charge of the project was Stefan Hurlebaus. The United States Government and the State of Texas do not endorse products or manufacturers. Trade or manufacturers' names appear herein solely because they are considered essential to the object of this report.

ACKNOWLEDGMENTS

This project was conducted in cooperation with TxDOT and FHWA under Project 0-6893, with Chris Glancy serving as project manager. The authors thank Dominique Bechle, Michelle Romage-Chambers, Nicholas Nemas, and Steven Austin.

The project was conducted at Texas A&M University through the Texas A&M Transportation Institute. The authors would like to acknowledge the support of Maria Medrano and Kanchan Pandey. Experimental tests were conducted in the High Bay Structural and Materials Testing Laboratory, with assistance from Dr. Peter Keating, Charles Droddy, and Matthew Potter. The support of graduate and undergraduate student workers in fabricating, instrumenting, and testing the bent caps is greatly appreciated. These students include Hung Joo Kwon, Nick Danney, Josh Ortiz, Ricardo Espinoza, Walker Needles, Katherine Burns, Jorge Sosa, Cameron Crockett, Mary B. Keating, Ana Ruiz, Erick Albo, Judong Lee, Codi McKee, Kevin Yole, Natasha Boger, Alexis Velazquez, Brandon Oxley, and John Teets.

Fiber reinforced polymer sheets were donated by BASF. The contributions of BASF are gratefully acknowledged.

TABLE OF CONTENTS

	Page
List of Figures	xi
List of Tables	xv
Chapter 1: Introduction	1
1.1 Overview.....	1
1.2 Project Objectives	2
1.3 Summary of Previous Work Reported in Volume 1	2
1.4 Organization.....	3
Chapter 2: Experimental Test Program	5
2.1 Specimen Description	5
2.2 Retrofit Descriptions	11
2.2.1 Solution 3: End-Region Stiffener.....	12
2.2.2 Solution 8: Clamped Threadbar with Channel.....	12
2.2.3 Solution 14: Load-Balancing PT	14
2.2.4 Solution 16: Concrete Infill with Partial-Depth FRP Anchored by Steel Waling.....	18
2.2.5 Solution 17: Concrete Infill with Full-Depth FRP Anchored by Steel Waling	18
2.2.6 Solution 18: Large Bearing Pad.....	19
2.3 Test Matrix.....	22
2.4 Specimen Construction	24
2.4.1 Bent Cap Construction.....	24
2.4.2 Column Construction.....	31
2.4.3 Specimen Assembly.....	31
2.4.4 End-Region Stiffener Installation	33
2.4.5 Threadbar with Channel Installation.....	36
2.4.6 Load-Balancing PT Installation	38
2.4.7 FRP Installation	38
2.5 Material Properties.....	43
2.6 Test Setup and Load Protocol.....	47
2.7 Instrumentation	50
Chapter 3: Experimental Results	55
3.1 Hanger-Deficient Specimen 1	55
3.1.1 Exterior Hanger Reference—T1W1	55
3.1.2 Interior Hanger Reference—T1I1	59
3.1.3 Exterior Solution 8(a)—T1E1.....	61
3.2 Hanger-Deficient Specimen 2.....	64
3.2.1 Exterior Solution 3—T2E1	64
3.2.2 Exterior Solution 14—T2W1.....	68
3.2.3 Exterior Solution 17 (Post-Crack)—T2W2	71
3.2.4 Interior Solution 14—T2I1	74
3.2.5 Interior Solution 17 (Post-Crack)—T2I2.....	76
3.3 Ledge-Deficient Specimen 3.....	79
3.3.1 Exterior Punch Reference (Small Pad)—T3W1	79

3.3.2 Exterior Punch Solution 18 (Large Pad)—T3E1	83
3.3.3 Interior Punch Reference (Small Pad)—T3I1	85
3.3.4 Interior Punch Solution 18 (Large Pad)—T3I2 and T3I3	87
3.4 Ledge-Deficient Specimen 4	89
3.4.1 Exterior Solution 8(a)—T4W1	89
3.4.2 Exterior Solution 8(b)—T4E1	94
3.4.3 Interior Solution 8—T4I1	97
3.5 Ledge-Deficient Specimen 5	100
3.5.1 Exterior Ledge Reference—T5E1	100
3.5.2 Interior Ledge Reference—T5I1	104
3.5.3 Exterior Solution 3—T5W1	106
3.6 Ledge-Deficient Specimen 6	108
3.6.1 Exterior Solution 16—T6W1	109
3.6.2 Exterior Solution 17—T6E1	113
3.6.3 Interior Solution 16—T6I1	116
3.7 Ledge-Deficient Specimen 7	119
3.7.1 Exterior Solution 14—T7W1	119
3.7.2 Exterior Solution 14 (Post-Crack)—T7E1	123
3.7.3 Exterior Solution 3 (Post-Crack)—T7W2	126
3.7.4 Exterior Solution 8(a) (Post-Crack)—T7E2	129
3.7.5 Interior Punch Tests—T7I1 and T7I2	131
3.7.6 Interior Punch Tests—T7I3 and T7I4	135
3.8 Hanger-Deficient Specimen 8	139
3.8.1 Exterior Solution 8(b)—T8W1	139
3.8.2 Exterior Solution 8(a) (Post-Crack)—T8E1	143
3.8.3 Interior Solution 8—T8I1	146
Chapter 4: Data Analysis and Recommendations for Evaluating In-Service Bent Caps ..	149
4.1 Overview	149
4.2 Hanger Capacity	149
4.2.1 Code Provisions	150
4.2.2 Analysis of Experimental Results	151
4.3 Ledge Shear Friction and Flexure Capacity	153
4.3.1 Code Provisions	153
4.3.2 Analysis of Experimental Results	154
4.3.3 Proposed Modification	157
4.4 Punching Shear Capacity	158
4.4.1 Code Provisions	158
4.4.2 Analysis of Experimental Results	159
4.4.3 Proposed Modifications	160
4.5 Closing Remarks	163
Chapter 5: Data Analysis of Retrofit Solutions.....	165
5.1 Hanger-Deficient Specimens	165
5.1.1 Analysis of the Exterior Ledges	166
5.1.2 Analysis of the Interior Ledges	170
5.2 Ledge-Deficient Specimens	172
5.2.1 Analysis of the Exterior Ledges	173

5.2.2 Analysis of the Interior Ledges	177
Chapter 6: Summary and Conclusion.....	181
References	185

LIST OF FIGURES

	Page
Figure 1.1. Inverted-T Bent Cap in Downtown Austin.	1
Figure 2.1. Geometry of Inverted-T Bent Caps for Design of Specimens.	6
Figure 2.2. Geometry and Reinforcement of Prototype Bent Caps.	8
Figure 2.3. Reinforcement Details of Hanger-Deficient Specimen.	9
Figure 2.4. Reinforcement Details of Ledge-Deficient Specimen.	10
Figure 2.5. Solution 3—End-Region Stiffener.	12
Figure 2.6. Solution 8—Clamped Threadbar with Channel.	13
Figure 2.7. Solution 14—Load-Balancing PT.	15
Figure 2.8. Steel Plate for Locating PT Strand.	16
Figure 2.9. Anchor Plates for PT Strand.	17
Figure 2.10. Solution 16—Solution for Punching Shear and Ledge Shear Failure Using FRP Sheets with Concrete Infill and Steel Waling.	20
Figure 2.11. Solution 17—Solution for Hanger, Punching Shear, and Ledge Shear Failure Using FRP Sheets with Concrete Infill and Steel Waling.	21
Figure 2.12. Test Nomenclature.	22
Figure 2.13. Inverted-T Rebar Cage Assembly Steps.	25
Figure 2.14. Inverted-T Rebar Cage.	26
Figure 2.15. 3D View of the Formwork.	28
Figure 2.16. Formwork Assembly.	29
Figure 2.17. Casting of Inverted-T Specimens.	30
Figure 2.18. Uncovered Specimens.	30
Figure 2.19. Support Column with Lifting Hooks.	31
Figure 2.20. Column Details.	32
Figure 2.21. Leveling Column on Strong Floor.	33
Figure 2.22. Installing a Specimen on the Columns.	34
Figure 2.23. End-Region Stiffener Installation Procedures.	35
Figure 2.24. Installation Procedures for Threadbar with Channel.	37
Figure 2.25. Installation Procedures for Load-Balancing PT.	39
Figure 2.26. Construction of Concrete Infill for FRP Solutions.	40
Figure 2.27. Surface Treatments Prior to FRP Application.	41
Figure 2.28. Application of Epoxy Components to Substrate.	41
Figure 2.29. Application of FRP for Interior Region.	42
Figure 2.30. Application of FRP for Exterior Region.	42
Figure 2.31. Application of Second Layer of Epoxy and Steel Waling.	43
Figure 2.32. Compressive Strength Gain over Time.	44
Figure 2.33. Test Setup in Laboratory.	48
Figure 2.34. Overview of Experimental Test Setup Loading Locations.	48
Figure 2.35. Details of Loading Frame and Side View of Actuator Location.	49
Figure 2.36. Overall LVDT and String Pot Installation Plan.	51
Figure 3.1. Crack Maps for Tests T1W1, T1I1, and T1E1.	56
Figure 3.2. Load-Deflection Curve for T1W1.	57
Figure 3.3. Observed Damage for T1W1 at Different Load Levels.	58

Figure 3.4. Load-Deflection Curve for T1I1.	59
Figure 3.5. Observed Damage for T1I1 at Different Load Levels.....	60
Figure 3.6. Retrofit Solution 8(a) Installed on East End of Hanger-Deficient Specimen 1.	62
Figure 3.7. Load-Deflection Curve for T1E1.	62
Figure 3.8. Observed Damage for T1E1 at Different Load Levels.	63
Figure 3.9. Crack Maps for Tests T2W1, T2I1, and T2E1.....	65
Figure 3.10. Crack Maps for Tests T2W2 and T2I2.....	66
Figure 3.11. Retrofit Solution 3 Installed on East End of Hanger-Deficient Specimen 2.....	67
Figure 3.12. Load-Deflection Curve for T2E1.	67
Figure 3.13. Observed Damage for T2E1 at Final Load Levels.....	68
Figure 3.14. Retrofit Solution 14 Installed on West End of Hanger-Deficient Specimen 2.....	69
Figure 3.15. Load-Deflection Curve for T2W1 (Test Terminated Prior to Failure).....	70
Figure 3.16. Observed Damage for T2W1 at Test Termination Load.....	70
Figure 3.17. Retrofit Solution 17 Installed on West End of Hanger-Deficient Specimen 2.....	72
Figure 3.18. Load-Deflection Curve for T2W2.....	72
Figure 3.19. Observed Damage for T2W2 at Different Load Levels.	73
Figure 3.20. Retrofit Solution 14 Installed on Interior of Hanger-Deficient Specimen 2.	75
Figure 3.21. Load-Deflection Curve for T2I1.	75
Figure 3.22. Observed Damage for Test T2I1 at Test Termination Load.	76
Figure 3.23. Retrofit Solution 17 Installed on Interior of Hanger-Deficient Specimen 2.	77
Figure 3.24. Load-Deflection Curve for T2I2.	77
Figure 3.25. Observed Damage for Test T2I2 at Different Load Levels.....	78
Figure 3.26. Crack Maps for Tests T3I1 and T3E1.	80
Figure 3.27. Crack Maps for Tests T3I2, T3I3, and T3W1.....	81
Figure 3.28. Load-Deflection Curve for T3W1.....	82
Figure 3.29. Observed Damage for T3W1 at Final Load Level.	82
Figure 3.30. Load-Deflection Curve for T3E1.	84
Figure 3.31. Observed Damage for T3E1 at Final Load Level.	84
Figure 3.32. Load-Deflection Curve for T3I1.	86
Figure 3.33. Observed Damage for T3I1 at Final Load Level.....	86
Figure 3.34. Load-Deflection Curve for T3I2.	88
Figure 3.35. Load-Deflection Curve for T3I3.	88
Figure 3.36. Observed Damage for T3I2 and T3I3 at Final Load Level.....	89
Figure 3.37. Crack Maps for Tests T4W1, T4I1, and T4E1.....	91
Figure 3.38. Retrofit Solution 8(a) Installed on West End of Ledge-Deficient Specimen 4.....	92
Figure 3.39. Load-Deflection Curve for T4W1.....	92
Figure 3.40. Observed Damage for Test T4W1 at Final Load Levels.....	93
Figure 3.41. Retrofit Solution 8(b) Installed on East End of Ledge-Deficient Specimen 4.	95
Figure 3.42. Load-Deflection Curve for T4E1.	95
Figure 3.43. Observed Damage for Test T4E1 at Different Load Levels.....	96
Figure 3.44. Retrofit Solution 8 Installed on Interior of Ledge-Deficient Specimen 4.....	98
Figure 3.45. Load-Deflection Curve for T4I1.	98
Figure 3.46. Observed Damage for Test T4I1 at Different Load Levels.....	99
Figure 3.47. Crack Maps for Tests T5W1, T5I1, and T5E1.....	101
Figure 3.48. Load-Deflection Curve for T5E1.	102
Figure 3.49. Observed Damage for T5E1 at Different Load Levels.	103

Figure 3.50. Load-Deflection Curve for T5I1.	105
Figure 3.51. Observed Damage for T5I1 at Different Load Levels.....	105
Figure 3.52. Retrofit Solution 3 Installed on West End of Ledge-Deficient Specimen 5.	107
Figure 3.53. Load-Deflection Curve for T5W1.	107
Figure 3.54. Observed Damage for T5W1 at Final Load Level.	108
Figure 3.55. Crack Maps for Tests T6W1, T6I1, and T6E1.	110
Figure 3.56. Retrofit Solution 16 Installed on West End of Ledge-Deficient Specimen 6.	111
Figure 3.57. Load-Deflection Curve for T6W1.	111
Figure 3.58. Observed Damage for Test T6W1 at Different Load Levels.	112
Figure 3.59. Retrofit Solution 17 Installed on East End of Ledge-Deficient Specimen 6.....	114
Figure 3.60. Load-Deflection Curve for T6E1.	114
Figure 3.61. Observed Damage for Test T6E1 at Different Load Levels.....	115
Figure 3.62. Retrofit Solution 16 Installed on Interior of Ledge-Deficient Specimen 6.	117
Figure 3.63. Load-Deflection Curve for T6I1.	117
Figure 3.64. Observed Damage for Test T6I1.	118
Figure 3.65. Crack Maps for Tests T7W1, T7I1, T7I2, and T7E1.	120
Figure 3.66. Crack Maps for Tests T7W2, T7I3, T7I4, and T7E2.	121
Figure 3.67. Retrofit Solution 14 Installed on West End of Ledge-Deficient Specimen 7.	122
Figure 3.68. Load-Deflection Curve for T7W1.	122
Figure 3.69. Observed Damage for Test T7W1 at Test Termination Load.....	123
Figure 3.70. Observed Damage Before PT Jacking Operation.....	124
Figure 3.71. Load-Deflection Curve for T7E1.	125
Figure 3.72. Observed Damage for Test T7E1 at Test Termination Load.	125
Figure 3.73. Post-Crack Retrofit Solution 3 Installed on West End of Ledge-Deficient Specimen 7.	127
Figure 3.74. Load-Deflection Curve for T7W2.	127
Figure 3.75. Observed Damage for Test T7W2 at Different Load Levels.	128
Figure 3.76. Load-Deflection Curve for T7E2.	130
Figure 3.77. Observed Damage for Test T7E2 at Different Load Levels.....	130
Figure 3.78. Load-Deflection Curve for T7I1.	133
Figure 3.79. Load-Deflection Curve for T7I2.	133
Figure 3.80. Observed Damage for Test T7I1 and T7I2 at Different Load Levels.	134
Figure 3.81. Load-Deflection Curve for T7I3.	137
Figure 3.82. Load-Deflection Curve for T7I4.	137
Figure 3.83. Observed Damage for Test T7I3 and T7I4 at Different Load Levels.	138
Figure 3.84. Crack Maps for Tests T8W1, T8I1, and T8E1.	140
Figure 3.85. Retrofit Solution 8(b) Installed on West End of Hanger-Deficient Specimen 8. ...	141
Figure 3.86. Load-Deflection Curve for T8W1.	141
Figure 3.87. Observed Damage of Test T8W1 at Different Load Levels.....	142
Figure 3.88. Post-Crack Retrofit Solution 8(a) Installed on East End of Hanger-Deficient Specimen 8.	144
Figure 3.89. Load-Deflection Curve for T8E1.	144
Figure 3.90. Observed Damage for Test T8E1 at Different Load Levels.....	145
Figure 3.91. Retrofit Solution 8 Installed on Interior of Hanger-Deficient Specimen 8.	147
Figure 3.92. Load-Deflection Curve for T8I1.	147
Figure 3.93. Observed Damage for Test T8I1 at Different Load Levels.....	148

Figure 4.1. Notation and Potential Crack Locations for Ledge Beams (AASHTO, 2014).	150
Figure 4.2. Notation for Interior Girder Hanger Capacity at the Strength Limit State (AASHTO, 2014).....	151
Figure 4.3. Observed Damages and AASHTO Distribution Widths for Hanger-Deficient Reference Tests.	152
Figure 4.4. Notation and Distribution Width for Capacity Analysis (AASHTO, 2014).	155
Figure 4.5. Observed Cracks and AASHTO Distribution Widths for Ledge-Deficient Reference Tests.	156
Figure 4.6. AASHTO LRFD and Proposed Distribution Width.....	157
Figure 4.7. Punching Shear of Beam Ledge (AASHTO, 2014).	159
Figure 4.8. Observed Crack Angle for Punching Shear Tests.	161
Figure 4.9. Comparison of Existing and Proposed Punching Shear Capacity Equations with Experimental Results.	162
Figure 5.1. Load-Deflection Curves for Hanger-Deficient Exterior Tests.	168
Figure 5.2. Load-Deflection Curves for Hanger-Deficient Interior Tests.	171
Figure 5.3. Load-Deflection Curves for Ledge-Deficient Exterior Tests.	175
Figure 5.4. Load-Deflection Curves for Ledge-Deficient Interior Tests.	178

LIST OF TABLES

	Page
Table 2.1. Prototype Model Capacities.....	8
Table 2.2. Failure Hierarchy for Designed Reference Specimen.	11
Table 2.3. Test Matrix.....	23
Table 2.4. Compressive Test Results for Concrete Cylinders.	44
Table 2.5. Tensile Test Result for Reinforcing Rebar.	45
Table 2.6. Material Properties for Retrofit Solutions.	46
Table 2.7. Typical Mechanical Properties with Steel Grade.	46
Table 2.8. Estimated Limit State Loads for Documentation of Test Results.	50
Table 2.9. String Pot Installation Plan.	52
Table 2.10. LVDT Installation Plan.....	53
Table 4.1. Summary of Capacity Analysis for Hanger-Deficient Reference Specimen.....	151
Table 4.2. Summary of Capacity Analysis for Ledge-Deficient Reference Specimen.	155
Table 4.3. Estimated Capacity and Ratio of Estimated-to-Measured Capacity.....	158
Table 4.4. Summary of Punching Shear Test on Ledge-Deficient Specimen.	160
Table 4.5. Estimated Capacity and Ratio of Estimated-to-Measured Capacity.....	162
Table 5.1. Comparison of Expected and Observed Deficiency of Hanger-Deficient Reference Specimens.	166
Table 5.2. Summary of Capacity Analysis and Test Result for Hanger-Deficient Exterior.....	167
Table 5.3. Summary of Capacity Analysis and Test Result for Hanger-Deficient Interior.....	171
Table 5.4. Comparison of Expected and Observed Deficiency of Ledge-Deficient Reference Specimen.	173
Table 5.5. Summary of Capacity Analysis and Test Result for Ledge-Deficient Exterior.	174
Table 5.6. Summary of Capacity Analysis and Test Result for Ledge-Deficient Interior.....	177
Table 6.1. Summary of Test Results and Capacity Analyses.	183

CHAPTER 1: INTRODUCTION

1.1 Overview

Inverted-T bent caps have been widely used in Texas to maximize the clearance beneath the bridge deck and to provide an aesthetically pleasing substructure alternative. Figure 1.1 shows inverted-T bent caps that are part of the substructure supporting the upper deck of IH 35 in downtown Austin. The loads from the girders are applied to the ledges at the bottom of the inverted-T section and transferred to the web through the stirrups that serve as hangers. The bottom flange (ledge) must have sufficient transverse and punching shear capacity to enable the transfer of applied loads to the web.



Figure 1.1. Inverted-T Bent Cap in Downtown Austin.

Plans to increase traffic on lanes on the IH 35 upper deck in Austin and observed cracks at web-ledge interfaces in other in-service bent caps have led to the need to design and evaluate potential strengthening solutions for inverted-T bent caps. A primary objective of Texas Department of Transportation (TxDOT) Project 0-6893 is to demonstrate and validate through experimental testing the satisfactory performance of retrofit solutions. This report volume presents the findings of an experimental test program consisting of eight half-scale specimens with hanger or ledge deficiencies. Thirty-three individual tests were conducted to investigate six distinct strengthening solutions. Designs of the test specimens and strengthening solutions were based on the results of the previous volume; a summary of these findings is presented in Section 1.3. Organization of this volume is provided in Section 1.4.

1.2 Project Objectives

This project is focused on the design and validation of satisfactory performance of strengthening existing inverted-T bent cap ledges through experimental testing. A primary objective is to demonstrate and validate, through experimental testing, the satisfactory performance of strengthening existing inverted-T bent caps. The research objectives are to:

- Evaluate existing inverted-T bent caps based on field visits and current design methodologies.
- Propose technical concepts to retrofit inverted-T bent caps found to be deficient using current design methodologies.
- Evaluate the proposed retrofit solutions and make recommendations for testing.
- Conduct experimental tests on half-scaled specimens and analyze the results.
- Develop design recommendations and provide design examples for the tested retrofit solutions.

The solutions developed by this research are expected to provide increased capacity of existing substructure components on numerous direct connectors and other bridges including the highly congested IH 35 upper deck through downtown Austin.

1.3 Summary of Previous Work Reported in Volume 1

Strengthening of Existing Inverted-T Bent Caps—Volume 1: Preliminary Design (hereafter, Volume 1) presented:

- A detailed literature review including a review of inverted-T bent caps to guide the analysis of inverted-T bent caps and develop retrofit solutions.
- The evaluation of in-service inverted-T bent caps.
- The development of retrofit solutions for the inverted-T bent caps with deficient capacity.
- The evaluation of the proposed retrofit solutions.

Following is a summary of the findings of the evaluation of in-service inverted-T bent caps and retrofit solutions:

- Based on two field visits, as documented in Volume 1 (Hurlebaus et al., 2018a), one key damage type observed from in-service inverted-T bent caps was cracks on the end face, originating at the corner of the web-ledge interface.

- Southbound Bent 13 and northbound Bent 22, which have the largest load demands, were found to be deficient.
- Eighteen potential retrofit solutions were proposed and designed to address the most critical failure modes of Bent 13 and Bent 22: hanger, ledge flexure, and punching shear.
- All proposed solutions were evaluated in terms of six criteria: strength increase, total cost, constructability, clearance constraints, durability, and ease of monitoring.
- Using a weighted sum model with specified weight factors, the retrofit solutions were ranked to create a decision matrix to choose the most viable solutions.
- The top-ranked solutions selected to test in the lab were:
 - Solution 3 (end-region stiffener).
 - Solution 8 (clamped threadbar with channel).
 - Solution 14 (load-balancing post-tensioning [PT]).
 - Solution 16 (concrete infill with partial-depth fiber-reinforced polymer [FRP] anchored by steel waling).
 - Solution 17 (concrete infill with full-depth FRP anchored by steel waling)
 - Solution 18 (large bearing pad)

1.4 Organization

Specimens with six retrofit solutions were designed for the experimental program, and thirty-three tests were conducted. Chapter 2 provides an overview of the experimental test program, including specimen and retrofit solution design, test matrix, construction details, material properties, test setup/loading, and instrumentation. Chapter 3 summarizes the results of each test. Chapter 4 presents the result of data analysis of reference test. An evaluation of each retrofit solution is addressed in Chapter 5. Chapter 6 provides a summary of findings and a description of future work.

CHAPTER 2: EXPERIMENTAL TEST PROGRAM

Six retrofit solutions for inverted-T bent caps, as identified in Volume 1 (Hurlebaus et al., 2018a), were implemented in an experimental test program. Retrofit solutions investigated were end-region stiffener (Solution 3), clamped threadbar with channel (Solution 8), load-balancing PT (Solution 14), concrete infill with partial- and full-depth FRP anchored by steel wailing (Solutions 16 and 17), and large bearing pad (Solution 18).

Experimental tests consisted of thirty-three individual tests on eight half-scale specimens adapted from the designs of multi-column bents on IH 35 in Austin. The full specimens consisted of a bent cap supported on two columns with identical overhangs, providing tests of both interior and exterior regions. Two types of specimens were designed to emphasize hanger and ledge deficiencies.

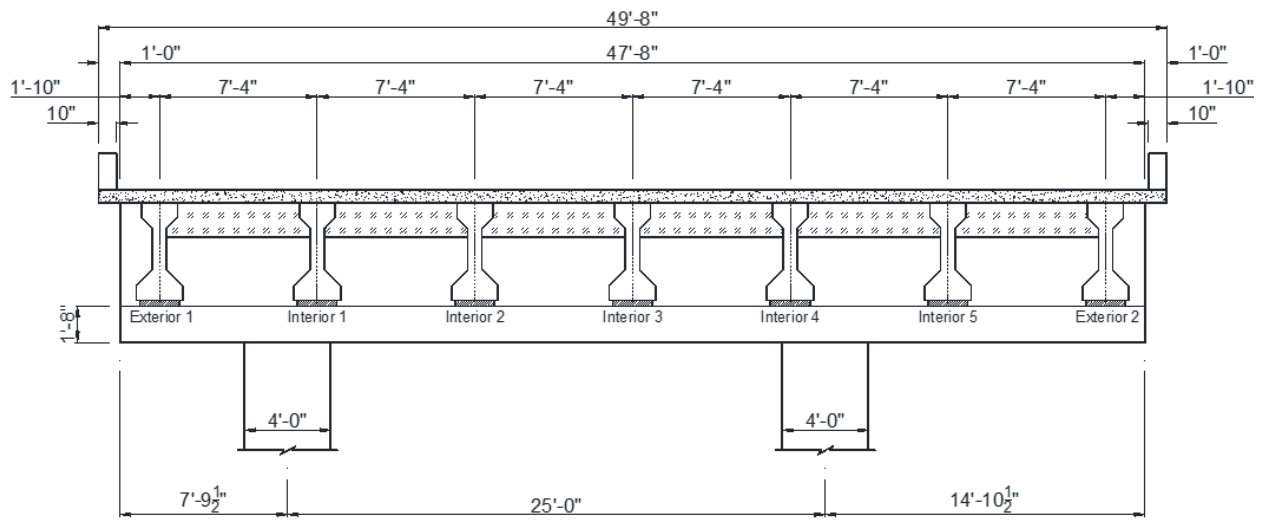
This chapter provides an overview of the experimental test program. Sections 2.1 and 2.2 provide descriptions of the inverted-T specimens and the retrofit solutions. Section 2.3 provides an overview of the test matrix. Sections 2.4 and 2.5 describe specimen construction and material properties. Sections 2.6 and 2.7 describe the test setup and instrumentation. Results and analysis of the experimental tests are provided in Chapters 3, 4, and 5.

2.1 Specimen Description

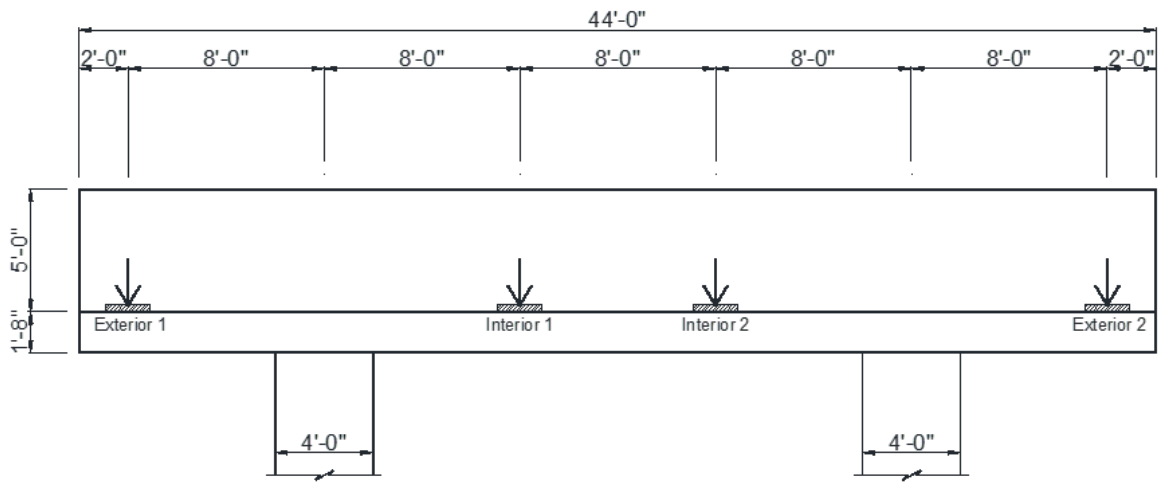
The test specimens were one-half scaled inverted-T bent caps designed for strain and stress similitude to represent characteristics and deficiencies of the IH 35 double-column inverted-T bents documented in Volume 1 (Hurlebaus et al., 2018a).

A full-scale prototype was adapted from Bent 13 with geometry altered slightly to account for laboratory constraints. Figure 2.1 provides a comparison of Bent 13 and the full-scale prototype structure geometry. Both structures have an average girder span of 115 ft.

The prototype structure included identical overhang lengths to provide consistency amongst test specimens. The overall prototype height was slightly reduced to accommodate clearance limits for the half-scale tests. Girders directly above the columns in Bent 13 were excluded from the prototype. Exterior girder locations were increased 2 in. from the edge of the bent cap, and interior girder spacing was increased 6 in. based on laboratory tie-down constraints. A consistent spacing of reinforcement was used in the prototype structure. A half-scale prototype was then defined with geometry equal to one-half that of the full-scale prototype. The bearing pad dimensions were 8 in. by 21 in. for the full-scale prototype and 5 in. by 12 in. for the half-scale prototype.



(a) Bent 13



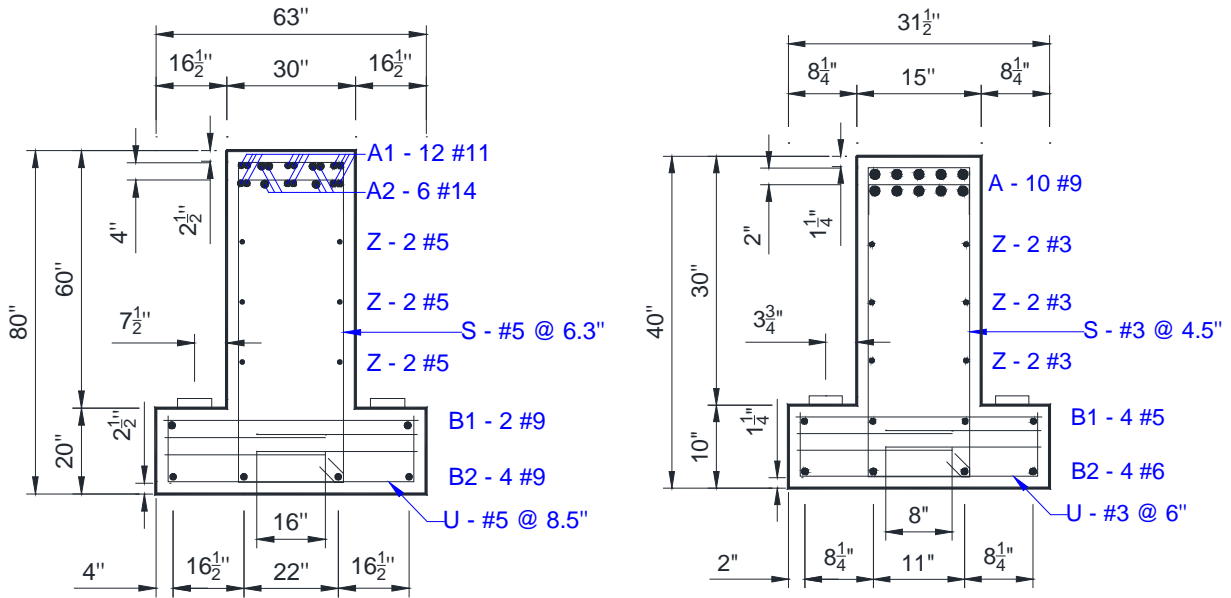
(b) Full-scale prototype

Figure 2.1. Geometry of Inverted-T Bent Caps for Design of Specimens.

Reinforcement of the full-scale prototype, shown in Figure 2.2(a), was adapted from the Bent 13 reinforcement, with adjustments made to reflect the changed geometry and to provide uniform spacing of reinforcement along the length. With material properties, the same in both prototypes, reinforcement for the half-scale prototype, shown in Figure 2.2(b), was scaled by adjusting the bar size and spacing. In the full-scale prototype, ledge and hanger reinforcement were #5 bars spaced at 8.5 in. and 6 in., respectively. In the half-scale prototype, ledge and hanger reinforcement were #3 bars spaced at 6 in. and 4.5 in., respectively. Flexural reinforcement was provided in the half-scale prototype to ensure sufficient strength to avoid flexural failure during testing of the retrofit solutions, with the layout of bars adjusted to allow for openings to secure specimens to the laboratory floor.

Table 2.1 provides a summary of the capacity of the full- and half-scale prototypes for deficiencies considered. The relative strengths for each failure mode were similar to those identified in the Volume 1 (Hurlebaus et al., 2018a) evaluation of IH 35 inverted-T bent caps.

In the experimental test program, the objective was to investigate the ability of retrofit solutions to strengthen specific deficiencies. To achieve this, the half-scale prototype was modified to provide two specimen designs with distinct deficiencies. For ease of construction, hanger and ledge reinforcement was specified to have the same spacing. Hanger-deficient specimens used an average spacing of 6 in. and increased the ledge reinforcement size from #3 to #4. Ledge-deficient specimens used an average spacing of 5.5 in. and increased the hanger reinforcement size from #3 to #4. Figure 2.3 and Figure 2.4 provide drawings of the hanger- and ledge-deficient specimens, respectively.



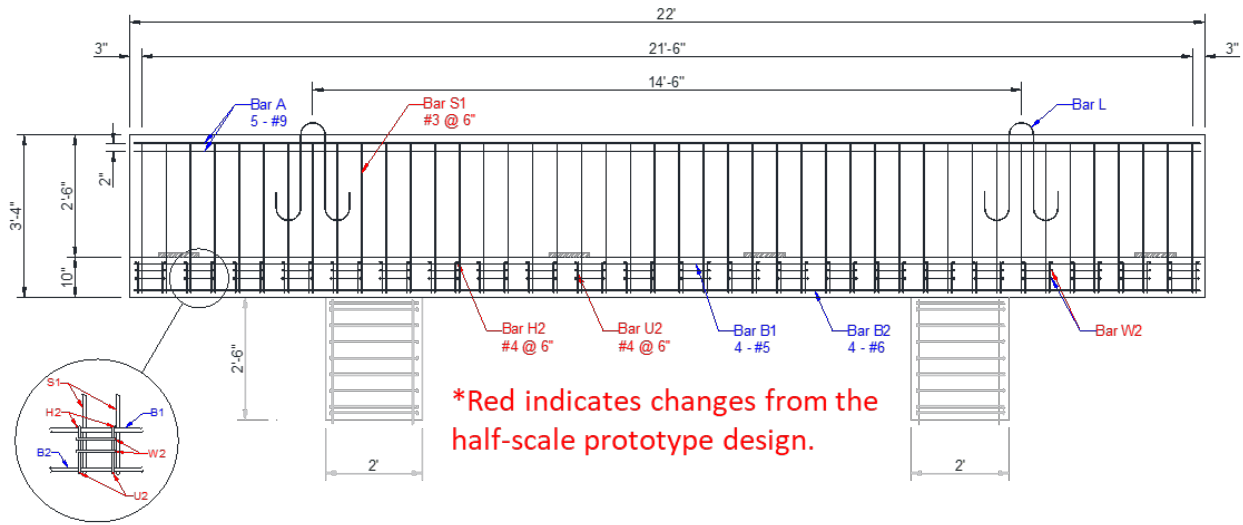
(a) Full-scale prototype

(b) Half-scale prototype

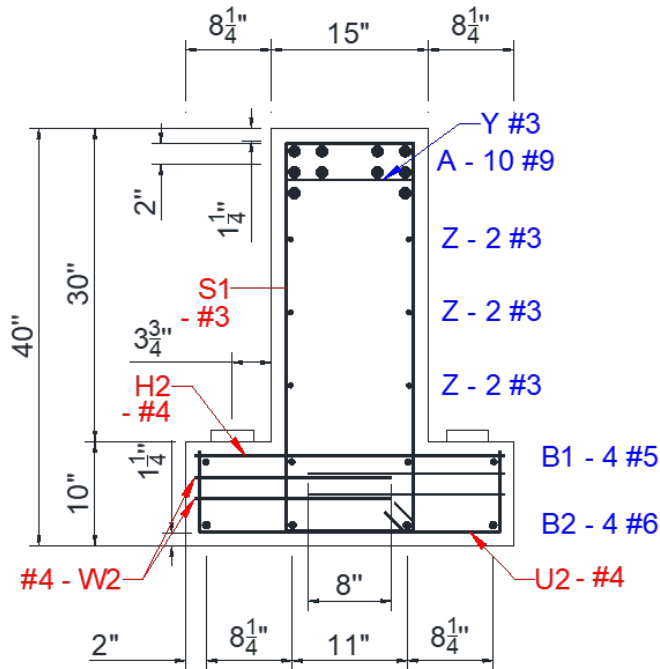
Figure 2.2. Geometry and Reinforcement of Prototype Bent Caps.

Table 2.1. Prototype Model Capacities.

Failure Mode	Part	Half-Scale Prototype (kips)	Full-Scale Prototype (kips)
Ledge Shear Friction	Ext.	151	605
	Int.	161	643
Ledge Flexure	Ext.	56	216
	Int.	83	320
Hanger	Ext.	53	206
	Int.	56	221
Punching Shear	Ext.	62	193
	Int.	76	299
Bearing	Ext.	253	937
	Int.	253	937

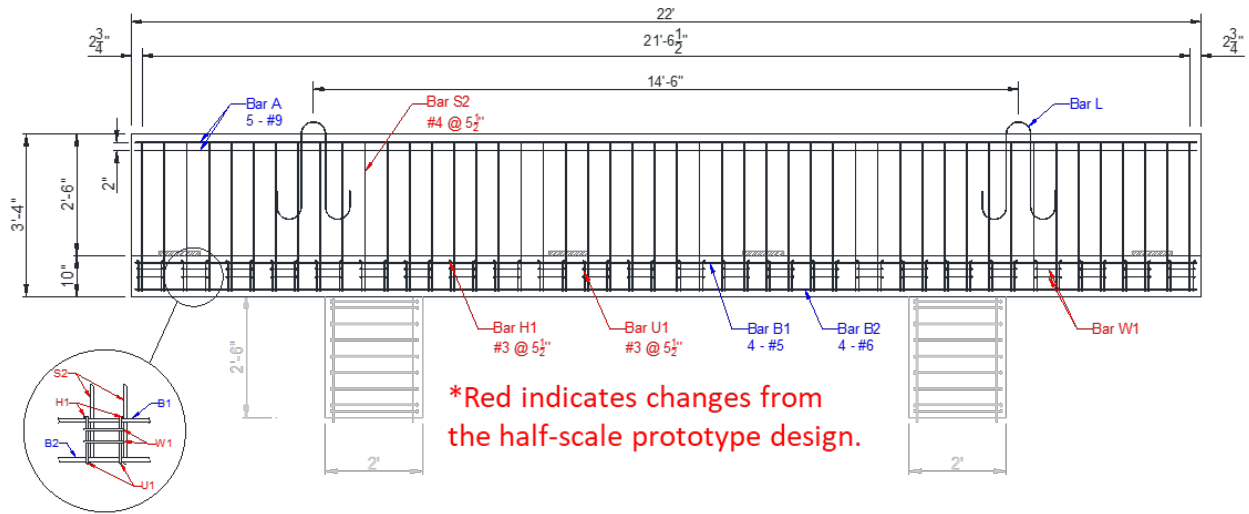


(a) Elevation

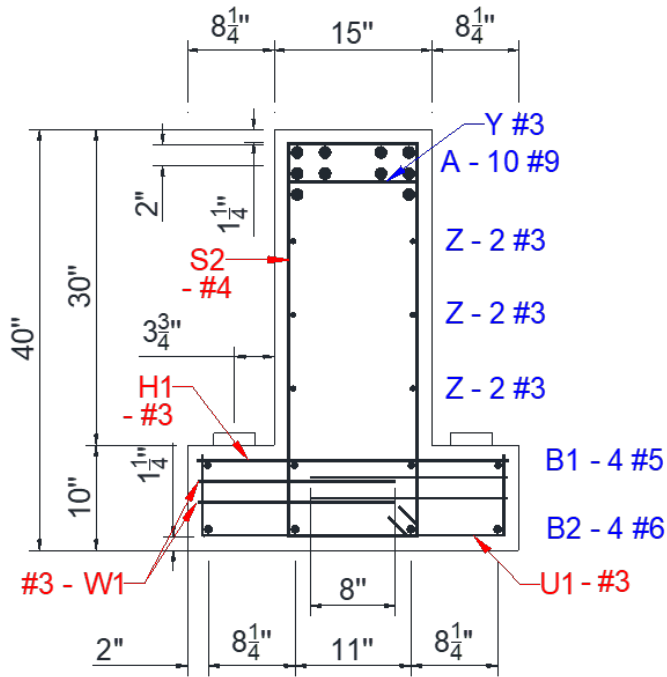


(b) Cross-section

Figure 2.3. Reinforcement Details of Hanger-Deficient Specimen.



(a) Elevation



(b) Cross-section

Figure 2.4. Reinforcement Details of Ledge-Deficient Specimen.

Table 2.2 presents the capacity hierarchy of the hanger-deficient and ledge-deficient specimens. The capacities shown in the table are single girder loads. The web shear and flexure capacities were calculated according to American Association of State and Highway Transportation Officials (AASHTO) load and resistance factor design (LRFD) specifications (AASHTO, 2014). Two punching shear capacities are provided. The first, which is used to establish failure mode hierarchy, uses the pad size for the scaled prototype. The second is a smaller pad size (4 in. by 4 in.) used to investigate the impact of pad size on punching shear capacity.

Table 2.2. Failure Hierarchy for Designed Reference Specimen.

Hanger-Deficient			Ledge-Deficient		
Exterior			Exterior		
Hierarchy	Part	Capacity (kips)	Hierarchy	Part	Capacity (kips)
1	Hanger	40	1	Ledge flexure	45
2	Punching shear	59	2	Punching shear	59 (49)*
3	Ledge flexure	80	3	Hanger	81
4	Ledge shear friction	130	4	Ledge shear friction	130
5	Beam shear	199	5	Beam shear	199
6	Flexure	217	6	Flexure	217
7	Bearing	284	7	Bearing	234
Interior			Interior		
Hierarchy	Part	Capacity, (kips)	Hierarchy	Part	Capacity (kips)
1	Hanger	48	1	Ledge flexure	69
2	Punching shear	72	2	Punching shear	72 (53)*
3	Ledge flexure	124	3	Hanger	86
4	Beam shear	137	4	Beam shear	137
5	Ledge shear friction	146	5	Ledge shear friction	146
6	Flexure	193	6	Flexure	193
7	Bearing	284	7	Bearing	234

*Punching shear capacity was calculated based on TxDOT BDM (2015); the second value indicates punching shear capacity with a 4 in. x 4 in. bearing pad.

2.2 Retrofit Descriptions

The retrofit solutions were adapted from the solutions designed for IH 35 Bent 13, with appropriate adaptations made for the half-scale tests and laboratory constraints. Details of each solution are provided in the following sections.

2.2.1 Solution 3: End-Region Stiffener

The end-region stiffener solution provides an increase in the hanger, ledge flexure, and punching shear capacity of the end region of the bent cap. Figure 2.5 shows the geometric details and anchor hole configuration for the half-scale laboratory specimens.

Eight 1/2 in. diameter Grade B7 epoxy anchors with an ultimate strength of 125 ksi were used. Layout of the anchors was modified from that in the Bent 13 retrofit designs to accommodate layout of the internal reinforcements. The steel plate was 3/8 in. thick, with 2-3/8 in. extensions on the top and bottom.

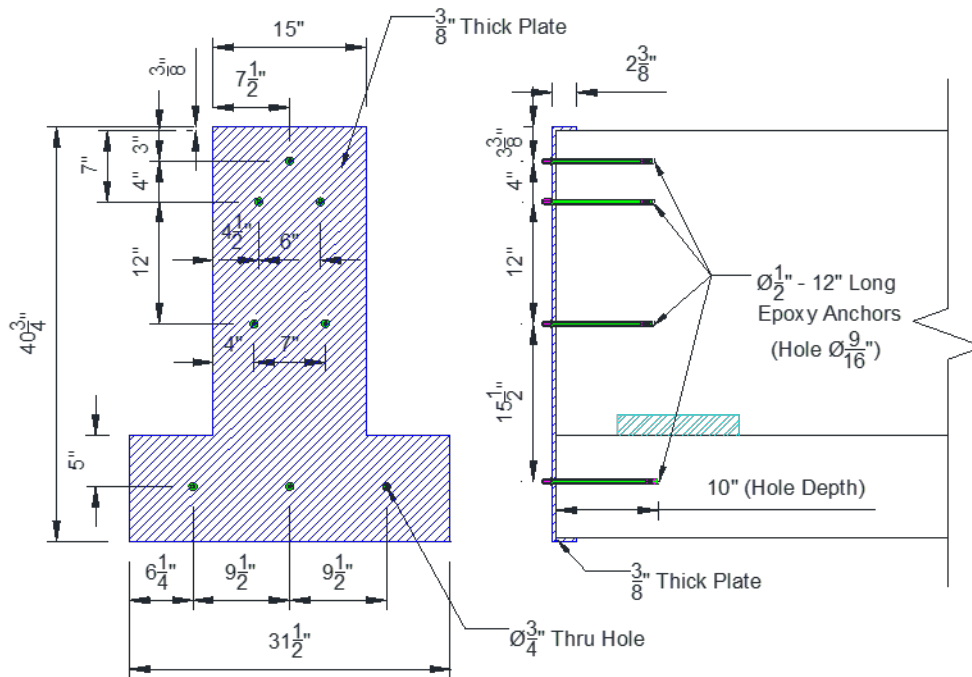
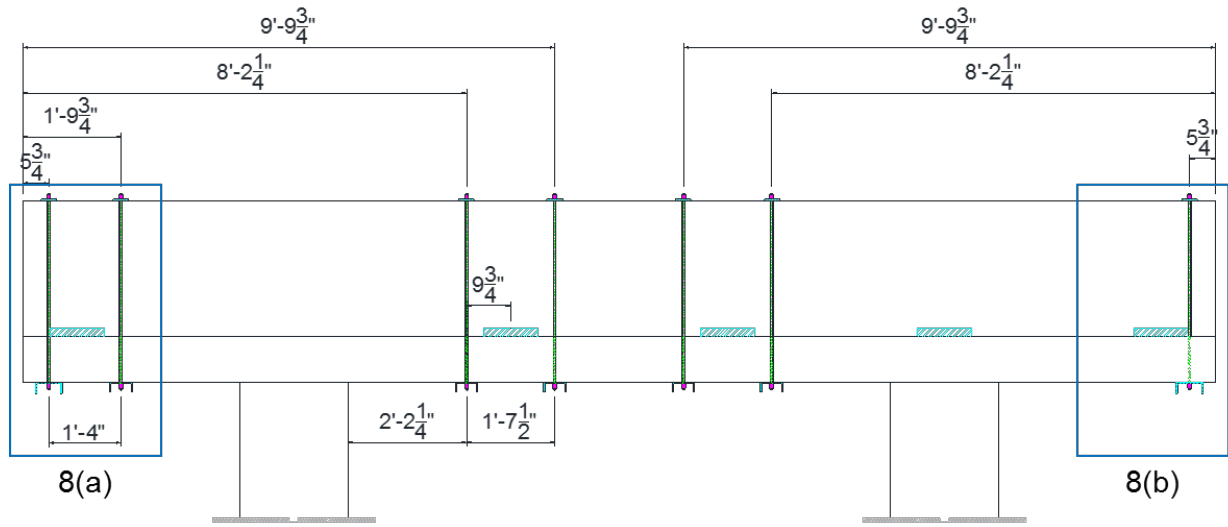


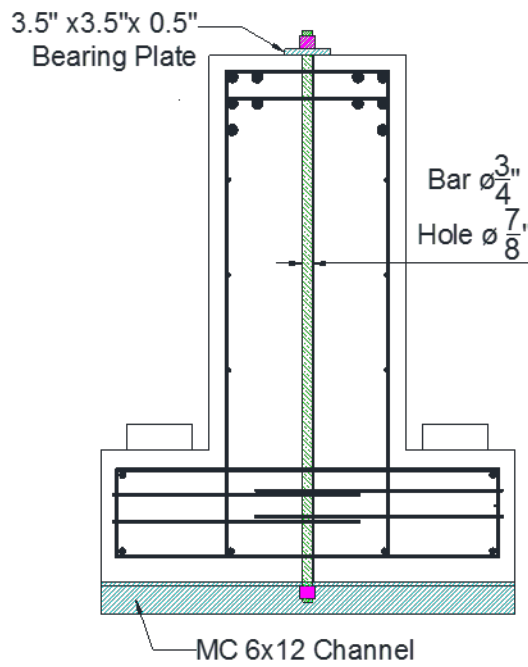
Figure 2.5. Solution 3—End-Region Stiffener.

2.2.2 Solution 8: Clamped Threadbar with Channel

In this solution, channels provide increased ledge flexure capacity and threadbars provide increased hanger capacity. Details of the solution for the half-scale specimens are shown in Figure 2.6. Two variations of the solution were implemented in the tests. Solution 8(a), used for both interior and exterior tests, included a threadbar and a channel on both sides of the applied load. Solution 8(b), used for exterior tests only, included a threadbar and a channel only on the exterior side of the applied load. In both variations, MC 6 x 12 channels were used with 3/4 in. Grade B7 high-impact threadbars with a 125 ksi ultimate strength. Bearing plates (0.5 in. x 3.5 in. x 3.5 in.) were provided at the top of the web.



(a) Elevation



(b) Cross-section

Figure 2.6. Solution 8—Clamped Threadbar with Channel.

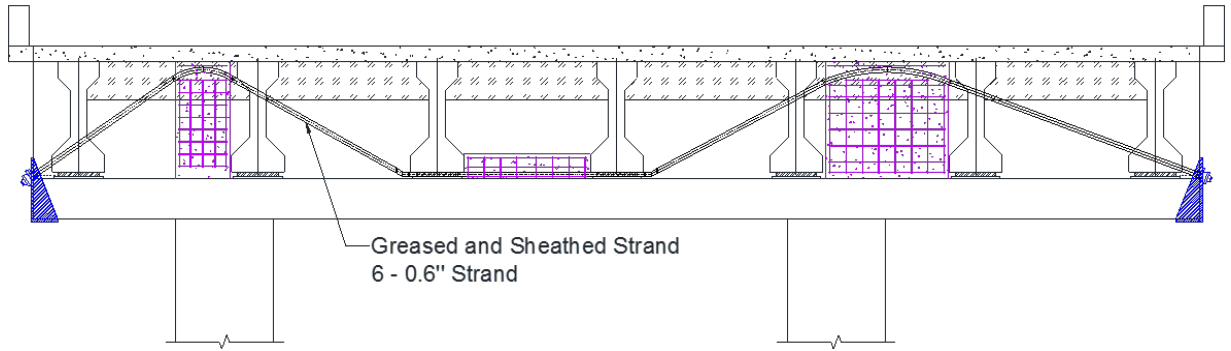
2.2.3 Solution 14: Load-Balancing PT

The load-balancing PT solution is applied to the full bent cap as shown in Figure 2.7(a) for Bent 13. The PT strands strengthen the hanger capacity of the bent cap by providing upward forces. By lifting the overhangs with the end-region anchor plate, the reaction forces to the PT are directly transferred into the columns. In the region between the two columns, the PT strands are placed beneath the girders.

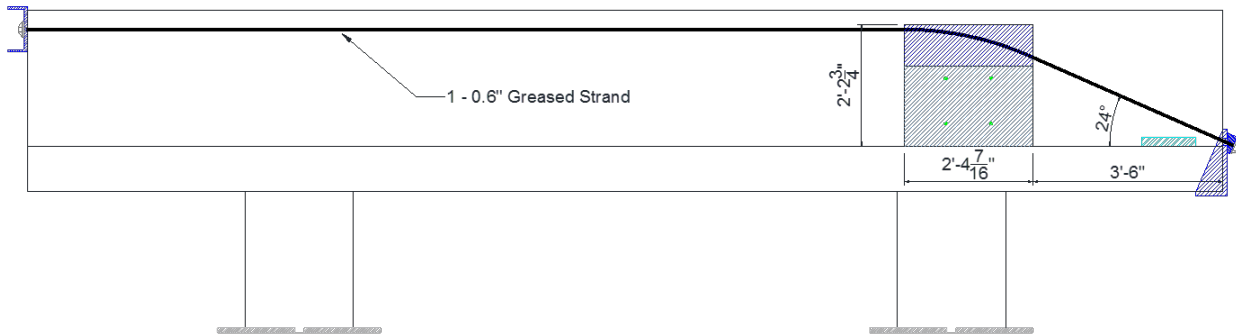
Unlike the prototype bent, the experimental tests load the interior and exterior regions separately, resulting in the tests for each region having a different PT strand configuration, shown in Figure 2.7(b) and (c), respectively. For ease of construction and testing, the concrete infill above the columns are replaced by steel deviator plates (Figure 2.8), attached with four Hilti Stainless Steel Kwik 3 Expansion Anchors with 5/8 in. diameter and 5-1/2 in. embedded depth.

For the half-scaled specimens, 0.6 in. strands are used. For exterior tests, one strand is used on each side of the stem. For interior tests, two strands are used on each side of the stem, with one strand passing in front of the load points and the other behind. The configuration of strands, including anchorage locations, is shown in Figure 2.8(c).

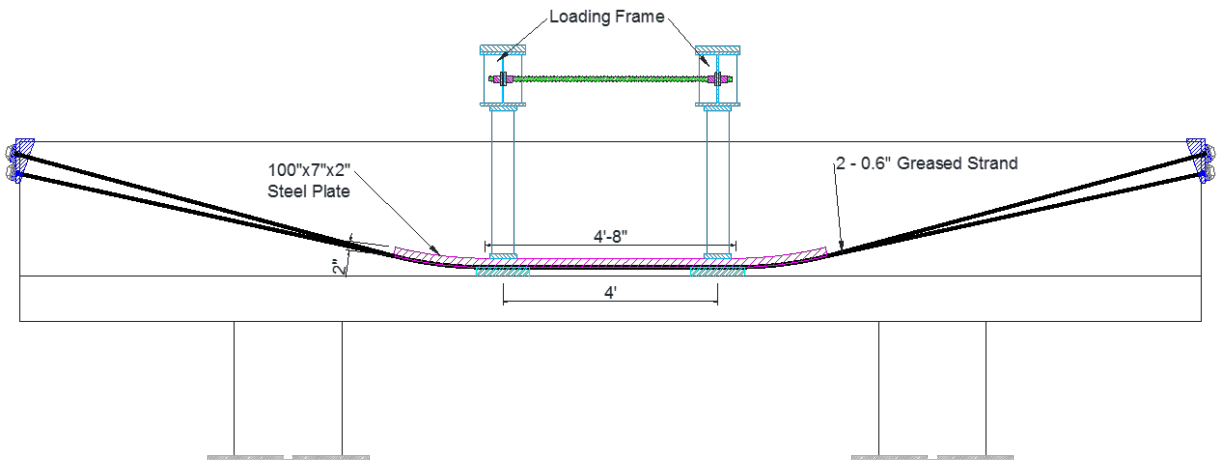
The angles for the interior and exterior tests are 14 degrees and 24 degrees, respectively. The post-tensioning force in each strand is 40 kips (70 percent of the ultimate strength of the strand), providing an uplift force of 19 kips and 16 kips for the interior and exterior portions, respectively. Anchor plates are designed based on bearing strength. Details of the anchor plates are shown in Figure 2.9.



(a) Side elevation view for Bent 13

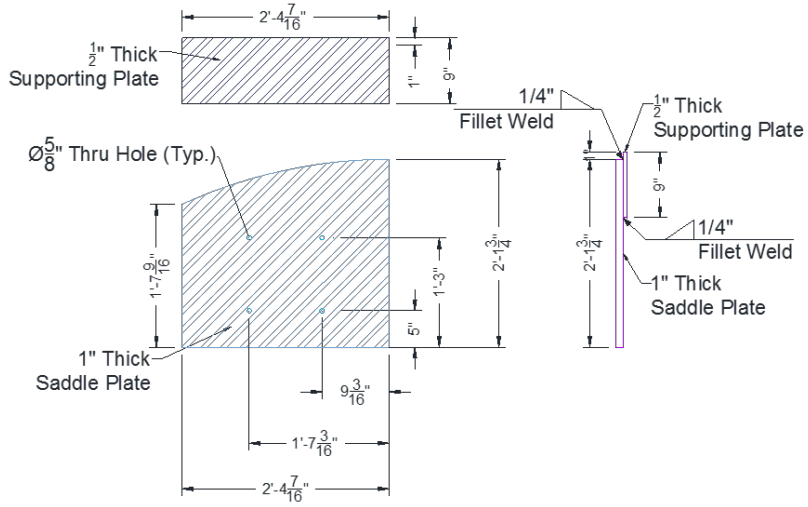


(b) Side elevation view for exterior part of specimen

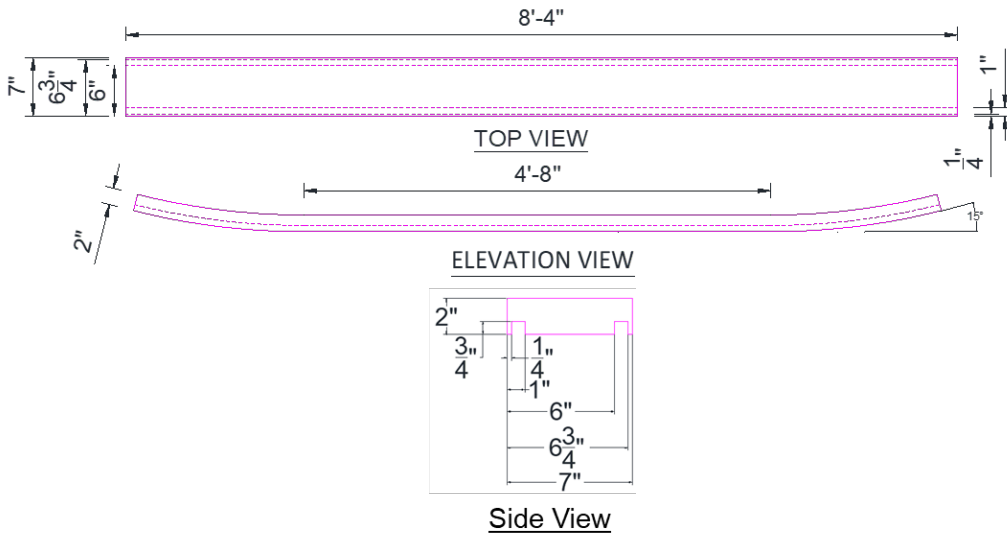


(c) Side elevation view for interior part of specimen

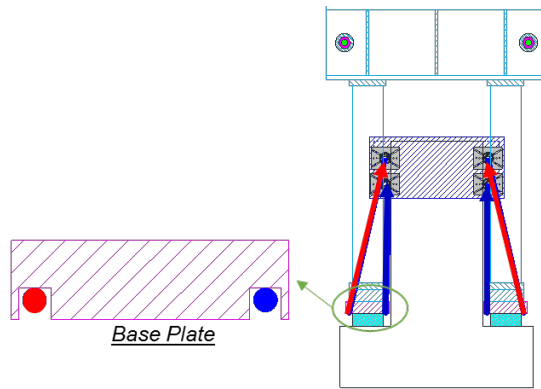
Figure 2.7. Solution 14—Load-Balancing PT.



(a) Steel deviator plate for exterior test

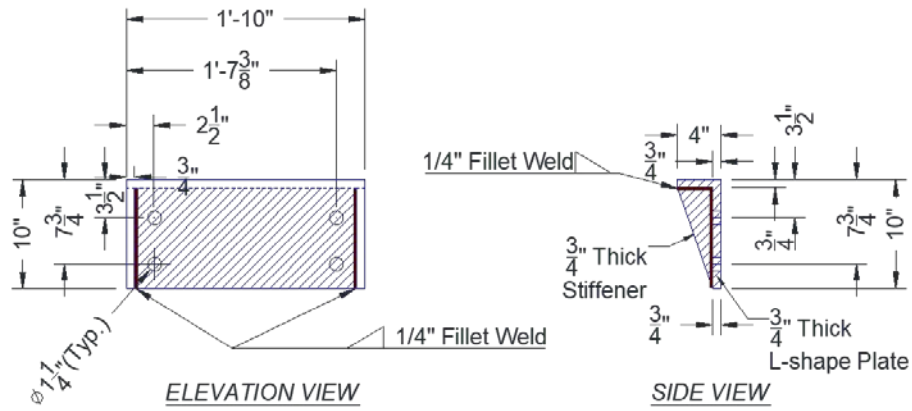


(b) Steel base plate for interior test

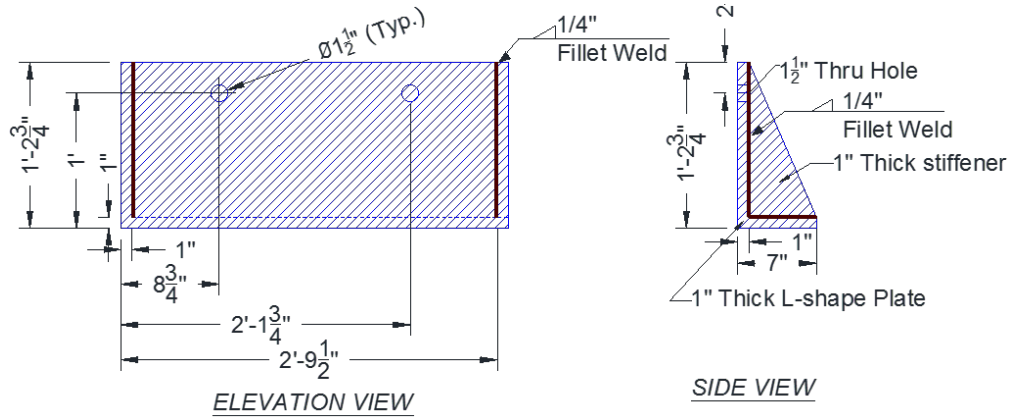


(c) Strand details for interior test

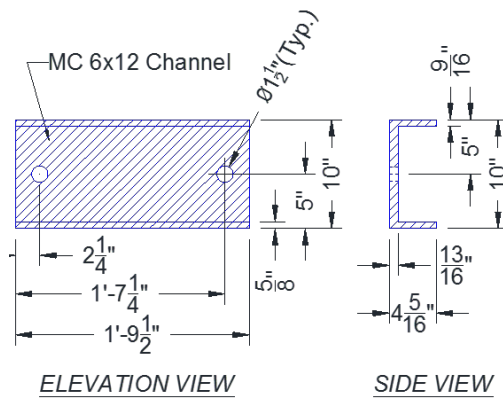
Figure 2.8. Steel Plate for Locating PT Strand.



(a) Anchor plate for interior strengthening



(b) Bottom anchor plate for exterior strengthening



(c) Top anchor channel for exterior strengthening

Figure 2.9. Anchor Plates for PT Strand.

2.2.4 Solution 16: Concrete Infill with Partial-Depth FRP Anchored by Steel Waling

Solution 16 utilizes a partial-depth FRP wrap. The solution is intended for bridges with a diaphragm and provides an increase in the ledge and punching shear capacities. Infill concrete provides a rectangular cross-section to minimize FRP bends. The FRP is held in place with steel walings.

Since the concrete infill is not loaded with significant force, minimum reinforcement is provided. Transverse reinforcement is arranged to avoid interference with the 1/2 in. diameter threadbars (150 ksi, Grade B7 high-impact threadbar) that provide (a) continuity between the new and old concrete, and (b) a location for attachment of the walings. Detailed drawings of the solution are shown in Figure 2.10(a) and (b).

The FRP was a unidirectional high-strength carbon fiber fabric, MasterBrace FIB 600/50 CFS, with epoxy components MasterBrace P 3500 (epoxy primer), MasterBrace F 2000 (epoxy paste), and MasterBrace SAT 4500 (epoxy encapsulation resin).

Figure 2.10(c) illustrates the FRP wrapping scheme for the exterior. Part 1 is a U-shaped FRP strip attached to the ledge and infill concrete block. Part 2 is a 5 in. wide side strip applied around the full section, with a splice of 15 in. at the top of the web. Part 3 and 4 are U-shaped strips applied to the end face. Part 3 has a 5 in. extension at the top and a 10 in. extension at the bottom. Part 4 extends 18 in. along the sides of the ledge, providing no overlap with Part 1. Interior solutions consist of Part 1 only.

2.2.5 Solution 17: Concrete Infill with Full-Depth FRP Anchored by Steel Waling

Solution 17 utilizes a full-depth FRP wrap. The solution is intended for bridges without a diaphragm and provides an increase in the hanger, ledge, and punching shear capacities. Infill concrete provides a rectangular cross-section to minimize FRP bends. The FRP is held in place with steel walings.

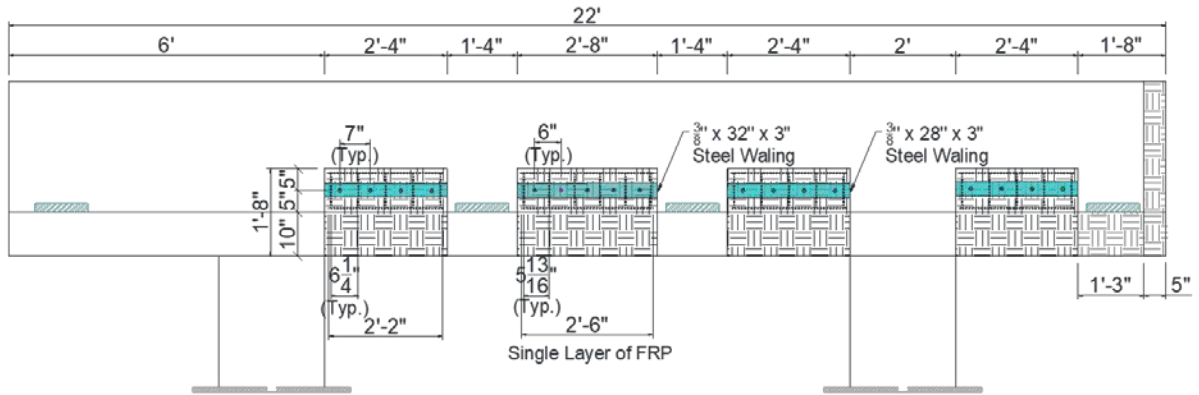
Since the concrete infill is not loaded with significant force, minimum reinforcement is provided. Transverse reinforcement is arranged to avoid interference with the 1/2 in. diameter threadbars (150 ksi, Grade B7 high-impact threadbars) that provide continuity between new and old concrete and a location of attachment for the walings. Detail drawings of the solution are shown in Figure 2.11(a) and (b). Threadbars are placed in two layers, with the steel waling at the top layer.

The FRP is a unidirectional high-strength carbon fiber fabric, MasterBrace FIB 600/50 CFS. Epoxy components are MasterBrace P 3500 (epoxy primer), MasterBrace F 2000 (epoxy paste), and MasterBrace SAT 4500 (epoxy encapsulation resin).

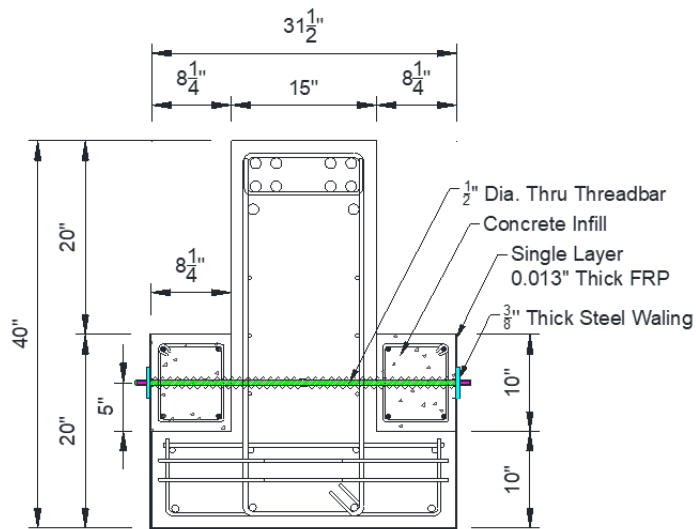
The wrapping scheme for exterior application of Solution 17 is similar to Solution 16. A longer development length is used for Part 4 of Solution 17. An additional 8 in. wide bandage strip passes below the ledge (adjacent to Strip 2, overlapping Strip 3 by 4 in.) to provide anchorage for the bottom of Part 3. For Solution 17(a), shown in Figure 2.11(c), the bandage strip extends to the center of the bearing pad. For Solution 17(b), shown in Figure 2.11(d), the bandage strip terminates at the top edge of the ledge.

2.2.6 Solution 18: Large Bearing Pad

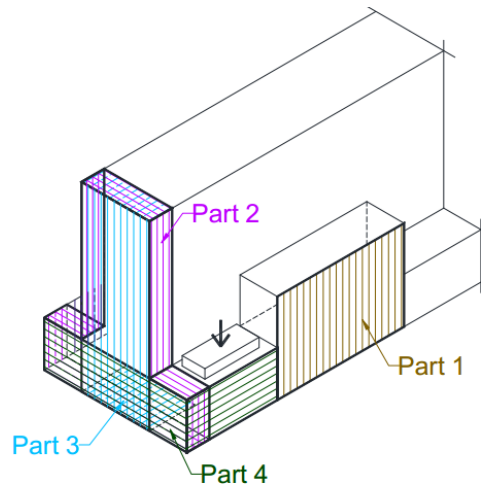
Solution 18 changes the current bearing pad size to improve the punching shear capacity. For the specimens, the half-scale bearing pad size is 5 in. x 12 in. Due to the small dimensions of the scaled specimens, an increase in the pad size was not practical. Thus, a smaller pad size (4 in x 4 in.) was adopted to assess the impact of pad size on punching shear capacity.



(a) Elevation

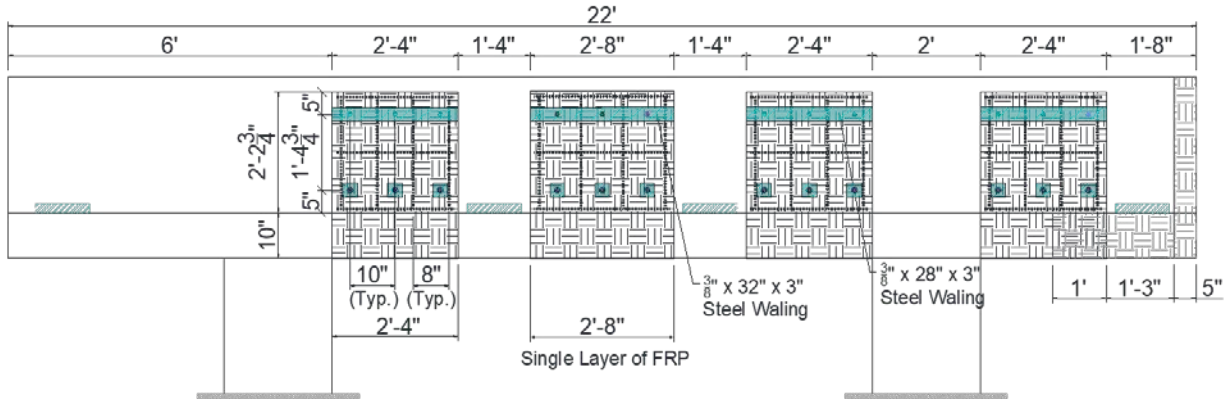


(b) Cross-section

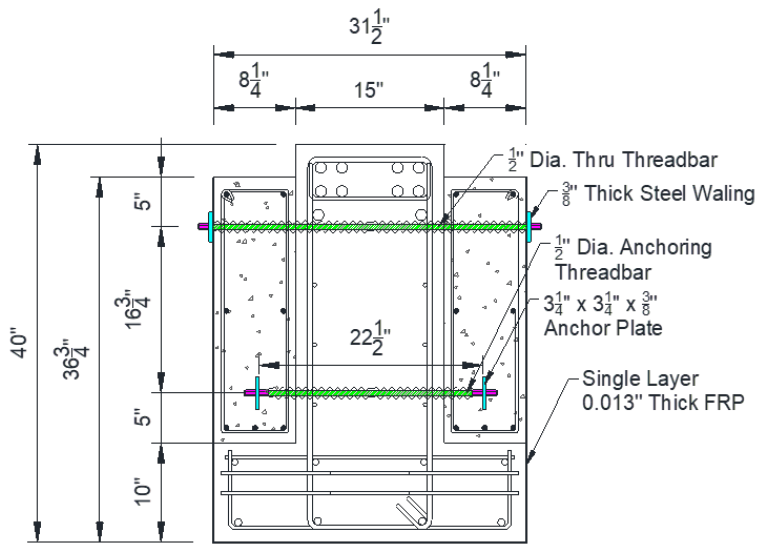


(c) Exterior application

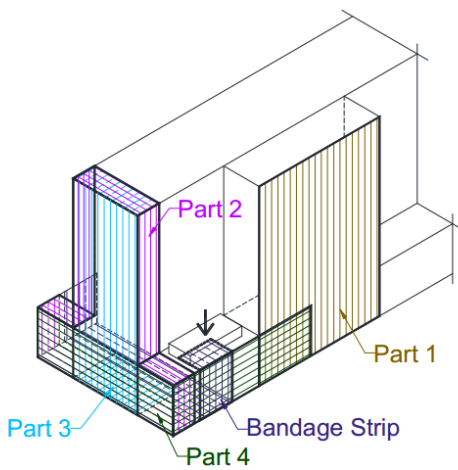
Figure 2.10. Solution 16—Solution for Punching Shear and Ledge Shear Failure Using FRP Sheets with Concrete Infill and Steel Waling.



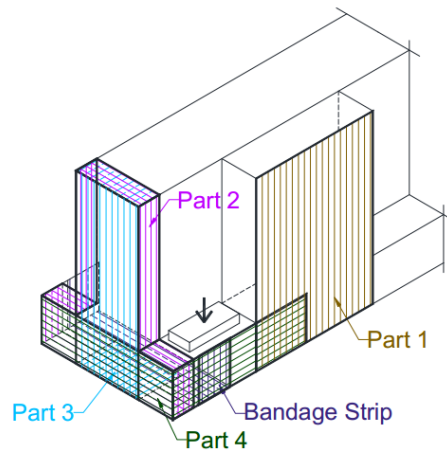
(a) Elevation



(b) Cross-section



(c) Exterior application for Solution 17(a)



(d) Exterior application for Solution 17(b)

Figure 2.11. Solution 17—Solution for Hanger, Punching Shear, and Ledge Shear Failure Using FRP Sheets with Concrete Infill and Steel Waling.

2.3 Test Matrix

Eight specimens, three hanger-deficient and five ledge-deficient, were constructed. Each test consisted of three test regions (two exteriors and one interior). Some test regions were tested multiple times, leading to thirty-three individual tests. Table 2.3 lists details for each specimen with their corresponding retrofit solutions. The nomenclature of the test name is defined in Figure 2.12.

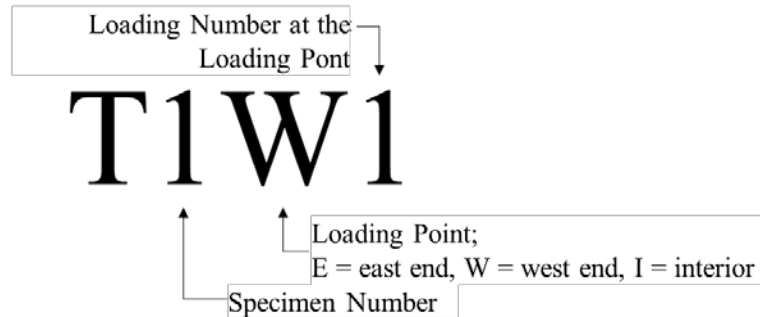


Figure 2.12. Test Nomenclature.

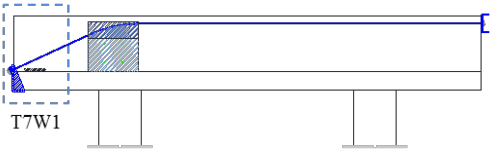
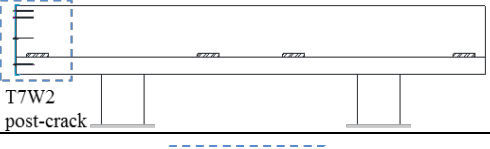
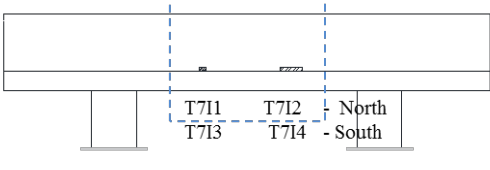
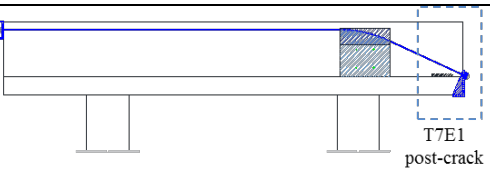
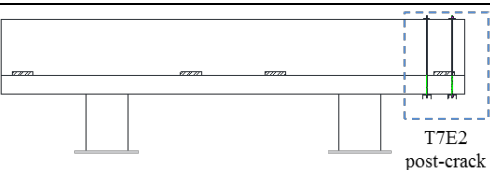
Control tests were conducted on both hanger-deficient (T1W1, T1E1) and ledge-deficient (T5E1, T5I1) specimens without retrofit solutions. Hanger-deficient specimen tests included retrofit Solution 14 (load-balancing PT), Solution 3 (end-region stiffener, exterior only), both variations of Solution 8 (threadbar with channel), and Solution 17 (full-depth FRP with steel waling); all Solution 17 tests and one Solution 8 test (T8E1) were implemented after cracks had occurred during prior tests. Ledge-deficient specimen tests included retrofit Solution 14 (load-balancing PT, exterior only), Solution 3 (end-region stiffener, exterior only), variation of Solution 8, Solution 16 (partial-depth FRP with steel waling), and Solution 17 (full-depth FRP with steel waling, exterior only); one Solution 3 (T7W2), one Solution 17 (T7E1), and one Solution 8 (T7E2) tests were implemented after cracks had occurred during prior tests. Punching shear tests with both pad sizes (Solution 18) were conducted on Specimens 3 and 7; smaller pad sizes are referred to as the reference punching strength tests.

Table 2.3. Test Matrix.

Specimen ¹	Test	Retrofit Solution	Purpose of Retrofit ²	Loading	Scheme
1 (HD)	T1W1	None	Hanger Reference	W Ext.	
	T1I1	None	Hanger Reference	Int.	
	T1E1	8(a)	H, L, P	E Ext.	
2 (HD)	T2W1	14	H, L, P	W Ext.	
	T2I1	14	H, L, P	Int.	
	T2I2	17 Post-crack	H, L, P	Int.	
	T2W2	17 Post-crack	H, L, P	W Ext.	
	T2E1	3	H, L, P	E Ext.	
8 (HD)	T8W1	8(b)	H, L, P	W Ext.	
	T8I1	8(a)	H, L, P	Int.	
	T8E1	8(a) Post-crack	H, L, P	E Ext.	
3 (LD)	T3W1	None	Punching Reference	NW Ext.	
	T3I1	None	Punching Reference	SW Int.	
	T3I2	18	P	NE Int.	
	T3I3	18	P	NW Int.	
	T3E1	18	P	SE Ext.	
4 (LD)	T4W1	8	H, L, P	W Ext.	
	T4I1	8	H, L, P	Int.	
	T4E1	8	H, L, P	E Ext.	
5 (LD)	T5E1	None	Ledge Reference	E Ext.	
	T5I1	None	Ledge Reference	Int.	
	T5W1	3	H, L, P	W Ext.	
6 (LD)	T6W1	16	L, P	W Ext.	
	T6I1	16	L, P	Int.	
	T6E1	17	H, L, P	E Ext.	

Note: HD = hanger-deficient, LD = ledge-deficient, H = hanger, L = ledge flexure, and P = punching shear.

Table 2.3. Test Matrix (Continued).

Specimen ¹	Test	Retrofit Solution	Purpose of Retrofit ²	Loading	Scheme
7 (LD)	T7W1	14	H, L, P	W Ext.	
	T7W2	3 Post-crack	H, L, P	W Ext.	
	T7I1	None	Punching Reference	NW Int.	
	T7I2	18	P	NE Int.	
	T7I3	None	Punching Reference	SW Int.	
	T7I4	18	P	SE Int.	
	T7E1	14 Post-crack	H, L, P	E Ext.	
T7E2	8(a) Post-crack	H, L, P	E Ext.		

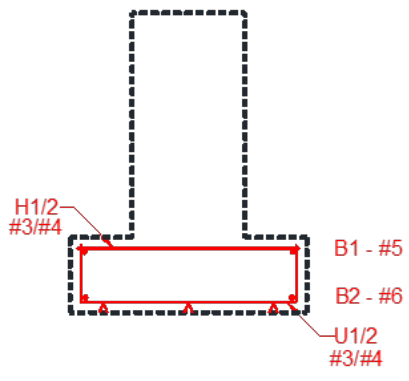
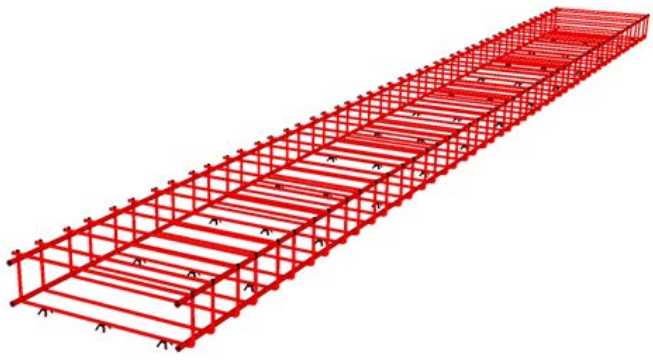
Note: HD = hanger-deficient, LD = ledge-deficient, H = hanger, L = ledge flexure, and P = punching shear.

2.4 Specimen Construction

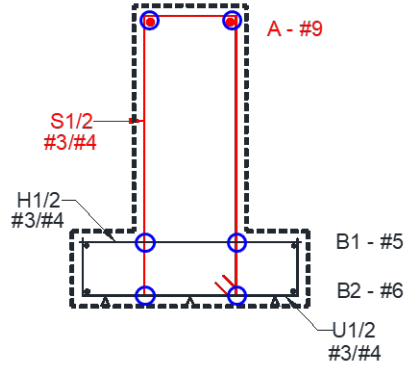
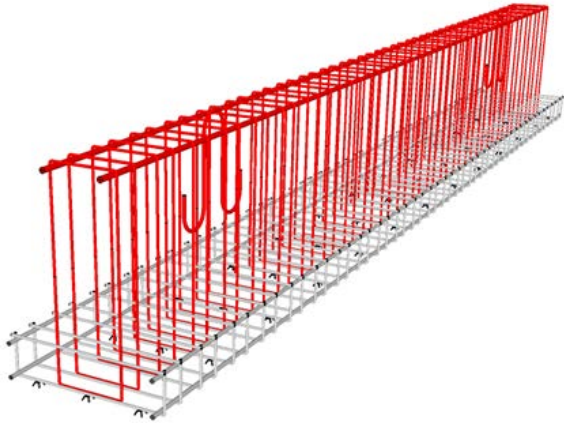
Eight bent cap specimens were constructed in pairs at the Texas A&M RELLIS Campus. Specimens were shipped to the High Bay Structural and Materials Testing Lab, where they were installed on reusable columns. All strengthening solutions were implemented after specimen installation. The following sections provide a detailed description of each stage of the construction process.

2.4.1 Bent Cap Construction

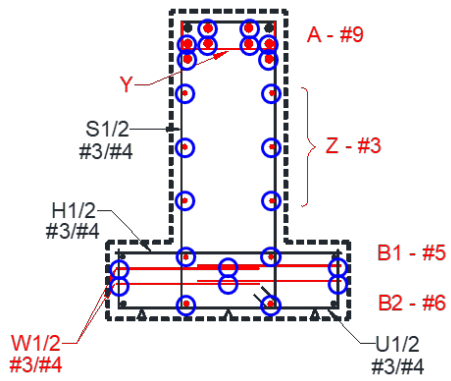
The rebar cages were tied prior to placement in the formwork. Figure 2.13 shows the assembly steps of the rebar cages; the rebar relevant to each step is shown in red, with blue circles indicating the rebar tying locations. Figure 2.14 shows the photos of each step after completion including a closer view of negative flexural and ledge shear friction reinforcement. The ledge reinforcement cage (U, H, B1, and B2 bars) was assembled first (Figure 2.13[a]).



(a) Step 1



(b) Step 2



(c) Step 3

Figure 2.13. Inverted-T Rebar Cage Assembly Steps.



(a) Step 1



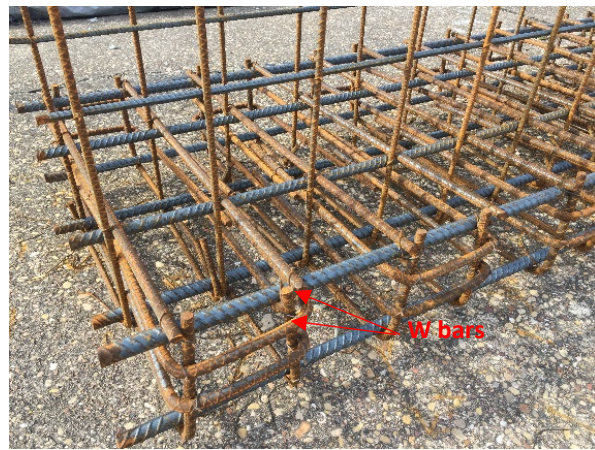
(b) Step 2



(c) Step 3



(d) Negative flexure reinforcement



(e) Shear friction reinforcement

Figure 2.14. Inverted-T Rebar Cage.

Chairs were tied to the cage every 2 ft along the length to provide clear cover of 1-1/4 in. At each location, three chairs were used in one transverse plane. Next, the hanger reinforcement (S1/S2 bars) and the top longitudinal reinforcement (A bars) were added to the cage (Figure 2.13[b]). Lifting hooks were placed at the third points. Two 2x4 studs were provided at each end of the steel cage in the opposite angles to brace the steel cage against sway during assembly (Figure 2.14[b]). Finally, the remaining reinforcing bars (Z, Y, A, and W bars) were added to the cage. The A bars were arranged to allow room for holes for specimen tie down and installation of retrofit solutions (Figure 2.13[c]).

Wooden formwork was constructed for fabrication of two specimens end to end. The formwork was reused for all four concrete pours. Figure 2.15 shows a three-dimensional (3D) view illustrating the fabrication of the formwork. The formwork consisted of six main components, as indicated in Figure 2.15(a) and (c): (1) bottom panel, (2) outside panel, (3) inside panel, (4) end panel, (5) diagonal braces, and (6) middle panel. Interior surfaces of the formwork were painted with semi-gloss latex paint. The formwork components were assembled using wood screws. Figure 2.16 shows photos of the formwork assembly process. The bottom panels were screwed together to form the floor of the formwork. The outside panels were then erected on the bottom panels and laterally supported by the diagonal braces. The steel cages were placed into the formwork using a forklift (Figure 2.16[a]). The inside panels were lowered into the formwork and fixed from the outside wall at their corresponding positions (Figure 2.16[b]). Then the end panels and mid-panel were placed in position to enclose and seal the formwork (Figure 2.16[c] and [d]). All the interior surfaces of the formwork were cleaned and oiled before closure. Wood holding frames were installed to keep the embedded steel pipe in position (Figure 2.16[e]). Chairs were provided on the sides of the steel cage to ensure the required clear side cover (Figure 2.16[f]). Figure 2.16(g) shows formwork ties provided every 8 ft to prevent lateral expansion. The concrete for the specimens was provided by local ready-mix concrete company Martin Marietta Materials. Slump tests were performed according to ASTM C143 (ASTM, 2012) for every pour. Figure 2.17 shows photos during a typical concrete pour. The concrete was directly placed into the formwork from the concrete truck (Figure 2.17[a]). Proper consolidation was achieved using rod vibrators (Figure 2.17[b]). The specimen surface was finished with smooth trowels (Figure 2.17[c]). Approximately one hour after concrete placement, filleted trowels were used to provide smooth round edges at the top surface of the specimen. Once the concrete hardened, the surface was watered and covered with soaked burlap mats and tarps for four days of moist curing. Formwork was removed after seven days. Figure 2.18 shows the specimens after removal of the formwork.

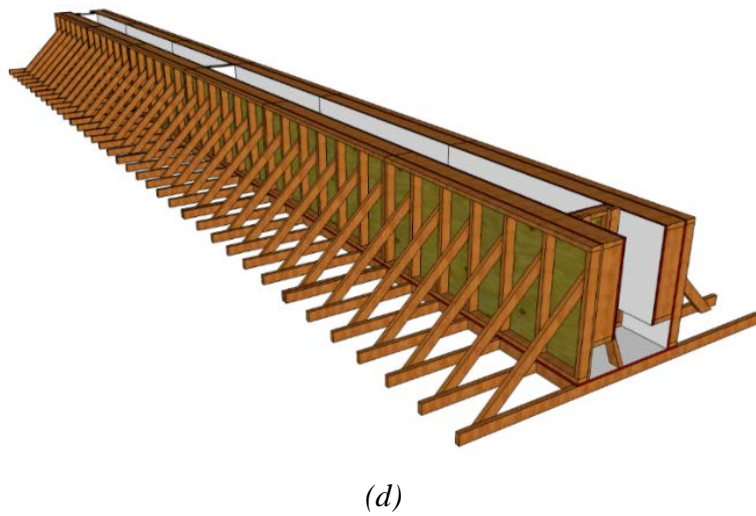
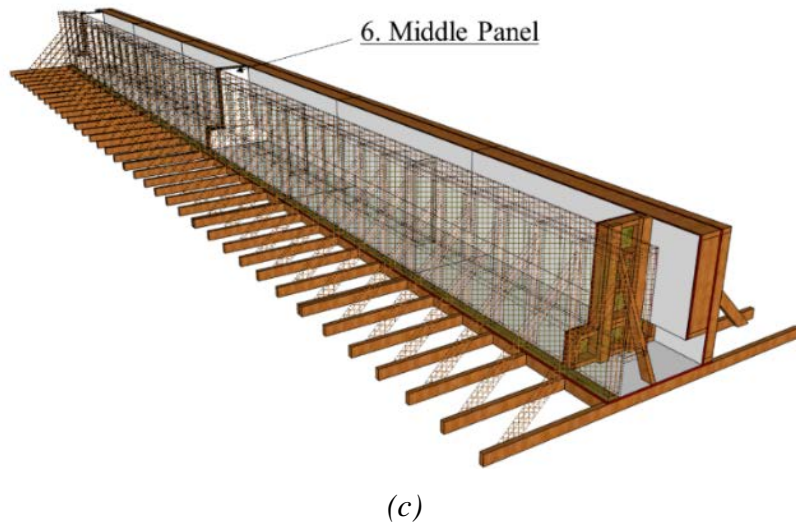
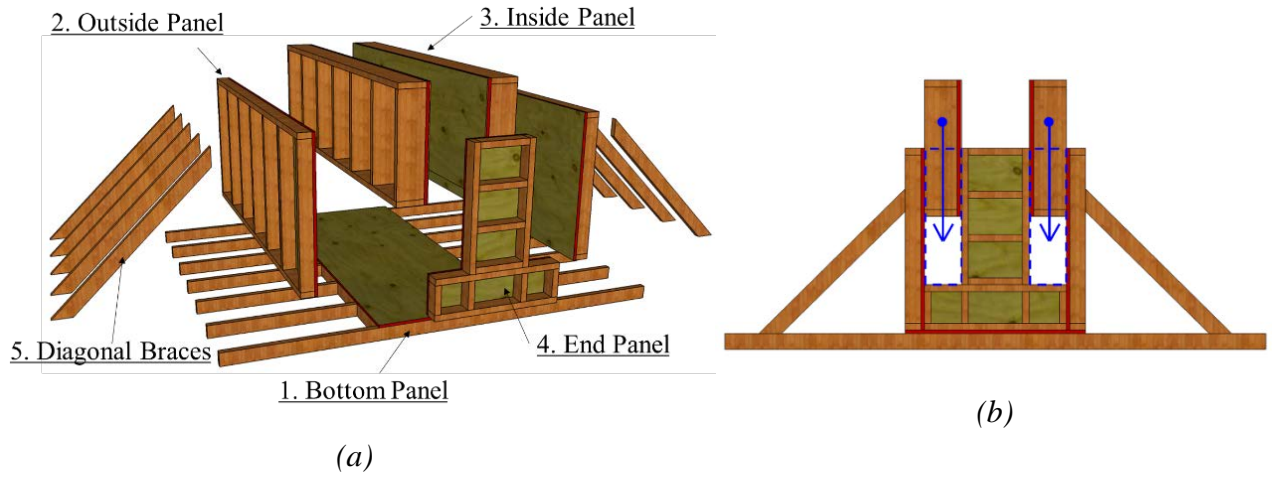


Figure 2.15. 3D View of the Formwork.



(a) *Placing rebar cages*



(b) *Lowering inside panels*



(c) *End panels*



(d) *Middle panel*



(e) *Steel pipe holding frame*



(f) *Side chair*



(g) *Formwork tie*

Figure 2.16. Formwork Assembly.



(a) Concrete placement



(b) Vibrating concrete



(c) Smoothing surface



(d) Finished surface

Figure 2.17. Casting of Inverted-T Specimens.



Figure 2.18. Uncovered Specimens.

2.4.2 Column Construction

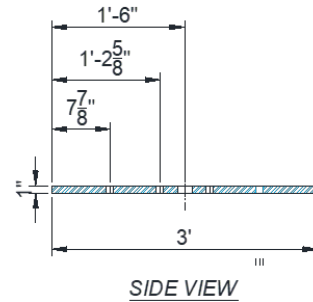
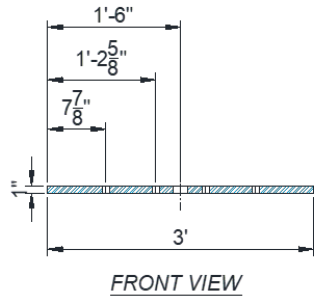
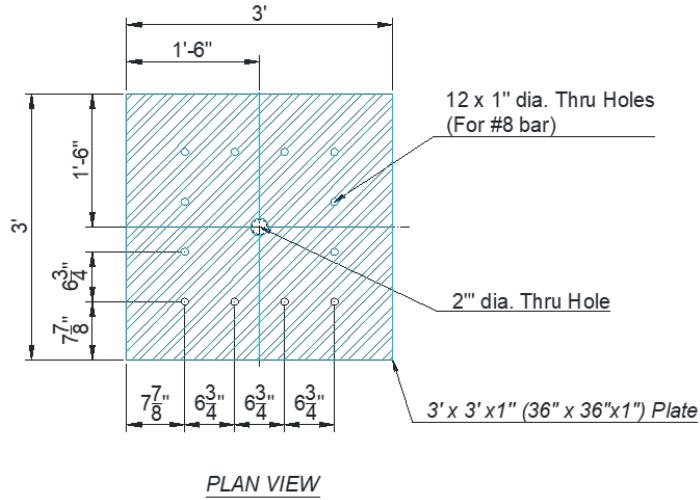
The column cross-section dimensions were half-scaled from the prototype structure, with reinforcement designed to resist expected laboratory load demands. Figure 2.19 shows the column after the formwork was removed. The column concrete had a design strength of 10 ksi to ensure minimal, if any, damage, thereby enabling reuse of the columns. Column reinforcement details are shown in Figure 2.20. A steel plate formed the bottom of the columns, with longitudinal bars welded into predrilled holes. Flexural reinforcement consisted of 12-#8 bars. Nine rectangular and octagonal #3 hoops spaced at 4 in. provided confinement (Figure 2.20[b]). A 1-1/2 in. diameter steel pipe in the center of the column allowed for a Dywidag bar to clamp the specimen, a column, and the strong floor together. Rebar extending from the sides of the columns was provided for assistance with column placement during test setup.



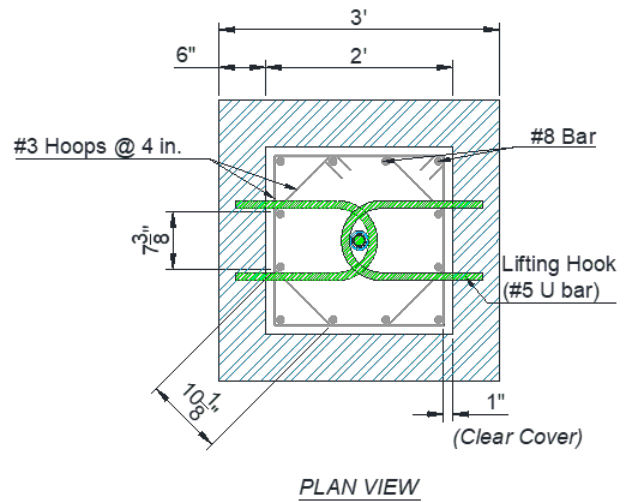
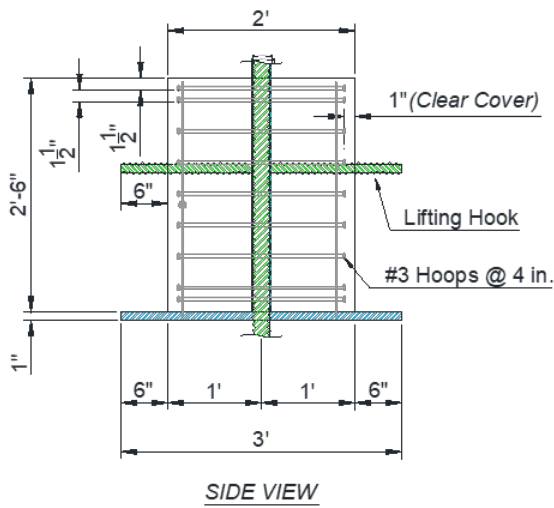
Figure 2.19. Support Column with Lifting Hooks.

2.4.3 Specimen Assembly

The column-base plate was leveled using dental stone, as shown in Figure 2.21. Once the columns were set on the floor, dental stone was placed on the top of the column to provide a level surface. Figure 2.22 shows the installation procedure of a specimen on the columns. A 1-3/8 in. Dywidag bar clamped the bent cap and a column together onto the strong floor. The bars were stressed with 75 kips force.



(a) Base plate design



(b) Column reinforcement

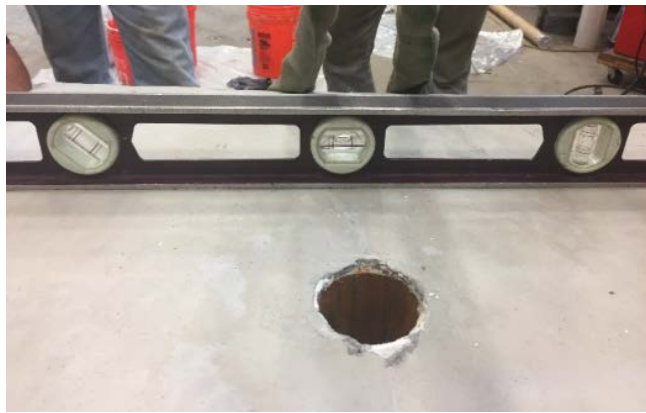
Figure 2.20. Column Details.



(a) Place Ziploc bag with dental stone



(b) Place column on the dental stone



(c) Check level of the column

Figure 2.21. Leveling Column on Strong Floor.

2.4.4 End-Region Stiffener Installation

The end-region stiffener (Solution 3) consists of a steel plate and eight epoxy anchors. First, the steel plate was placed to mark and drill the holes for the anchors (Figure 2.23[a]). Holes were drilled with a hammer drill. A rebar cutter bit was used to cut through bottom W bars on three specimens (T2 east end, south anchor; T5 west end, north and south anchors; T7 west end, north anchor). Holes drilled with the rebar cutter required approximately one hour per a hole; all other holes required approximately one minute per a hole. Once all holes were drilled, the steel plate was removed and holes were cleaned using an air gun and 3/4 in. nylon brush. Epoxy was put into the holes using a standard caulking gun and mixing nozzle (Figure 2.23[b]). The anchors were placed immediately.



(a) Shims to align column and specimen



(b) Mixing dental stone and filling on the top of column to level surface

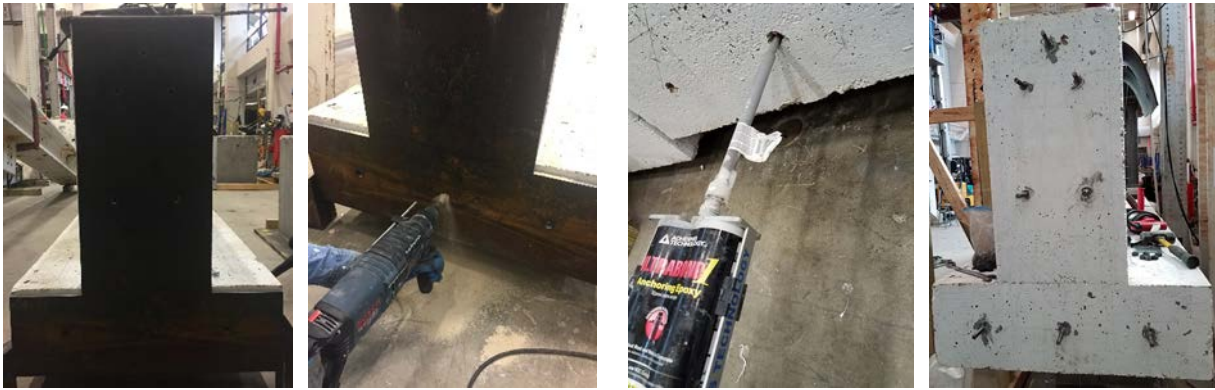


(c) Placement of specimen on column



(d) Stressing Dywidag bar to clamp specimen to floor

Figure 2.22. Installing a Specimen on the Columns.



(a) Place steel plate, mark holes, and drill the holes with hammer drill

(b) Put epoxy in the holes and place anchors



(c) Grout the end face



(d) Place the end plate and hold from bottom



(e) Fasten the anchors

Figure 2.23. End-Region Stiffener Installation Procedures.

End plates were installed a minimum of four hours after placement of anchors. The contact surface of the specimen was covered with a 1/4 in. thick layer of rapid hardening concrete repair grout with a stiff gel-like consistency (no slump), as described in the manufacturer's guide, to allow application on a vertical surface (Figure 2.23[c]). The steel plate was placed immediately following application of grout. Installation of the plate required two people. The plate was held in place from the bottom by leveling jacks, as shown in Figure 2.23(d). Anchors were fastened using a wrench.

The solution was installed on Specimens 2, 5, and 7 for tests T2E1, T5W1, and T7E2, respectively. A new steel plate was used for tests T2E1 and T5W1. The steel plate for T5W1 was reused for test T7E2 with new anchors. All tests were conducted a minimum of 24 hours following completion of end plate installation.

2.4.5 Threadbar with Channel Installation

Solution 8 consisted of a threadbar with channel. Holes for the threadbars were made using a core drill. A 12 in. long initial hole was drilled using a 14 in. long bit. The depth of the hole was increased using 24 in., 36 in., and 48 in. long bits. Each hole took approximately one hour. The threadbar was placed through the hole with the hex nut, washer, and bearing plate on the top of the bent cap. The channel (with predrilled hole) was secured to the bottom surface of the specimen with a rapid hardening grout, as shown in Figure 2.24(b). Leveling jacks and wood were used to hold the channel in place (Figure 2.24[c]). The threadbar was fastened within the 20-minute working time for the grout (Figure 2.24[d]). A minimum of four hours of curing time was allowed prior to testing.

Solution 8 was used for eight different tests: T1E1, T4W1, T4E1, T4I1, T8W1, T8E1, T8I1, and T7E2. The channels for test T1E1 were reused for the interior parts of test T4I1. The threadbars for tests T4W1 and T4E1 were also recycled for test T8I1. The reused channels and threadbars were not damaged and remained in original condition.



(a) Drill the holes using core dill



(b) Put grout on the channel



(c) Squeeze up and fix channel using leveling jack and wood support

(d) Place bearing plate, washer, and nut, and then fasten the threadbar using a wrench

Figure 2.24. Installation Procedures for Threadbar with Channel.

2.4.6 Load-Balancing PT Installation

Load-balancing PT was installed separately for interior and exterior tests. For both solutions, the anchor plates/channels were installed first using a rapid hardening grout (Figure 2.25[a]). The holes for mechanical anchors were then drilled with a hammer drill and mechanical anchors were installed to anchor the plate/channel. Base plates for the interior test and side plates for the exterior test were properly placed as shown in Figure 2.25(c) and (d).

For the interior test, the stands were individually placed in each notch of the base plate (Figure 2.25[e]) and anchored at the east and west ends of the specimen. Before inducing prestressing force, the service load was applied on the base plate at all loading points. In both interior and exterior tests, a prestressing force of 45 kips was applied in each strand, with one-half applied at each end (east end stressed first). New strands were used for each test.

2.4.7 FRP Installation

The installation of FRP solutions (Solutions 16 and 17) consisted of two main steps: constructing infill concrete blocks and installing the FRP. Details of Solutions 16 and 17 are shown in Figure 2.10 and Figure 2.11, respectively, including order of FRP application.

A hammer drill with 9/16 in. diameter drill bit was used to bore the holes for the threadbars passing through the stem. Figure 2.26 shows construction of infill concrete blocks. The rebar cages and timber forms for both FRP solutions were prepared and placed following installation of the threadbars. The concrete was then placed into the formwork, as shown in Figure 2.26(d). Proper consolidation was achieved using rod vibrators and the surface was finished smooth by trowels, as shown in Figure 2.26(e). The surface was moist cured and the forms were removed after three days. Figure 2.26(f) shows a typical infill concrete for Solution 16 after removal of all formwork.

Figure 2.27 shows the surface treatment prior to installation of the FRP. The bottom corners of the specimen were rounded with a minimum curvature of 1.5 in. to prevent sharp-corner-induced premature failure of the FRP, as shown in Figure 2.27(a). The removal of coatings, laitance, and all miscellaneous surface contaminates was performed subsequently performed, as shown in Figure 2.27(b). The surfaces were then smoothed with 80 grit sandpaper to meet the surface profile recommendation given by the manufacturer. Debris was removed with a vacuum and pressurized air (Figure 2.27[c]).



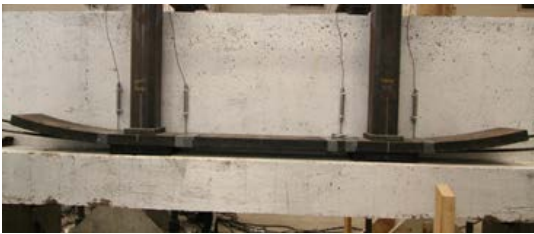
(a) Put grout on the anchor plate or channel and place the anchor plate or channel



(b) Mark holes, drill the holes, and place mechanical anchors



(c) Place side plate for the exterior test, mark and drill the holes, and install anchors



(d) Place base plate on the bearing pads for the interior test



(e) Place strands



(f) Jack the strands to induce prestress

Figure 2.25. Installation Procedures for Load-Balancing PT.

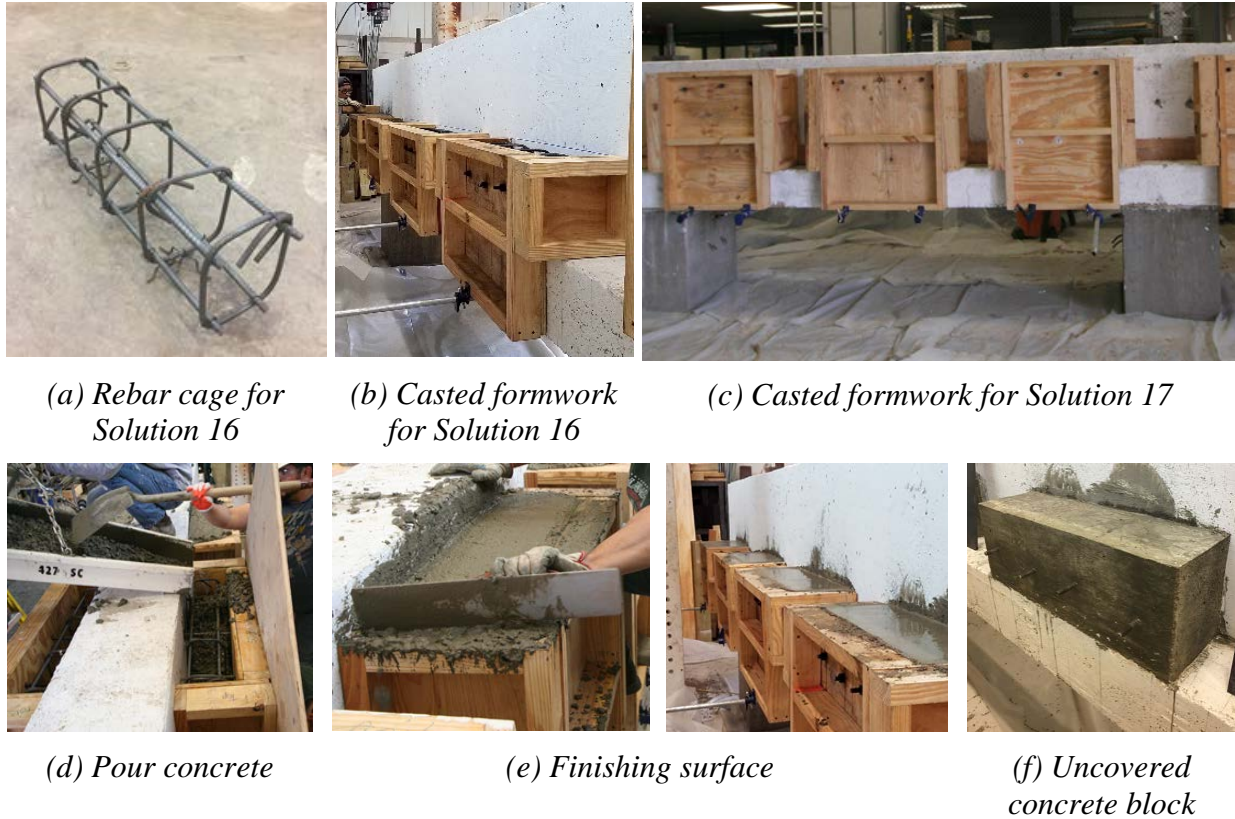


Figure 2.26. Construction of Concrete Infill for FRP Solutions.

A MasterBrace FRP composite strengthening system, which consists of unidirectional high-strength carbon fiber fabric (MasterBrace FIB 600/50 CFS), epoxy primer (MasterBrace P 3500), epoxy paste (MasterBrace F 2000), and epoxy encapsulation resin (MasterBrace SAT 4500), was used for FRP solutions. The carbon fiber fabrics were cut using a utility knife. Each epoxy component (epoxy primer, epoxy paste, and epoxy encapsulation resin) consisted of two parts, combined following manufacturer ratios. Components were mixed using a low-speed drill for a minimum of five minutes and a mixing paddle with manufacturer-provided mixing ratios.

Figure 2.28 shows the application of epoxy components to the substrate. First, the primer was uniformly applied to the substrate using 3/8 in. nap rollers and brushes, as shown in Figure 2.28(a). Two hours later, the paste was applied with a steel trowel to level small surface defects, as shown in Figure 2.28(b). The next day, the resin was applied using 3/8 in. nap rollers and brushes to a wet film thickness of 0.46 mm to 0.56 mm (Figure 2.28[c]).



(a) Round sharp corner (b) Remove coating (c) Clean surface

Figure 2.27. Surface Treatments Prior to FRP Application.



(a) Applying epoxy primer (b) Applying epoxy paste (c) Applying epoxy encapsulation resin

Figure 2.28. Application of Epoxy Components to Substrate.

Figure 2.29 and Figure 2.30 show the application of the carbon fabric fibers for interior and exterior portions of the specimen, respectively. The fabric was attached immediately following application of the epoxy encapsulation resin. The fabric was pressed against the substrate tightly by rolling parallel to the fiber orientation until visual signs of uncured epoxy encapsulation resin bled through the fabric. For the exterior application, a side strip that enclosed the entire inverted-T section (Figure 2.30[a]) was applied first. The vertical strip wrapping the stem (Figure 2.30[b]) and the horizontal strip wrapping the flange of the specimen (Figure 2.30[c]) were applied next. Different wrapping schemes for exterior application of Solution 16 and Solution 17(a) and (b) were adopted as described in Sections 2.2.5 and 2.2.6. Additional bandage strips for Solution 17(a) and (b) were used to provide anchorage to the bottom tip of the vertical strip that wrapped the stem of the specimen.

The second layer of epoxy encapsulation resin was applied over the fabric to a wet film thickness of 0.46 mm to 0.56 mm, as shown in Figure 2.31(a) and (b). The steel waling plates were installed on the specimen after the FRP application. As shown in Figure 2.31(c), the epoxy encapsulation resin was applied to the surface of the steel waling plate prior to placing it in position. The steel waling plates were positioned and tightened slightly to avoid damaging the fabric but to ensure uniform contact was achieved. Figure 2.31(d) shows the installed waling plates.

Tests were conducted a minimum of 14 days after concrete placement and 24 hours after FRP installation.



(a) Press FRP against substrate

(b) Attach fabric over the corner

(c) After application

Figure 2.29. Application of FRP for Interior Region.



(a) Applying side strip

(b) Applying vertical strip

(c) Applying horizontal strip

(d) After application

Figure 2.30. Application of FRP for Exterior Region.



(a) Applying second layer of epoxy



(b) After application



(c) Applying epoxy to waling plate



(d) Install waling plate

Figure 2.31. Application of Second Layer of Epoxy and Steel Waling.

2.5 Material Properties

For the bent caps, a 3.6 ksi 28-day strength modified Class C concrete with 3/8 in. aggregate was specified. Slump tests (following ASTM C143 [ASTM, 2012]) were conducted prior to each concrete pour. Standard 4 in. x 8 in. test cylinders were made in accordance with ASTM C31 (2015) and ASTM C192 (2016) specifications. The cylinders were transported to the lab, demolded, and placed in the curing room. Uniaxial compression testing following the guidelines provided in ASTM C39 (2017) was conducted at 3, 7, 14, and 28 days. Table 2.4 lists the measured material properties. Figure 2.32 shows strength gain over time in a log scale plot.

Table 2.4. Compressive Test Results for Concrete Cylinders.

Pour No.	Specimen No.	Slump (in.)	7-day strength (ksi)	14-day strength (ksi)	28-day strength (ksi)	Days at test day	Test day strength (ksi)
1	1	5.5	2.23	2.65	3.39	175	4.35
	2					248	3.90
2	3	5.0	2.32	2.83	3.27	83	3.84
	4					173	4.07
3	5	5.5	2.51	2.95	3.54	125	4.45
	6					183	4.05
4	7	5.0	2.49	3.19	3.60	229	5.21
	8					187	4.21
5	Columns	5.25	7.47	—	10.00	—	—

Note: Design strength of concrete for specimens is 3.6 ksi.

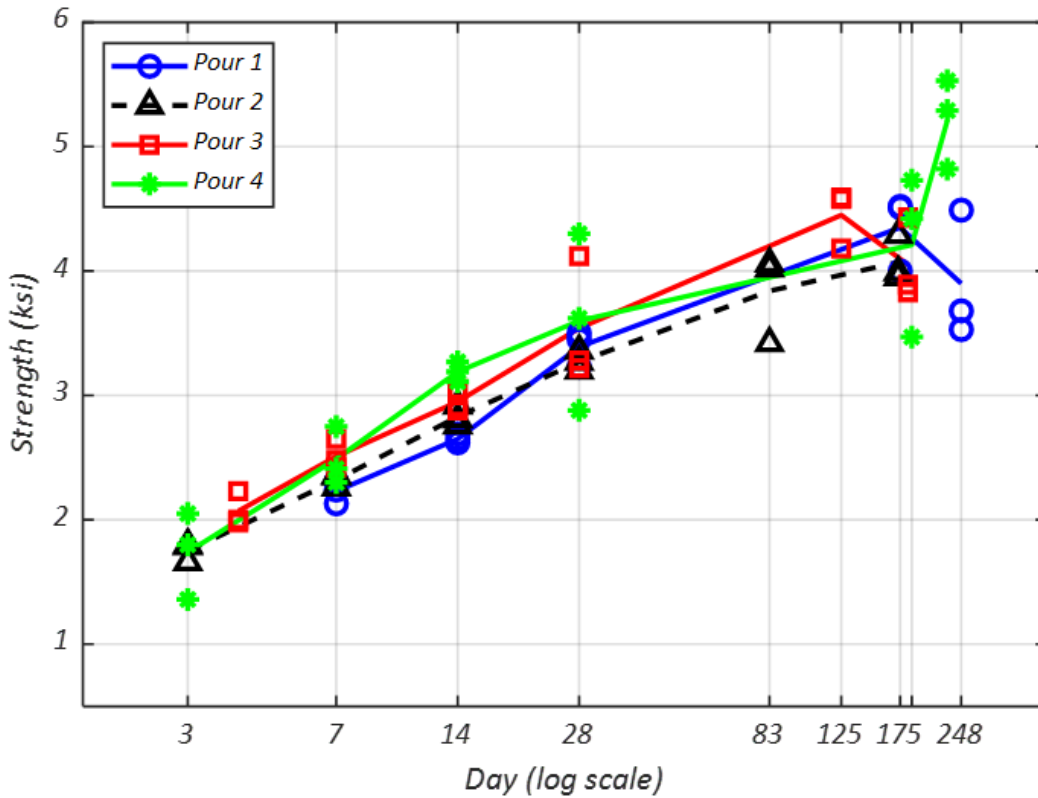


Figure 2.32. Compressive Strength Gain over Time.

Tensile tests for the reinforcing rebar used for the bent cap specimens were conducted by ATS Inc. Each rebar was tested with three 8 in. long specimens. The measured yield strength and ultimate strength of the rebar are listed in Table 2.5.

Table 2.6 lists material properties for each retrofit solution. Table 2.7 lists typical mechanical properties, ultimate strength, and yield strength, based on the steel grade. Other material properties are those provided by manufacturers.

Commercial grade grout for rapid hardening repair of vertical and horizontal surfaces was used for Solutions 3, 8, and 14. Typical compressive strength (provided by the manufacturer) is 5.5 ksi strength at 7 days and 6.5 ksi at 28 days, which is modified ASTM C109 (2016). For Solution 3, epoxy anchors were used to anchor the steel plate, and the used epoxy anchor consisted of two parts: threadbar and epoxy. The threadbar was 1/2 in. Grade B7 bar. The epoxy bond strength was 1.3 ksi at 2 days and 1.7 ksi at 4 days. Solution 14 used 0.6 in. diameter unbonded strands with a nominal area of 0.217 in. and a tensile strength of 270 ksi.

Table 2.5. Tensile Test Result for Reinforcing Rebar.

Bar No.	Yield Strength (ksi)		Ultimate Strength (ksi)	
#3	63.5	64	99.5	99.8
	64		100	
	64.5		100	
#4	67.5	67.7	95.5	96
	66.5		95	
	69		97.5	
#5	63.5	64	104	104.7
	64.5		105	
	64		105	
#6	62	61.7	104	104
	61.5		104	
	61.5		104	
#9	67.5	69.5	113	113
	72		113	
	69		113	

Table 2.6. Material Properties for Retrofit Solutions.

Solution No.	Item	Properties
3	Steel plate (end-region stiffener)	Gr. 50
	Epoxy anchor—threadbar	Gr. B7
	Epoxy anchor—epoxy	$\tau = 1.3$ ksi
	Grout	ASTM C109 (2016) Modified
8	Steel channel (MC 6 x 12)	A36
	Grout	ASTM C109 (2016) Modified
	Gr. B7 high-impact threadbar	Gr. B7
	Steel bearing plate	A36
14	0.6" PT strand	270 ksi
	Anchor channel	A36
	Steel plate for both interior and exterior setup (Figure 2.8)	Gr. 50
	Anchor plate (Figure 2.9)	Gr. 50
	Grout	ASTM C109 (2016) Modified
16	FRP sheet 35" wide roll	$E_f = 33000$ ksi $t_f = 0.013$ in/ply
	Infill concrete	$f'_c = 3.6$ ksi
	Gr. B7 high-impact threadbar	Gr. B7
	Steel waling	A36
	Steel bearing plate	A36
17	FRP sheet 35" wide roll	$E_f = 33000$ ksi $t_f = 0.013$ in/ply
	Infill concrete	$f'_c = 3.6$ ksi
	Gr. B7 high-impact threadbar	Gr. B7
	Steel waling	A36
	Steel bearing plate	A36
18	Bearing pad	Elastomer 50 Neoprene Rubber

Note: Gr. = Grade.

Table 2.7. Typical Mechanical Properties with Steel Grade.

Steel Grade	Yield Strength, f_y (ksi)	Ultimate Strength, f_u (ksi)
A36	36	58–80
Grade 50	50	65
Grade B7	105	125

2.6 Test Setup and Load Protocol

Figure 2.33 shows overview photographs of the test setup in the Texas A&M High Bay Structural and Materials Testing Laboratory. The 22 ft long bent caps were centered on two 2 ft square columns spaced 12 ft on center.

Figure 2.34 shows the three test regions that were used for each specimen: two exteriors and one interior. Exterior tests (Figure 2.34[a]) simulated one girder line centered at 1 ft. Interior tests (Figure 2.34[b]) simulated two girder lines spaced at 4 ft, centered on the specimen, from the edge; an additional loading point was provided over the adjacent column. A plan view of the loading points is provided in Figure 2.34(c).

At each simulated girder line, a 600 kip jack applied loads to a frame (Figure 2.35) that transferred loads to each ledge. Frames consisted of an I-beam with stiffeners that transfer load to hollow structural sections (HSS). Frames were connected by 1 in. diameter threaded rods to provide stability during testing. Two layers of 1 in. thick steel plates with a dimension of 4 in. by 14 in. piled up on a 15 in. long MC 6 x 12 channel were built up between the bottom of the loading frame and the bearing pad to evenly distribute the load to the bearing pad, as shown in Figure 2.35(c).

For ledge and hanger tests, the jack was centered on the loading frame (Figure 2.35[d]) to provide equal loads on each ledge. Interior tests increased each jack equally. Exterior tests increased each jack equally up to dead load, at which point the load over the column was held constant. For punching shear tests, the actuator was placed 5-5/8 in. off center (Figure 2.35[e]) to allow for larger loading on one side. The off-center position was determined as that to provide dead load on the far side when the near side was at the design load. Both interior and exterior punching shear tests increased each jack equally up to dead load. After reaching dead load, only a single jack was increased in most tests. An exception occurred for tests T7I1 and T7I2, during both of which actuators were loaded equally to the ultimate load state. Once the ultimate load state was attained, the subsidiary jack was retracted to hold the dead load and the main jack was increased.

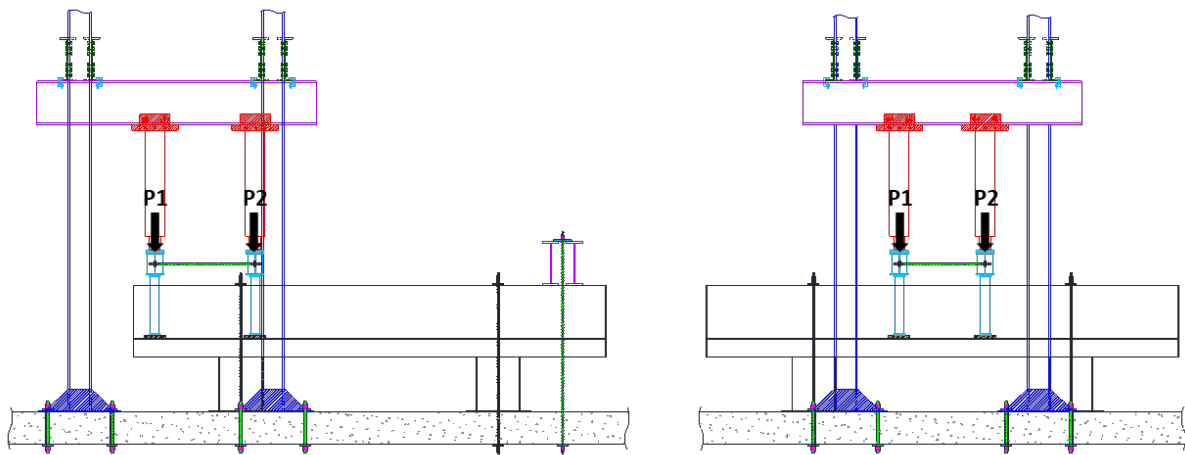
The loading protocol was developed to provide guidelines in terms of loading rate and critical loading points during ultimate load testing of the specimens. The critical loading points for the half-scale test specimens was calculated based on dead, service, and ultimate load demands of a typical double-column bent (Bent 13) in IH 35. The load was locked at critical loading points to check cracks and condition of the specimen as benchmark comparison points between control and retrofitted specimens. The actual stop and locked loading points were 10 percent less than the calculated load demand. The test specimens were loaded until specimen failure.



(a) Exterior test setup

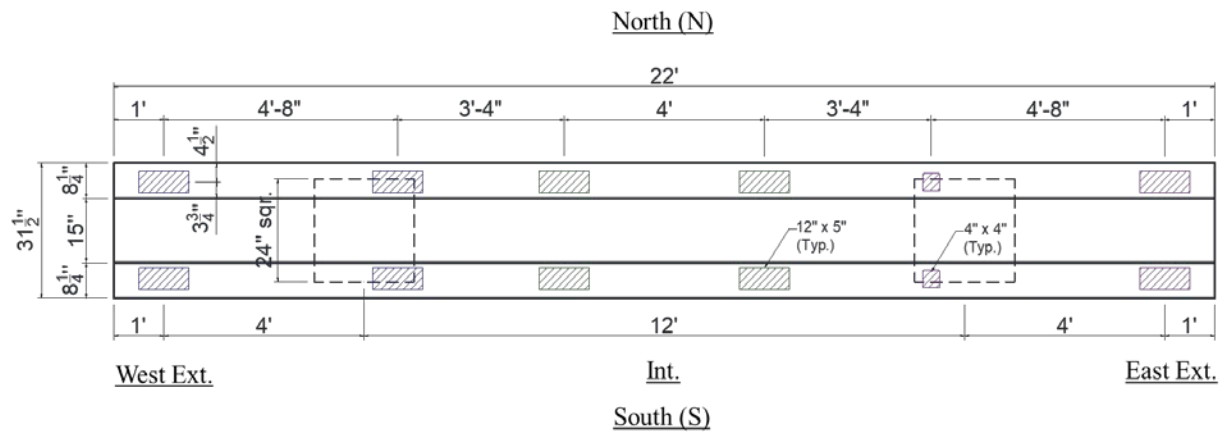
(b) Interior test setup

Figure 2.33. Test Setup in Laboratory.



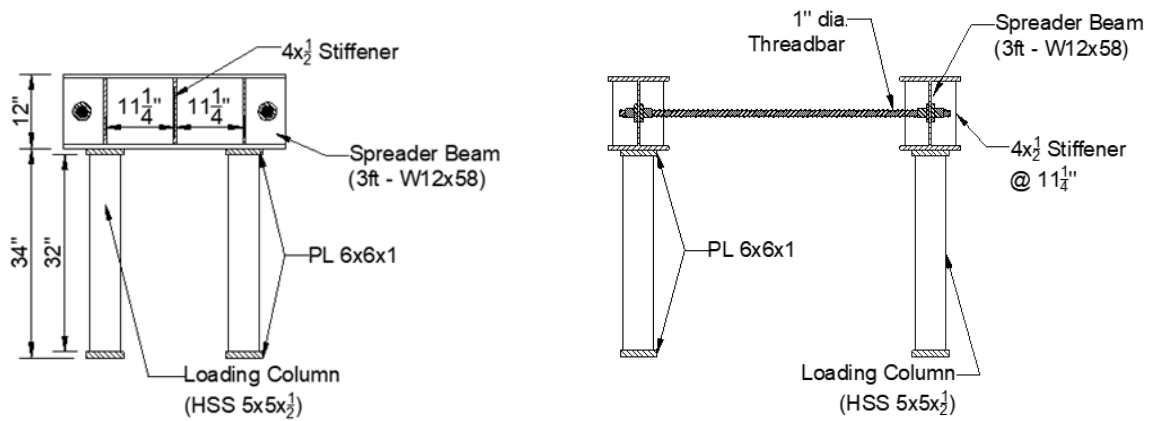
(a) Exterior test

(b) Interior test



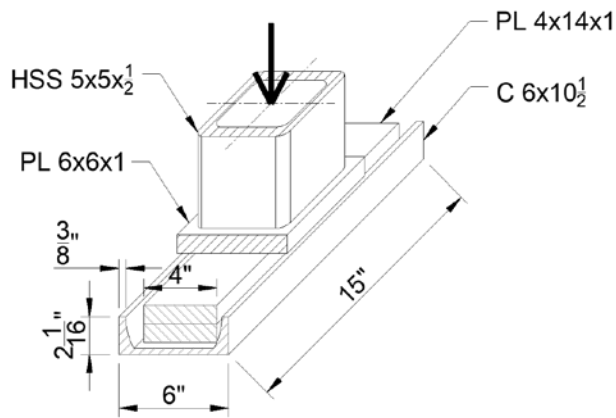
(c) Plan view of loading points

Figure 2.34. Overview of Experimental Test Setup Loading Locations.

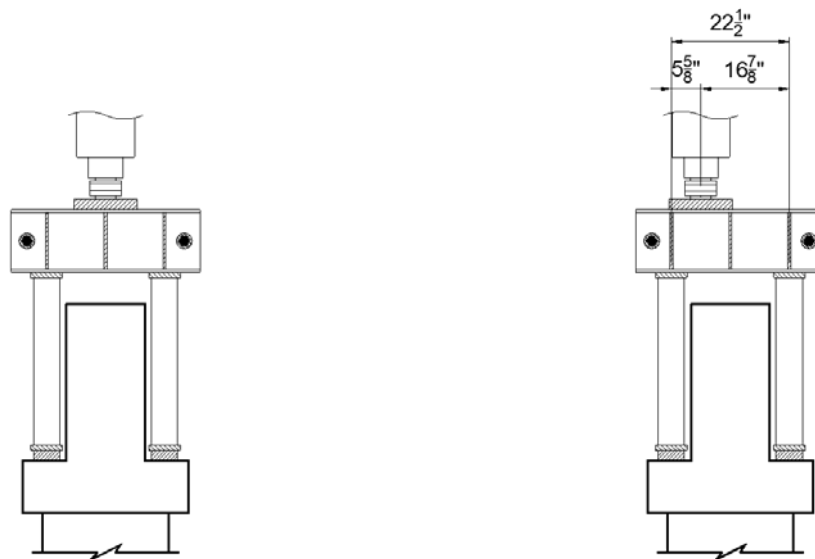


(a) Loading frame

(b) Connection of loading frames



(c) Built-up bearing steel parts



(d) Ledge and hanger tests

(e) Punching shear tests

Figure 2.35. Details of Loading Frame and Side View of Actuator Location.

Each test was paused at dead load, service load state (SLS), and ultimate load state (ULS), as estimated from the full-scale prototype. Specified actuator loads at these pauses are provided in Table 2.8. Following ultimate loads, loads were increased to failure on the specimen. In each test, additional pauses were made as necessary based on observed damage. For some tests, loading was continued beyond failure to assess the residual capacity of the bent cap, or tests were terminated prior to failure to preserve the integrity of the specimen for subsequent tests or to avoid potential damage to instrumentation and the test setup. Details of each test are described and discussed in the following experimental results chapter.

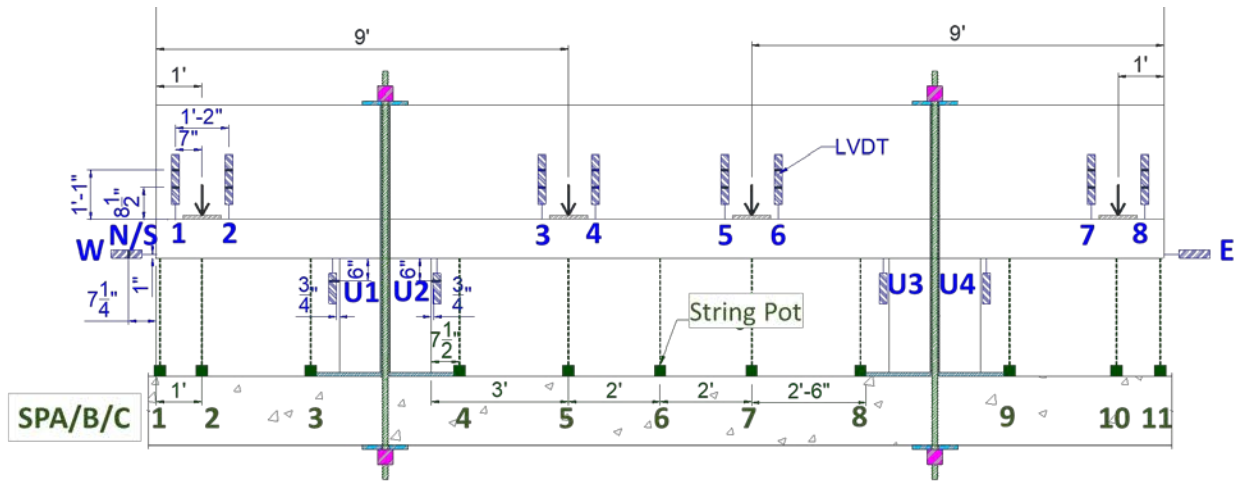
Table 2.8. Estimated Limit State Loads for Documentation of Test Results.

Interior Test						
	Hanger/Ledge Flexure		Punching Shear			
	P1 (kip)	P2 (kip)	P1 (kips)		P2 (kips)	
			R_n	R_f	R_n	R_f
Dead Load	53	53	33		33	
			25	8	25	8
Service Load (SLS)	98	98	66		33	
			50	16	25	8
Ultimate Load (ULS)	157	157	96		33	
			72	24	25	8
Exterior Test						
	Hanger/Ledge Flexure		Punching Shear			
	P1 (kip)	P2 (kip)	P1 (kips)		P2 (kips)	
			R_n	R_f	R_n	R_f
Dead Load	46	46	30		30	
			23	7	23	7
Service Load (SLS)	90	46	60		30	
			45	15	23	7
Ultimate Load (ULS)	136	46	90		30	
			68	22	23	7

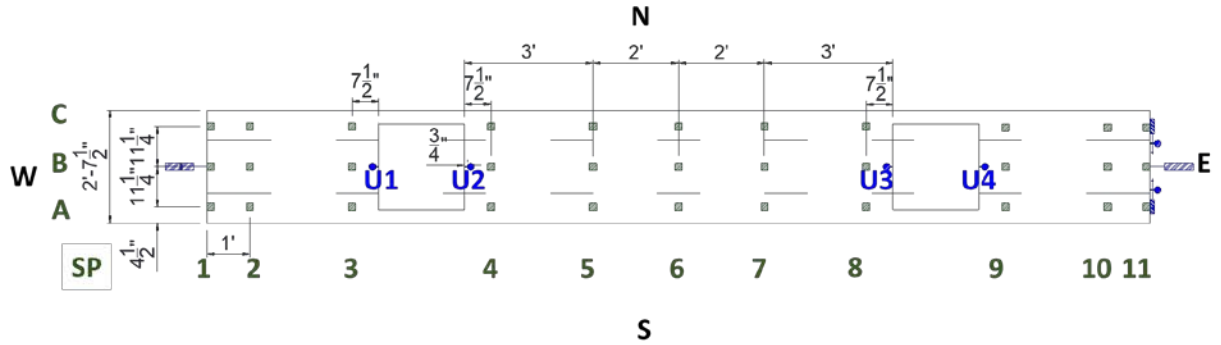
Note: R_n = reaction force on a testing bearing pad; R_f = reaction force on a false loading bearing pad; for hanger/ledge flexure test, $R_n = P1/2$ and $R_f = P2/2$.

2.7 Instrumentation

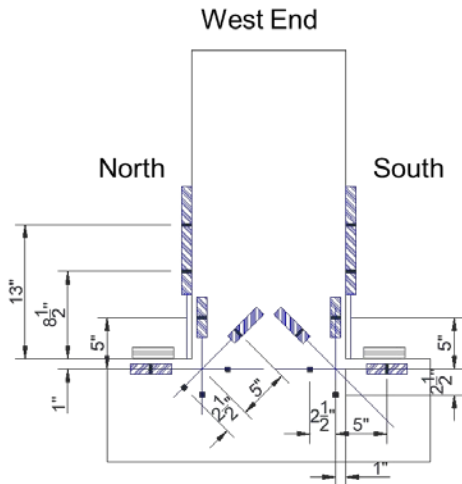
Figure 2.36 shows the instrument plan. Linear variable differential transducers (LVDTs) were used to measure differential displacement on each side of the loading point, at the edges or the columns, and on the end surfaces (exterior only). String potentiometers (string pots) were placed at 11 longitudinal stations to measure the vertical deflections. At each station, up to three string pots were placed in the transverse. String pots in Rows A and C (underneath ledge) were only used in the tested region.



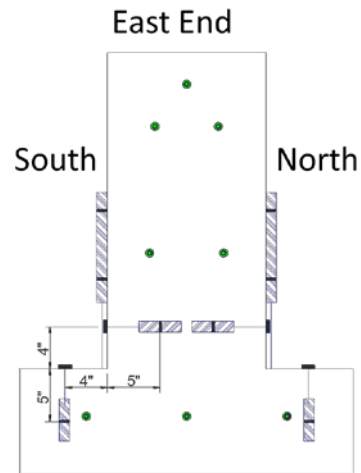
(a) Side elevation view



(b) Bottom view



(c) South end surface



(d) End face plan for Solution 3

Figure 2.36. Overall LVDT and String Pot Installation Plan.

Table 2.9 lists string pot installation details, with label names corresponding with Figure 2.36.

Table 2.9. String Pot Installation Plan.

	Label Name	Test Region		
		W Ext.	Int.	E Ext.
Row A	SPA01	SP1		
	SPA02	SP2		
	SPA03	SP3		
	SPA04		SP1	
	SPA05		SP2	
	SPA06		SP3	
	SPA07		SP4	
	SPA08		SP5	
	SPA09			SP1
	SPA10			SP2
	SPA11			SP3
Row B	SPB01	SP6	SP6	SP6
	SPB02	SP7	SP7	SP7
	SPB03	SP8	SP8	SP8
	SPB04	SP9	SP9	SP9
	SPB05	SP10	SP10	SP10
	SPB06	SP11	SP11	SP11
	SPB07	SP12	SP12	SP12
	SPB08	SP13	SP13	SP13
	SPB09	SP14	SP14	SP14
	SPB10	SP15	SP15	SP15
	SPB11	SP16	SP16	SP16
Row C	SPC01	SP17		
	SPC02	SP18		
	SPC03	SP19		
	SPC04		SP17	
	SPC05		SP18	
	SPC06		SP19	
	SPC07		SP20	
	SPC08		SP21	
	SPC09			SP17
	SPC10			SP18
	SPC11			SP19

For the tests with Solution 3 (end-region stiffener), the end face instrumentation plan moved the LVDTs to measure relative displacement between the end plate and specimen (Figure 2.36[d]). Table 2.10 lists LVDT installation details, with label names corresponding with Figure 2.36. For tests with Solution 3, LV5 and 6 were installed vertically, while LV7 and 8 were installed horizontally, as shown in Figure 2.36(d). LV9 and 10 were not used.

Table 2.10. LVDT Installation Plan.

Label Name		Test Region		
		W Ext.	Int.	E Ext.
Ledge	S1	LV1		
	S2	LV2		
	S3		LV3	
	S4		LV4	
	S5		LV1	
	S6		LV2	
	S7			LV1
	S8			LV2
	N1	LV3		
	N2	LV4		
	N3		LV7	
	N4		LV8	
	N5		LV9	
	N6		LV10	
	N7			LV3
	N8			LV4
End Face	SV	LV5		LV5
	NV	LV6		LV6
	SH	LV7		LV7
	NH	LV8		LV8
	SD	LV9		LV9
	ND	LV10		LV10
	W	LV15	LV15	LV15
	E	LV16	LV16	LV16
Column	U1	LV11	LV11	LV11
	U2	LV12	LV12	LV12
	U3	LV13	LV13	LV13
	U4	LV14	LV14	LV14

CHAPTER 3: EXPERIMENTAL RESULTS

This chapter presents the experimental results for 33 tests on eight inverted-T bent cap specimens to evaluate the effectiveness of various rehabilitation techniques in strengthening ledge and hanger deficiencies. Hanger-deficient specimens (1, 2, and 8) were designed to have hanger failure. Ledge-deficient specimens (3, 4, 5, 6, and 7) were designed to have ledge failure. The full test matrix is provided in Table 2.3. The experimental results are organized first by specimen, and then by test. Reference (un-retrofitted) tests are presented before retrofitted tests. Exterior tests (both ends) are presented before interior tests.

All tests were paused at dead, SLS, and ULS to document damage, with additional pauses made in some tests. Demands and estimated capacities were calculated per AASHTO *LRFD Bridge Design Specifications* (AASHTO, 2014). Crack maps are provided at SLS, ULS, and post-failure. The response is characterized by load-deflection curves, with load and deflection reported at individual load points. In discussing the results, the measured ultimate load refers to the peak load reached during testing. For tests terminated prematurely, the peak load during testing is referred to as the termination load. A description of damage progression, including photos, is provided for each test.

3.1 Hanger-Deficient Specimen 1

Hanger-deficient Specimen 1 provided hanger reference tests on the exterior (T1W1) and interior (T1I1) and an exterior test of the clamped threadbar Solution 8(a) (T1E1). Figure 3.1 shows crack patterns at SLS, ULS, and failure.

3.1.1 Exterior Hanger Reference—T1W1

T1W1 is the exterior reference test for hanger-deficient specimens. Figure 3.2 shows the load-deflection plots for the north and south load points, with horizontal lines indicating SLS, ULS, and estimated capacity, and diamonds indicating the measured ultimate load.

The measured ultimate load of 66 kips was 57 percent larger than the estimated capacity of 42 kips, but 2 kips less than ULS (68 kips). Loads were removed after documenting damage at the measured ultimate load. The controlling failure mechanism was hanger failure, as expected. Figure 3.3 shows the observed damage for test T1W1.

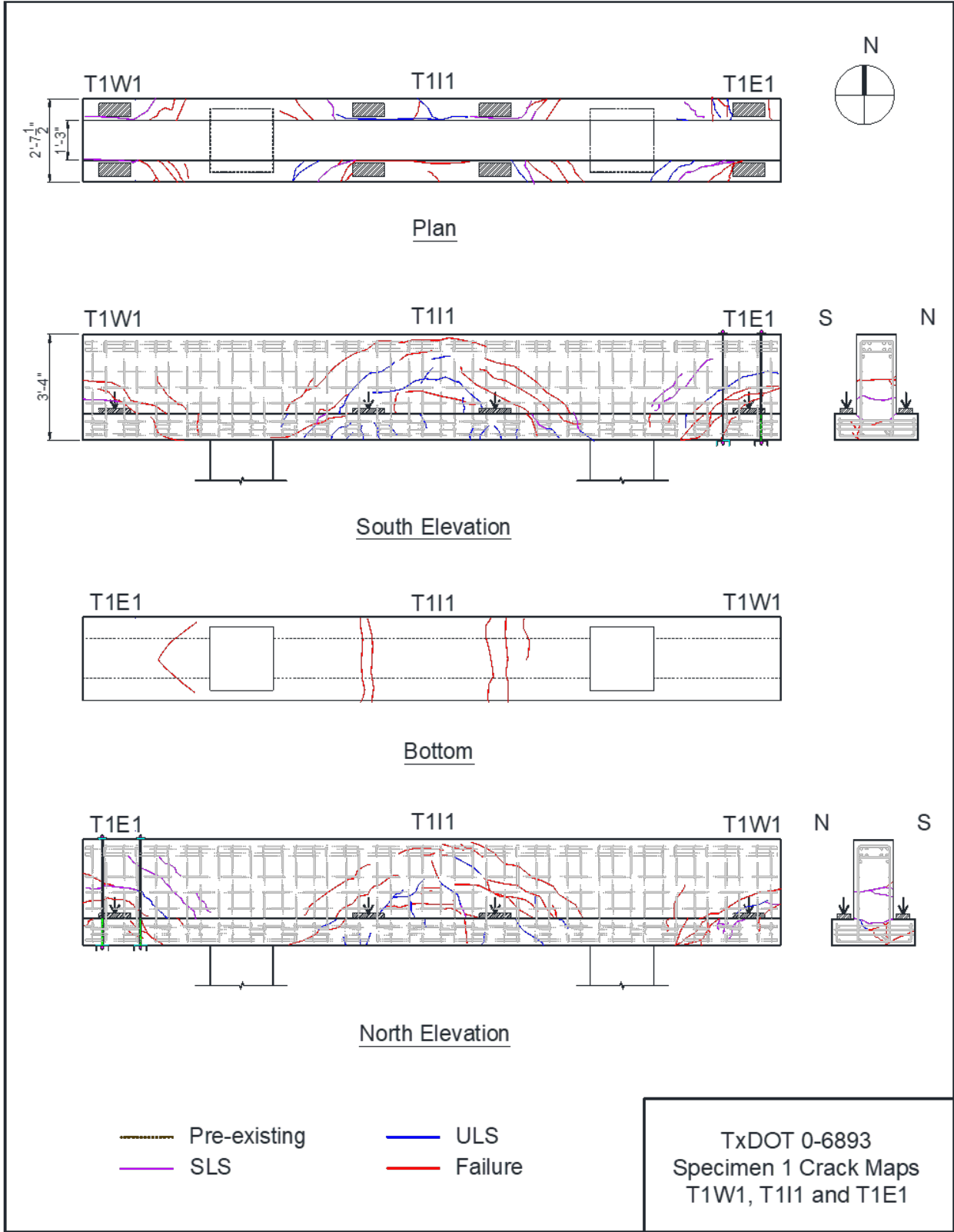


Figure 3.1. Crack Maps for Tests T1W1, T1I1, and T1E1.

The initial crack, observed at 35.5 kips, was a hanger crack at the web-ledge interface, as shown in Figure 3.3(a). At SLS, an additional hanger crack formed near the neutral axis, as shown in Figure 3.3(b), with a width of 5 mm. The widths of the lower and upper hanger cracks were 3 mm and 5 mm, respectively. Cracks at the web-ledge interface extended behind the bearing pad, and on the north ledge turned diagonally from the inner edge of the bearing pad to the side face of the ledge. At loads beyond SLS, crack extensions and new crack formations were observed. At 57 kips, a third hanger crack formed on the end face 7 in. above the second hanger crack. Figure 3.3(c) and (d) show the damage on the end face and north side ledge at the measured ultimate load (66 kips), respectively. The widths of the first, second, and third hanger cracks were 15 mm, 1 mm, and 0.7 mm, respectively. Diagonal shear cracks were detected on both sides of the web, with an approximate angle of 30 degrees. New cracks also formed on the top and side face of the ledge, with more cracks on the north side than the south side.

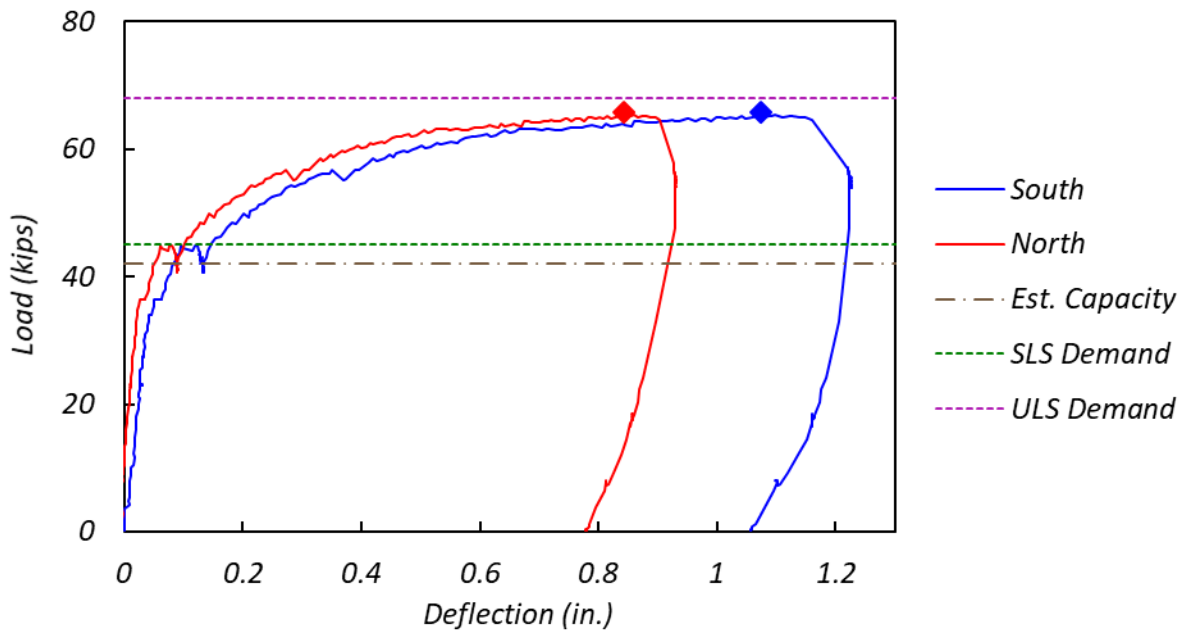


Figure 3.2. Load-Deflection Curve for T1W1.



(a) First crack at 35.5 kips



(b) SLS—end face



(c) Final load level—end face



(d) Final load level—north side

Figure 3.3. Observed Damage for T1W1 at Different Load Levels.

3.1.2 Interior Hanger Reference—T1I1

T1I1 is the interior reference test for hanger-deficient specimens. Figure 3.4 shows the load-deflection plots for all load points.

The measured ultimate load of 90 kips was 84 percent larger than the estimated capacity of 49 kips. Loads were removed after documenting damage at the measured ultimate load. The controlling failure mechanism was hanger failure, as expected. Figure 3.5 shows the observed damage for test T1I1.

The initial cracks were observed at 49 kips. Figure 3.5(a) shows the cracks at SLS. The cracks formed at the web-ledge interface propagated between the two bearing pads. On the outside of the bearing pad, the cracks extended diagonally, starting at the outside edge of the bearing pads to the side face of the ledge. A 10 in. long vertical crack formed on the web about 18 in. away from the center of the west bearing pad. Crack extensions and new crack formations were observed as the load increased. Flexural cracks were found on the bottom of the bent cap at 56 kips. Web shear cracks started forming at 65 kips.

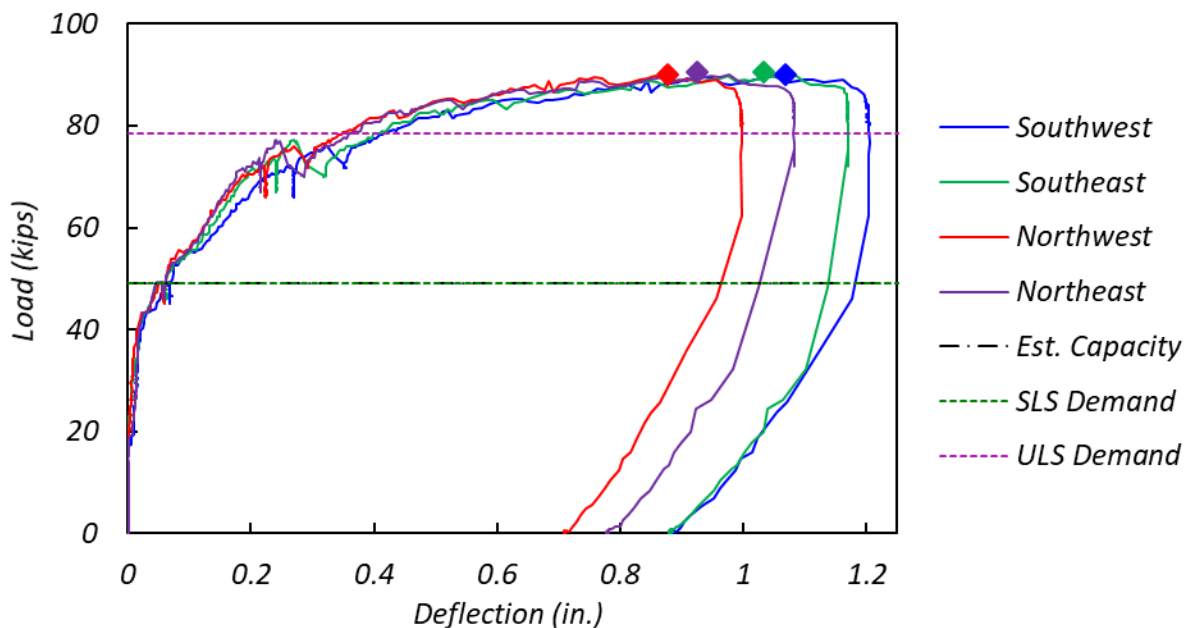
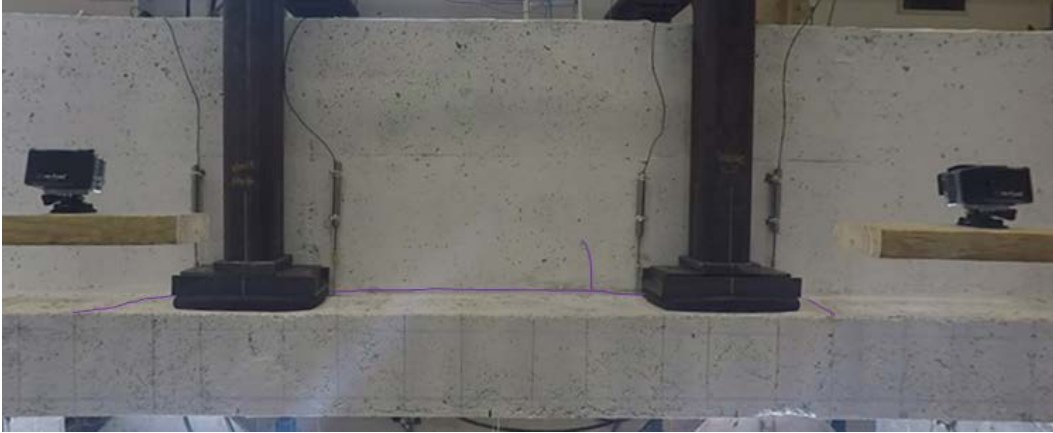


Figure 3.4. Load-Deflection Curve for T1I1.



(a) SLS—north side



(b) ULS—north side



(c) Final load level—north side

Figure 3.5. Observed Damage for T1I1 at Different Load Levels.

At the ULS of 78.5 kips, web shear cracks at an approximate angle of 45 degrees were detected on both sides of the web. Figure 3.5(b) shows the cracks at ULS. The maximum width of the web shear cracks was 4.5 mm. The flexural cracks on the bottom extended to the side face of the ledge. On the outside of the bearing pads, diagonal cracks formed on the side of the ledge.

Crack length and width grew as the load increased while new web shear cracks were forming. Web shear cracks started to rotate and propagate horizontally as they extended toward the top of the web. At the measured ultimate load of 90 kips, web shear cracks initiated from the outside of the bearing pads that were connected and formed the interior hanger cracks, as shown in Figure 3.5(c). The maximum width of the web shear cracks was 2.5 mm.

3.1.3 Exterior Solution 8(a)—T1E1

T1E1 is an exterior test using two clamped threadbars (Solution 8[a]). Figure 3.6 shows the Solution 8(a) installed on the east end of the specimen. Figure 3.7 shows the load-deflection plots for the north and south load points.

Solution 8(a) is expected to increase the hanger, ledge, and punching shear capacity of the bent cap. The measured ultimate load was 106 kips, which is 38 percent larger than the estimated capacity of 77 kips and 61 percent larger than the exterior hanger-deficient reference capacity. The test was ended after documenting damage at the measured ultimate load. Figure 3.8 shows the observed damage at different load levels and the hanger failure mode at the ultimate load level.

At the SLS of 45 kips, only a hairline crack was detected at the web-ledge interface behind the south bearing pad. The crack propagated 10 in. from the center of the bearing pad. The first hanger crack on the end face formed at the estimated capacity of 77 kips near the web-ledge interface, as shown in Figure 3.8(a). The second hanger crack formed near the neutral axis of the bent cap right after the first hanger crack. The crack widths of the first and second hanger cracks were 0.45 mm and 0.2 mm, respectively. On the top of the ledge, the cracks behind the bearing pad extended diagonally to the side face of the ledge. Web shear cracks were also detected on both sides of the web. Crack extension and new crack formation were observed as load increased.

At the ULS of 68 kips, more cracks were detected on the web and ledge. On the end face, the width of the first and second hanger cracks were increased to 0.45 mm and 1.5 mm, respectively. Figure 3.8(b) shows the end face of the bent cap at ULS. Significant extensions of existing cracks and new crack formations were detected while the load increased. At the measured ultimate load of 106 kips, more cracks formed on the web, ledge, and end face. The width of the first and second hanger cracks opened up to 2.5 mm and 10 mm, respectively.



Figure 3.6. Retrofit Solution 8(a) Installed on East End of Hanger-Deficient Specimen 1.

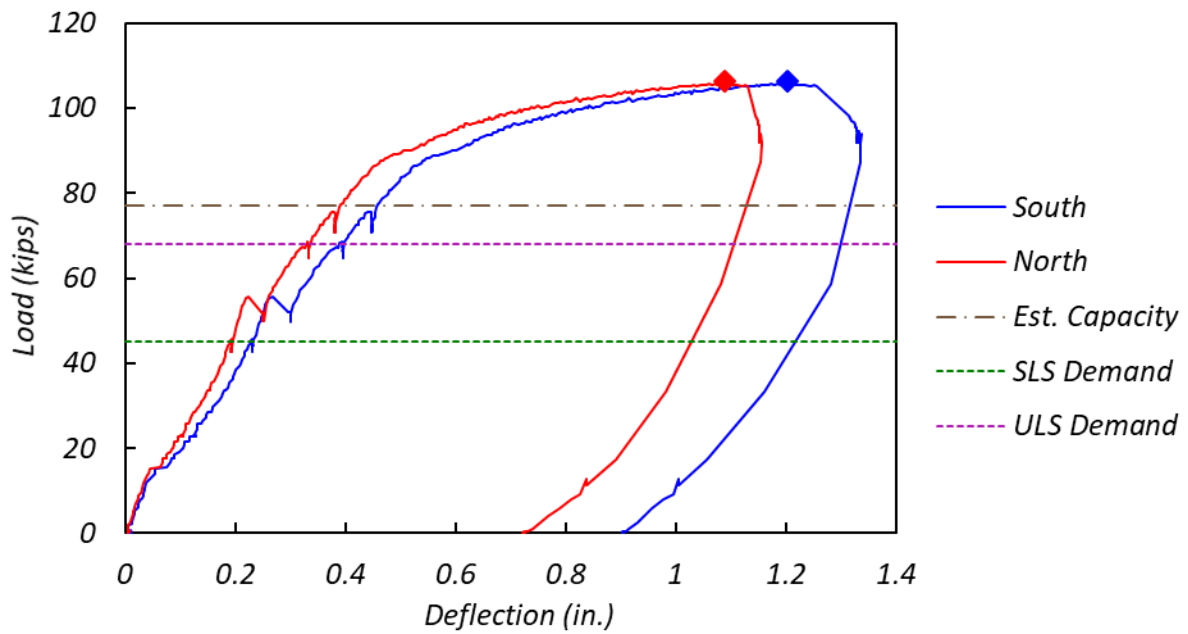


Figure 3.7. Load-Deflection Curve for T1E1.



(a) End face at estimated capacity



(b) End face at ULS



(c) End face at final load level



(d) North side at final load level

Figure 3.8. Observed Damage for T1E1 at Different Load Levels.

3.2 Hanger-Deficient Specimen 2

Hanger-deficient Specimen 2 had three exterior tests (T2W1, T2E1, and T2W2) and two interior tests (T2I1 and T2I2). Test T2E1 tested the end-stiffener retrofit solution (Solution 3). Tests T2W1 and T2I1 tested the load-balancing PT solution (Solution 14) for the exterior and interior; both tests were stopped prior to failure. The retrofits were removed to test the full-depth FRP solution (Solution 17) for the exterior (T2W2) and interior (T2I2). Figure 3.9 shows crack patterns for tests T2W1, T2I1, and T2E1. Figure 3.10 shows crack patterns for tests T2W2 and T2I2, with cracks from previous tests marked by gray lines.

3.2.1 Exterior Solution 3—T2E1

T2E1 is an exterior test using an end stiffener (Solution 3). Figure 3.11 shows Solution 3 installed on the east end of the specimen. Figure 3.12 shows the load-deflection plots for the north and south load points, with horizontal lines indicating SLS, ULS, and estimated capacity, and diamonds indicating the measured ultimate load.

Solution 3 is expected to increase the hanger, ledge, and punching shear capacity of the exterior portion of the bent cap. The measured ultimate load was 78 kips, which is 5 percent larger than the estimated capacity of 74 kips and 18 percent larger than exterior hanger-deficient reference capacity. The test was ended when the applied load dropped to about 90 percent of the measured ultimate load. Figure 3.13 shows the observed damage at different load levels. The bent cap experienced a ledge shear failure.

No damage was observed when test was paused at SLS. The first cracks (flexure cracks on north side of web) were observed at 55 kips. At 60.5 kips, cracks formed at the web-ledge interface behind the bearing pad on both sides.

At ULS (68 kips), new cracks formed on the web and on the top and side face of the ledge. Diagonal ledge cracks on the side face of the ledge were observed under the bearing pads. Diagonal web cracks were also detected on both sides of the web. As the applied load increased to the measured ultimate load, crack extensions and new crack formations were observed on both the web and the ledge.

At the measured ultimate load of 78 kips, the end plate was bent at the bottom tip and in the stem near the neutral axis. New cracks had formed on the web and the side of the ledge. There were fewer cracks at the inside of the bearing pad compared to the reference test, which may have been due to the restraint provided by the end plate. The diagonal cracks on the outside of the bearing pad were steeper than the inside cracks.

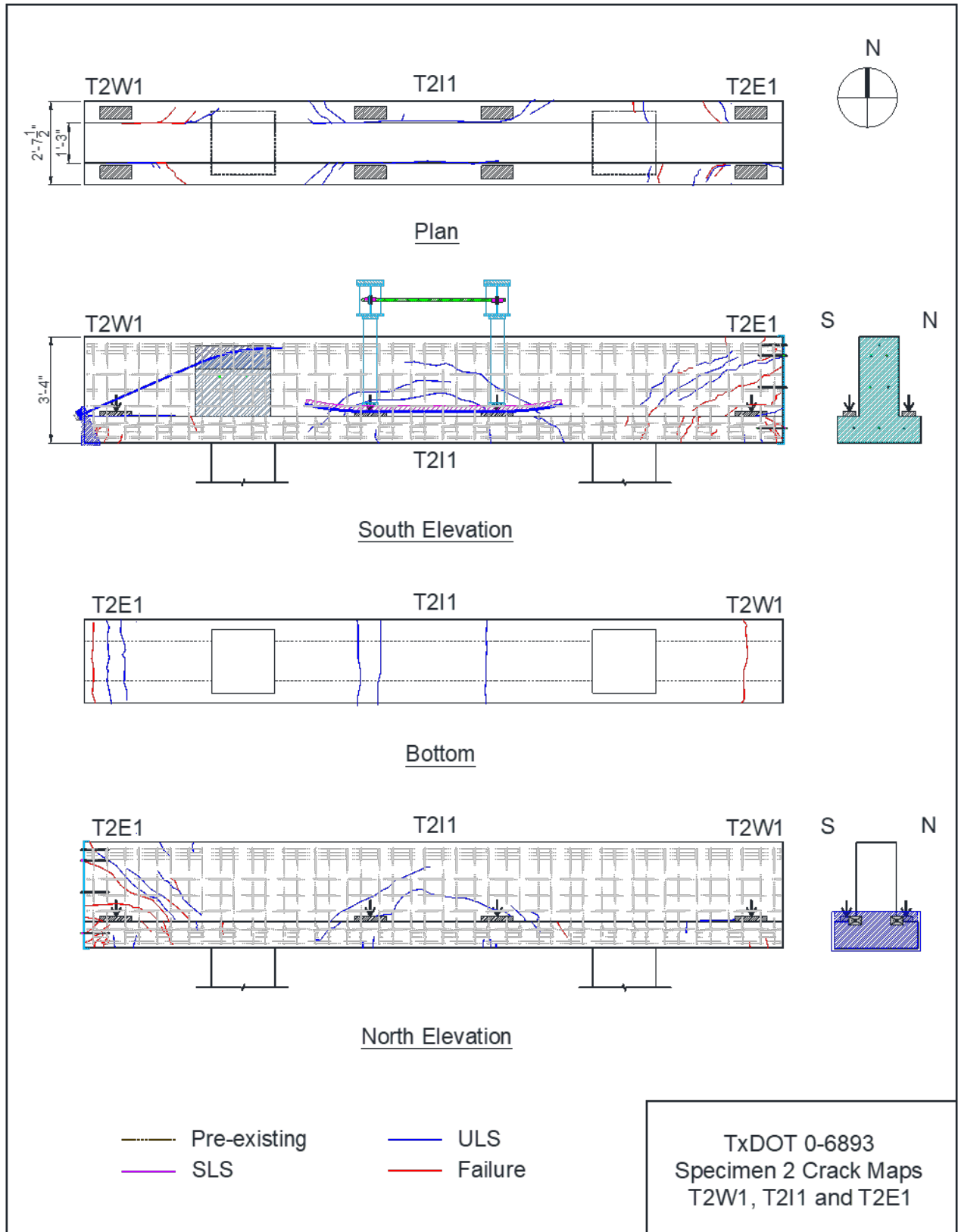


Figure 3.9. Crack Maps for Tests T2W1, T2I1, and T2E1.

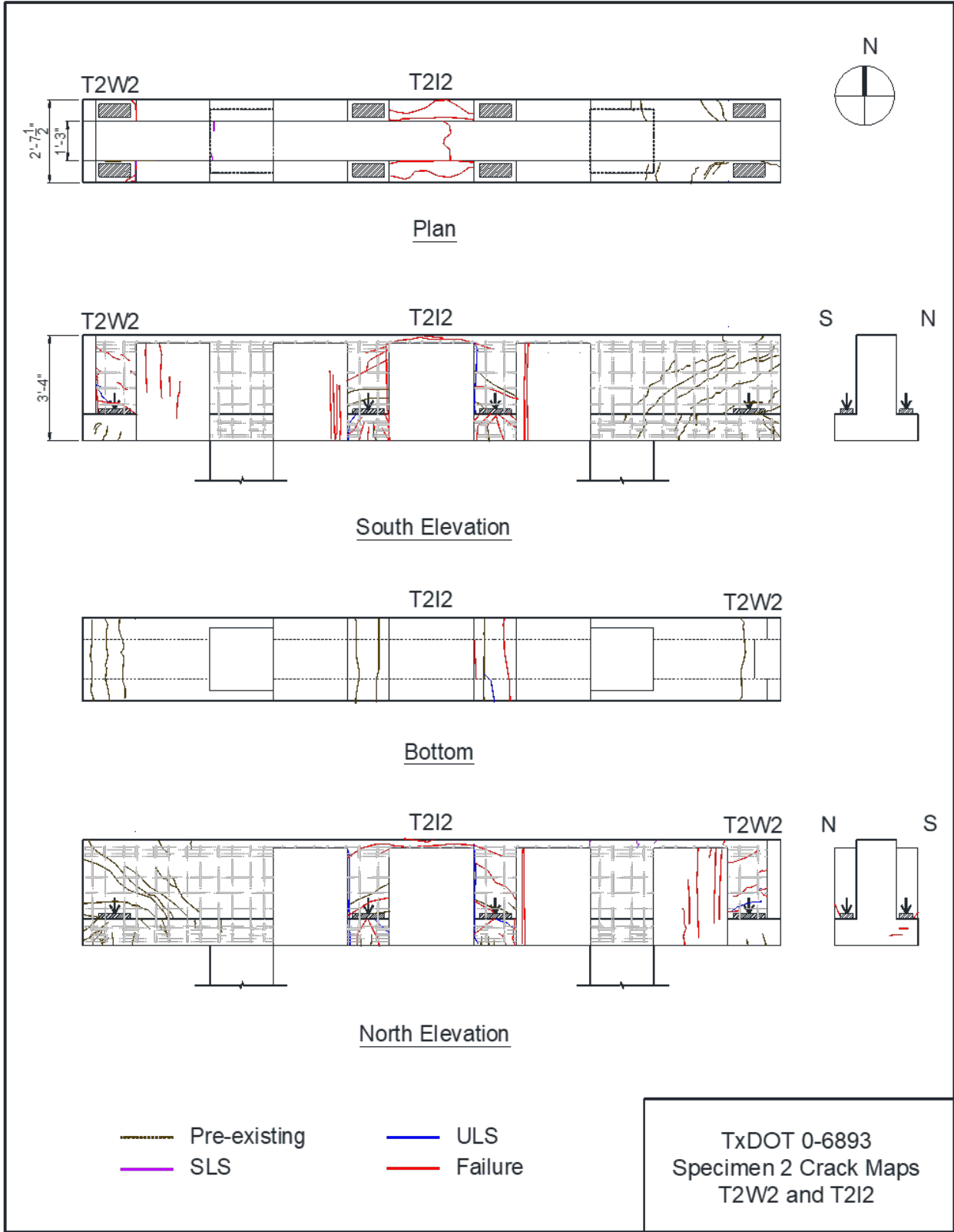


Figure 3.10. Crack Maps for Tests T2W2 and T212.



Figure 3.11. Retrofit Solution 3 Installed on East End of Hanger-Deficient Specimen 2.

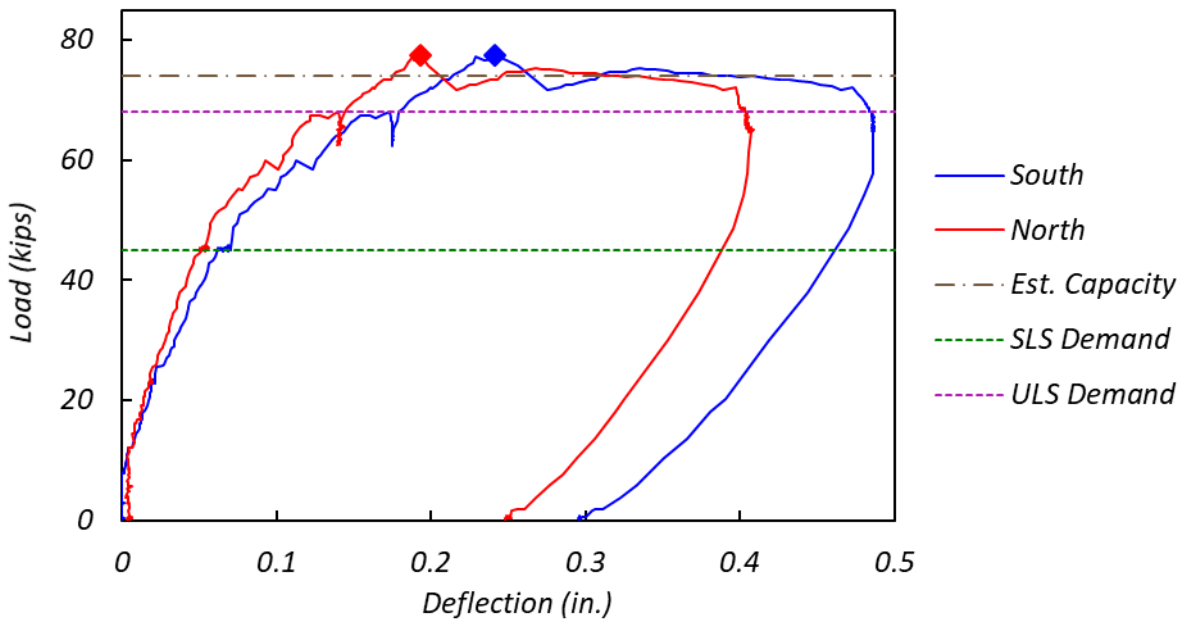


Figure 3.12. Load-Deflection Curve for T2E1.



(a) South side at ULS



(b) South side at final load level



(c) North side at final load level



(d) South side bottom tip at final load level



(e) North side bottom tip at final load level

Figure 3.13. Observed Damage for T2E1 at Final Load Levels.

3.2.2 Exterior Solution 14—T2W1

T2W1 is an exterior test using the load-balancing PT retrofit solution (Solution 14). Figure 3.14 shows Solution 14 installed on the west end of the specimen. The test was terminated prior to failure or reaching a measured ultimate load. The test termination load (82 kips) was determined by adding the capacity contribution of the PT strands (16 kips) to the ultimate load capacity of the hanger-deficient exterior reference test (66 kips). Figure 3.15 shows the load-deflection plots for the north and south load points, with the diamond indicating the termination load.

Solution 14 is expected to increase the hanger, ledge, and punching shear capacity. Figure 3.16 shows the observed damage at the test termination load. The specimen maintained a load carrying capacity with a moderate level of damage at an applied load 24 percent larger than the ultimate load capacity of the hanger-deficient exterior reference test.

No damage was detected until the ULS demand of 68 kips. At ULS, cracks formed at the web-ledge interface behind the bearing pad on both sides. On the top of the north side ledge, the cracks behind the bearing pad propagated toward the column 30 in. and extended diagonally to the side face of the ledge. The interface ledge crack on the south side also propagated toward the column 15 in. but extended diagonally on the top face only 2 in. On the bottom, two horizontal cracks formed all the way through near the tip of the end steel plate. All the cracks were hairline cracks.

At the test termination load, new cracks formed on the ledge and bottom of the specimen. Diagonal cracks on the side face of the ledge under the bearing pads were detected on both sides. The cracks that started at the bottom of the bent cap propagated about half the depth of the ledge toward the center of the bearing pad from the outside. Diagonal cracks on the side of the ledge were hairline cracks. The width of the cracks at the web-ledge interface increased to 1 mm. New diagonal cracks were also detected on top of the ledge. One more horizontal crack formed on the bottom and 3 in. from the end of the specimen. It was detected after removal of the retrofit parts.



Figure 3.14. Retrofit Solution 14 Installed on West End of Hanger-Deficient Specimen 2.

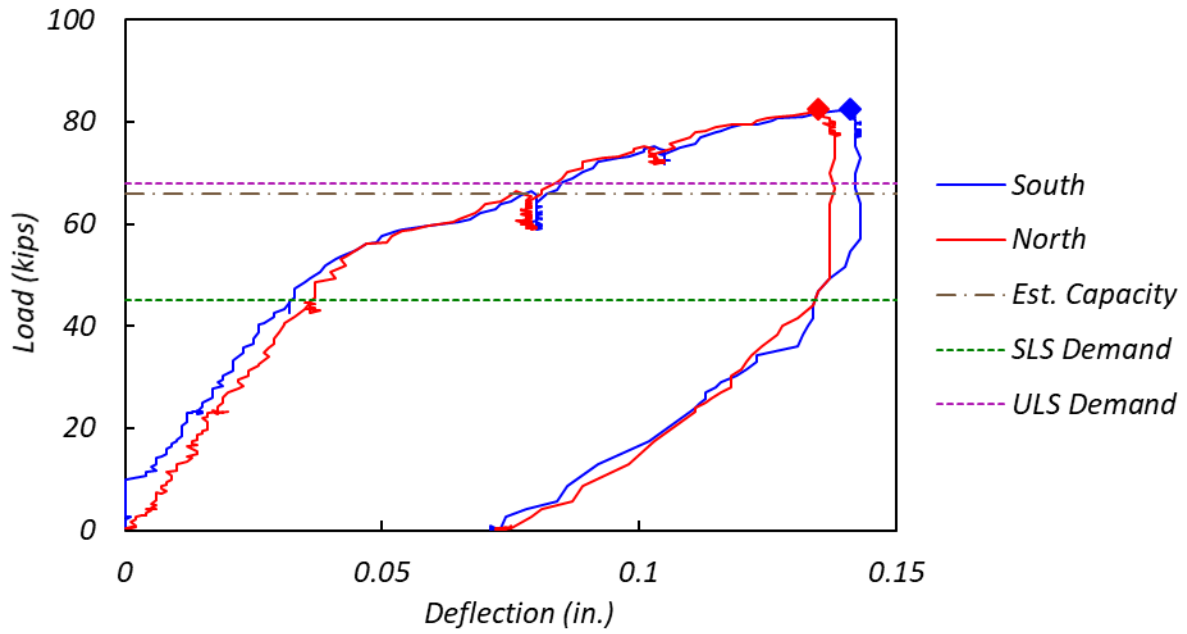


Figure 3.15. Load-Deflection Curve for T2W1 (Test Terminated Prior to Failure).



Figure 3.16. Observed Damage for T2W1 at Test Termination Load.

3.2.3 Exterior Solution 17 (Post-Crack)—T2W2

T2W2 is an exterior test using the full-depth FRP retrofit solution (Solution 17) and was implemented with previous damage that occurred during test T2W1. Figure 3.17 shows the post-crack Solution 17 installed on the west end of the specimen. Figure 3.18 shows the load-deflection plots for the north and south load points.

The measured ultimate load (92 kips) was 26 percent larger than the estimated capacity of 73 kips and 39 percent larger than the exterior hanger-deficient reference capacity. The test was ended when the applied load dropped to about 70 percent of the measured ultimate load. Figure 3.19 shows the observed damage at different load levels. The bent cap experienced a combined hanger and ledge flexure failure at the final load level.

At the SLS of 45 kips, the initial cracks formed at the interface between the concrete block and the ledge on both sides. Negative flexure cracks were detected on the north side web. Initial web shear cracks were detected at 62.5 kips.

At the ULS of 68 kips, cracks formed at the interface between the concrete block and the ledge beside the south side bearing pad. Figure 3.19(a) shows the observed damage on the north side ledge at current load level. Web shear cracks were detected on both sides of the web at the east side of the concrete block. More cracks were observed on the web as the load increased. Horizontal cracks on the flange of the end face started forming at 78.5 kips. Interface cracks between the north side concrete block and the ledge were detected at 81.5 kips.

At the measured ultimate load of 92 kips, the bottom tip of the web FRP de-bonded, as shown in Figure 3.19(b). On the south side concrete block, vertical cracks formed on the FRP wrap. Shear-cracking-induced debonding of the FRP was observed near the center of the south side concrete block. No notable damage was detected on the end face.

The specimen was further loaded after documenting the damage at the measured ultimate load. The applied load was sustained at 90 kips for about two minutes and then dropped to 80 kips. Figure 3.19(e) and (f) show the observed damage at the final load level. Additional cracks formed, and the FRP wrap de-bonded at the top of the south side concrete block. Vertical- and shear-crack-induced FRP debonding was also detected on the north side. FRP separation was observed at the web-ledge interface near the end of the bent cap. The damage increased significantly while the load was sustained at 80 kips for approximately three minutes. The test was ended when the load dropped to 65 kips which was 30 percent lower than the measured ultimate load.



Figure 3.17. Retrofit Solution 17 Installed on West End of Hanger-Deficient Specimen 2.

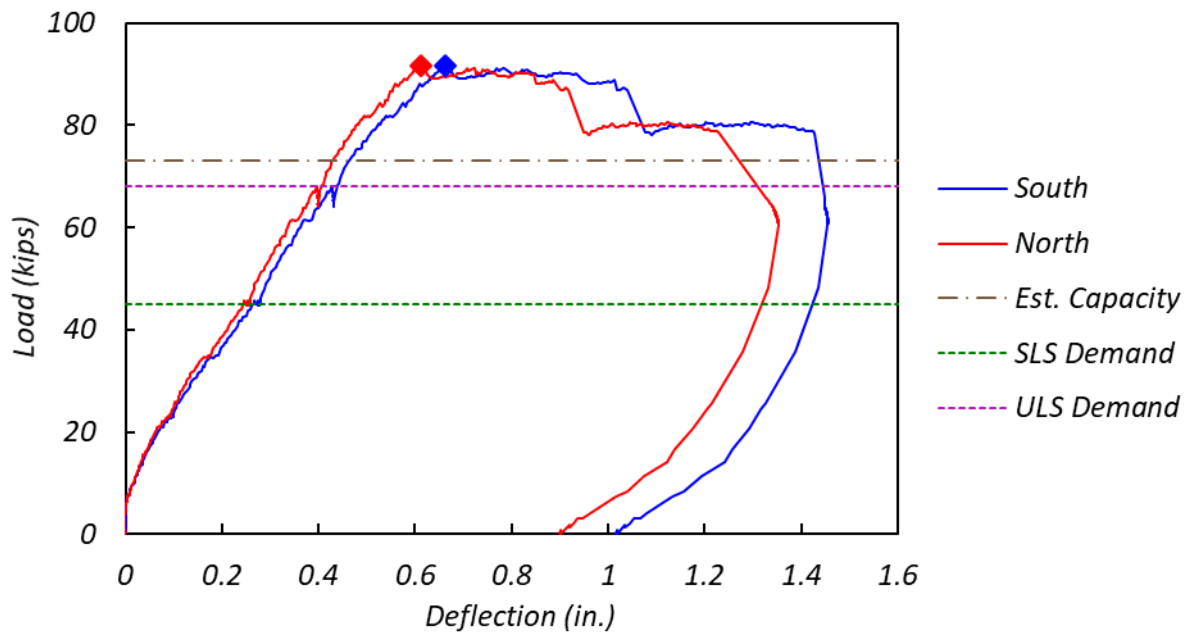
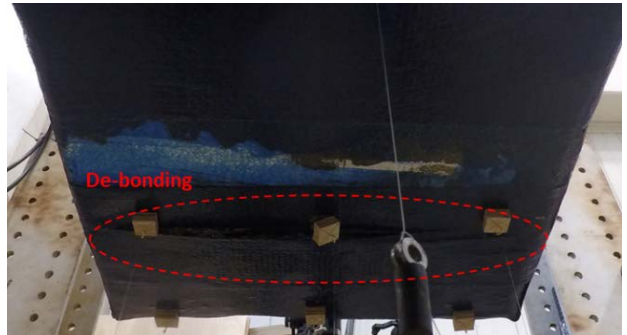


Figure 3.18. Load-Deflection Curve for T2W2.



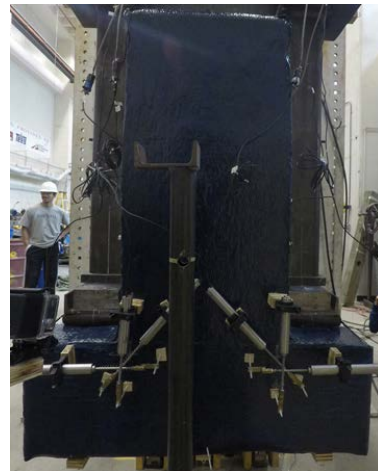
(a) North side at ULS



(b) Bottom at measured ultimate load



(c) North side at measured ultimate load



(d) End face at measured ultimate load



(e) North side at final load level



(f) End face at final load level

Figure 3.19. Observed Damage for T2W2 at Different Load Levels.

3.2.4 Interior Solution 14—T2I1

T2I1 is an interior test using the load-balancing PT retrofit solution (Solution 14). In the interior region, the load balancing works by lifting the girders, thereby reducing the demands on the ledge. In order for the test to reflect conditions of field implementation, the specimen was loaded to dead load prior to stressing the strands. Implementation of the solution is shown in Figure 3.20. The strands were stressed one at a time using a mono strand jack, as shown in Figure 3.20(b). After the PT operation, the specimen was loaded to a test termination load of 105 kips which was determined by adding the capacity contribution of the PT strands (15 kips) to the ultimate load capacity of the hanger-deficient interior specimen (90 kips). Figure 3.21 shows the load-deflection plots for all load points, with diamond symbols indicating the test termination load.

Figure 3.22 shows the observed damage at the test termination load. The specimen maintained a load carrying capacity with a moderate level of damage at the test termination load that was 17 percent larger than the ultimate load capacity of the hanger-deficient interior reference specimen.

No damage was observed until the ULS of 78.5 kips. At ULS, cracks formed at the web-ledge interface behind the bearing pads. The interface cracks propagated through the mid-span between the two bearing pads on both sides of the web. Diagonal shear cracks that initiated at the outside of the bearing pads and propagated toward the center of the specimen were formed on both sides of the web. The angle of the web shear cracks appeared to decrease as they got close to the center of the bent cap. Flexure cracks were detected on the bottom of the bent cap under the bearing pads. At the test termination load of 105 kips, the length and width of existing cracks increased, but no new cracks formed.



(a) Assemblies before testing



(b) Jacking of PT strands after dead load

Figure 3.20. Retrofit Solution 14 Installed on Interior of Hanger-Deficient Specimen 2.

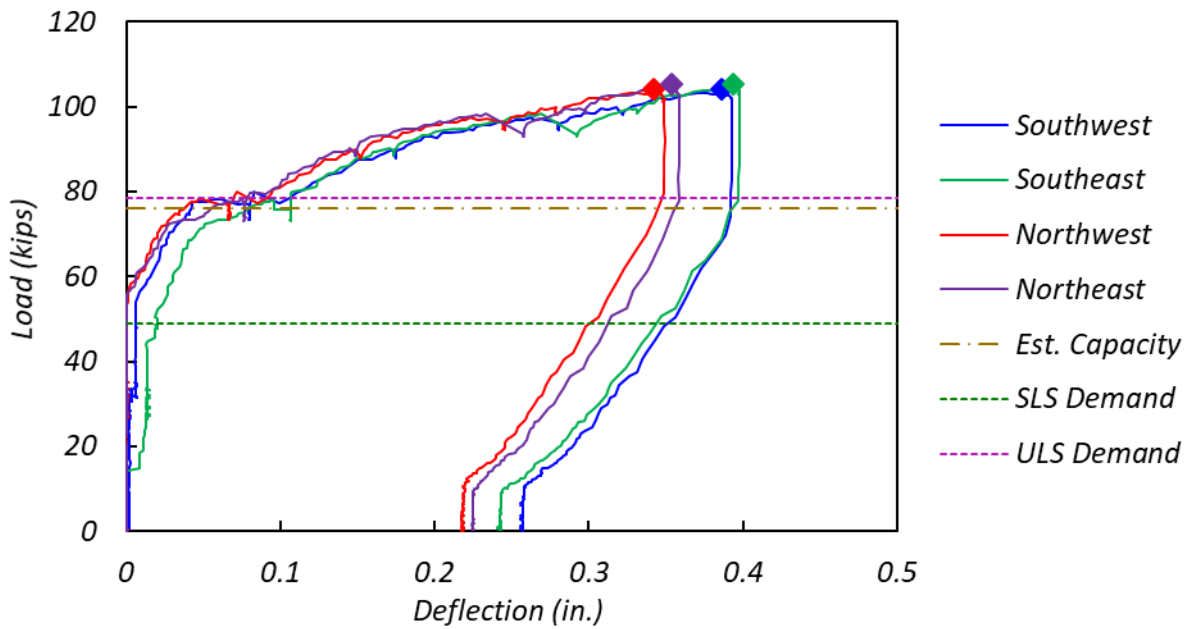


Figure 3.21. Load-Deflection Curve for T2I1.



Figure 3.22. Observed Damage for Test T2I1 at Test Termination Load.

3.2.5 Interior Solution 17 (Post-Crack)—T2I2

T2I2 is an interior test using the full-depth FRP retrofit (Solution 17) and was implemented with previous damage that occurred during test T2I1. Figure 3.23 shows Solution 17 installed on the interior of the specimen. Figure 3.24 shows the load-deflection plots for all load points.

The measured ultimate load of 111 kips was 63 percent larger than the estimated capacity of 68 kips and 23 percent larger than the interior hanger-deficient reference capacity. The test was ended after documenting damage at the measured ultimate load. Figure 3.25 shows the observed damage at different load levels. The bent cap experienced a combined hanger and ledge failure.

At the SLS of 49 kips, no new cracks formed. At a load of 74 kips, diagonal cracks formed on the side face of the ledge under the bearing pads. At the ULS of 78.5 kips, the cracks formed at the interface of the concrete blocks and the ledge. Flexure cracks were also detected on the bottom along the interface of the FRP strip and the bent cap. Crack extensions and new crack formations were observed as load increased. More diagonal shear cracks formed on the web behind the loading points. Near the top of the bent cap, the cracks on the web propagated horizontally.

End interfacial debonding of FRP was detected at the east end of the southwest concrete block at 109 kips. At the measured ultimate load of 111 kips, intermediate shear-crack-induced interfacial debonding of the FRP was observed at all inner ends of the concrete blocks.



Figure 3.23. Retrofit Solution 17 Installed on Interior of Hanger-Deficient Specimen 2.

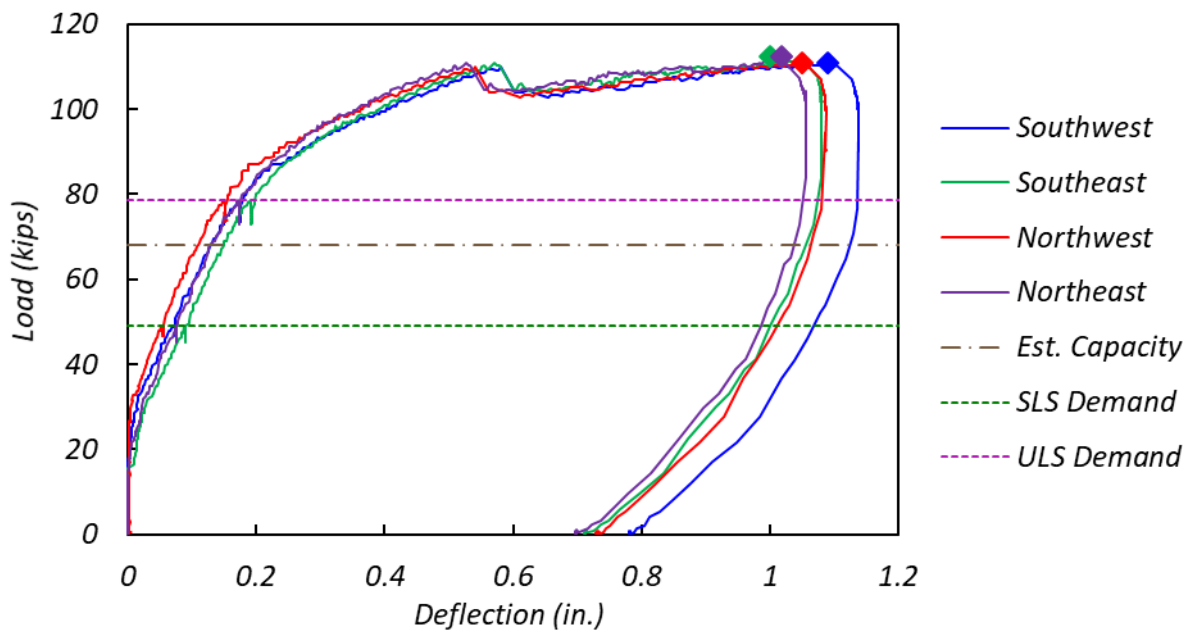


Figure 3.24. Load-Deflection Curve for T2I2.



(a) North side at ULS



(b) North side at measured ultimate



(c) North side at final load level

Figure 3.25. Observed Damage for Test T2I2 at Different Load Levels.

3.3 Ledge-Deficient Specimen 3

Ledge-deficient Specimen 3 provided punching shear tests with small bearing pads (4 in. by 4 in.) used as the reference capacity (T3W1 and T3I1) and larger bearing pads (12 in. by 5 in.) used as the retrofit solution (Solution 18). Figure 3.26 shows the crack patterns for test T3E1 and T3I1. Figure 3.27 shows the crack patterns for test T3W1, T3I2, and T3I3.

3.3.1 Exterior Punch Reference (Small Pad)—T3W1

T3W1 is the exterior reference test for punching shear capacity of ledge-deficient specimens. The small-size bearing pad (4 in. by 4 in.) was used. Figure 3.28 shows the load-deflection plot under the main load point, with horizontal lines indicating SLS, ULS, and estimated capacity, and a diamond indicating the measured ultimate load.

The measured ultimate load (70 kips) was 37 percent larger than the estimated capacity (51 kips). The test was ended when the applied load dropped to about 70 percent of the measured ultimate load. Figure 3.29 shows the observed damage for test T3W1 at the final load level. The specimen showed a punching shear failure, evidenced by the concrete cone punched out from the ledge, as shown in Figure 3.29(a).

At approximately the service load, a 3 in. long diagonal crack formed at the north reentrant corner of the end face. At SLS (45 kips), a new crack formed at the web-ledge interface behind the bearing pad and propagated to the end of the specimen. The cracks were progressively extended until ULS.

At ULS (68 kips), a new crack formed on the top of the ledge 16 in. from the inner side of the bearing pad. Right after ULS, the concrete cone cracks began to form on the side of the ledge. A change of slope in the load-deflection curve was observed. As the loading increased, new cracks formed primarily from the edge of the bearing pad on top of the ledge and extending diagonally to the vertical surface of the ledge and the end surface of the bent cap. The measured ultimate load of 70 kips was observed within 60 seconds after the initiation of the cone cracks. The formation of the main concrete cone was clearly visible before the failure took place. The maximum width of the cone crack was 2 mm at the measured ultimate load.

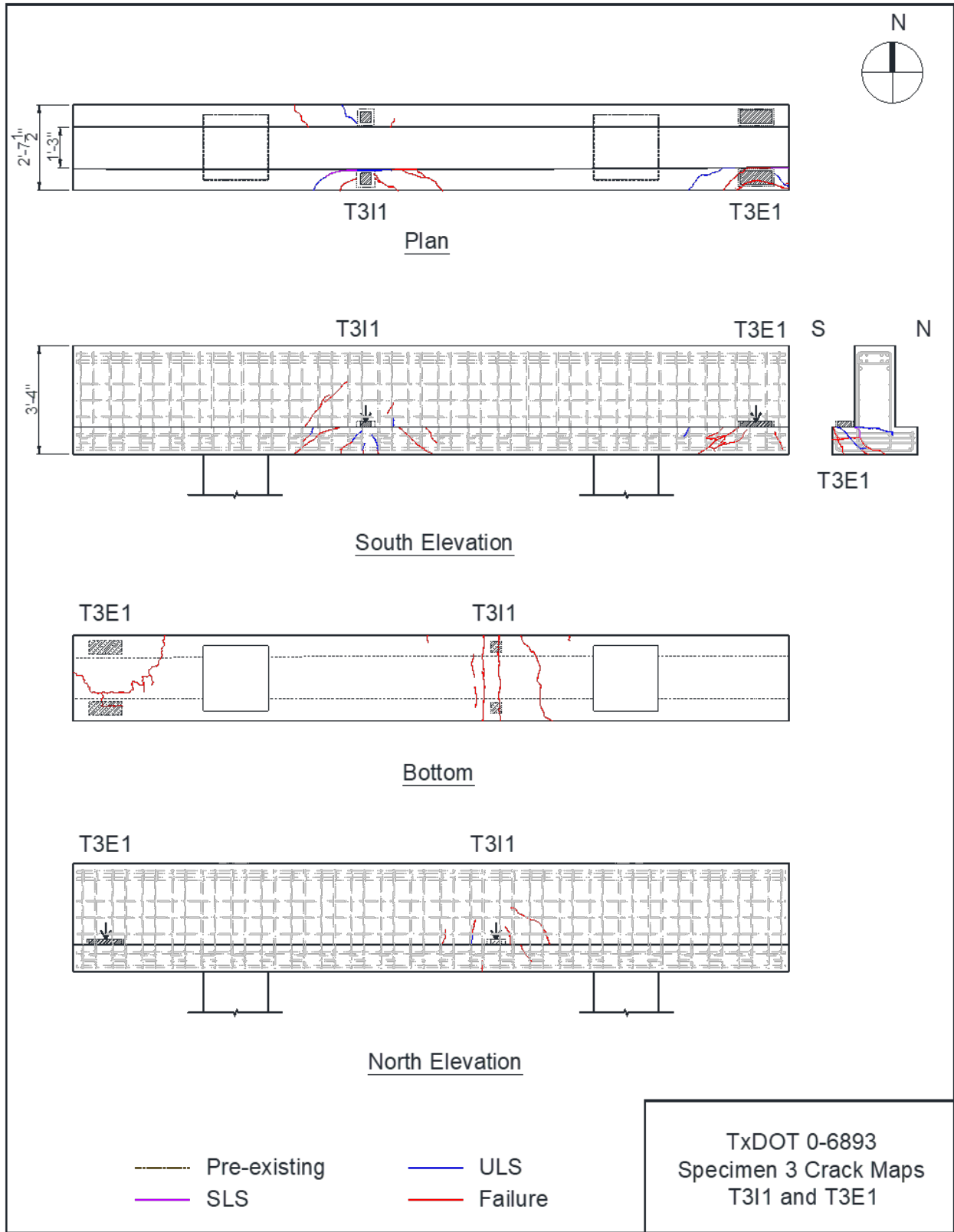


Figure 3.26. Crack Maps for Tests T3I1 and T3E1.

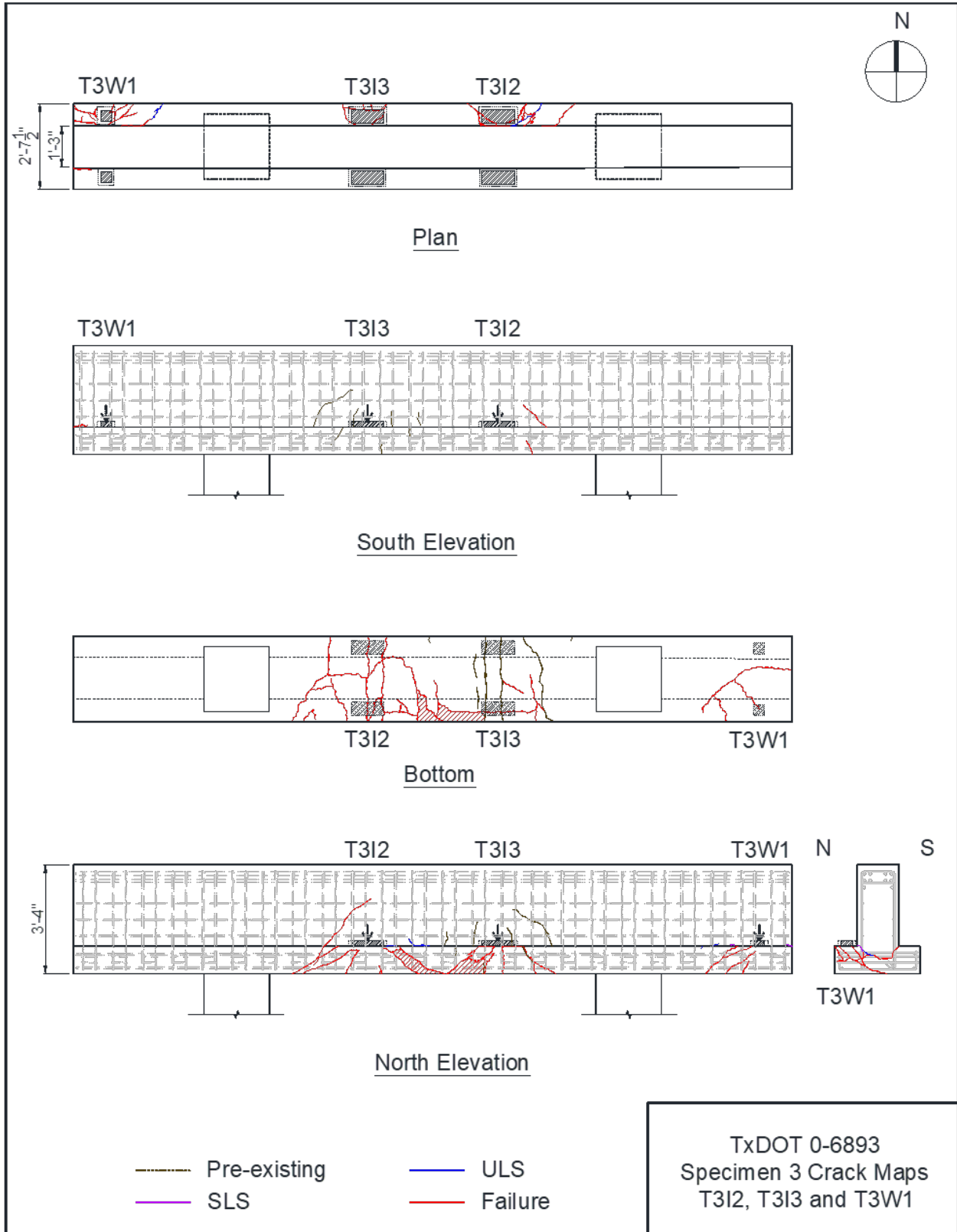


Figure 3.27. Crack Maps for Tests T3I2, T3I3, and T3W1.

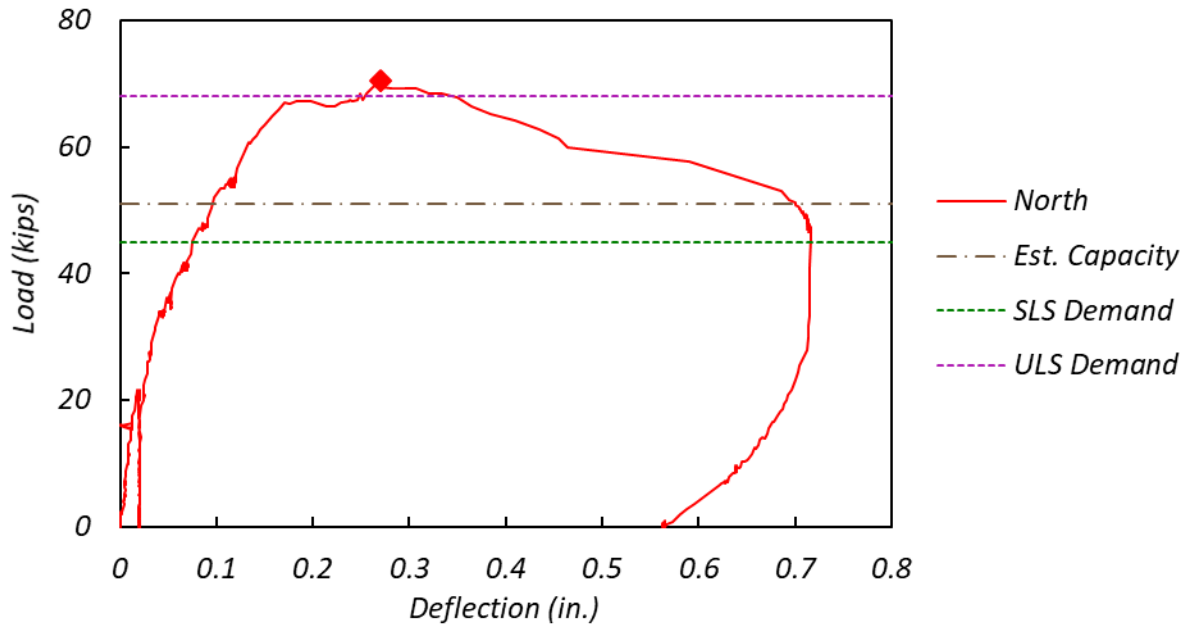


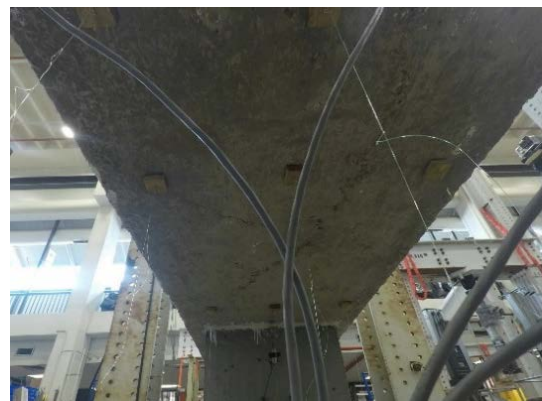
Figure 3.28. Load-Deflection Curve for T3W1.



(a) North side



(b) End face



(c) Bottom

Figure 3.29. Observed Damage for T3W1 at Final Load Level.

The specimen was loaded further after the measured peak, and significant damage progression was observed. The test was stopped when the load dropped to 52 kips. Final failure of the ledge was obtained as the cracks reached the bottom surface of the ledge either on the side surface of the ledge or the end surface of the bent cap. The maximum width of the cone crack was 7 mm at the final load level. The average angle of the main concrete cone was 32.5 degrees, which was shallower than the expected angle of 45 degrees.

3.3.2 Exterior Punch Solution 18 (Large Pad)—T3E1

T3E1 is an exterior test using a large (12 in. by 5 in.) bearing pad (Solution 18). Figure 3.30 shows the load-deflection plot under main loading point.

The measured ultimate load (80 kips) was 31 percent larger than the estimated capacity of 61 kips and 14 percent larger than the measured ultimate load capacity of the exterior punching shear test with the small bearing pad. The test was ended when the applied load dropped to about 50 percent of the measured ultimate load. Figure 3.31 shows the observed damage for T3E1 at the final load level. The bent cap failed in punching shear when a clear concrete cone formed under the loading point.

The damage progression was similar to that observed for T3W1. The initial crack was observed at the SLS of 45 kips. A diagonal crack formed at the south reentrant corner of the end surface of the bent cap with a length of 4 in. This crack also extended toward the inner side of the bent cap along the web-ledge interface about 6 in. and progressively extended as the loading increased.

At the ULS of 68 kips, a new crack was found on the end surface that formed from the south reentrant corner and extended almost horizontally about 14 in. Another diagonal crack on the end surface that connected to the outside edge of the bearing pad and on the top surface of the ledge that also initiated from the inner edge of the bearing pad was also detected. Extensive cracks began to form as the load increased above ULS. Similar crack patterns as T3W1 were observed, and most of the cracks formed from the edge of the bearing pad and diagonally extended to the side of the ledge. The main concrete cone crack initiated at a load of 78 kips, accompanied by a slope change in the load-deflection curve. The crack quickly extended to the bottom of the bent cap. The measured ultimate load of 80 kips was observed shortly after the cone crack took place. The maximum width of the cone crack at the measured peak was 2 mm.

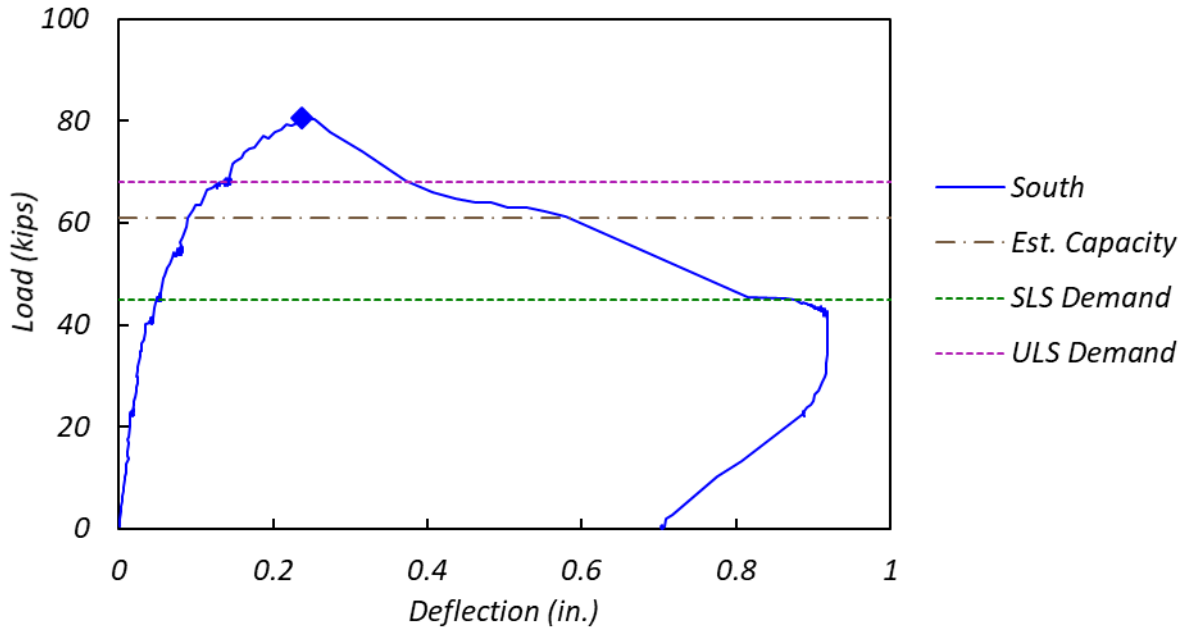
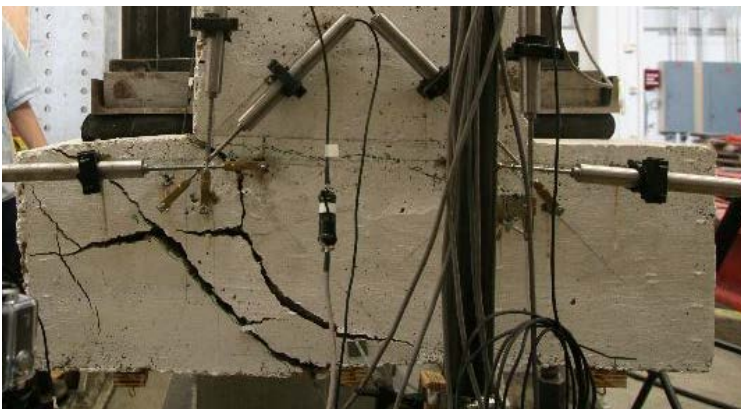


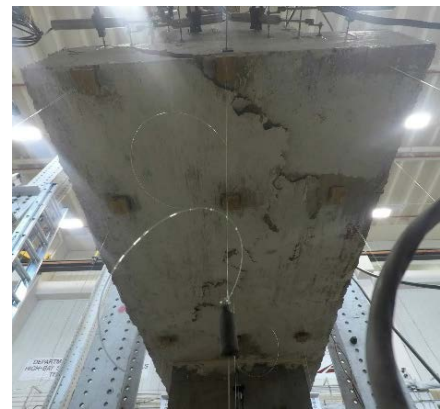
Figure 3.30. Load-Deflection Curve for T3E1.



(a) Side



(b) End face



(c) Bottom

Figure 3.31. Observed Damage for T3E1 at Final Load Level.

The specimen was loaded further after the measured peak. More cracks formed and the width of the cone cracks were increased significantly. The test was ended when the load dropped to 43 kips. The width of the cone crack on the side of the ledge was 10 mm at the final load level. An average angle of 32.5 degrees was observed for T3E1, which was the same as T3W1.

3.3.3 Interior Punch Reference (Small Pad)—T3I1

T3I1 is the interior reference test for punching shear capacity of ledge-deficient specimens. The small-size bearing pad (4 in. by 4 in.) was used. Figure 3.32 shows the load-deflection plot under the main loading point.

The measured ultimate load (104 kips) was 89 percent larger than the estimated capacity of 55 kips. The test was ended when the applied load dropped to about 90 percent of the measured ultimate load. Figure 3.33 shows the damage for test T3I1 at the final load level. A clear punching shear failure was observed in which a truncated concrete pyramid punched out from the ledge.

The first cracks were observed at the service load. A crack began to form at the corner of the bent cap behind the bearing pad and extended 11 in. away from the pad. This crack extended to the side surface of the ledge as the loading reached the ultimate state. At the ultimate loading, different crack patterns formed compared to the previous tests. An almost vertical crack formed on the side surface of the stem that was 6 in. away from the south side of the bearing pad, and one more vertical crack formed on the other side surface of the stem. Moreover, cracks formed right underneath the bearing pad on the side surface of the ledge, extended to the bottom of the ledge, and went all the way through the flange of the bent cap on the bottom surface. The main concrete cone began to form at 92 percent of the failure load, and more cracks formed on the side surface of the stem. A notable difference in the crack pattern for test T3I1 was that the cracks on the stem and on the bottom went through the flange of the bent cap. The ledge failed as the main concrete cone cracks reached the bottom of the ledge. The formation of the concrete cone was obvious on the side surface of the ledge. However, there was no punching action on the bottom surface of the bent cap. Crack angles were 30 degrees on the west side and 35 degrees on the east side.

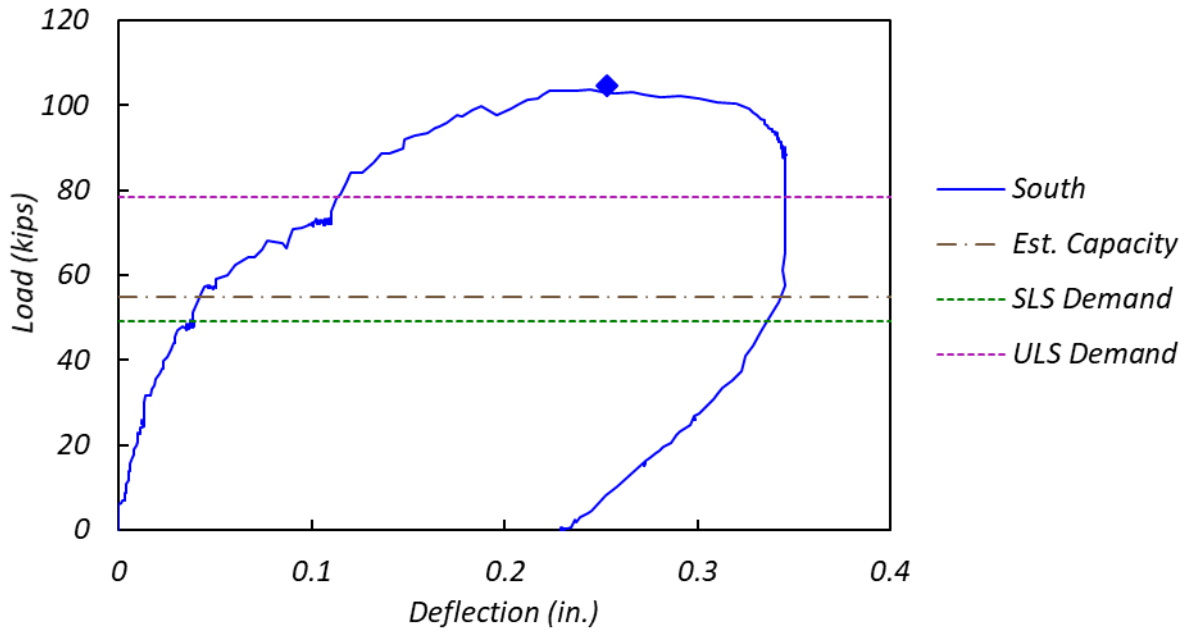


Figure 3.32. Load-Deflection Curve for T3I1.



(a) Side

(b) Bottom

Figure 3.33. Observed Damage for T3I1 at Final Load Level.

3.3.4 Interior Punch Solution 18 (Large Pad)—T3I2 and T3I3

T3I2 and T3I3 are interior tests using a large (12 in. by 5 in.) bearing pad (Solution 18). Tests were conducted independently. Figure 3.34 and Figure 3.35 show the load-deflection plot for test T3I2 and T3I3 under main loading points, respectively.

The measured ultimate load for T3I2 and T3I3 (94 kips) was 25 percent larger than the estimated capacity of 75 kips but 10 percent smaller than the measured ultimate load capacity of the interior punching shear test with the small-size bearing pad. The test was ended when the applied load dropped to about 75 percent of the measured ultimate load. Figure 3.36 shows the observed damage for T3I2 and T3I3 at final load level. Both the tested regions experienced punching shear failure with truncated pyramid-shaped failure surfaces forming under the loading points.

The observed crack patterns and failure shapes for both tests were similar to the interior punching shear test with the small-size bearing pad. No cracks were found at SLS. Right after SLS, a crack formed in a similar way from the corner behind the bearing pad and extended diagonally about 11 in. away from the pad. The crack extended to the side surface of the ledge as the loading increased to the ultimate loading state. A small diagonal crack formed on the stem at the ultimate loading. Significant cracks formed when the load increased to 90 kips. A long 45-degree shear crack formed on the stem, and the main concrete cone also began to form at this loading stage. Similar crack patterns were formed on the bottom surface for test T3I2 as well.

The ledge failed as the concrete cone completely formed but with a relatively lower strength of 94 kips, even though it was loaded with the large bearing pad. Therefore, to have one more set of the data, T3I3 was conducted right beside the T3I2 location and loaded up to failure without stopping the load. A similar pattern was observed, and the ledge failed at the same load as T3I2 (94 kips), even though there were preexisting cracks at the location of T3I3 that were caused from T3I1. Moreover, the concrete cones from T3I2 and T3I3 intersected since the loading points were located closer to each other. The set of average crack angles for the concrete cone was 30 to 35 degrees and 40 to 45 degrees for T3I2 and T3I3, respectively.

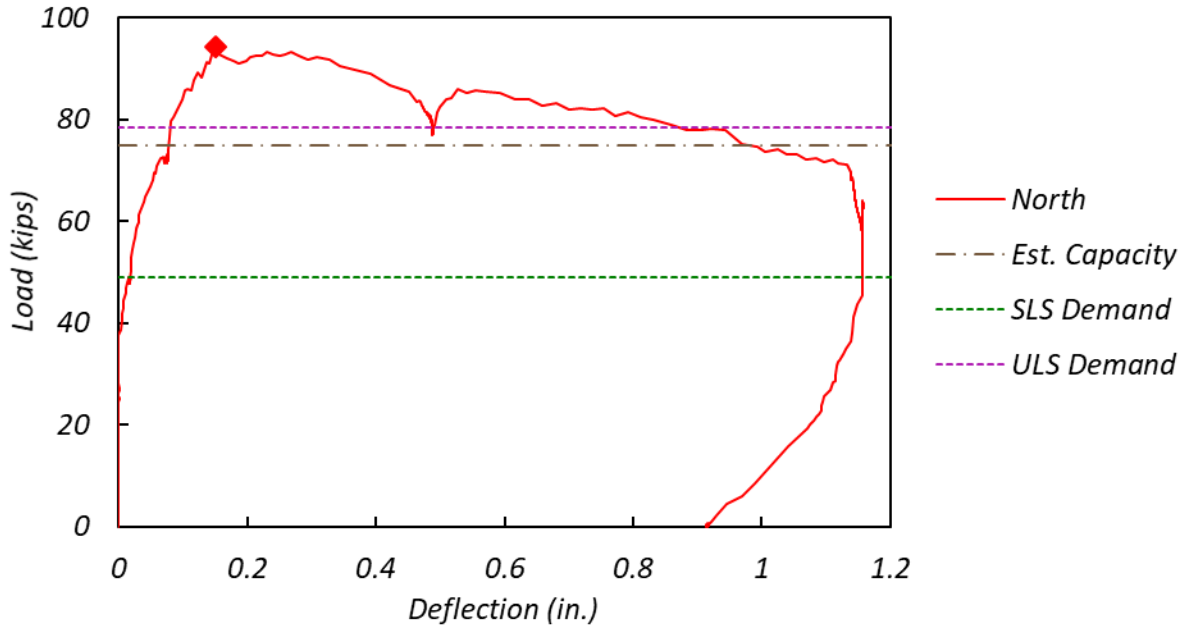


Figure 3.34. Load-Deflection Curve for T3I2.

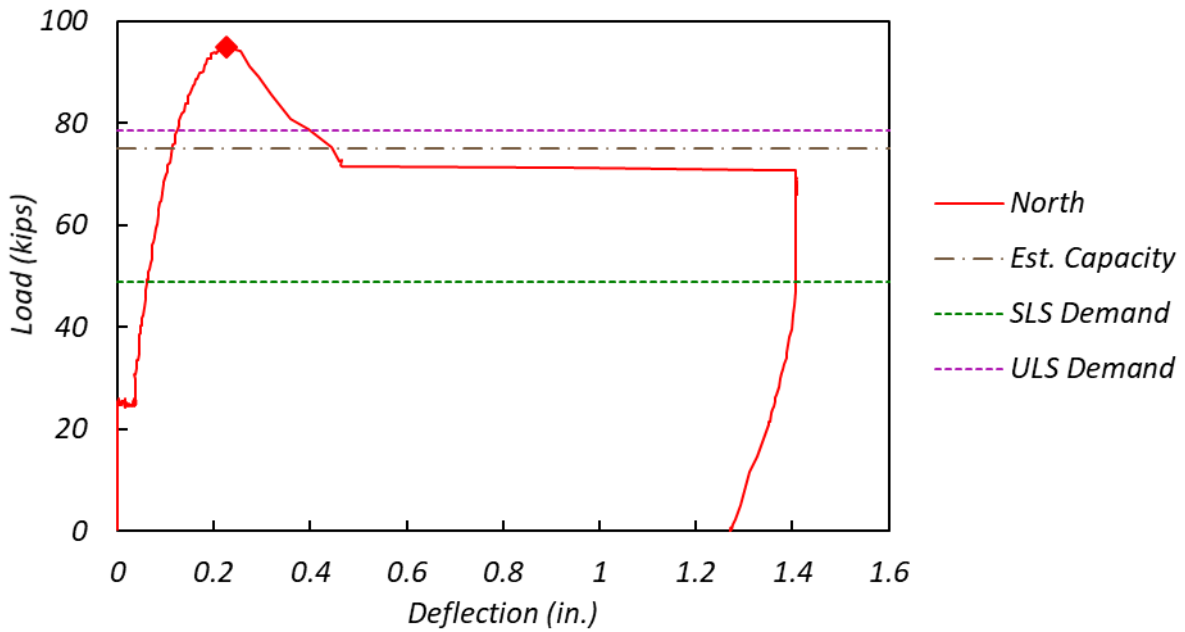
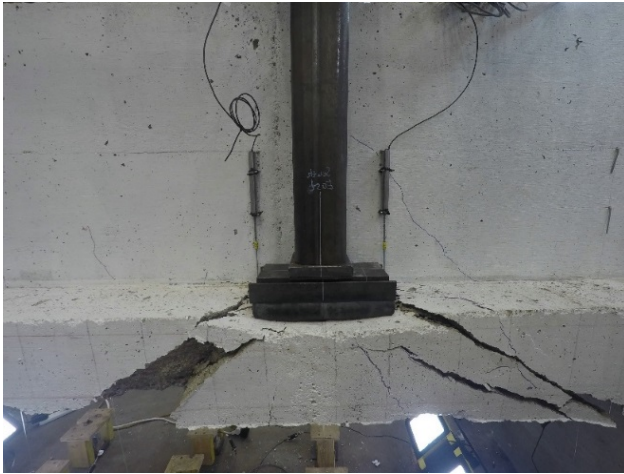


Figure 3.35. Load-Deflection Curve for T3I3.



(a) T3I2



(b) T3I3

Figure 3.36. Observed Damage for T3I2 and T3I3 at Final Load Level.

3.4 Ledge-Deficient Specimen 4

Specimen 4 provided tests of all clamped threadbar solution variations (Solution 8) on a ledge-deficient specimen. Figure 3.37 shows crack patterns at SLS, ULS, and failure.

3.4.1 Exterior Solution 8(a)—T4W1

T4W1 is an exterior test using a single clamped threadbar (Solution 8[a]). Figure 3.38 shows Solution 8(a) installed on the west end of the specimen. Figure 3.39 shows the load-deflection plots for the north and south load points, with horizontal lines indicating SLS, ULS, and estimated capacity, and diamonds indicating the measured ultimate load.

The measured ultimate load (90 kips) was 14 percent larger than the estimated capacity (79 kips) and 36 percent larger than the exterior ledge-deficient reference capacity. The test was ended when the applied load dropped to about 80 percent of the measured ultimate load. Figure 3.40 shows the observed damage at the final load level. The specimen experienced a combined ledge flexure and punching shear failure, with more extensive damage occurring on the south side.

The initial crack formed at SLS (45 kips) at the web-ledge interface behind the south side bearing pad. It propagated to the end of the specimen along the web-ledge interface. On the end face, the crack extended diagonally at an approximate angle of 30 degrees.

Under the ULS demand of 68 kips, crack extensions and new crack formations were observed. The cracks at the web-ledge interface propagated toward the column. On the top of the ledge, the cracks at the web-ledge interface extended diagonally to the side face of the ledge. Diagonal shear cracks were also detected on both sides of the web. On the end face, another diagonal crack formed at the north corner. The two diagonal cracks on the end face started at the reentrant corner, propagated horizontally, and connected. A hanger crack formed on the end face 26 in. above the bottom of the bent cap.

Significant extension of existing cracks and new crack formations on the entire tested region were observed as the load went higher than ULS. More diagonal cracks formed on the top of the ledge and further extended to the side face. On the web, new diagonal shear cracks were also presented. New cracks were only formed on the ledge part of the bent cap on the end face. The cracks at the web-ledge interface behind the south bearing pad had a maximum crack width of 8 mm. The maximum crack width observed on the end face was 7 mm. The deflection of the outside channel under the bent cap was visible to the naked eye at the measured ultimate load.

After marking the cracks at the measured ultimate load, the bent cap was loaded further. Crack widths increased except on the hanger crack, with wider cracks on the south side ledge. The bent cap lost its load carrying capacity gradually. The test was ended when the load dropped to 71 kips, which was 20 percent lower than the measured ultimate load.

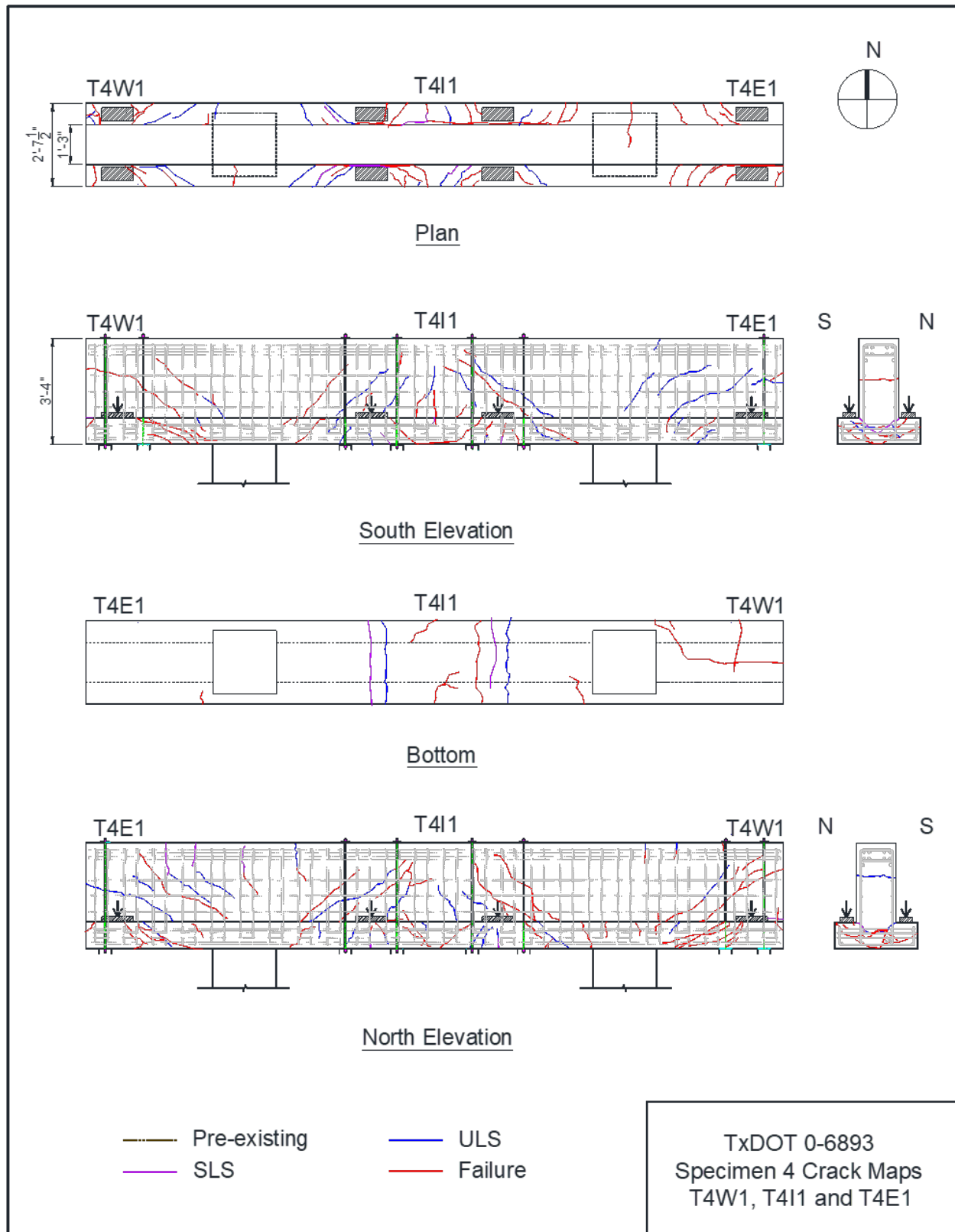


Figure 3.37. Crack Maps for Tests T4W1, T4I1, and T4E1.



Figure 3.38. Retrofit Solution 8(a) Installed on West End of Ledge-Deficient Specimen 4.

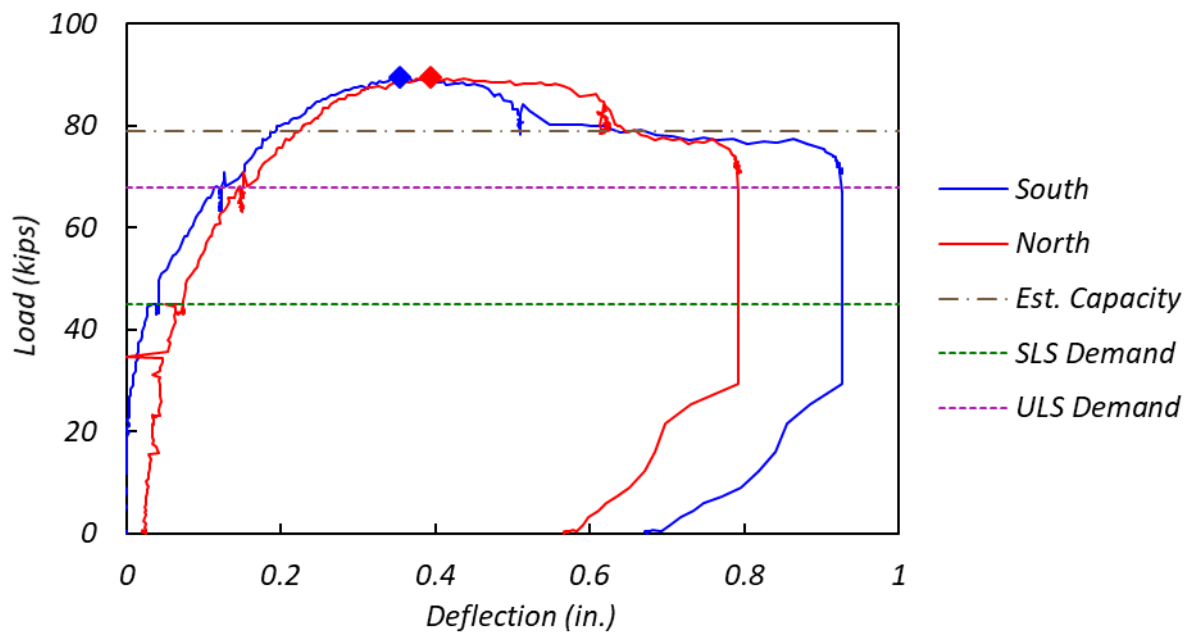


Figure 3.39. Load-Deflection Curve for T4W1.



(a) End face at SLS



(b) End face at ULS



(c) End face at final load level



(d) North side at final load level



(e) South side at final load level

Figure 3.40. Observed Damage for Test T4W1 at Final Load Levels.

3.4.2 Exterior Solution 8(b)—T4E1

T4E1 is an exterior test using a single clamped threadbar (Solution 8[b]). Figure 3.41 shows Solution 8(b) installed on the east end of the specimen. Figure 3.42 shows the load-deflection plots for the north and south load points.

The measured ultimate load (80 kips) was about 27 percent larger than the estimated capacity (63 kips) and 21 percent larger than the interior ledge-deficient specimen reference capacity. The test was ended when the applied load dropped to about 90 percent of the measured ultimate load. Figure 3.43 shows the observed damage at final load level. A combined ledge and punching shear failure occurred, with greater damage on the north side.

The initial cracks formed at 40 kips at the web-ledge interface behind the south bearing pad. Negative flexure cracks were detected on the north side of the web. At the SLS of 45 kips, interface cracks behind the bearing pads were found at both sides of the ledge. On the end face, cracks propagated diagonally at an angle of 32° toward the center of the bent cap.

At a load of 57 kips, initiation of diagonal shear cracks was observed on both sides of the web. A hanger crack formed 24.5 in. above the bottom of the bent cap on the end face. At the ULS of 68 kips, more web cracks appeared. On the top of the ledge, the cracks behind the bearing pad extended diagonally, starting at the inner edge of the bearing pad and going to the side face of the ledge. More ledge cracks formed near the web-ledge interface on the end face. The maximum width of the ledge cracks on the end face was 0.9 mm, and the width of the hanger crack was 0.5 mm.

As the load exceeded ULS, the bent cap showed significant crack length and width extensions and new cracks formed. Most of the new cracks formed on the ledge. More cracks formed on the north side of the ledge than on the south side. At the measured ultimate load of 80 kips, diagonal cracks formed on the top of the ledge on both sides. On the side of the ledge, new cracks mainly formed on the north side ledge, with a maximum width of 4.5 mm. One more web shear crack formed on the north side, while no new crack formations were observed on the south side of the web. The negative cracks on the north side of the web extended farther. On the end face, new ledge cracks were detected. As shown in Figure 3.43(d) and (e), more cracks formed on the north part. The maximum crack width on the end face was 6 mm. The width of the hanger cracks remained the same.



Figure 3.41. Retrofit Solution 8(b) Installed on East End of Ledge-Deficient Specimen 4.

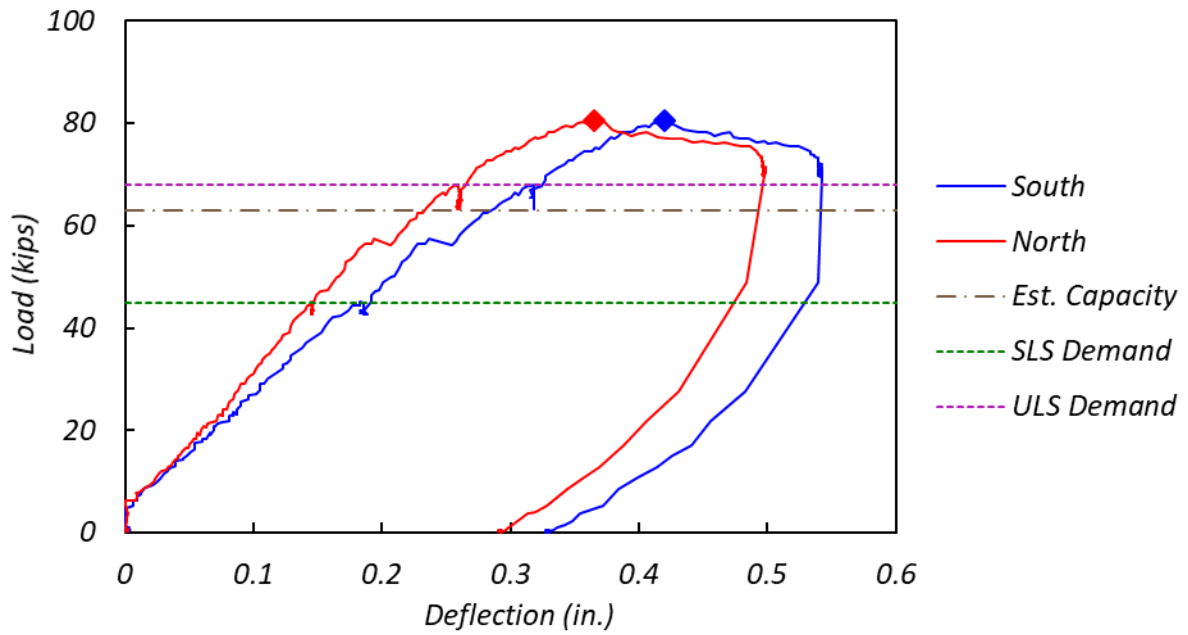
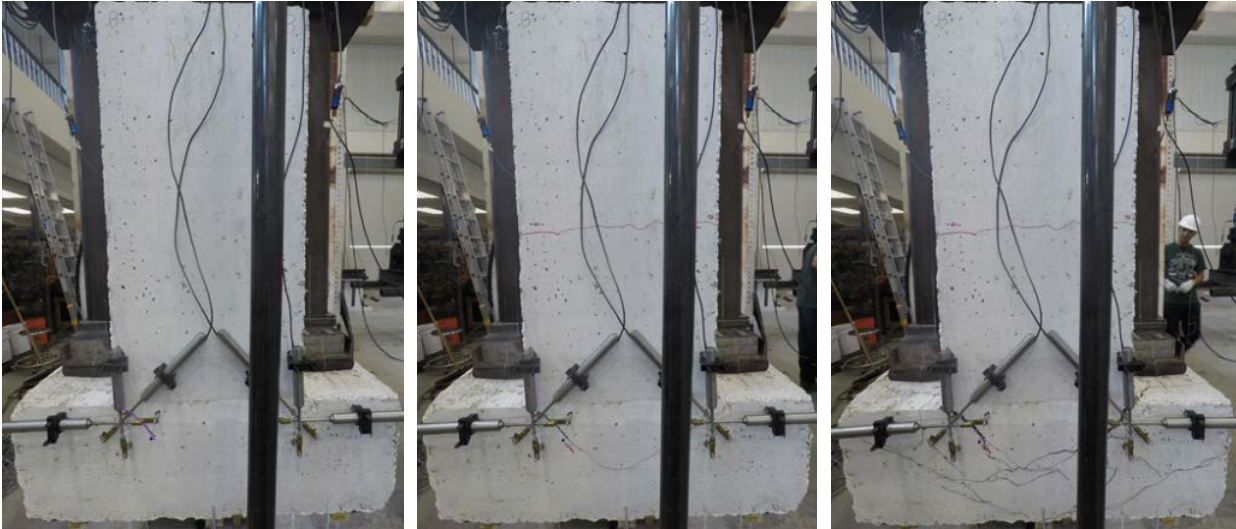


Figure 3.42. Load-Deflection Curve for T4E1.



(a) End face at SLS

(b) End face at ULS

(c) End face at final load level



(d) South side at final load level



(e) North side at final load level

Figure 3.43. Observed Damage for Test T4E1 at Different Load Levels.

3.4.3 Interior Solution 8—T4I1

T4I1 is an interior test retrofitted with clamped threadbars (Solution 8). Figure 3.44 shows Solution 8 installed on the mid-span of the specimen. Figure 3.45 shows the load-deflection plots for all load points.

The measured ultimate load (99 kips) was 6 percent smaller than the estimated capacity of 105 kips and 16 percent larger than the interior ledge-deficient reference test measured ultimate load. The test was ended after documenting the damages at the measured ultimate load. Figure 3.46 shows the observed damage. The bent cap failed in a combined ledge flexure and punching shear.

The initial cracks were found at the SLS of 49 kips at the web-ledge interface behind the bearing pads. The cracks at the interface propagated about 10 in. toward both sides of the bearing pad, and diagonally extended to the top of the ledge. Flexure cracks were detected on the bottom of the bent cap under the loading points.

Crack extensions and new crack formations were observed as the load increased. Initiation of shear cracks on both sides of the web were detected at a load of 64.5 kips. The web shear cracks on this state were formed at the outside of the bearing pads toward the center of the bent cap.

At the ULS of 78.5 kips, more diagonal shear cracks were formed on both sides of the web. The shear cracks close to the center of the bent cap had steeper angles than the cracks near the columns. More diagonal cracks formed at the top of the ledge. Diagonal cracks were detected on the side face of the ledge at the outside of the bearing pads with the exception of the northwest bearing pad. Cracks formed on the inside as well as around the northwest bearing pad. The maximum crack width of the diagonal cracks on the side face of the ledge was 2 mm. On the bottom of the bent cap, two more flexure cracks were detected.

A significant crack width increase of ledge cracks was observed as the load was increased above the ULS demand. New crack formations were observed on the entire test region. At the measured ultimate load of 99 kips, the deflection of the two outside channels was visible. Diagonal cracks on the side face of the ledge had a maximum width of 5 mm. A clear pyramid-shaped cone formed under all the bearing pads. The outside diagonal cracks on the ledge were wider than the inside cracks.



Figure 3.44. Retrofit Solution 8 Installed on Interior of Ledge-Deficient Specimen 4.

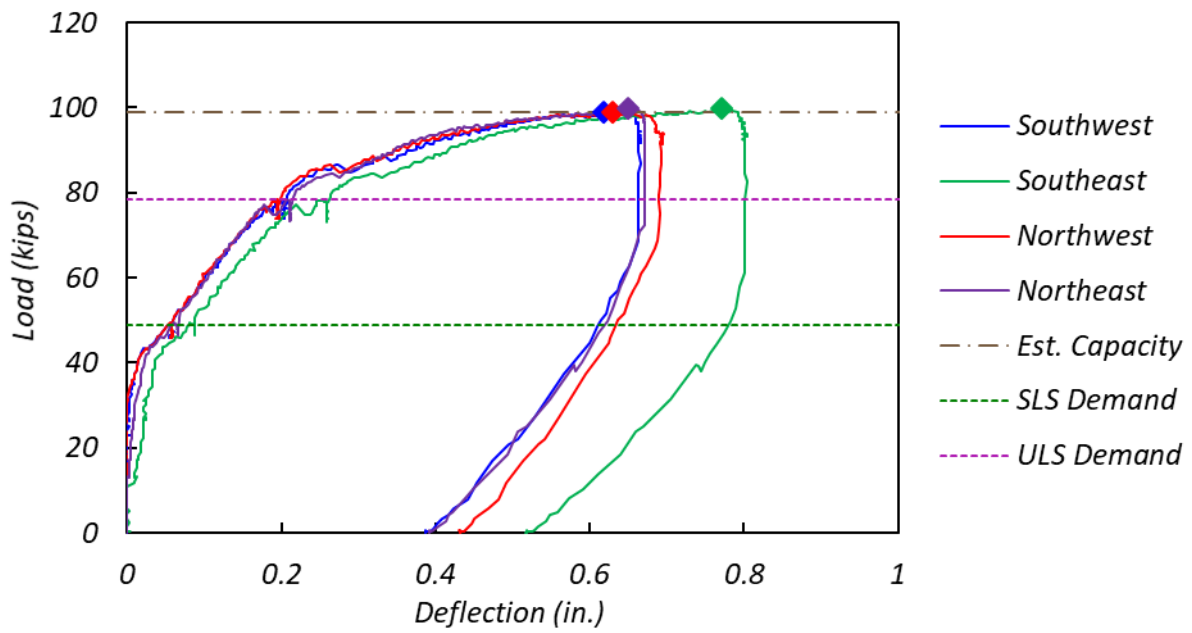


Figure 3.45. Load-Deflection Curve for T4I1.



(a) North side at SLS



(b) North side at ULS



(c) North side at final load level



(d) Channels at final load level

Figure 3.46. Observed Damage for Test T4I1 at Different Load Levels.

3.5 Ledge-Deficient Specimen 5

Ledge-deficient Specimen 5 provided ledge reference tests on the exterior (T5E1) and interior (T5I1) and an exterior test of the end-stiffener retrofit solution (Solution 3). Figure 3.47 shows crack patterns at SLS, ULS, and failure.

3.5.1 Exterior Ledge Reference—T5E1

T5E1 is the exterior reference test for ledge-deficient specimens. Figure 3.48 shows the load-deflection plots for the north and south load points, with horizontal lines indicating SLS, ULS, and estimated capacity, and diamonds indicating the measured ultimate load.

The measured ultimate load (66 kips) was 37 percent larger than the estimated capacity (48 kips). Loading continued after the measured ultimate load until the applied load dropped to about 45 percent of the measured peak load. Figure 3.49 shows the observed damage for test T5E1 at different load levels. The failure started as a ledge flexure failure and finally formed a combined ledge flexure and punching shear failure.

The initial crack formed at 41 kips at the web-ledge interface behind the south bearing pad. At SLS, similar cracks formed behind the northern bearing pad. The cracks behind the bearing pad propagated along the web-ledge interface to the end face. On the end face, cracks extended diagonally at an angle of approximately 30 degrees, as shown in Figure 3.49(a). On the top of the ledge, the cracks behind the bearing pad extended diagonally, starting at the inner edge of the bearing pad and going to the side face of the ledge. The cracks that formed at SLS were all hairline cracks.

At the estimated capacity of 54 kips, the diagonal cracks from two reentrant corners on the end face connected horizontally with a width of 1 mm, as shown in Figure 3.49(b). Crack extensions and new crack formations were observed as the load increased.

The load reached the measured ultimate load of 66 kips, which was less than the ULS demand of 68 kips, and then dropped to 55 kips. Figure 3.49(c) shows the damage on the end face at the measured ultimate load. A hanger crack—horizontal crack through the web on the end face, as shown in Figure 3.49(c)—formed near the neutral axis of the bent cap. More ledge cracks formed on the flange on the end face. The crack near the web-ledge interface on the end face opened up to 2.5 mm. Diagonal shear cracks were present on both sides of the web about 20 in. from the edge of the bearing pad. More cracks also formed at the top and side faces of the ledge.

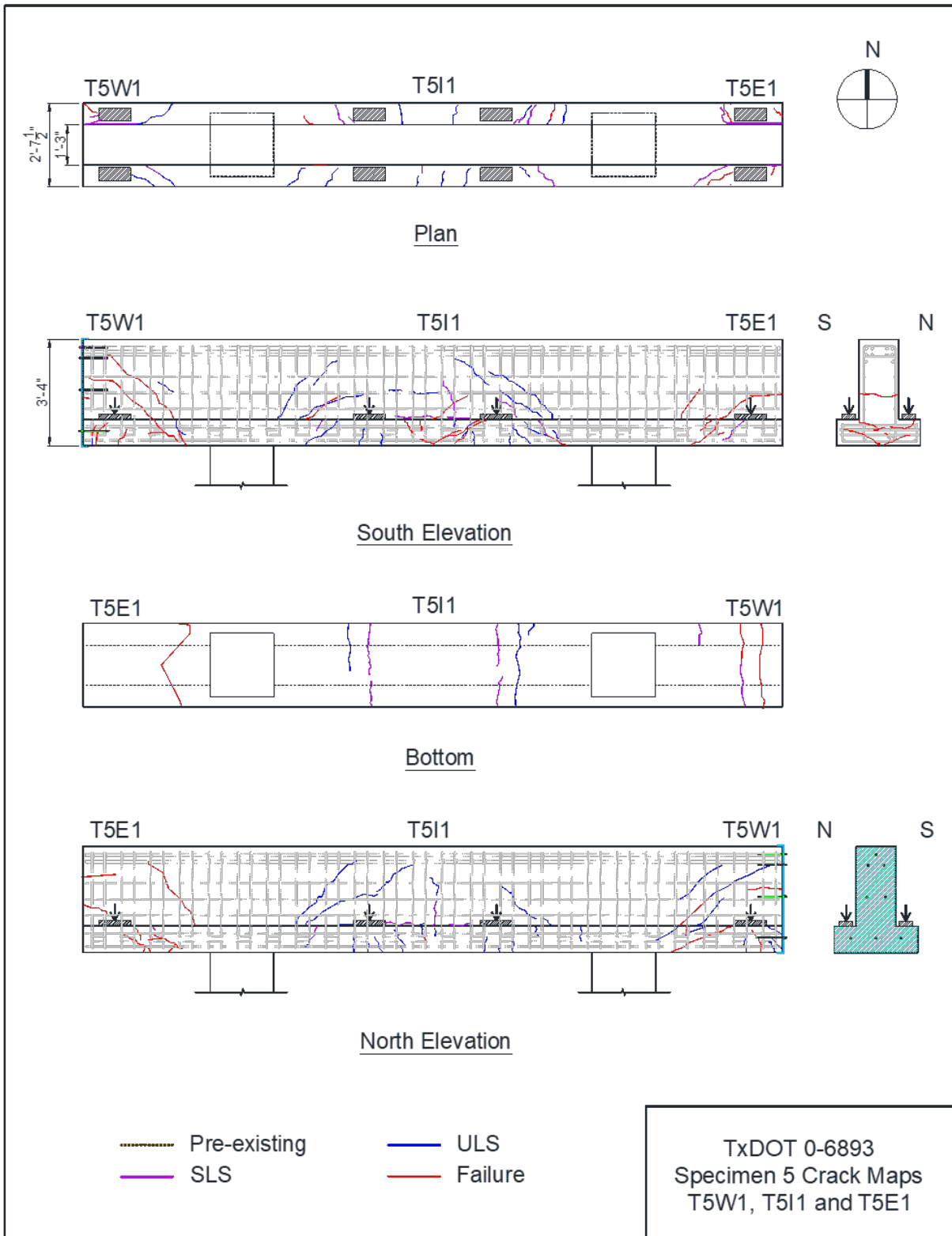


Figure 3.47. Crack Maps for Tests T5W1, T5I1, and T5E1.

After marking cracks at the measured ultimate load, the specimen was further loaded by adding the same amount of pressure to the actuator. The load was then increased to 62.5 kips and then dropped to 37.5 kips. Crack length and width growth of existing cracks except the hanger crack was observed. The maximum width of the ledge cracks on the end face increased to 4 mm, while the width of the hanger cracks remained the same. New crack formations on the side and bottom of the ledge were also detected. The cracks on the side of both ledges extended to form a cone shape. The cone started from each side of the ledge and connected on the bottom of the bent cap, as shown in Figure 3.49(f). The load was sustained at about 32 kips while it was loaded again and then dropped to 23 kips at the final stage.

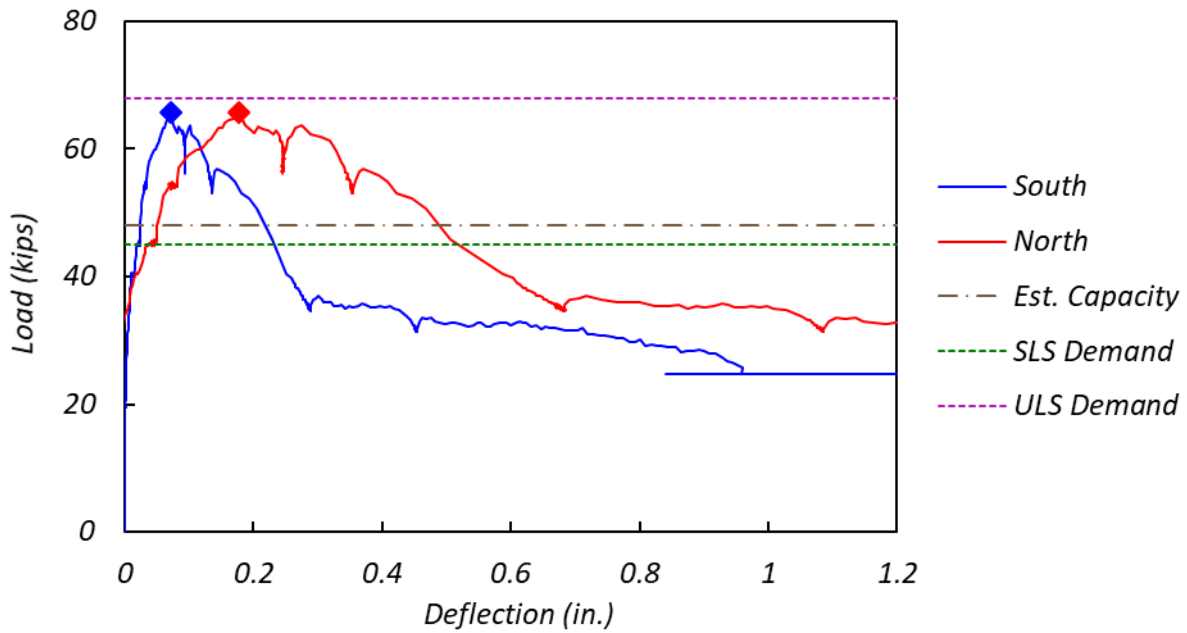


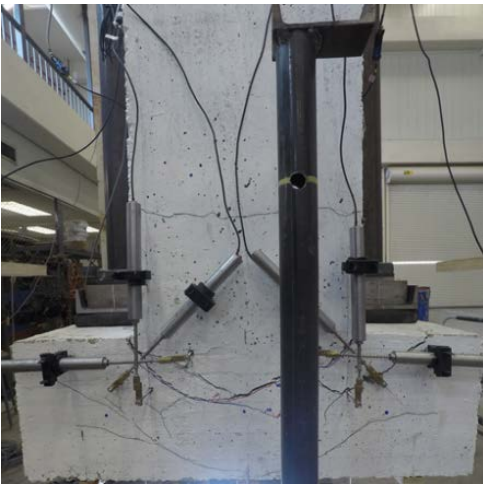
Figure 3.48. Load-Deflection Curve for T5E1.



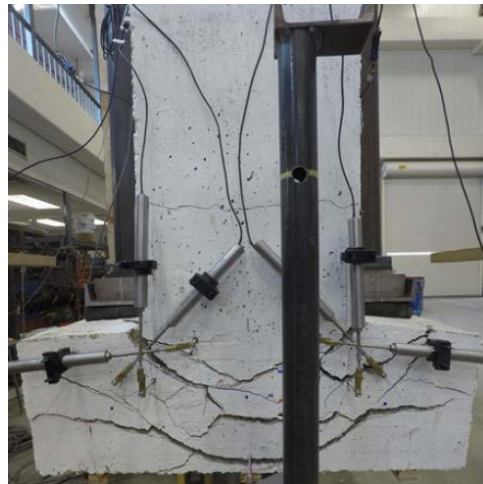
(a) End face at SLS



(b) End face at estimated capacity



(c) End face at measured ultimate load



(d) End face after peak—37.5 kips



(e) South side after peak—37.5 kips



(f) Bottom after peak—37.5 kips

Figure 3.49. Observed Damage for T5E1 at Different Load Levels.

3.5.2 Interior Ledge Reference—T5I1

T5I1 is the interior reference test for ledge-deficient specimens. Figure 3.50 shows the load-deflection plots for all load points.

The measured ultimate load (85 kips) was 15 percent larger than the estimated capacity (74 kips). The test was ended when the applied load dropped to about 70 percent of the measured ultimate load. Figure 3.51 shows the observed damage at different load levels. The tested region experienced a ledge shear failure, with more extensive damage on the north side.

The initial cracks were observed at SLS on the web-ledge interface behind the bearing pads. Figure 3.51(a) shows the observed damage at SLS around the northwest loading points. The cracks at the interface extended about 10 in. from the center of the load points toward the center of the bent cap. On the outside of the bearing pads, the web-ledge interface cracks started from the edge and propagated diagonally to the side face of the ledge. A 75-degree-angle web shear crack and an 85-degree-angle web shear crack were observed near the center of the bent cap on the north and south sides, respectively. Flexural cracks were also detected on the bottom of the bent cap. The cracks observed at SLS were all hairline cracks.

Under the ULS demand, crack extension and new crack formation were observed. Figure 3.51(b) shows the observed damage at ULS around the northwest loading point. Diagonal cracks on the top face of the ledge started at the web-ledge interface and propagated all the way to the side face of the ledge. Web shear cracks on the web that initiated from the web-ledge interface were formed on the outside of the bearing pad. More flexural cracks were observed on the bottom of the bent cap. The maximum width of the web-ledge interface cracks and ledge shear cracks was 2.5 mm and 0.8 mm, respectively.

Under the measured ultimate load, width extension of existing cracks and new crack formations around the northwest bearing pad were detected. Figure 3.51(c) shows the observed damage on the north side. It is evident in the figures that more damage occurred on the north side than on the south side. New cracks mainly formed on the side face of the ledge. The width of the diagonal ledge shear crack on the outside of the northwest bearing pad was 3.5 mm. Web-ledge interface cracks on the north side increased to 3.5 mm.

The bent cap was further loaded after the measured ultimate load by pumping the same amount of pressure to both actuators. The east and west actuator loads were sustained at around 73 kips and 75 kips, respectively. Figure 3.51(d) shows the extent of damage at a post-failure load of 45 kips, when the cracks further opened and the north side ledge region deformed outward and downward from the web.

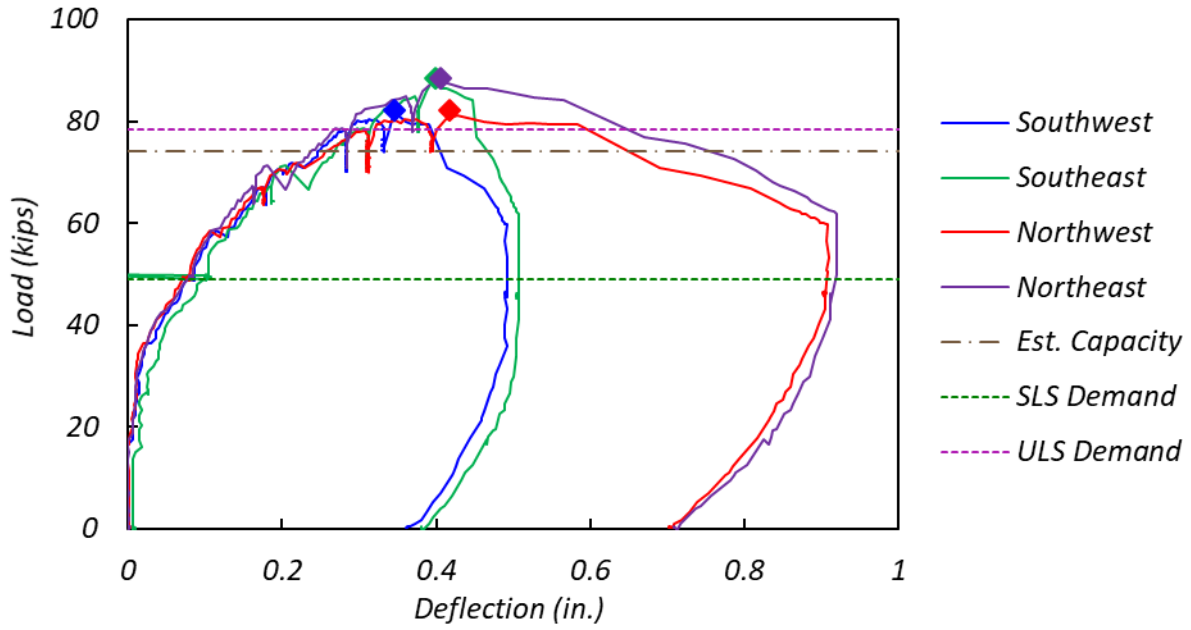


Figure 3.50. Load-Deflection Curve for T5I1.



(a) SLS—northwest loading point



(b) ULS—northwest loading point



(c) Measured ultimate load—north side



(d) After peak—north side

Figure 3.51. Observed Damage for T5I1 at Different Load Levels.

3.5.3 Exterior Solution 3—T5W1

T5W1 is an exterior test using an end-stiffener retrofit solution (Solution 3). Figure 3.52 shows Solution 3 installed on the west end of the specimen. Figure 3.53 shows the load-deflection plots for the north and south load points.

The measured ultimate load (86 kips) was 69 percent larger than the estimated capacity of 51 kips and 30 percent larger than the exterior ledge-deficient reference capacity. The test was ended when the applied load dropped to about 80 percent of the measured ultimate load. Figure 3.54 shows the observed damage at the final load level. The specimen failed in punching shear on the north side.

The initial cracks formed at the web-ledge interface behind the bearing pads at SLS. The cracks extended about 20 in. along the interface. On the south side ledge, the interface crack propagated diagonally to the top face of the ledge about 7 in. with an angle of 35 degrees. Overall, light levels of damage were detected at SLS compared to the reference test. Crack extensions and new crack formations were observed as the load increased. Web shear cracks initiated at a load of 54 kips.

Under the ULS of 68 kips, new cracks formed on the web and on the top and side face of the ledge. Diagonal ledge cracks were observed around the bottom corner of the ledge side face. Diagonal web cracks were also detected on the web.

During loading to the measured ultimate load, crack extensions and new crack formations were observed on both the web and ledge. The grout cracks between the end plate and the bent cap formed at 80 kips. Under the measured ultimate load of 86 kips, the bottom tip of the end plate deformed outward, as shown in Figure 3.54(b). More damage occurred on the north side than on the south side. Significant extensions of existing cracks and new crack formations on the north side ledge are seen in Figure 3.54(d). A hanger crack was detected near the neutral axis of the bent cap. There were fewer cracks at the inside of the bearing pad compared to the reference test, which may have been due to the restraint provided by the end plate. The diagonal cracks outside of the bearing pad showed a steeper angle than the inside cracks. The bottom of the end plate deformed outward and downward about 0.5 in. at the end of the test.



Figure 3.52. Retrofit Solution 3 Installed on West End of Ledge-Deficient Specimen 5.

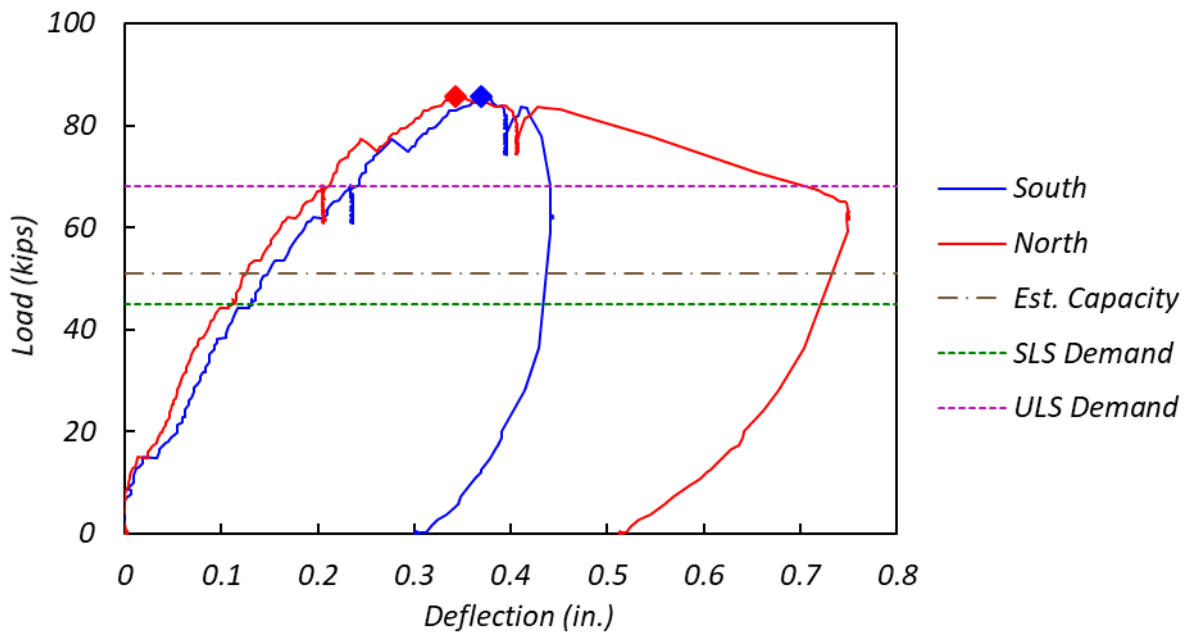


Figure 3.53. Load-Deflection Curve for T5W1.



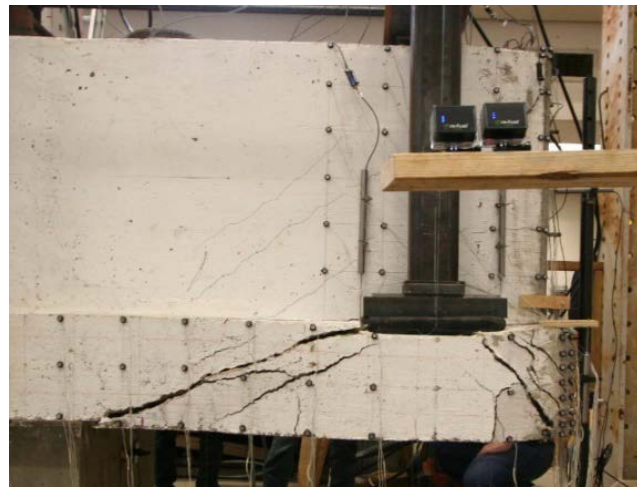
(a) Concrete cracks at corner



(b) Deformation of end plate



(c) South side



(d) North side

Figure 3.54. Observed Damage for T5W1 at Final Load Level.

3.6 Ledge-Deficient Specimen 6

Ledge-deficient Specimen 6 provided exterior (T6W1) and interior (T6I1) of the partial-depth FRP retrofit solution (Solution 16) and an exterior test (T6E1) of the full-depth FRP retrofit solution (Solution 17). Figure 3.55 shows crack patterns for all three tests at SLS, ULS, and failure.

3.6.1 Exterior Solution 16—T6W1

T6W1 is an exterior test using the partial-depth FRP retrofit (Solution 16). Figure 3.56 shows Solution 16 installed on the west end of the specimen. The FRP strip wrapping the stem of the specimen is expected to contribute strength to hanger capacity. The remaining FRP is expected to strengthen the ledge and punching shear capacity. Figure 3.57 shows the load-deflection plots for the north and south load points, with horizontal lines indicating SLS, ULS, and estimated capacity, and diamonds indicating the measured ultimate load.

The measured ultimate load (102 kips) was 46 percent larger than the estimated capacity (66 kips) and 55 percent larger than the exterior ledge-deficient reference capacity. The test was ended when the applied load dropped to about 55 percent of the measured ultimate load. Figure 3.58 shows the observed damage. The specimen showed a significant increase in ductility compared to the exterior ledge-deficient reference test. The tested region experienced a ledge flexure failure, with more extensive damage on the south side.

No damage was found before the load reached the ULS demand. At the ULS of 68 kips, end interfacial debonding of the FRP occurred at the west end of the concrete block along with vertical shear cracks. Cracks were also detected at the interface of the concrete block and the ledge. A vertical crack formed on the south side web behind the bearing pad. Web shear cracks formed starting at 90 kips.

The load reached the measured ultimate load of 102 kips and then dropped to 90 kips. At the measured ultimate load, intermediate shear-crack-induced interfacial debonding of the FRP was detected at the end of the concrete block on both sides. The same crack patterns were observed on the web at the end of the side FRP strip. On the bottom of the bent cap, an end interfacial debonding of the stem FRP strip was observed. On the end face, horizontal cracks formed over the FRP strip on the flange due to the shear cracks.

After the described damage, the bent cap was loaded again from the load of 90 kips. The load reached a post-peak 90 kips and then gradually decreased. Significant extensions of existing cracks and new crack formations were detected. More horizontal cracks formed on the flange of the end face while the load decreased to 90 kips. Side FRP strip separation was observed at the web-ledge interface. Concrete cover separation was observed on the end of the concrete block and on the side face of the north side ledge. The south side ledge experienced more deflection than the north side. The test was ended when the load dropped to 60 kips, which was 40 percent lower than the measured ultimate load.

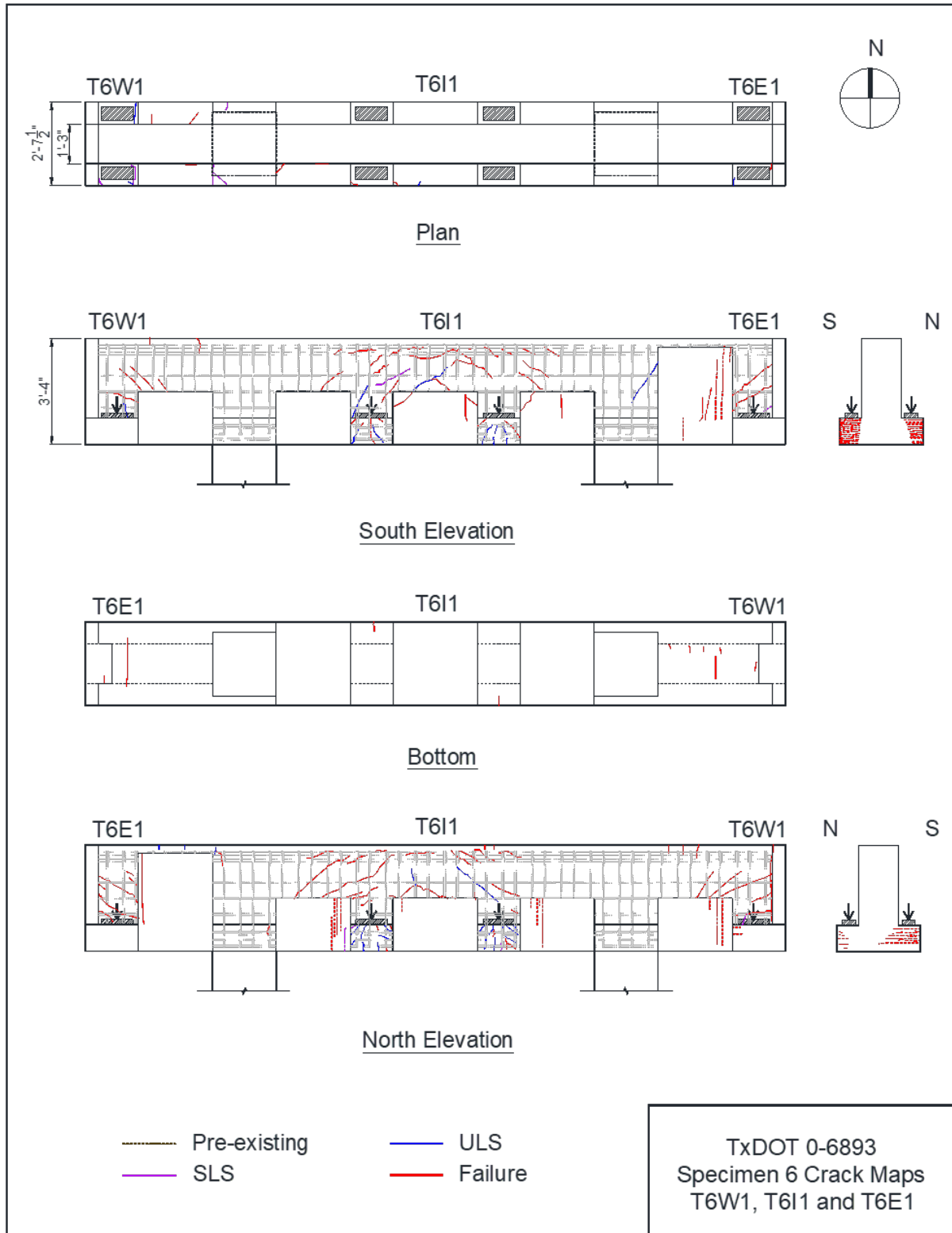


Figure 3.55. Crack Maps for Tests T6W1, T6I1, and T6E1.



Figure 3.56. Retrofit Solution 16 Installed on West End of Ledge-Deficient Specimen 6.

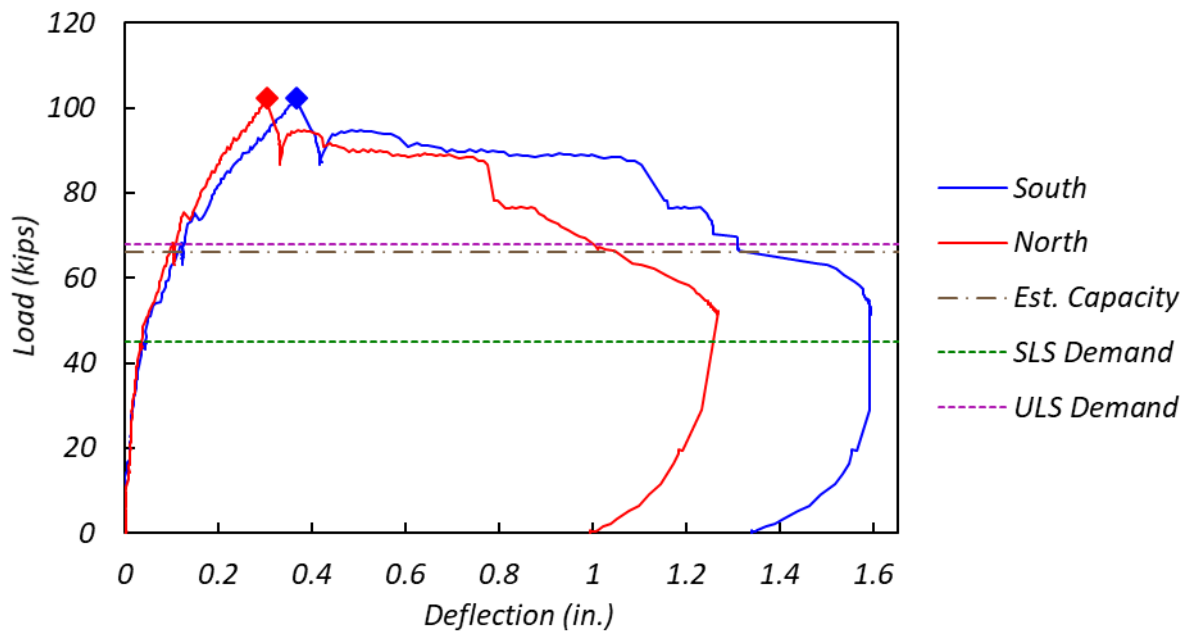
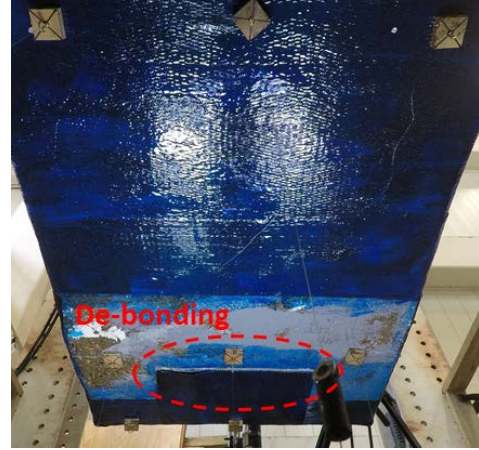


Figure 3.57. Load-Deflection Curve for T6W1.



(a) South side at measured ultimate load



(b) Bottom at measured ultimate load



(c) South side at post-peak 75 kips



(d) North corner at post-peak 75 kips



(e) South side at final load level



(f) North corner at final load level

Figure 3.58. Observed Damage for Test T6W1 at Different Load Levels.

3.6.2 Exterior Solution 17—T6E1

T6E1 is an exterior test using the full-depth FRP retrofit solution (Solution 17). Figure 3.59 shows Solution 17 installed on the east end of the specimen. Solution 17 is aimed at strengthening the hanger, ledge, and punching shear capacity of the bent cap.

Additional bandages were applied to provide anchorage to the bottom termination region of the FRP strip, which was applied on the end face to vertically wrap the stem of the specimen and connect the horizontal FRP strip on the end face and the vertical FRP strip attached on the concrete block. Figure 3.60 shows the load-deflection plots for the north and south load points.

The measured ultimate load (120 kips) was 69 percent larger than the estimated capacity (71 kips) and 82 percent larger than the exterior ledge-deficient reference capacity. The test was ended when the applied load dropped to about 75 percent of the measured ultimate load. Figure 3.61 shows the observed damage. The specimen at final load level showed a combined ledge flexure and punching shear failure.

No damage was visible until the ULS demand of 68 kips. At ULS, cracks formed at the interface between the concrete block and the ledge beside the south side bearing pad. A web shear crack was detected on the south side web at the inner side of the concrete block. Negative flexure cracks formed on the north side of the web.

More cracks on the web were observed as the load increased. A hanger crack formed at 88 kips. At a load of 102.5 kips, horizontal cracks started to form on the flange at the end face. Intermediate shear-crack-induced debonding of the FRP occurred at the end of the concrete block on the bearing pad side. More separations of the FRP strip were observed at the end of the concrete block as the load went higher. At a load of 112.5 kips, a separation of the FRP was observed at the web-ledge interface near the end of the bent cap. At the measured ultimate load of 120 kips, end interfacial debonding of the FRP was observed at the end of the south side concrete block. The load dropped to 100 kips, accompanied by a loud sound, due to shear rupture of the FRP at the end region of the concrete block.



Figure 3.59. Retrofit Solution 17 Installed on East End of Ledge-Deficient Specimen 6.

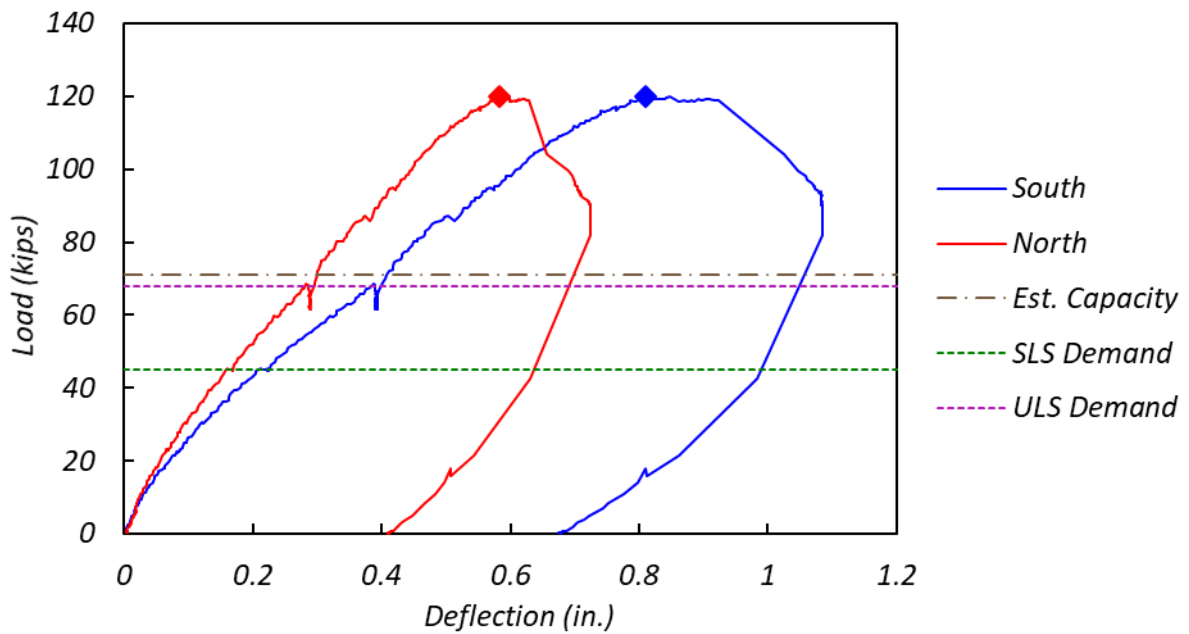


Figure 3.60. Load-Deflection Curve for T6E1.



(a) North side at measured ultimate load



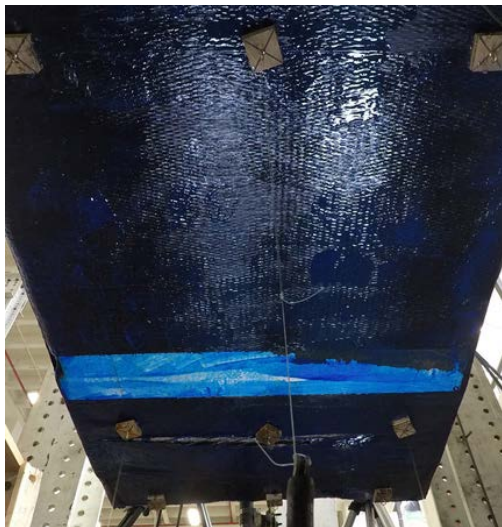
(b) North corner at measured ultimate load



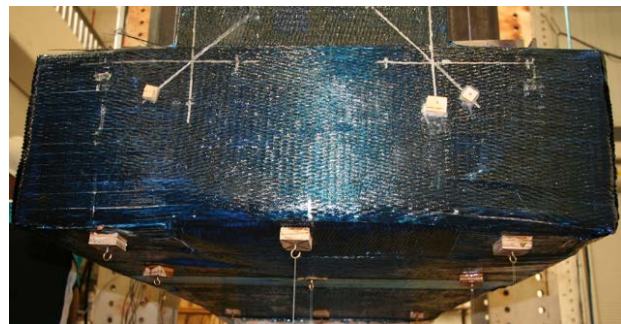
(c) North side at final load level



(d) North corner at final load level



(e) Bottom at final load level



(f) Ledge after removal of load

Figure 3.61. Observed Damage for Test T6E1 at Different Load Levels.

3.6.3 Interior Solution 16—T6I1

T6I1 is an interior test using the partial-depth FRP retrofit solution (Solution 16). Figure 3.62 shows Solution 16 installed on the interior of the specimen. Solution 16 for interiors is aimed at improving the ledge and punching shear capacity. Figure 3.63 shows the load-deflection plots for all load points.

The measured ultimate load (103 kips) was 6 percent larger than the estimated capacity (97 kips) and 21 percent larger than the interior ledge-deficient reference capacity. The test was ended when the applied load dropped to about 90 percent of the measured ultimate load. Figure 3.64 shows the observed damage at the final load level. The specimen at the final load level showed a combined hanger and punching shear failure.

At the SLS of 49 kips, the initial cracks formed at the interface of the northwest concrete block and the ledge. Flexure cracks were detected on the bottom along the interface of the FRP strip and the bent cap. More cracks formed on the side face of the north side ledge at the interface of the FRP strip and bent cap. At a load of 75 kips, the first diagonal shear cracks were detected on the web behind the southwest load point.

At the ULS of 78.5 kips, more cracks had formed at the interface between the FRP and bent cap. Diagonal shear cracks were detected on both sides of the web. On the side face of the ledge, diagonal cracks formed under the bearing pad between the concrete blocks. Crack extensions and new crack formations were observed as the load increased.

End interfacial debonding of the FRP was detected at the east end of the southwest concrete block at 84 kips. More cracks formed on the web. As the load increased, the web shear crack angles appeared to decrease, tending more toward horizontal angles between the loading points. More end interfacial debonding of the FRP occurred at the end of the concrete blocks. At a load of 99 kips, intermediate shear-crack-induced interfacial debonding was observed at the end of the southeast concrete block. The web shear cracks from the outside of the bearing pads connected horizontally near the top of the bent cap formed interior hanger cracks. At the measured ultimate load of 103 kips, intermediate shear-crack-induced interfacial debonding of the FRP was observed at all inner ends of the concrete blocks. The maximum crack width of the interior hanger cracks was 5.5 mm.

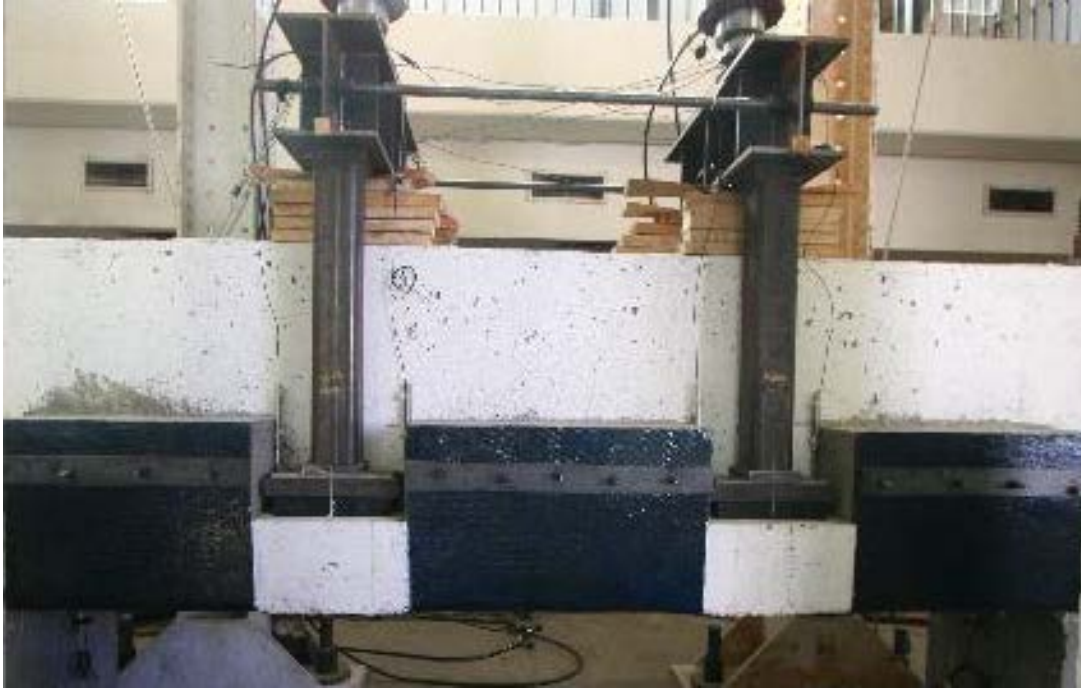


Figure 3.62. Retrofit Solution 16 Installed on Interior of Ledge-Deficient Specimen 6.

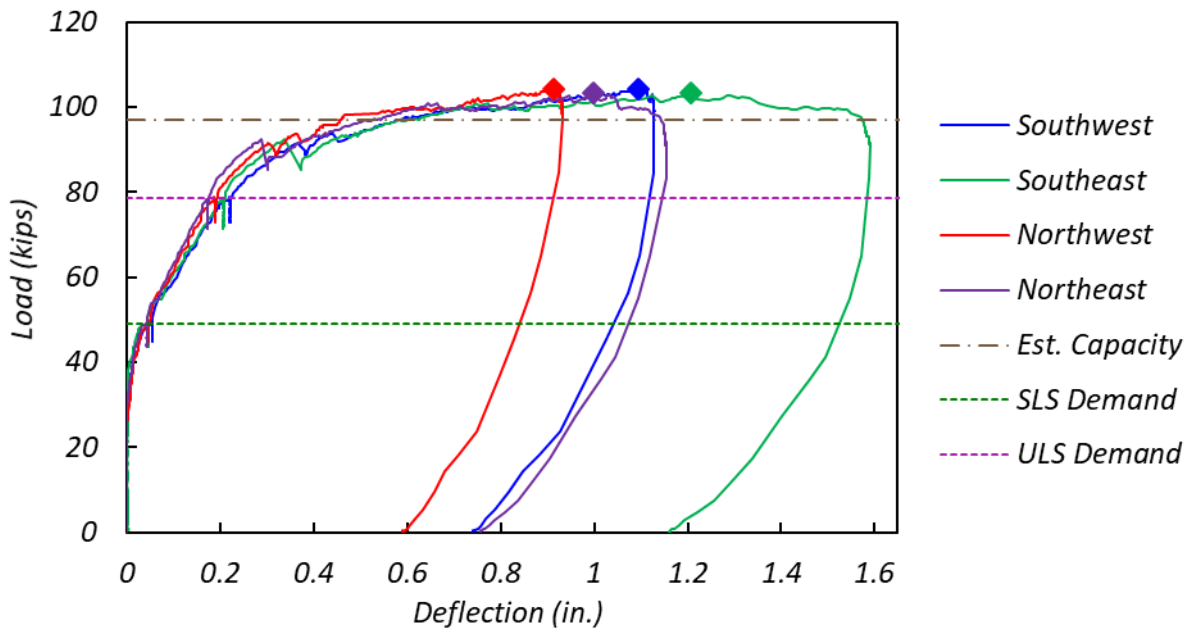


Figure 3.63. Load-Deflection Curve for T6I1.



(a) North side at ULS



(b) North side at measured ultimate



(c) North side at final load level



(d) Southwest at final load level



(e) Southeast at final load level

Figure 3.64. Observed Damage for Test T6I1.

3.7 Ledge-Deficient Specimen 7

Ledge-deficient Specimen 7 had four exterior tests and four interior tests. Exterior tests with post-tensioning (Solution 14) were tested first, with one end pre-cracked (T7E1). The post-tensioning was then removed to allow the end-stiffener (Solution 3) and clamped threadbar (Solution 8[a]) solutions to be tested. All interior tests were punching shear tests. T7I1 and T7I2 used small (4 in. by 4 in.) and large (12 in. by 5 in.) pads, respectively, on the north side ledge. T7I3 and T7I4 used small and large bearing pads, respectively, on the south side ledge. Figure 3.65 shows crack patterns for tests T7W1, T7I1, T7I2, and T7E1. Figure 3.66 shows crack patterns for tests T7W2, T7I3, T7I4, and T7E2.

3.7.1 Exterior Solution 14—T7W1

T7W1 is an exterior test using the load-balancing PT retrofit solution (Solution 14). Figure 3.67 shows Solution 14 installed on the west end of the specimen. The test was terminated prior to failure or reaching a measured ultimate load. The test termination load (82 kips) was determined by adding the capacity contribution of the PT strands (16 kips) to the ultimate load capacity of the ledge-deficient exterior reference specimen (66 kips). Figure 3.68 shows the load-deflection plots for the north and south load points, with horizontal lines indicating SLS, ULS, and estimated capacity, and diamonds indicating the test termination load.

Solution 14 is expected to increase the hanger, ledge, and punching shear capacity. Figure 3.69 shows the observed damage at the test termination load. The specimen maintained its load carrying capacity with a moderate level of damage at a load 21 percent larger than the ultimate load capacity of the ledge-deficient exterior reference test.

No damage was detected at the SLS demand. The first crack occurred at a load of 64 kips at the web-ledge interface behind the bearing pads on the north side of the ledge. At the ULS demand of 68 kips, cracks formed at the web-ledge interface behind the bearing pad on both sides. On the top of the north side ledge, the cracks behind the bearing pad propagated along the web-ledge interface toward the column. Horizontal cracks formed on the bottom of the bent cap beneath the bearing pad. All the cracks detected at ULS were hairline cracks.

At the test termination load of 82 kips, the cracks at the web-ledge interface propagated diagonally to the side face of the ledge on both sides of the bent cap. Diagonal cracks on the side face of the ledge under the bearing pads were detected on both sides. Cracks at the bottom of the bent cap propagated at about two-thirds of the ledge toward the center of the bearing pad from the outside. The maximum widths of the interface and ledge cracks were 0.25 mm and 0.1 mm, respectively.

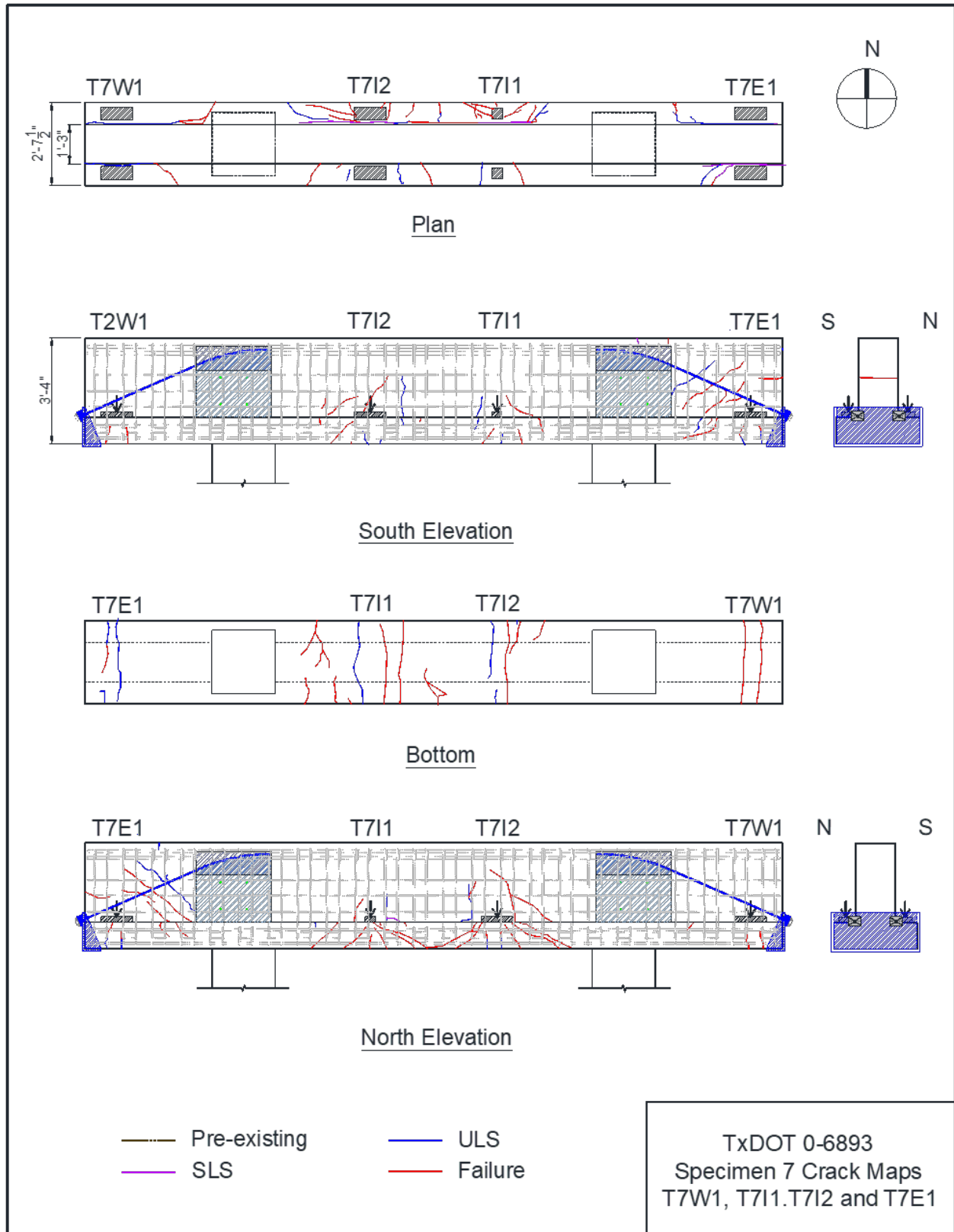


Figure 3.65. Crack Maps for Tests T7W1, T7I1, T7I2, and T7E1.

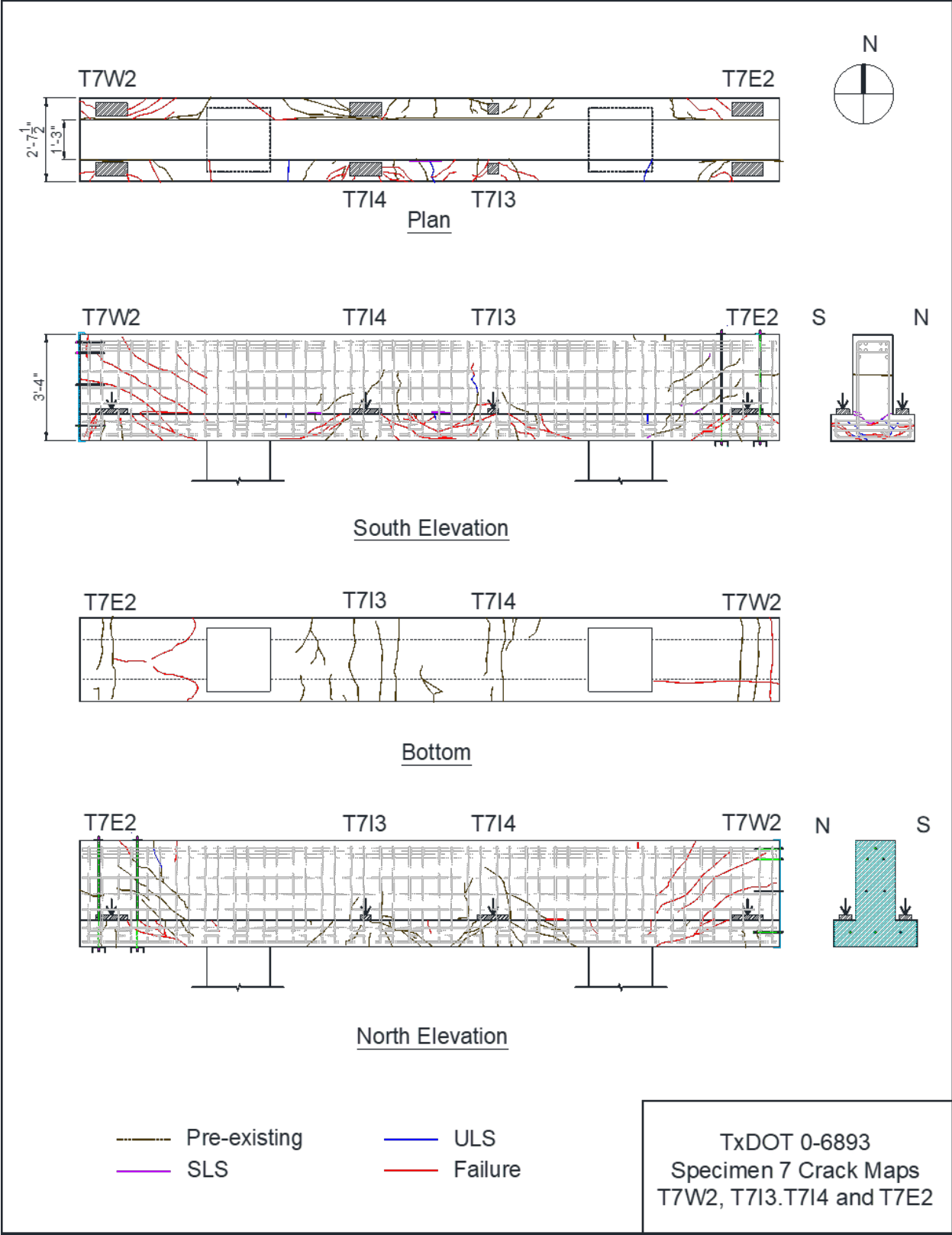


Figure 3.66. Crack Maps for Tests T7W2, T7I3, T7I4, and T7E2.



Figure 3.67. Retrofit Solution 14 Installed on West End of Ledge-Deficient Specimen 7.

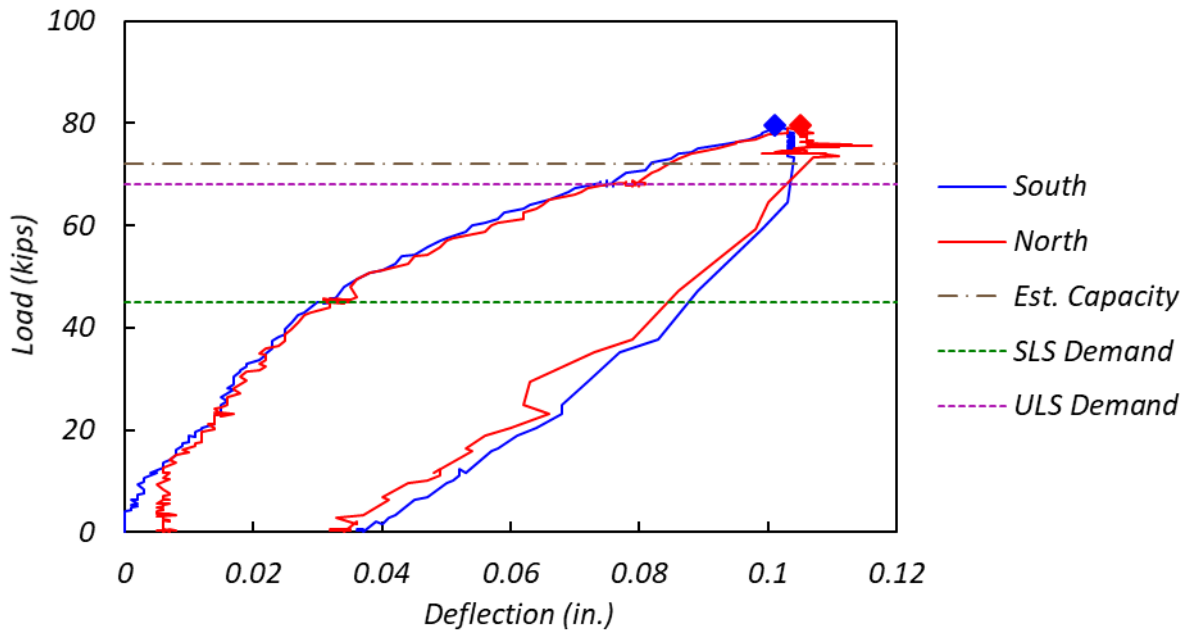


Figure 3.68. Load-Deflection Curve for T7W1.



Figure 3.69. Observed Damage for Test T7W1 at Test Termination Load.

3.7.2 Exterior Solution 14 (Post-Crack)—T7E1

T7E1 is an exterior test using the load-balancing PT retrofit solution (Solution 14) implemented with existing cracks. The assemblies for Solution 14 were preinstalled on the specimen, but the PT strands were not prestressed until cracking was induced by loading the specimen to 63 kips. Figure 3.70 shows the damage prior to prestressing. Unlike in the reference test, there were no cracks at the service load state, possibly as a result of increased capacity provided by the preinstalled steel assemblies. The PT strands were tensioned after the load reached 63 kips. Then the specimen was loaded gradually to the test termination load of 100 kips, determined based on the observation of the damage level. Figure 3.71 shows the load-deflection plots for the north and south load points.

Figure 3.72 shows the observed damage at the test termination load. The specimen maintained a load carrying capacity with a moderate level of damage at the test termination load that was 50 percent larger than the ultimate load capacity of the ledge-deficient exterior reference specimen.

New cracks were observed on the south side ledge at the SLS demand after the PT strands were tensioned. More cracks on the ledge and web were detected at the ULS demand of 68 kips.

Diagonal shear cracks were formed on both sides of the web. The web-ledge interface cracks were propagated diagonally to the top of the ledge. Cracks on the side face of the ledge under the bearing pad were observed on both sides. The maximum width of the cracks on the side face of the ledge was 0.5 mm. Crack extensions and new crack formations were observed as the load increased.

At the test termination load of 100 kips, more cracks were observed on the web and ledge on both sides of the bent cap. The maximum width of the ledge cracks was increased to 0.7 mm. A hanger crack formed on the end face 26 in. above the bottom of the bent cap.



Figure 3.70. Observed Damage Before PT Jacking Operation.

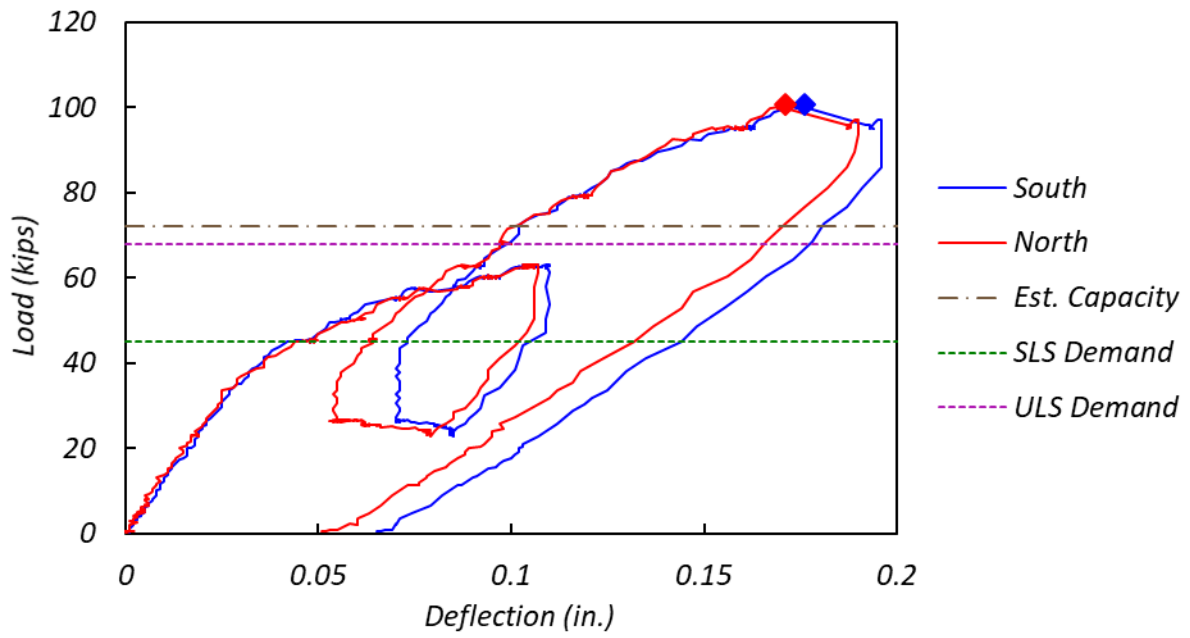


Figure 3.71. Load-Deflection Curve for T7E1.



Figure 3.72. Observed Damage for Test T7E1 at Test Termination Load.

3.7.3 Exterior Solution 3 (Post-Crack)—T7W2

T7W2 is an exterior test using an end stiffener (Solution 3) installed with existing cracks from the T7W1 test. Figure 3.73 shows the post-crack Solution 3 installed on the west end of the specimen. Figure 3.74 shows the load-deflection plots for the north and south load points.

The measured ultimate load (88 kips) was 63 percent larger than the estimated capacity of 54 kips and 33 percent larger than the ultimate load capacity of the exterior ledge-deficient reference capacity. The test was ended when the applied load dropped to about 60 percent of the measured ultimate load. Figure 3.75 shows the observed damage at the final load level. The bent cap experienced a punching shear failure on the north side. Damage was more extensive on the north side of the bent cap.

Existing cracks opened during loading, with the first new cracks observed at SLS demand. The maximum crack width of the web-ledge interface cracks behind the bearing pads increased to 0.3 mm from 0.25 mm, and the maximum width of the cracks on the side face of the ledge increased to 0.15 mm from 0.1 mm.

Under the ULS of 68 kips, diagonal shear cracks on both sides of the web were detected. The web-ledge interface cracks extended diagonally to the top of the ledge. More diagonal cracks formed on the side face of the ledge on both sides. A negative flexure crack was detected on the north side web.

During loading to the measured ultimate load, crack extensions and new crack formations were observed on both the web and ledge. The bottom corner of the end plate started to open as the load reached 77 kips. At a load of 82.5 kips, vertical cracks formed on both sides of the web at the top of the end plate. At the measured ultimate load of 88 kips, more cracks were observed on both sides of the web and ledge. The north side of the ledge had more severe damage than the south side. A clear pyramid-shaped cone formed under the north side bearing pad.

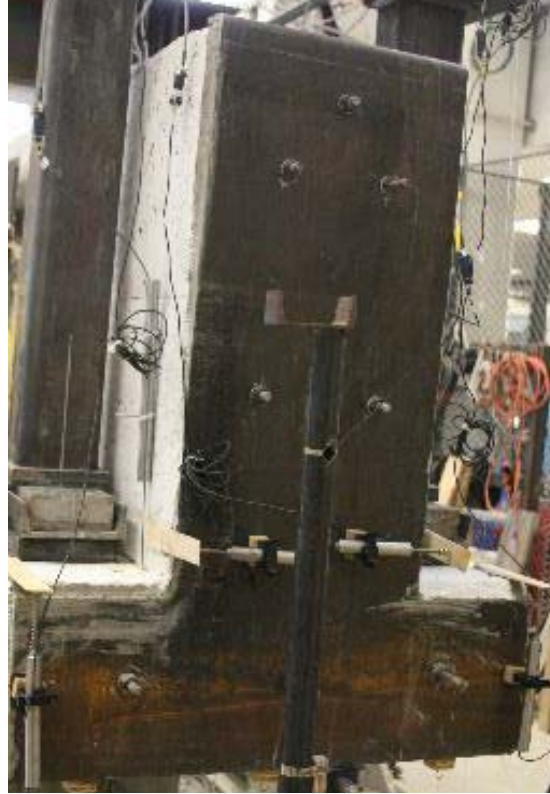


Figure 3.73. Post-Crack Retrofit Solution 3 Installed on West End of Ledge-Deficient Specimen 7.

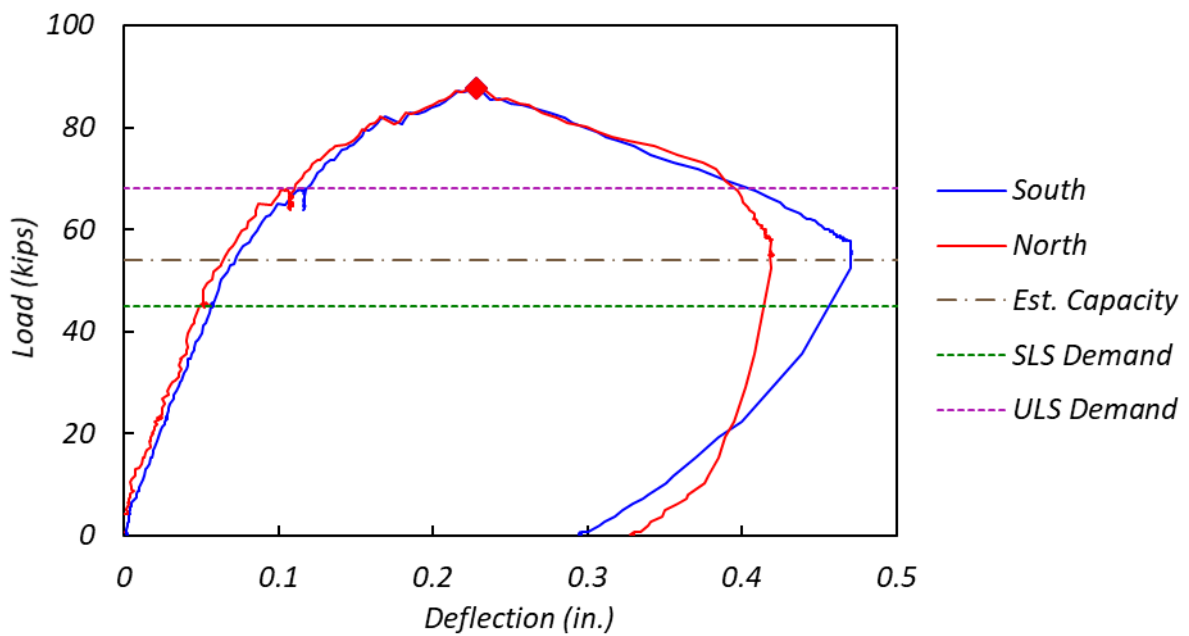


Figure 3.74. Load-Deflection Curve for T7W2.



(a) North side at SLS



(b) North side at ULS



(c) North side at final load level



(d) South side at final load level

Figure 3.75. Observed Damage for Test T7W2 at Different Load Levels.

3.7.4 Exterior Solution 8(a) (Post-Crack)—T7E2

T7E2 is an exterior test using two clamped threadbars (Solution 8[a]) installed with existing cracks from test T7E1. Figure 3.76 shows the load-deflection plots for the north and south load points.

The measured ultimate load (101 kips) was 26 percent larger than the estimated capacity of 80 kips and 53 percent larger than the ledge-deficient exterior reference capacity. The test was ended when the applied load dropped to about 90 percent of the measured ultimate load. Figure 3.77(a) shows the observed damage on the end face before the test. Figure 3.77(b) shows the observed damage on the end face at SLS, and Figure 3.77(c), (d), and (e) show the observed damage at the final load level.

The width of the existing cracks increased a bit while the load increased to the SLS of 45 kips. A new hanger crack near the web-ledge interface on the end face was observed at SLS. It was a parabolic-shaped crack that connected the two corners of the end face, as shown in Figure 3.77(b). The old hanger crack on the end face above the neutral axis was the widest crack at SLS, with a width of 0.2 mm.

At the ULS of 68 kips, more diagonal cracks formed on the end face. A flexure crack was detected on the north side web. The width of the old hanger crack on the end increased to 0.4 mm, and the width of the new hanger crack that formed at SLS near the web-ledge interface was 0.5 mm at ULS.

Crack extensions and new crack formations were observed as the load went above ULS. A pyramid-shaped cone started to form under the bearing pad on both sides of the specimen when the load exceeded 90 kips, accompanied by a slope change in load-deflection curve. Significant damage progression was observed after 90 kips. The measured ultimate load of 101 kips was observed in 90 seconds. The width of the cone cracks on the side ledge, and of the hanger crack near the web-ledge interface on the end face, increased extensively during this stage. The width of the old hanger crack on the end face above the neutral axis did not increase. The maximum width of the cone cracks and hanger crack at the measured ultimate load were both 2.5 mm. The test was stopped when the load dropped to 93 kips. More damage on the south side than the north side was observed after the measured ultimate load. The maximum widths of the cone cracks on the south side and north side were 4 mm and 2.5 mm at the final load level, respectively. The widths of the new and old hanger cracks on the end face were 3.5 mm and 0.5 mm at the final load level, respectively.

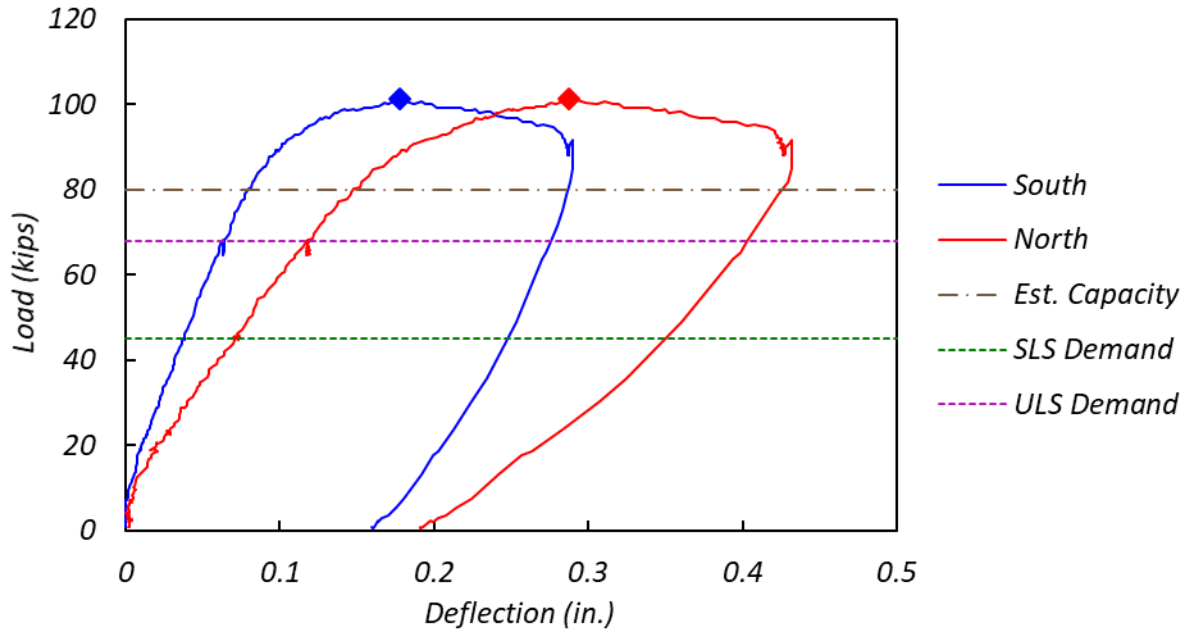
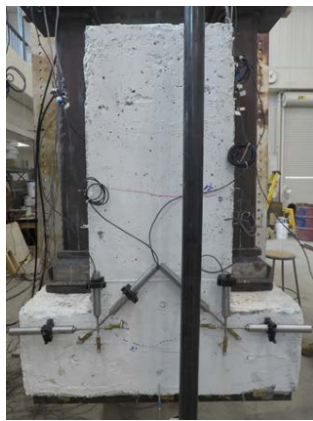


Figure 3.76. Load-Deflection Curve for T7E2.



(a) End face before test



(b) End face at SLS



(c) End face at final load level



(d) South side at final load level



(e) North side at final load level

Figure 3.77. Observed Damage for Test T7E2 at Different Load Levels.

3.7.5 Interior Punch Tests—T7I1 and T7I2

T7I1 and T7I2 are interior punching shear tests with small (4 in. by 4 in.) and large (12 in. by 5 in.) bearing pads, respectively. Both tests were conducted on the north side of the bent cap and loaded simultaneously until the ultimate load state. After the load reached ULS, the test region of T7I1 was loaded to ultimate failure, while the load was kept at the dead load for the test region of T7I2. After T7I1 failed, the applied load for T7I1 was retracted to the dead load. T7I2 was then loaded to failure. Figure 3.78 and Figure 3.79 show the load-deflection plots for T7I1 and T7I2, respectively, with horizontal lines indicating SLS, ULS, and estimated capacity.

The measured ultimate load for test T7I1 (112 kips) was 75 percent larger than the estimated capacity (64 kips). The measured ultimate load for test T7I2 (119 kips) was 37 percent larger than the estimated capacity (87 kips) and 6 percent larger than the measured ultimate load capacity of T7I1. Both tests were ended when the applied load dropped to about 85 percent of the measured ultimate load. Figure 3.80 shows the observed damage for tests T7I1 and T7I2. Both tested regions showed punching shear failure with truncated pyramids forming under the loading areas.

The initial cracks formed at the web-ledge interface behind both bearing pads at 45 kips before reaching SLS. At the SLS of 49 kips, the cracks behind the two bearing pads extended toward the center of the specimen along the web-ledge interface and connected. The cracks also extended toward the support columns along the interface about 12 in. and 22 in. away from the center of the west and east bearing pads, respectively. More cracks formed on the ledge and web as the load increased.

At 90 kips, diagonal cracks formed on top of the ledge 15 in. from the center of the bearing pads. The cracks initiated from the web-ledge interface and propagated to the side face of the ledge toward the support columns. At the ULS of 78.5 kips, flexure cracks were found on the bottom of the specimen beneath the two bearing pads. The cracks propagated through the bent cap in the transverse direction and further extended to the side face of the ledges on both sides. Nearly vertical cracks formed on both sides of the web at the inner sides of the T7I1 and T7I2 bearing pads, which were 6 in. and 12 in. away from the center and raised 6 in. and 14 in., respectively.

The load for T7I2 retracted to dead load level and increased to ultimate failure for T7I1. Crack extensions and new cracks were observed as the load increased beyond ULS. The formation of the main concrete cone cracks started at 105 kips accompanied by a slope change of the load-

deflection curve. The west side of the main cone crack formed first on the side of the ledge at 105 kips. The east side crack formed at 110 kips. The measured ultimate load of 112 kips was observed within 30 seconds after the main concrete cone cracks formed. The width of the west and east side cone cracks was 1.5 mm and 0.5 mm at the measured ultimate load, respectively. The starting point of the west side cone crack on the ledge was 11 in. away from the west tip of the bearing pad, whereas the east side started at about the center of the bearing pad. More cracks on the ledge were detected at measured ultimate load.

Diagonal cracks were detected on both sides of the web and on the side of the ledge under the bearing pad. Additional flexure cracks on the bottom of the specimen under the bearing pad were also detected. The load dropped gradually after reaching the measured ultimate load. The test ceased when the load dropped to 95 kips. The width of the existing cracks increased significantly during this stage. The width of the west and east side of the cone cracks was 2.5 mm and 1.5 mm, respectively, at final load level.

The load for T7I2 increased to ultimate failure after retraction of the load for T7I1 to the dead load level. The main concrete cone cracks started forming under the bearing pad at 100 kips accompanied by a slope change of the load-deflection curve. The west side of the main concrete cone crack formed first at 105 kips, and the east side crack formed at 115 kips. The measured ultimate load of 119 kips occurred shortly after the cone cracks formed. The width of the west and east cone cracks was 2 mm and 1.5 mm at the measured ultimate load, respectively. Both sides of the cone crack started at about the tip of the bearing pad. Diagonal cracks on both sides of the web east of the bearing pad, and additional diagonal cracks on the side of the ledge under the bearing pad, were detected at measured ultimate load. More flexure cracks on the bottom were also observed. The load dropped gradually after reaching the peak, and the test was stopped when the load dropped to 100 kips. The widths of the west and east sides of the cone cracks were 3.5 mm and 3 mm at the final load level, respectively.

No intersection of the failure planes for T7I1 and T7I2 was observed at final load level.

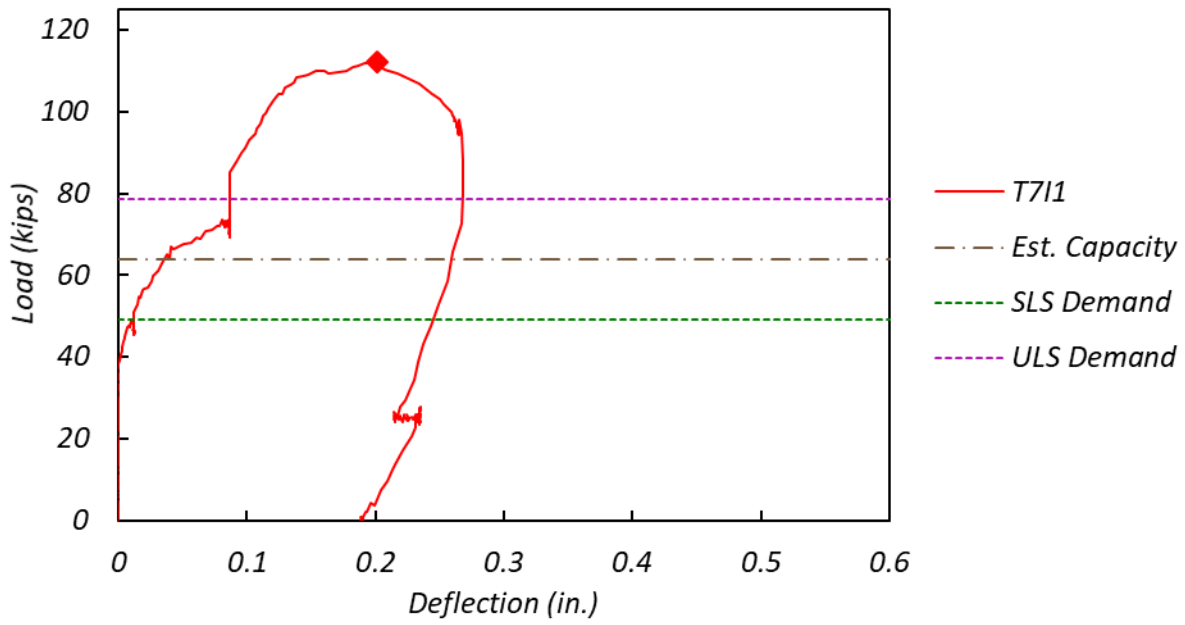


Figure 3.78. Load-Deflection Curve for T7I1.

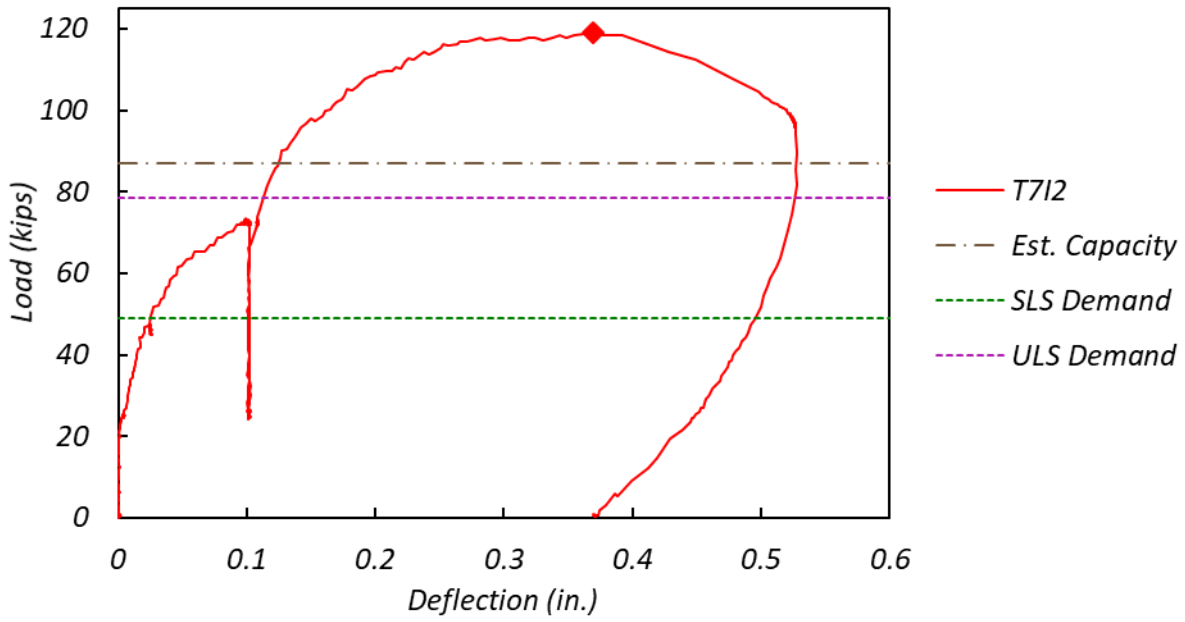


Figure 3.79. Load-Deflection Curve for T7I2.



(a) North side at ULS (loaded simultaneously)



(b) North side at final load level



(c) T7I1 at final load level



(d) T7I2 at final load level

Figure 3.80. Observed Damage for Test T7I1 and T7I2 at Different Load Levels.

3.7.6 Interior Punch Tests—T7I3 and T7I4

T7I3 and T7I4 are interior punching shear tests with small (4 in. by 4 in.) and large (12 in. by 5 in.) bearing pads, respectively. Both tests were conducted on the south side of the bent cap. The tested regions were cracked slightly during the T7I1 and T7I2 tests on the north side of the specimen. The two tests were loaded simultaneously until the dead load. T7I4 (large pad) was loaded to ultimate failure, while the load for T7I3 was held at the dead load. After the ultimate failure of T7I4, the load for T7I4 was retracted to the dead load and T7I3 (small pad) was loaded to the ultimate failure. Figure 3.81 and Figure 3.82 show the load-deflection plots for T7I3 and T7I4, respectively.

The measured ultimate load for test T7I3 was 112 kips, which was 75 percent larger than the estimated capacity (64 kips). The measured ultimate load for test T7I4 was 113 kips, which was 30 percent larger than the estimated capacity (87 kips) and 1 percent larger than the measured ultimate capacity of T7I3. Tests T7I3 and T7I4 were stopped when the applied load dropped to about 70 percent and 85 percent of the corresponding measured ultimate load, respectively. Figure 3.83 shows the observed damage for tests T7I3 and T7I4. Both tested regions experienced punching shear failure.

All the existing cracks were hairline cracks before the test. At the dead load, no new cracks had formed. The load for T7I4 was then increased to ultimate failure, while for T7I3, it was held at the dead load level. At the SLS of 49 kips, the width of the existing cracks increased a bit and a new crack formed at the web-ledge interface between the two bearing pads. The interface crack was the widest crack at SLS, with a width of 0.2 mm.

At the ULS of 78.5 kips, a new crack formed on top of the ledge near the center of the specimen. More new crack formations and extension of the existing cracks were observed as the load increased upon ULS. A diagonal crack propagated diagonally from the northwest corner of the bearing pad to the side of the ledge at 90 kips. The formation of the main cone cracks initiated at 100 kips. The west side of the cone crack formed first at 100 kips, accompanied by a slope change of the load-deflection curve. The east side of the cone crack formed at 108 kips. The measured ultimate load of 113 kips was observed within 60 seconds after both sides of the main cone cracks formed. The widths of the west and east side of the cone cracks were 1.5 mm and 1 mm at the measured ultimate load, respectively. The starting point of the west side cone crack on the side of the ledge was 4 in. away from the west tip of the bearing pad, whereas the east side

started at the east tip of the bearing pad. More diagonal cracks were detected on the top and side of the ledge. The load dropped gradually after the peak, and the test was ended when the load dropped to 95 kips. The widths of the west and east side of the cone cracks were increased to 2.5 mm and 2 mm at the final load level, respectively.

The load for T7I3 increased to ultimate failure after the load for T7I4 was retracted to the dead load level. Extension of the existing cracks was observed at the SLS of 49 kips. At the ULS of 78.5 kips, new diagonal cracks formed on top of the ledge. The diagonal cracks on the side of the ledge beneath the bearing pad extended about 2 in. The main cone cracks started to form at 105 kips. The east side of the cone crack formed first, resulting in a slope change in the load-deflection curve. The west side of the cone formed at 112 kips. The applied load reached the measured ultimate load (113 kips) shortly after both sides of the cone crack formed. The widths of the west and east sides of the cone cracks were 1.5 mm and 2 mm, respectively, at the measured ultimate load. The starting points for the west and east side of the cone cracks on the side of the ledge were 12 in. and 14 in. away from the west and east tip of the bearing pad, respectively. More diagonal cracks on the side of the ledge that had shallower angles than the main cone cracks were formed at the measured ultimate load. These cracks started at the tip of the bearing pads and connected to the main cone cracks at about half the depth of the ledge on both sides. More cracks formed on top of the ledge, and the cracks on the web extended. The load dropped gradually after reaching the measured ultimate load. The test was stopped when the applied load dropped to 80 kips. The widths of the west and east side of the cone cracks were 3.5 mm and 4 mm at the final load level, respectively.

The west side of the failure plane for T7I3 intersected with the one for T7I4 that was conducted before T7I3 (Figure 3.83[b]).

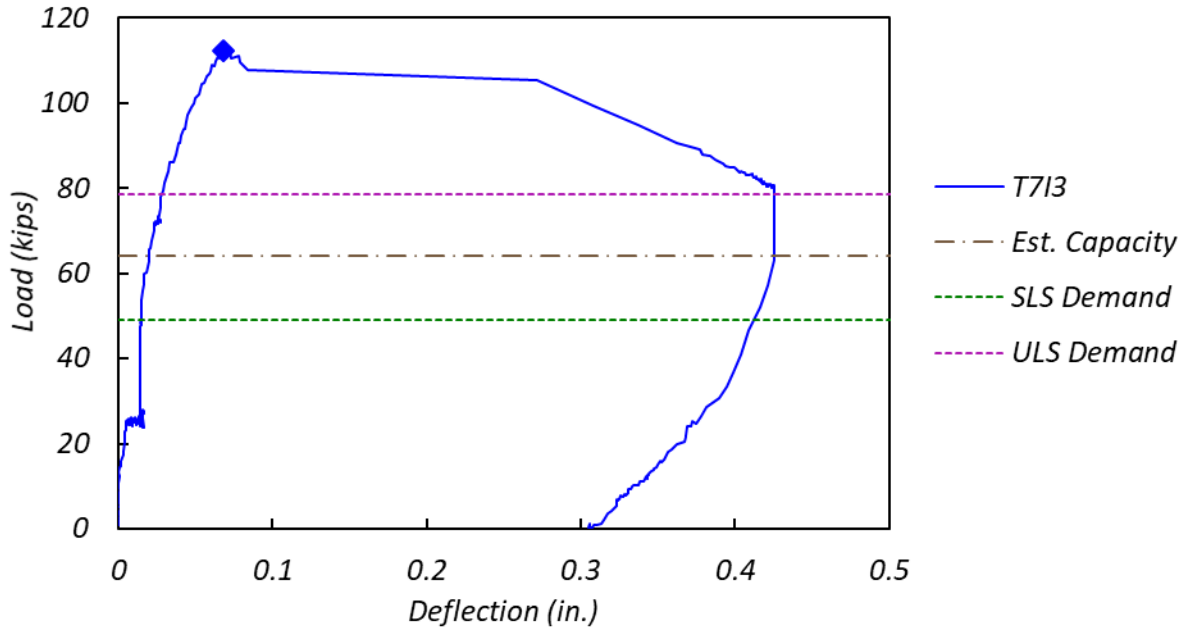


Figure 3.81. Load-Deflection Curve for T7I3.

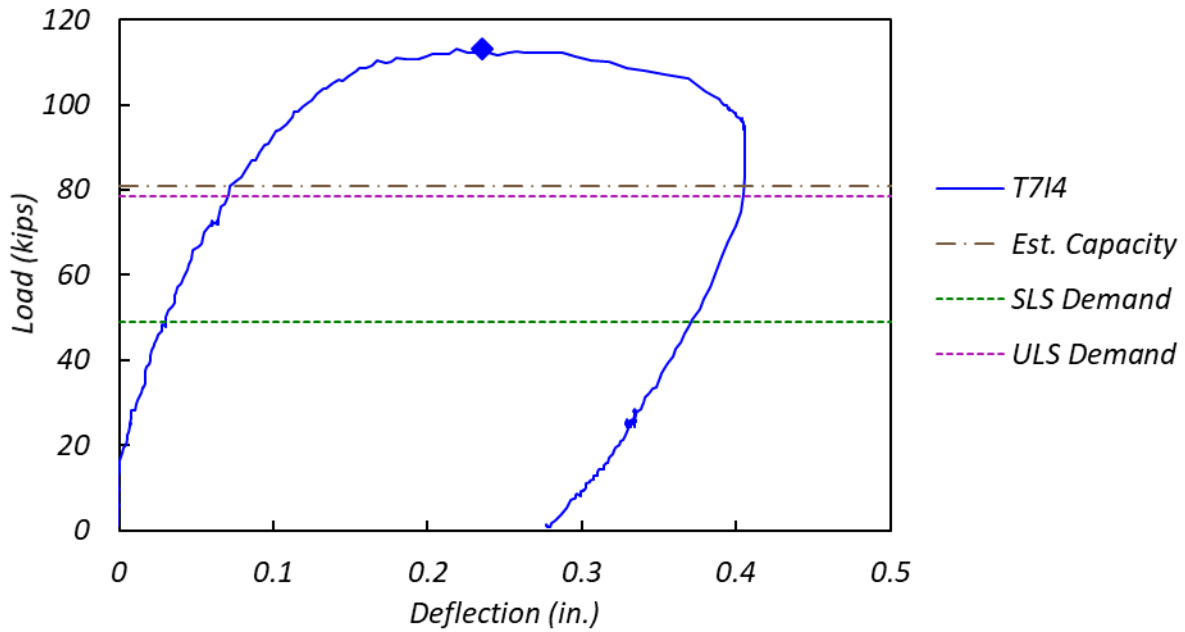
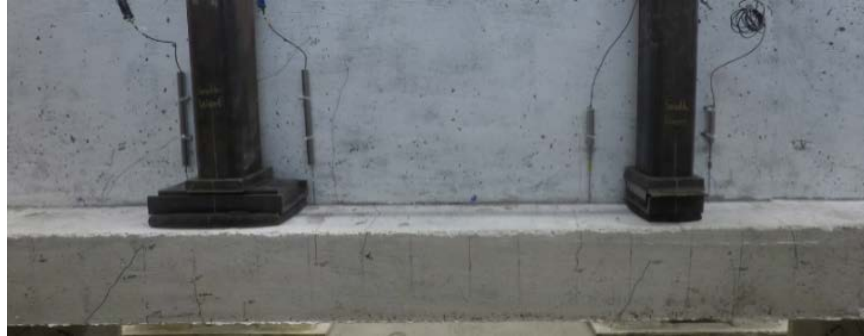


Figure 3.82. Load-Deflection Curve for T7I4.



(a) South side at dead load (loaded simultaneously)



(b) South side at final load level



(c) T7I3 at final load level



(d) T7I4 at final load level

Figure 3.83. Observed Damage for Test T7I3 and T7I4 at Different Load Levels.

3.8 Hanger-Deficient Specimen 8

Specimen 8 provided tests of all clamped threadbar solution variations (Solution 8) on a hanger-deficient specimen. Test T8E1 was a post-crack exterior test with two clamped threadbars (Solution 8[a]). Test T8I1 was an interior test with clamped threadbars (Solution 8). Figure 3.84 shows crack patterns at SLS, ULS, and failure.

3.8.1 Exterior Solution 8(b)—T8W1

T8W1 is an exterior test using a single clamped threadbar (Solution 8[b]). Figure 3.85 shows Solution 8(b) installed on the west end of the specimen. Figure 3.86 shows the load-deflection plots for the north and south load points, with horizontal lines indicating SLS, ULS, and estimated capacity, and diamonds indicating the measured ultimate load.

The measured ultimate load (88 kips) was 37 percent larger than the estimated capacity (64 kips) and 33 percent larger than the exterior hanger-deficient reference capacity. The test was ended when the applied load dropped to about 70 percent of the measured ultimate load. Figure 3.87 shows the observed damage at the final load level. The bent cap experienced a hanger failure.

The initial crack, observed at the SLS of 45 kips, formed at the web-ledge interface behind the bearing pad on both sides of the ledge, extending to the end of the specimen. On the end face, the crack extended diagonally at an approximate angle of 32 degrees. The two diagonal cracks on the end face started at the reentrant corner, propagated horizontally, and connected at a load of 60 kips.

Under the ULS of 68 kips, crack extensions and new crack formations were observed. The cracks at the web-ledge interface propagated toward the column of the bent cap. On the top of the ledge, the cracks at the web-ledge interface extended diagonally to the side face of the ledge. Diagonal shear cracks were detected on the south side of the web. Negative flexure cracks were detected on the north side of the web. The crack near the web-ledge interface on the end face had a maximum crack width of 0.9 mm.

Significant extensions of existing cracks and new crack formations on the entire tested region were observed as the load went higher than ULS. Web shear cracks formed on the north side at 73 kips. More diagonal cracks formed on the top of the ledge and further extended to the side face. A hanger crack formed on the end face near the neutral axis of the bent cap at 82 kips. The hanger cracks were propagated to the web at 84 kips.

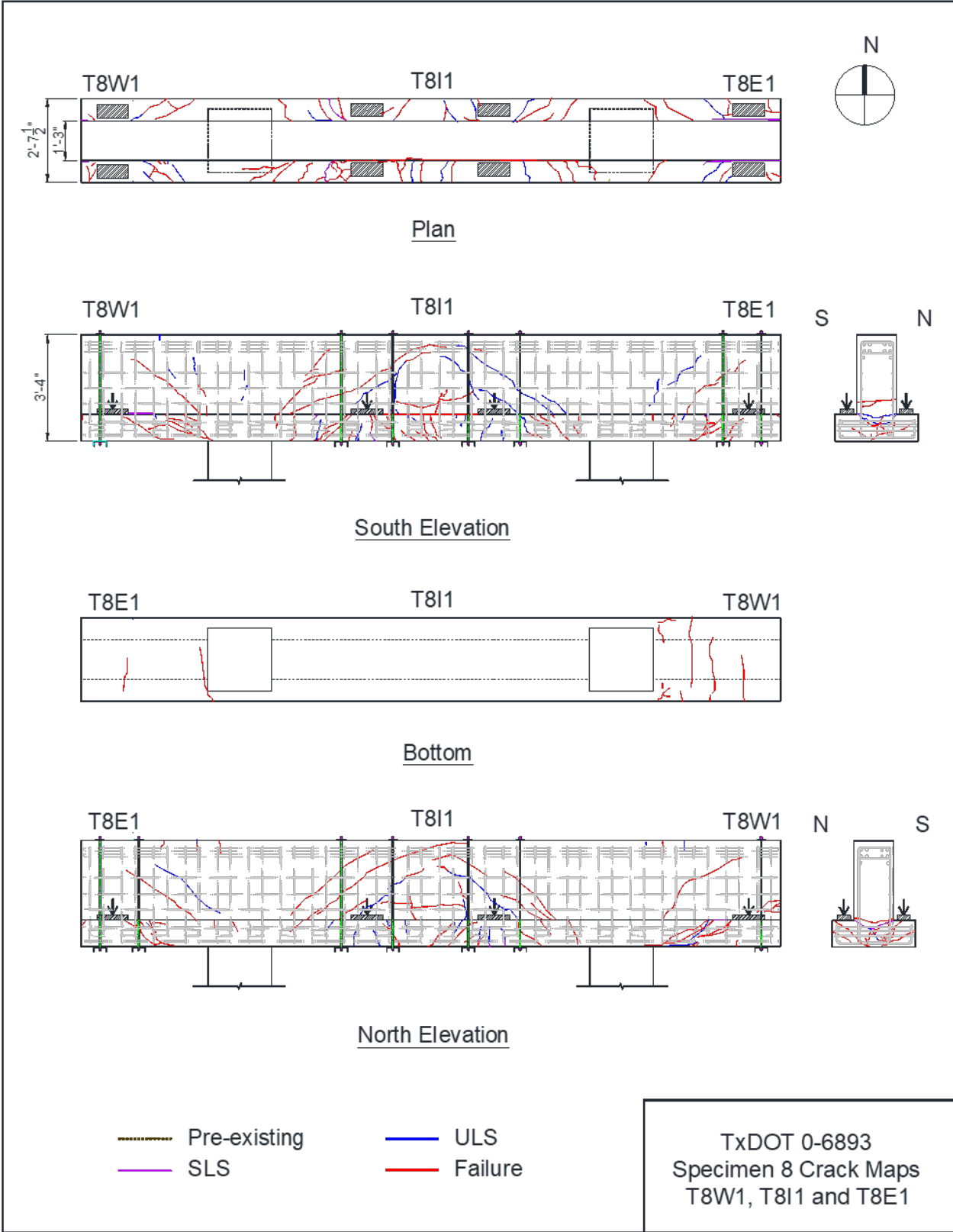


Figure 3.84. Crack Maps for Tests T8W1, T8I1, and T8E1.

At the measured ultimate load of 88 kips, new ledge shear cracks had formed on the end face. The horizontal crack on the end face near the web-ledge interface opened up to 7 mm. The second hanger formed near the neutral axis and had a width of 5 mm. More diagonal cracks were detected on the side face of the ledge with a maximum width of 11 mm. The deflection of the outside channel under the bent cap was visible at the measured ultimate load.



Figure 3.85. Retrofit Solution 8(b) Installed on West End of Hanger-Deficient Specimen 8.

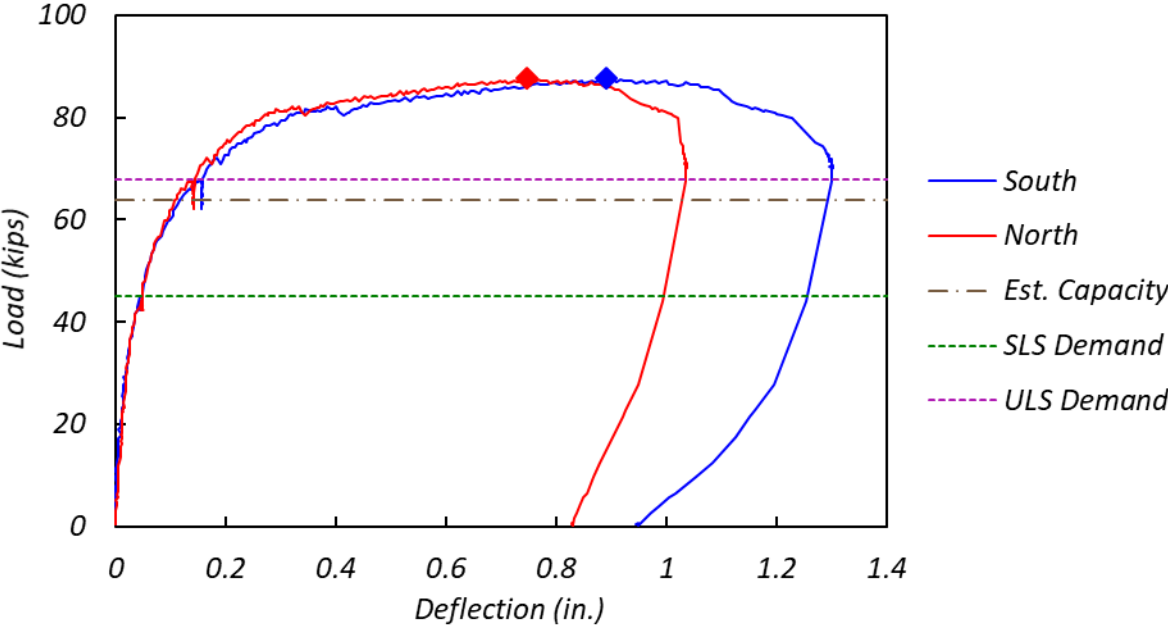


Figure 3.86. Load-Deflection Curve for T8W1.



(a) End face at SLS



(b) End face at ULS



(c) End face at final load level



(d) End face at SLS

Figure 3.87. Observed Damage of Test T8W1 at Different Load Levels.

3.8.2 Exterior Solution 8(a) (Post-Crack)—T8E1

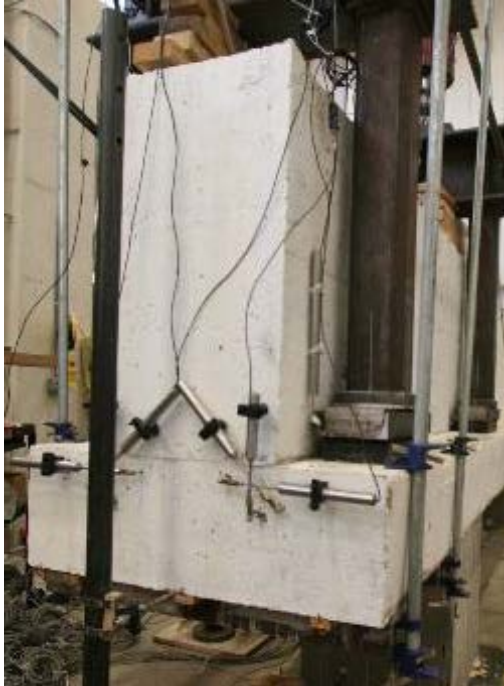
T8E1 is an exterior test using two clamped threadbars (Solution 8[a]) installed with existing cracks. As shown in Figure 3.88(a), the two clamped threadbars and channels were preinstalled before loading the specimen, but threadbars were not fastened. The specimen was then loaded to the SLS of 45 kips to simulate the demands of in-service bridges. Cracks were marked at SLS and two threadbars were fastened, as shown in Figure 3.88(b). The specimen was then loaded to ultimate failure. Figure 3.89 shows the load-deflection plots for the north and south load points.

The measured ultimate load (98 kips) was 19 percent larger than the estimated capacity (82 kips) and 48 percent larger than the exterior hanger-deficient reference capacity. The test was ended when the applied load dropped to about 90 percent of the measured ultimate load. Figure 3.90 shows the observed damage. The damage was more extensive on the south side.

Cracks formed before SLS and the retrofit solution installation was completed by stressing the threadbars. The cracks formed at the web-ledge interface behind the bearing pad. The bent cap was loaded again to SLS. No new crack formation was observed. The existing cracks remained as hairline cracks.

At the ULS of 68 kips, shear cracks were detected on both sides of the web. The diagonal cracks that started at the two reentrant corners on the end face were propagated horizontally and connected to each other. The width of the crack was 1 mm. At the top of the ledge, the cracks behind the bearing pad extended diagonally, starting at the inner edge of the bearing pad and going to the side face of the ledge.

As the load exceeded ULS, the bent cap showed significant crack length and width extensions with the formation of new cracks. Most of the new cracks formed on the ledge. At a load of 75 kips, a hanger crack formed on the end face near the neutral axis of the bent cap. At the measured ultimate load of 98 kips, more diagonal cracks had formed on the top and side face of the ledge on both sides. New shear cracks were also detected on both sides of the web. On the end face, new ledge cracks were detected. The width of the crack near the web-ledge interface on the end face increased to 5.5 mm.



(a) Threadbar through the web before fastening



(b) Fastening of threadbars after service load

Figure 3.88. Post-Crack Retrofit Solution 8(a) Installed on East End of Hanger-Deficient Specimen 8.

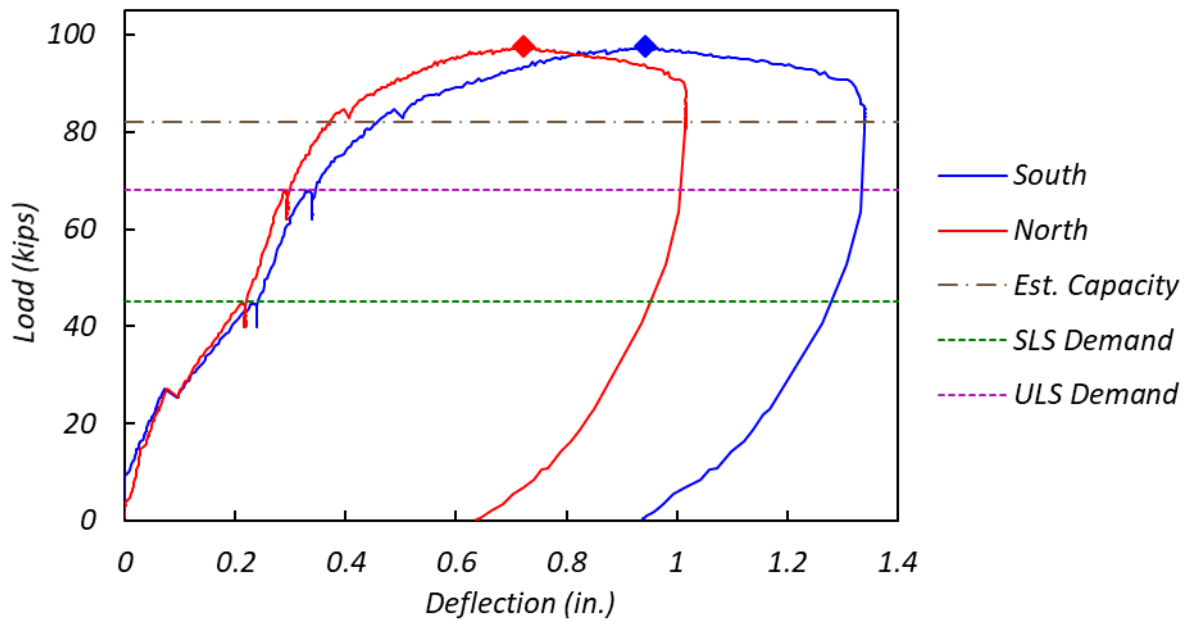


Figure 3.89. Load-Deflection Curve for T8E1.



(a) End face at SLS (after fastened threadbars)



(b) End face at ULS



(c) End face at final



(d) South side at final

Figure 3.90. Observed Damage for Test T8E1 at Different Load Levels.

3.8.3 Interior Solution 8—T8I1

T8I1 is an interior test with clamped threadbars (Solution 8). Figure 3.91 shows Solution 8 installed on the interior of the specimen. Figure 3.92 shows the load-deflection plots for all load points.

The measured ultimate load (109 kips) was 30 percent larger than the estimated capacity (84 kips) and 21 percent larger than the interior hanger-deficient reference test measured ultimate load. The test was ended when the applied load dropped to about 90 percent of the measured ultimate load. Figure 3.93 shows the observed damage. The specimen failed in hanger.

The initial cracks were found at the SLS of 49 kips at the web-ledge interface behind the bearing pads. The cracks at the interface propagated toward both sides of the bearing pad and diagonally extended to the top of the ledge on the outside of the bearing pad. Flexure cracks were detected on the bottom of the bent cap right under the loading points. Crack extensions and new cracks were observed as the load increased.

At the ULS of 78.5 kips, diagonal shear cracks were formed on both sides of the web. The web shear cracks at this state were formed on the outside of the bearing pads, going toward the center of the bent cap. More diagonal cracks were formed on top of the ledge. Diagonal cracks were also detected on the side face of the ledge near the bearing pads. The maximum crack widths of the diagonal cracks on the side face of the ledge and the web shear cracks were 1 mm and 0.3 mm, respectively.

New cracks formed throughout the specimen, and ledge crack widths increased significantly. At the measured ultimate load of 109 kips, deflections of the two outside channels were visible. More diagonal shear cracks formed on both sides of the web. The angles of the shear cracks decreased as they propagated toward the center of the bent cap. The maximum width of the web shear cracks was 0.9 mm.



Figure 3.91. Retrofit Solution 8 Installed on Interior of Hanger-Deficient Specimen 8.

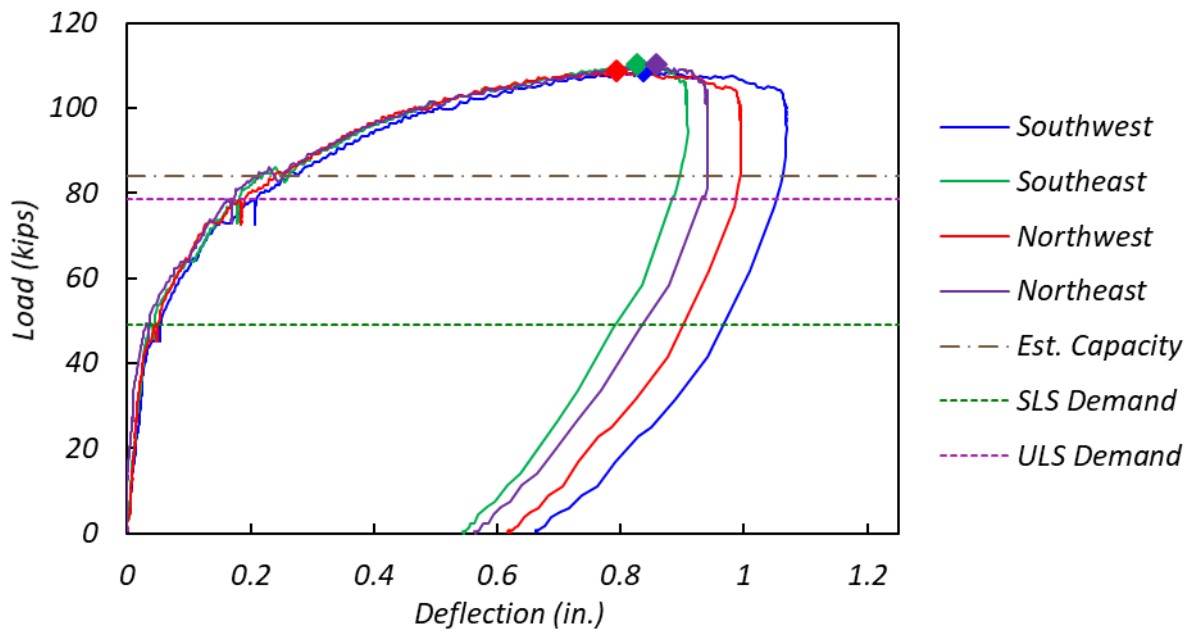


Figure 3.92. Load-Deflection Curve for T8I1.



(a) North side at SLS



(b) North side at ULS



(c) North side at final load level

Figure 3.93. Observed Damage for Test T8I1 at Different Load Levels.

CHAPTER 4: DATA ANALYSIS AND RECOMMENDATIONS FOR EVALUATING IN-SERVICE BENT CAPS

4.1 Overview

This chapter presents the evaluation of the accuracy of AASHTO LRFD procedures in estimating the capacity of in-service inverted-T bent caps and, where appropriate, provides proposed modifications. The capacities of the tested inverted-T bent cap specimens were calculated in accordance with the AASHTO LRFD Bridge Design Specifications (2014) as prescribed in the TxDOT (2015) *Bridge Design Manual—LRFD*. Experimental results, analysis results using AASHTO LRFD procedures, and analysis results using modified AASHTO equations are compared for reference specimens. The ratio of the estimated-to-measured capacities is provided to investigate the accuracy of code-based capacity calculations. Where deemed appropriate, the researchers make recommendations for revised capacity calculations.

AASHTO LRFD (2014) specifies the design methods for the beam ledges in Section 5.13.2.5. Figure 4.1 shows potential cracks and their locations on the ledge of an inverted-T bent cap. AASHTO LRFD (2014) indicates that the beam ledges should resist (a) flexure, shear, and horizontal forces; (b) tension force in the supporting element; (c) punching shear at points of loading; and (d) bearing force. The cracks specified in Figure 4.1 are referred to as “Ledge Shear Friction and Ledge Flexure (Crack 1),” “Hanger (Crack 2),” “Punching Shear (Crack 3),” and “Bearing (Crack 4).” While the ledge of the inverted-T bent cap should have sufficient bearing capacity to resist the load on the bearing pad as described in Article 5.7.5 of AASHTO LRFD (2014), the bearing capacity is generally sufficient to resist the load from the girder. Therefore, bearing capacity is not accounted for as a critical failure mode in this report. Sections 4.1, 4.2, and 4.3 provide analysis of the hanger, ledge, and punching shear capacities, respectively. Section 4.3 summarizes key findings of this chapter.

4.2 Hanger Capacity

The hangers resist tension forces at the location of Crack 2 in Figure 4.1, referred to as the hanger crack. The calculation of the hanger capacity assumes a distribution width within which the hangers are capable of transferring load from the ledge to the web, with all reinforcement within

this width assumed to yield. AASHTO LRFD (2014) defines two equations for calculating the hanger capacity, with the lesser value controlling the capacity.

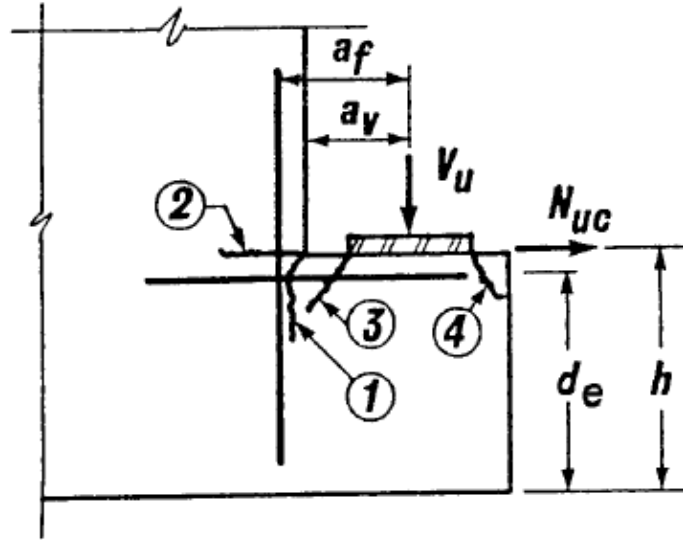


Figure 4.1. Notation and Potential Crack Locations for Ledge Beams (AASHTO, 2014).

4.2.1 Code Provisions

For interior girders, the nominal shear resistance for hanger reinforcement is the lesser of:

$$V_n = \frac{A_{hr}f_y}{s}S \quad (4.1)$$

$$V_n = 0.063\sqrt{f'_c}b_f d_f + \frac{A_{hr}f_y}{s}(W + 2d_f) \quad (4.2)$$

where A_{hr} = area of hanger reinforcement; S = spacing of bearing pads (girder spacing); s = spacing of hanger reinforcements; b_f = width of the bottom flange; and d_f = depth of the center of gravity of negative flexural reinforcements, as notated in Figure 4.2.

For exterior girders, the nominal shear resistance for hanger reinforcement is the lesser of:

$$V_n = \frac{A_{hr}f_y}{s}\left(\frac{S}{2} + c\right) \quad (4.3)$$

$$V_n = 0.063\sqrt{f'_c}b_f d_f + \frac{A_{hr}f_y}{s}\left(\frac{W + 2d_f}{2} + c\right) \quad (4.4)$$

where c = spacing from the centerline of the bearing to the end of the beam ledge.

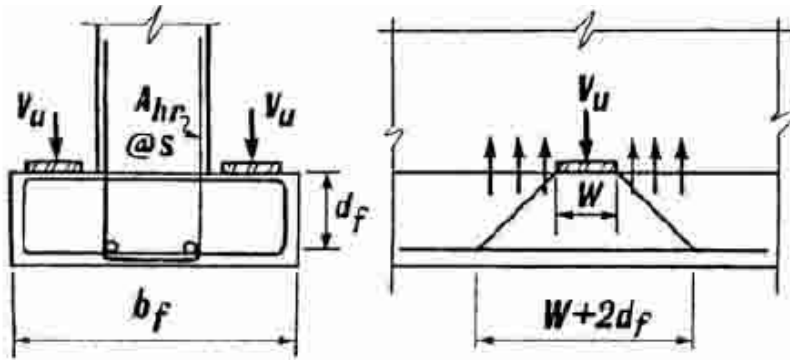


Figure 4.2. Notation for Interior Girder Hanger Capacity at the Strength Limit State (AASHTO, 2014).

4.2.2 Analysis of Experimental Results

Table 4.1 compares the estimated and measured capacity of the hanger-deficient reference specimen. Estimated capacity is calculated using the AASHTO LRFD provisions and the test day material strengths. The exterior hanger capacity of 42 kips is governed by Equation (4.3). The interior hanger capacity of 49 kips is governed by Equation (4.2). The measured capacity is taken as the maximum load observed during the experimental test. At the exterior girder, the observed ultimate strength of 66 kips is 24 kips larger than the estimated capacity. At the interior girder, the observed ultimate strength of 90 kips is 41 kips larger than the estimated capacity.

To understand the large discrepancy between estimated and observed capacities, and to assess if AASHTO design equations are appropriate, the progression of damage throughout the tests should be evaluated. To support this, Figure 4.3 shows the observed damage and the distribution widths used for calculation of the estimated capacity; the boxed distribution width indicates that which controls the capacity calculation.

Table 4.1. Summary of Capacity Analysis for Hanger-Deficient Reference Specimen.

Test ID		Estimated Capacity by Failure Mode					Est. Capacity (kips)	Meas. Ult. Load (kips)	Est./Meas.
		LSF (kips)	LF (kips)	H (kips)	P (kips)	B (kips)			
Ext.	T1W1	144	91	42/46	65	344	42	66	0.64
Int.	T1I1	162	140	56/ 49	79	344	49	90	0.55

Note: LSF = ledge shear friction, LF = ledge flexure, H = hanger, P = punching shear, and B = bearing.

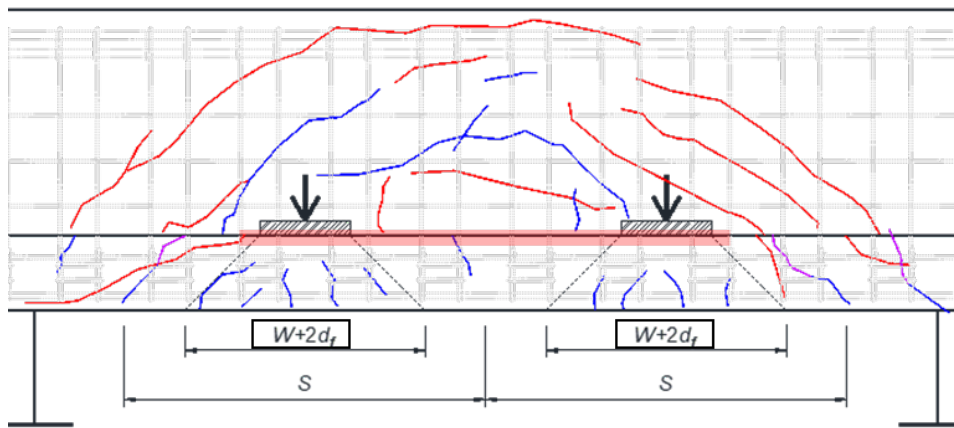
¹ Exterior hanger capacity is smaller amount (in bold) of Eq. (4.3)/(4.4).

² Interior hanger capacity is smaller amount (in bold) of Eq. (4.1)/(4.2).

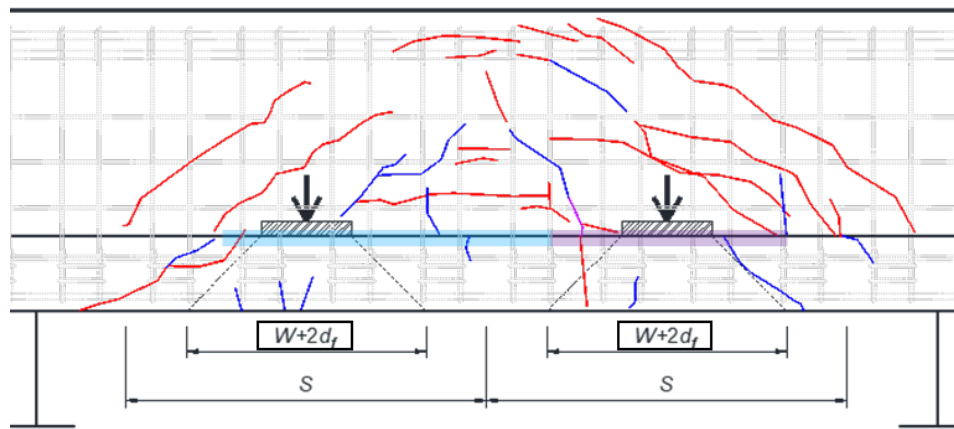


(a) South side of T1W1

(b) North side of T1W1



(c) South side of T1I1



(d) North side of T1I1

Note: W = bearing pad width, d_f = distance from ledge top to the center of bottom flexural reinforcement, S = spacing between bearing pads, and c = distance from the center of bearing pad to the end face of specimen.

Figure 4.3. Observed Damages and AASHTO Distribution Widths for Hanger-Deficient Reference Tests.

For the exterior girder, damage beyond the initial crack (horizontal at the web-ledge interface) first occurred at 45 kips, which is approximately the estimated capacity calculated by Equation (4.4). At this load, a second horizontal crack formed, accompanied by a small drop in load. Although this is not the ultimate capacity of the specimen, it should be interpreted as the hanger capacity for comparison to design equations since the behavior beyond this point is beyond an acceptable level for in-service structures. The increase in specimen capacity beyond the initial hanger capacity is a result of (a) post-yield strength of reinforcement, and (b) extension of the hanger crack along the bent cap length. An estimate of strain based on measured widths suggests the outermost hanger reinforcement is well beyond the strain hardening plateau, with stresses as large as $0.7 f_u$. The interface cracks at 45 kips and observed ultimate load are highlighted in purple and blue, respectively, in Figure 4.3(a) and (b).

The behavior for the interior tests was similar to that of the exterior tests, with secondary hanger cracks forming in the web at a load of 65 kips. An initial hanger failure could not be as clearly defined as it was for the exterior. This is largely due to a greater ability of the response mechanism to change in the interior region, evidenced by the formation of flexure and shear cracks, as documented in Section 3.1.2. The length of the interface hanger cracks, highlighted in Figure 4.3(c) and (d), indicate the distribution width used is reasonable.

The ratio of the estimated hanger to observed hanger capacities, as established by the initial hanger failure, is 0.93 for exterior and 1.02 for interior. From this, along with a comparison of hanger crack lengths to the labeled distribution widths in Figure 4.3, it can be concluded that the AASHTO design equations are appropriate for assessing the capacity of in-service inverted-T bent caps.

4.3 Ledge Shear Friction and Flexure Capacity

The ledge of the inverted-T bent cap must resist shear, flexural, and axial tension forces at the location of Crack 1 shown in Figure 4.1. Although the ledge-deficient specimen is designed to have a ledge flexure deficiency, the capacity estimation procedures for both ledge shear friction and flexure capacities are described in this subsection.

4.3.1 Code Provisions

Nominal ledge shear friction (or interface shear) capacity of the specimens is the lesser of:

$$V_n = 0.2f'_c b_w d_e \quad (4.5)$$

$$V_n = 0.8b_w d_e \quad (4.6)$$

where V_n = nominal shear friction; f'_c = specified compressive strength of concrete in ksi; d_e = depth to the center of gravity of negative flexural reinforcements as noted in Figure 4.1; $b_w = W + 4a_v$ (interior) or c (exterior) = distribution width for shear friction, as shown in Figure 4.4(a); and a_v = distance from the center of the bearing pad to the face of the web.

The ledge flexure capacity accounts for the flexure and horizontal resistance of the ledge. The nominal flexure capacity for the specimen is calculated with the nominal flexure resistance specified in Article 5.7.3.2.2 with the specified distribution width for ledge flexure as shown in Figure 4.4(b). Therefore, the ledge flexure capacity is obtained by:

$$M_n = A_s f_y \left(d_e - \frac{a}{2} \right) \quad (4.7)$$

where A_s = area of ledge flexure reinforcement indicated in Figure 4.4; f_y = yield stress of ledge flexure reinforcement; and a = depth of the equivalent stress block with axial tension.

The concurrent horizontal axial tension, N_u , increases the depth of the equivalent stress block, a , and decreases the ledge flexure capacity based on the equilibrium equation:

$$\frac{N_u}{\phi} + A_s f_y = 0.85f'_c a b_m \quad (4.8)$$

where $b_m = W + 5a_f$ (interior) or $2c$ (exterior) = distribution width for ledge flexure and axial tension for interior and exterior, respectively; and a_f = distance from the center of the bearing pad to the center of the nearest stirrup, as shown in Figure 4.4(b).

Therefore, the depth of the equivalent stress block, a , with axial tension is obtained by:

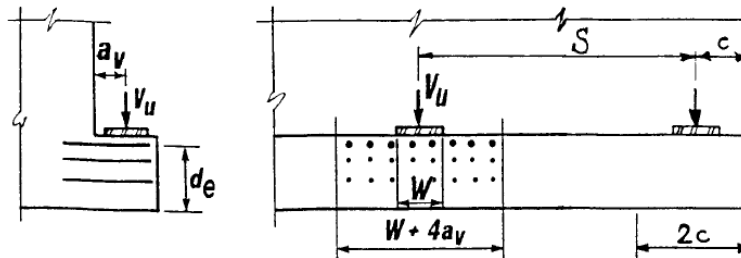
$$a = \frac{\frac{N_u}{\phi} + A_s f_y}{0.85f'_c b_m} \quad (4.9)$$

where N_u = axial tension force, which is the maximum 20 percent of factored ultimate load demand, V_u ; and c = distance from the center of the exterior bearing pad to the end of the inverted-T bent cap.

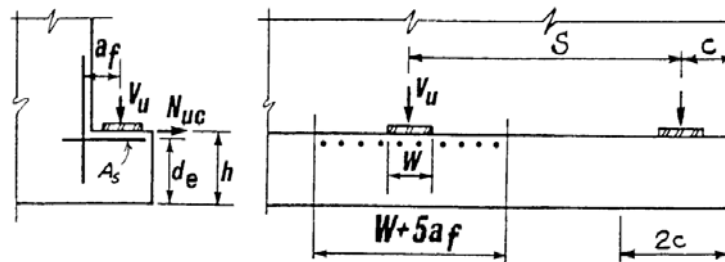
4.3.2 Analysis of Experimental Results

Table 4.2 compares the estimated and measured capacity of the ledge-deficient reference specimen. Estimated capacity is calculated using the AASHTO LRFD provisions and the test day material strengths. The exterior and interior capacities of 48 kips and 78 kips, respectively, are

governed by the ledge flexure capacity. The measured capacity is taken as the maximum load observed during the experimental tests. The specimen failed in ledge flexure at 65 kips and 85 kips at the exterior and interior, respectively. The ratio of estimated-to-measured load for the exterior is 0.72, while the ratio for the interior is 0.86.



(a) Ledge shear friction



(b) Ledge flexure and axial tension

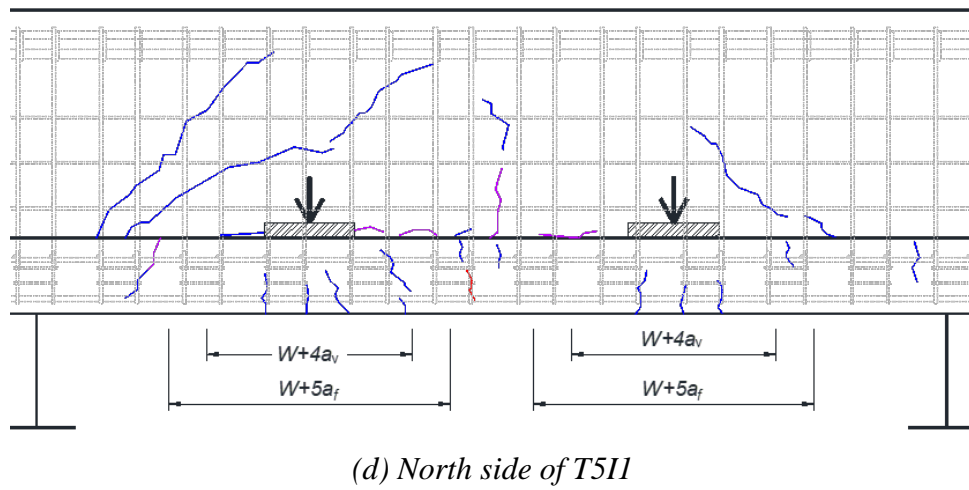
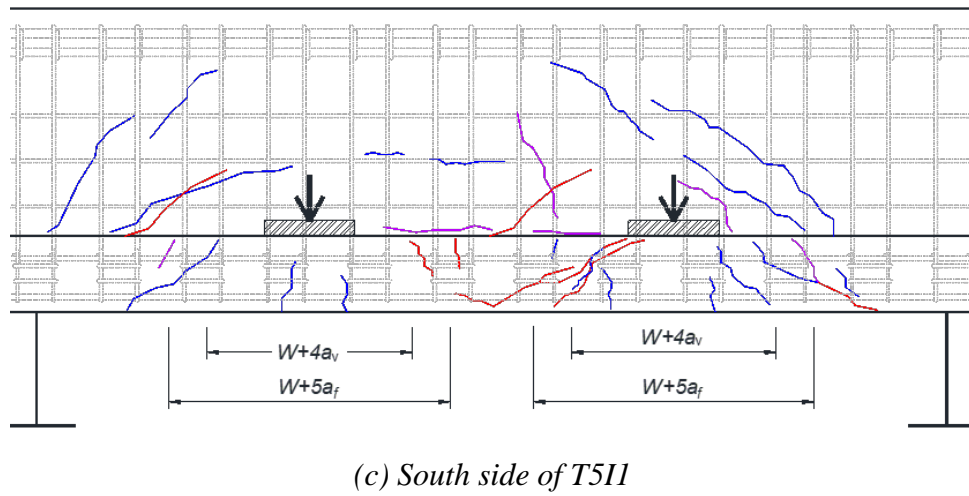
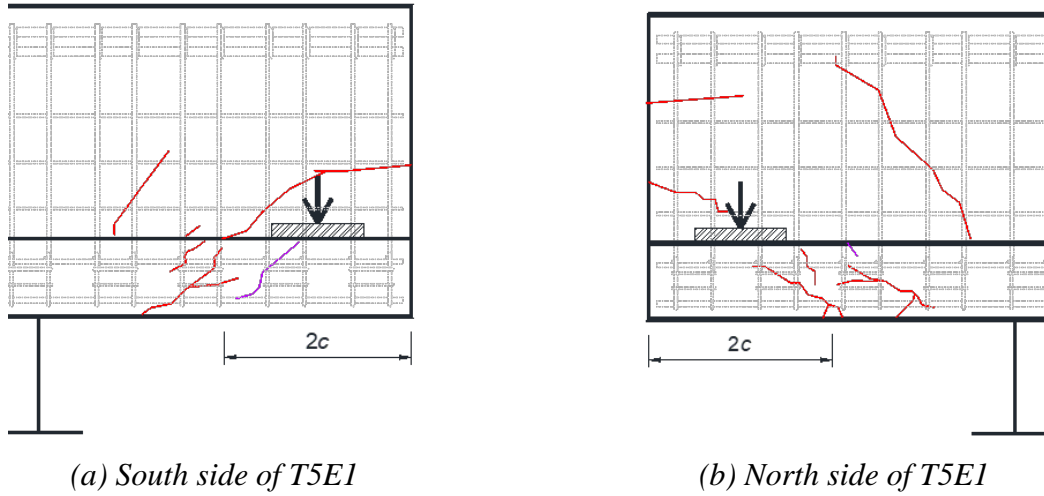
Figure 4.4. Notation and Distribution Width for Capacity Analysis (AASHTO, 2014).

Table 4.2. Summary of Capacity Analysis for Ledge-Deficient Reference Specimen.

Test ID		Capacity Analysis—AASHTO LRFD					Est. Capacity (kips)	Meas. Ult. Load (kips)	Est./Meas.
		LSF (kips)	LF (kips)	H (kips)	P (kips)	B (kips)			
Ext.	T5E1	144	48	81	65	352	48	66	0.72
Int.	T5I1	162	74	86	80	352	74	85	0.86

Note: LSF = ledge shear friction, LF = ledge flexure, H = hanger, P = punching shear, and B = bearing.

To assess if AASHTO design equations are appropriate, Figure 4.5 shows the observed damage and the distribution widths used for calculation of the estimated capacity. For the exterior ledge, the distribution width ($2c$) is considerably smaller than the width of the observed damage. For the interior ledges, the distribution width is similar to the width of the observed damage. Thus, to provide a better estimation of exterior ledge capacities for in-service bent caps, a rational modification of the distribution width for both ledge flexure and shear friction is described in the following subsection.



Note: W = bearing pad width, a_f = distance from web surface to the center of nearest stirrup, and c = distance from the center of bearing pad to the end face of specimen.

Figure 4.5. Observed Cracks and AASHTO Distribution Widths for Ledge-Deficient Reference Tests.

4.3.3 Proposed Modification

The AASHTO LRFD (2014) distribution width for shear friction is the minimum of S , $(W+4a_v)$, and $2c$. The distribution width for ledge flexure is the minimum of S , $(W+5a_f)$, and $2c$ for ledge flexure at the exterior girder location of the bent caps. In general, the distance $2c$ is smaller than other values, and thus it controls the distribution width for both ledge shear friction and flexure. However, based on the damages shown in Figure 4.5, the actual distribution width is larger than $2c$. Thus, based on experimental observations, it is suggested to replace $2c$ with the smaller of $c+S/2$ or $c+(W+4a_v)/2$ for shear friction or $c+(W+5a_f)/2$ for ledge flexure, as shown in Figure 4.6. This is based on the distribution width of $(W+4a_v)$ and $(W+5a_f)$, and the fact that generally, c is smaller than half of the distribution width. Although the exterior ledge of the bent cap has a smaller distribution width than the interior ledge, the inside distribution width is more consistent, with half of the smaller of S or $(W+4a_v)$ for shear friction or $(W+5a_f)$ for flexure. With this proposed distribution, capacity estimations are improved and provide more accurate prediction than AASHTO LRFD (2014).

Table 4.3 lists the ratios of the estimated capacities based on AASHTO LRFD (2014) and proposed modified equations for measured ultimate capacities. The estimated capacities with modified distribution widths provide more accurate values to the measured ultimate strengths than AASHTO distribution width. The proposed modification improves the accuracy of the capacity estimation by 20 percent compared to AASHTO LRFD (2014) provisions.



Figure 4.6. AASHTO LRFD and Proposed Distribution Width.

Table 4.3. Estimated Capacity and Ratio of Estimated-to-Measured Capacity.

	Est. Capacity (kips)	Meas. Ult. (kips)	Est./Meas.
AASHTO LRFD (2014)	48	65	0.73
Proposed	61		0.93

4.4 Punching Shear Capacity

The ledge of the inverted-T bent cap should have sufficient capacity to resist punching shear (failure surface shown as Crack 3 in Figure 4.1) at all points of loading. Punching shear tests were conducted on the ledge-deficient specimens to assess the effect of bearing pad size on the punching shear capacity. Two sizes of the pad were investigated: small bearing pad (4 in. x 4 in.) and large bearing pad (12 in. x 5 in.).

4.4.1 Code Provisions

Figure 4.7 shows the truncated pyramid area of concrete resisting punching shear that is specified in Article 5.13.2.5.4 of AASHTO LRFD (2014). The area of the truncated pyramid is approximated as the average of the perimeter of the bearing pad and the perimeter at depth, d_e , assuming 45-degree slopes in AASHTO LRFD (2014).

When calculating nominal punching shear resistance, TxDOT uses d_f instead of d_e (see Figure 4.7[b]). This is because d_f has traditionally been used for inverted-T bents and was also used in the study of inverted-T beams conducted by Furlong and Mirza (1974). With modifications from the *Bridge Design Manual—LRFD*, Chapter 4, Section 5, design criteria (TxDOT, 2015), the nominal punching shear resistance for interior girders is:

$$V_n = 0.125\sqrt{f'_c}(W + 2L + 2d_f)d_f \quad (4.10)$$

where L = length of the bearing pad.

The nominal punching shear capacity for the exterior is the lesser of Equation (4.10) or:

$$V_n = 0.125\sqrt{f'_c}\left(\frac{W}{2} + L + d_f + c\right)d_f \quad (4.11)$$

In general, c is less than $W/2 + L + d_f$, and Equation (4.11) controls the punching shear capacity.

Table 4.4 compares the estimated (AASHTO LRFD) and measured (maximum load during test) capacity for the punching shear tests. The estimated capacities utilized the test day material

properties, leading to different values for the same pad size and location; for brevity, only the ledge flexure and punching shear estimated capacities are shown. Although the ledge flexure capacity was estimated to control the failure for a few tests, all tests failed in punching shear; thus, analysis of the results used the punching shear estimated capacity.

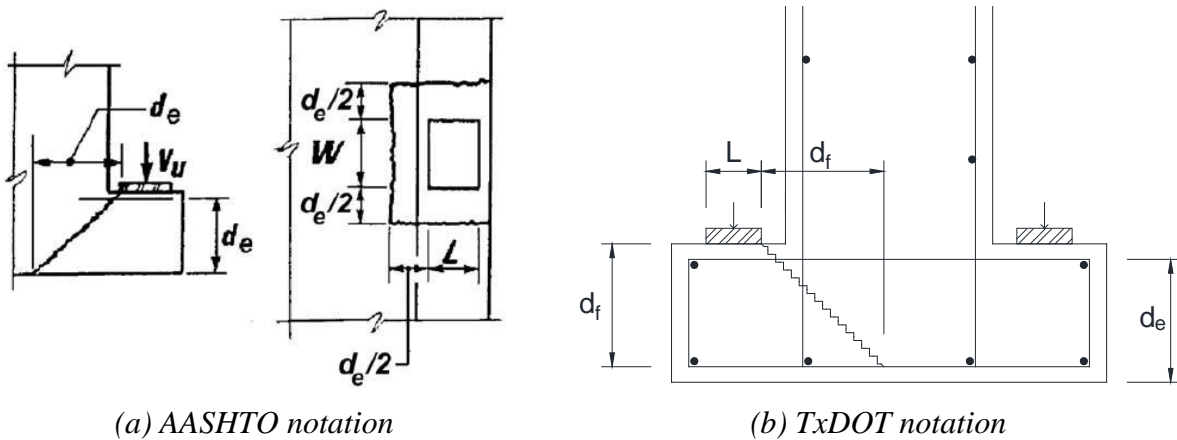


Figure 4.7. Punching Shear of Beam Ledge (AASHTO, 2014).

4.4.2 Analysis of Experimental Results

For all tests, the observed capacity exceeded the estimated capacity; however, the larger bearing pads did not provide the significant increase expected. At the exterior girders, the increase was expected to be 20 percent, but only a 14 percent increase was observed. At the interior girders, a 36 percent increase was expected, yet for Specimen 3 tests, the large pads provided 10 percent *less* capacity than the small pads. To investigate further, additional interior punching shear tests were conducted on Specimen 7, in which the large bearing pad increased the punching shear capacity by 1 percent to 6 percent.

In interpreting these findings, there are two questions to consider:

1. Are the AASHTO equations appropriate for calculating punching shear capacity of in-service bent caps?
2. Why is the increase in bearing pad size more effective at the exterior than the interior?

Table 4.4. Summary of Punching Shear Test on Ledge-Deficient Specimen.

Test ID		Bearing Pad Size	LF (kips)	P (kips)	Est. Capacity ¹ (kips)	Meas. Ult. Load (kips)	Est./Meas.	Est. Large/Small	Meas. Large/Small
Ext.	T3W1	Small	53	51	51	70	0.73	1.00	1.00
	T3E1	Large	53	61	61	80	0.76	1.20	1.14
Int.	T3I1	Small	63	55	55	104	0.53	1.00	1.00
	T7I1	Small	64	64	64	112	0.57	1.00	1.00
	T7I3	Small	64	64	64	112	0.57	1.00	1.00
	T3I2	Large	81	75	75	94	0.80	1.36	0.90
	T3I3	Large	81	75	75	94	0.80	1.36	0.90
	T7I2	Large	82	87	87	119	0.73	1.36	1.06
	T7I4	Large	82	87	87	113	0.77	1.36	1.01

Note: LF = ledge flexure, P = punching shear.

¹ Estimated capacity is taken as the punching shear capacity due to the observed punching shear failure.

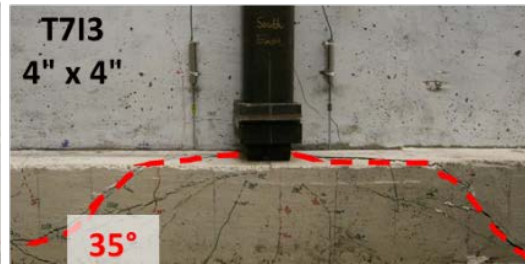
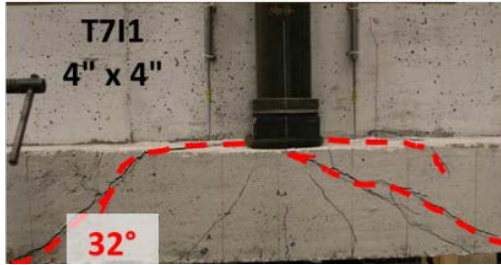
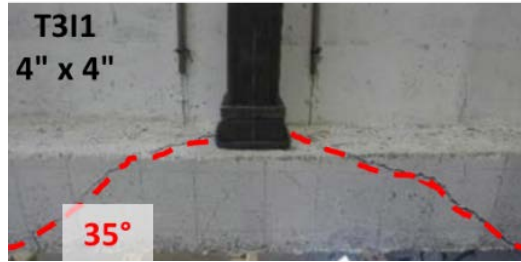
To address the first question, the observed damage can be considered. Figure 4.8 shows the observed punching shear damage, with the angle of the primary cracks indicated. On average, cracks have a 35-degree angle, shallower than the 45-degree assumed in the AASHTO LRFD (2014) calculations. Based on this observation, a rational modification of the equations for punching shear capacity calculation is proposed in Section 4.4.3. With regards to the second question, the observed damage and instrumentation readings are unable to provide a rational explanation; however, a number of hypotheses can be made. These include (a) influence of adjacent loading points (interior tests have two load points per ledge, while the exterior tests have a single point); and (b) ledges on the tension chord of the bent cap (interior) rather than on the compression chord (exterior). Further investigation is needed to explore these hypotheses.

4.4.3 Proposed Modifications

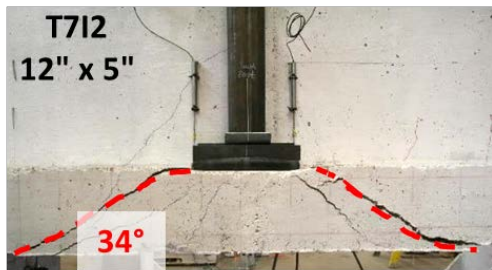
As indicated in Section 4.2, AASHTO LRFD provisions with TxDOT modification significantly underestimate the punching shear capacity for the ledges. Thus, it is proposed to modify the punching shear capacity equation to incorporate the observed behavior:

$$V_n = 0.125\sqrt{f'_c} \left(\frac{W}{2} + L + d_f \cot(35^\circ) + c \right) d_f \quad (4.12)$$

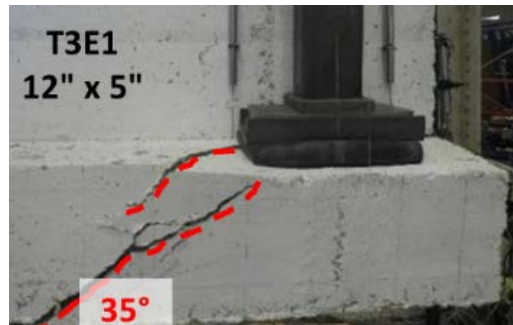
$$V_n = 0.125\sqrt{f'_c} (W + 2L + 2d_f \cot(35^\circ)) d_f \quad (4.13)$$



(a) Interior ledge with small bearing pad



(b) Interior ledge with large bearing pad



(c) Exterior ledge with small bearing pad

(d) Exterior ledge with large bearing pad

Figure 4.8. Observed Crack Angle for Punching Shear Tests.

Table 4.5 lists the estimated capacities and the ratios of estimated capacities to measured capacities for each test. Figure 4.9 shows the comparison of estimated capacities based on AASHTO LRFD, TxDOT BDM—LRFD, and the proposed equation with measured ultimate load from test results. With the proposed modification in the punching shear capacity equation, the accuracy of capacity estimation is improved by 14 percent to 28 percent compared to the AASHTO equation, while it is improved by 8 percent to 18 percent compared to the TxDOT equation.

Table 4.5. Estimated Capacity and Ratio of Estimated-to-Measured Capacity.

	Pad Size (Test ID)	Meas. (kips)	AASHTO (2014)		TxDOT (2015)		Proposed	
			Est. (kips)	Est./Meas.	Est. (kips)	Est./Meas.	Est. (kips)	Est./Meas.
Ext.	Small (T3W1)	70	47	0.67	51	0.73	57	0.81
	Large (T3E1)	80	45	0.56	61	0.66	67	0.84
Int.	Small (T3I1)	104	49	0.47	55	0.53	68	0.65
	Small (T7I1)	112	58	0.52	64	0.57	79	0.71
	Small (T7I3)	112	58	0.52	64	0.57	79	0.71
	Large (T3I2 & T3I3)	94	68	0.72	75	0.80	87	0.93
	Large (T7I2)	119	79	0.66	87	0.69	102	0.86
	Large (T7I4)	113	79	0.70	87	0.73	102	0.90

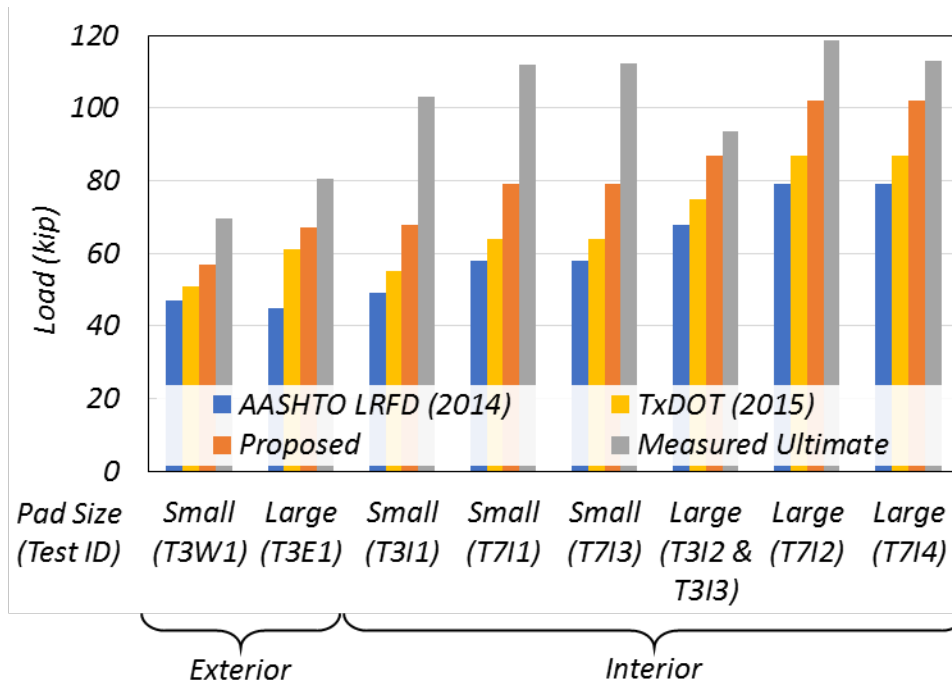


Figure 4.9. Comparison of Existing and Proposed Punching Shear Capacity Equations with Experimental Results.

4.5 Closing Remarks

In this chapter, the estimated capacities in accordance with AASHTO LRFD (2014) and TxDOT (2015) specifications were discussed with the reference test results. The accuracy of the capacity estimation was evaluated, and modifications were proposed for ledge flexure and shear friction capacities of the exterior portion of the caps and punching shear capacities of entire bents. The ratios of the estimated-to-measured capacities are provided to investigate the accuracy of code-based capacity calculations and proposed calculations. For ledge flexure and shear friction, the distribution widths are modified based on the observations from tests. Equation for the punching shear capacity calculation are proposed to modify the parameter of the truncated pyramid based on the test observation. The capacity estimations based on the rational modifications improve by 8 percent to 20 percent for exterior ledge flexure capacity and 16 percent to 28 percent for punching shear capacity.

CHAPTER 5: DATA ANALYSIS OF RETROFIT SOLUTIONS

In this chapter, the test results for the retrofit solutions are discussed. Experimental test results for retrofitted specimens are compared to those for the reference specimens to evaluate their effectiveness. The ratios of the retrofitted strengths are compared to the reference strengths and the estimated strengths to quantify the capacity increase provided by each solution. The estimated capacities are calculated based on the AASHTO LRFD equations described in Chapter 4 and considered the actual measured material properties from the day of the test. The evaluation of the ultimate capacity increase alone is not always sufficient to assess the impact of a particular solution. Load deformation plots are provided to illustrate the impact on stiffness and ductility. Where appropriate, the progression of damage is discussed. Section 5.1 discusses retrofit solutions to strengthen hanger deficiencies. Section 5.2 discusses retrofit solutions to strengthen ledge deficiencies.

5.1 Hanger-Deficient Specimens

Table 5.1 provides a summary of the estimated and observed capacity, deficiency, and overstrength factor for the reference hanger-deficient specimen.

Capacity deficiency is calculated as:

$$Deficiency = \frac{Demand}{\phi} - Capacity \quad (5.1)$$

where ϕ = resistance factor, 0.9 for all failure modes; *Demand* = AASHTO LRFD Strength 1 limit state girder load; and *Capacity* = AASHTO LRFD capacity.

The overstrength factor, Ω , listed in Table 5.1, is determined by:

$$\Omega = \frac{\phi V_n}{V_u} \quad (5.2)$$

where V_n = capacity for the bent, ledge shear friction, ledge flexure, hanger, punching shear, or bearing; and V_u = factored demand.

The failure mechanism was a hanger failure, as expected. Analysis of the test results in Section 4.2 showed that the AASHTO hanger capacity equations use an appropriate distribution width and provide a reasonable estimate of the load at which the *initial* hanger failure occurs. After the initial hanger failure, the specimen was able to sustain a significant increase in load, leading to small or no observed deficiencies and observed overstrength factors close to or greater than unity.

These numbers are misleading because the associated damage is unacceptable to permit use of the bent cap at such demands. In light of this, the analysis of retrofit solutions to improve hanger capacity does not focus on the ability to address a quantified deficiency but rather on the relative increase of the ultimate observed capacity. Where appropriate, the evaluation of retrofit effectiveness is supplemented by a discussion of observed damage at other points throughout the test.

Table 5.1. Comparison of Expected and Observed Deficiency of Hanger-Deficient Reference Specimens.

	Failure Mode	Demand (kips)	Estimated			Observed		
			Capacity (kips)	Deficiency (kips)	Ω	Capacity (kips)	Deficiency (kips)	Ω
Ext.	Ledge shear friction	63.0	144	—	2.06	66	4	0.94
	Ledge flexure		92	—	1.3			
	Hanger		42	28	0.60			
	Punching shear		65	5	0.93			
	Bearing		344	—	4.91			
Int.	Ledge shear friction	75.5	162	—	1.93	90	—	1.07
	Ledge flexure		142	—	1.6			
	Hanger		49	35	0.56			
	Punching shear		79	5	0.94			
	Bearing		344	—	4.10			

5.1.1 Analysis of the Exterior Ledges

The exterior portions of the hanger-deficient specimens were strengthened with an end-region stiffener (Solution 3), clamped threadbar with channel (Solution 8), load-balancing PT (Solution 14), and concrete infill with full-depth FRP anchored with steel waling (Solution 17). Table 5.2 summarizes the estimated capacity and measured ultimate load for each exterior hanger-deficient test. Retrofit values are normalized by the values for the reference test (T1W1) result. Figure 5.1 shows load-deflection curves for the hanger-deficient exterior tests, where the deflection is that of the ledge with greater deflection. Horizontal lines indicate the estimated capacity and ULS (63 kips).

All retrofit solutions successfully improved the hanger capacity at the exterior girders, with the failure mode shifting to other mechanisms in some tests. The retrofit solutions provided an 18 percent to 61 percent increase in hanger capacity. As a result of the strength increase provided by the retrofit solutions, the bent caps failed at load levels higher than the ultimate factored load.

Further evidence of the benefit of the solutions is the decreased damage at SLS, which was approximately the load at which the initial hanger failure occurred in the reference test. Retrofit solutions installed inside of the exterior bearing pad (Solutions 8[a] and 17) alter the initial stiffness of the structure, while the solutions installed outside of the bearing pad (Solutions 3, 8[b], and 14) do not significantly affect the initial stiffness of the structure. Each solution is discussed in depth in the following subsections.

Table 5.2. Summary of Capacity Analysis and Test Result for Hanger-Deficient Exterior.

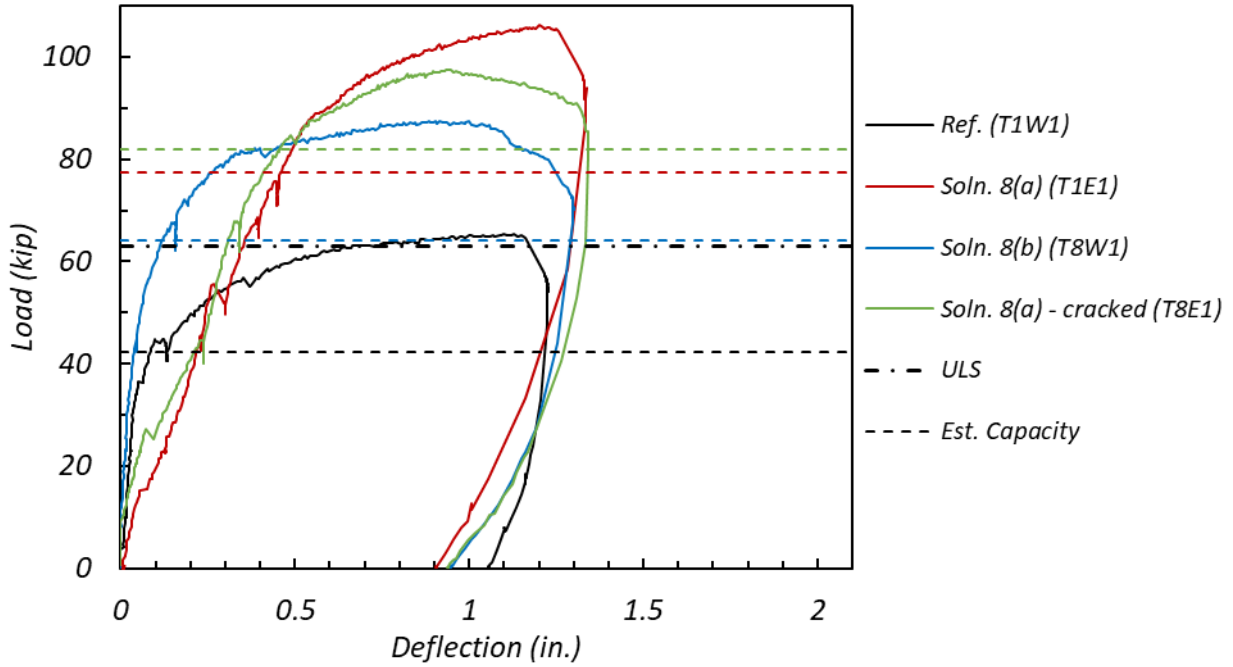
Test ID	Solution No.	Est. Capacity (kips)	Meas. Ult. Load (kips)	Est./Meas.	Est. Ret.**/Ref.	Meas. Ret./Ref.	Obs. Failure Mode
T1W1	Reference	42	66	0.64	1.00	1.00	Hanger
T1E1	8(a)	77	106	0.73	1.83	1.61	Hanger
T8W1	8(b)	64	88	0.73	1.52	1.33	Hanger
T8E1	8(a) Post-crack	82	98	0.84	1.94	1.48	Hanger
T2E1	3	74	78	0.95	1.75	1.18	Strut-tie
T2W1	14	66	82*	0.80	1.56	1.24	—
T2W2	17 Post-crack	73	92	0.79	1.73	1.39	Ledge flexure and punching

* Test termination load.

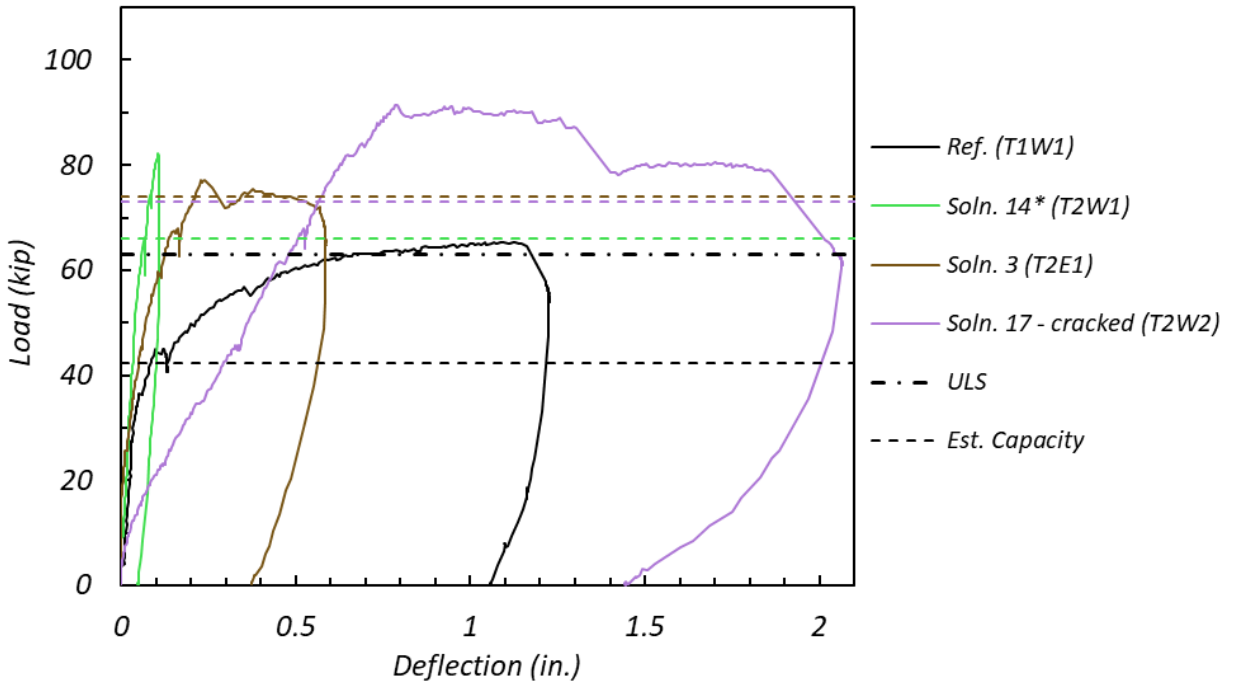
** Ret. = Retrofit.

5.1.1.1 Solution 3 (End-Region Stiffener)

Solution 3 (T2E1) increased the hanger-deficient specimen capacity by 12 kips (18 percent). Although this is slightly less than the estimated increase, it is not possible to establish the true increase of the hanger capacity using the end plate since the failure mechanism was not a hanger failure. In addition to providing increased hanger capacity, the end stiffener increased the punching capacity, thus preventing a brittle punching failure mechanism. The end region of the specimen failed because of stress exceedance at the strut-to-node interface. This is because the end plate could not resist the concentrated node stress at the bottom tip of the plates. In Hurlebaus et al. (2018b), recommendations are made for refining the end plate details to avoid such a failure mechanism.



(a) Solution 8



(b) Solutions 3, 14, and 17

Note: Solid lines: experimentally measured capacities; dashed lines: estimated capacities using empirical AASHTO (2014) LRFD procedures; dash-dot line: ultimate factored load demand (ULS) = V_u .

*T2W1 test was terminated at 66 kips.

Figure 5.1. Load-Deflection Curves for Hanger-Deficient Exterior Tests.

5.1.1.2 Solution 8 (Clamped Threadbar with Channel)

Solution 8 was tested with two installation conditions. Solution 8(a) has two threadbars and channels, while 8(b) has only one threadbar and channel. Also, threadbars were installed after cracking (after SLS) in test T8E1 to evaluate whether the retrofit solution is as effective as before the structure was damaged. A comparison of the test results of T1W1 and T1E1 shows that Solution 8(a) improves the capacity by 40 kips, which is larger than the estimated improvement of 35 kips. This is because in the capacity analysis, the yield strength of the threadbars is only accounted for in terms of improving hanger capacity, but the channels also contribute to slightly improve the capacity since Solution 8 consists of threadbars and channels.

The threadbars for Solution 8 are installed at the center of the stem and therefore contribute approximately equally to the ledges on each side of the web. When comparing test T1E1 and T8W1, this can be verified based on the measured ultimate load of 106 kip and 88 kip for T1E1 and T8W1, respectively. Based on the T8E1 test results, Solution 8(a) provided a 32 kip capacity increase for the cracked specimen compared to a 40 kip increase in the uncracked specimen. Furthermore, it was observed that the existing cracks under SLS were restrained with Solution 8(a). The capacity of the uncracked specimen was improved by 61 percent with Solution 8(a), while 48 percent improvement was observed in the cracked structure. As a result, Solution 8 can be used for strengthening the hanger capacity of the end regions of the inverted-T bent caps. This solution is the most effective one in terms of capacity increase among the tested retrofit methods.

5.1.1.3 Solution 14 (Load-Balancing PT)

The test of Solution 14 (T2W1) was terminated prior to failure due to safety concerns related to possible failure of strands. The load was applied up to 82 kips, referred to as the test termination load, 24 percent higher than failure of the reference test. At loads comparable to the initial hanger failure of the reference tests, no cracking was observed. At loads near the ultimate capacity of the specimen, hanger cracks were limited to hairline cracks and were smaller in the reference test. This reduced damage is further evidence that Solution 14 can successfully provide an alternative load path that alleviates the load on the ledges, and subsequently the hangers.

5.1.1.4 Solution 17 (Concrete Infill with Full-Depth FRP Anchored with Steel Waling)

To evaluate the effectiveness of FRP wraps for the hanger-deficient structure, Solution 17 was selected to test rather than Solution 16 since Solution 17 is designed to mainly improve the hanger capacity. Although the test with Solution 17 was conducted after test T2W1 at the same location, the cracks from T2W1 were very thin and negligible and not developed enough to affect the capacity of the structure. After constructing concrete infill blocks on the ledges, the existing cracks were concealed by the concrete block. Thus, the preexisting cracks under SLS are negligible by retrofitting the bent cap with the FRP wraps. Solution 17 improved the capacity of the exterior ledge by 39 percent compared to the reference specimen. Solution 17 increased the hanger capacity of the exterior ledge beyond the ultimate load demand and can be recommended for strengthening the hanger capacity of exterior bent cap ledges.

5.1.2 Analysis of the Interior Ledges

The interior portions of the hanger-deficient specimens were strengthened with two clamped threadbars with channels (Solution 8[a]), load-balancing PT (Solution 14), and full-depth FRP wraps with steel waling (Solution 17). Table 5.3 summarizes the estimated capacity and measured ultimate load for each test. Retrofit values are normalized by the values for the reference test (T1I1). Figure 5.2 shows load-deflection curves for the hanger-deficient exterior tests, where the deflection is that of the ledge with greater deflection. Horizontal lines indicate the estimated capacity and ULS (63 kips).

All three retrofit solutions were able to improve the interior hanger capacity of the bent cap, but the magnitude of the increase was less than the estimated deficiency of 35 kips. The solutions were designed to improve 38 percent to 70 percent of the hanger capacity, but provided only an approximately 20 percent increase of the interior hanger capacity. Given that the reference specimen did not have a deficiency as designed, it is difficult to know if the solutions would be more effective if applied to bent caps with significant deficiencies.

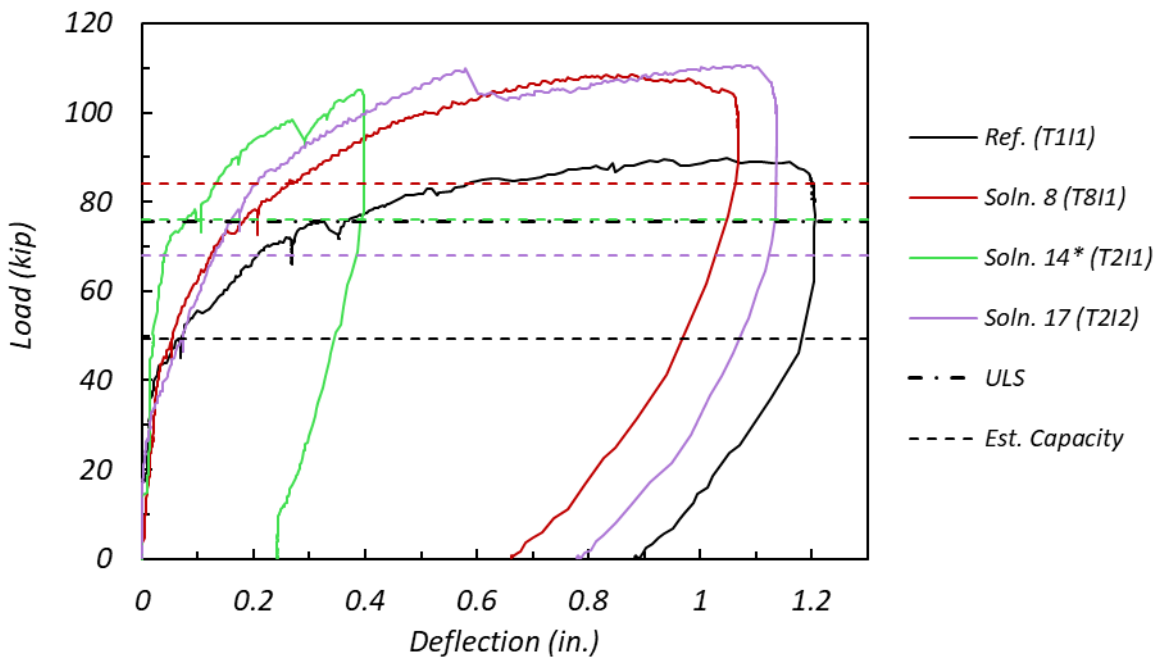
All three solutions did not affect the initial stiffness of the inverted-T bent caps. However, the retrofitted specimens resulted in less deflection at ULS than that of the reference specimens since solutions altered the post-crack stiffness of the structure. Each solution is discussed in depth in the following subsections.

Table 5.3. Summary of Capacity Analysis and Test Result for Hanger-Deficient Interior.

Test ID	Solution No.	Est. Capacity (kips)	Meas. Ult. Load (kips)	Est./Meas.	Est. Ret.**/Ref.	Meas. Ret./Ref.	Obs. Failure Mode
T1I1	Reference	49	90	0.55	1.00	1.00	Hanger
T8I1	8(a)	84	109	0.77	1.70	1.21	Hanger
T2I1	14	76	105*	0.72	1.54	1.17	—
T2I2	17 Post-crack	68	111	0.61	1.38	1.23	Ledge flexure and punching

*Test termination load.

**Ret. = retrofit.



Note: Solid lines: experimentally measured capacities; dashed lines: estimated capacities using empirical AASHTO LRFD (2014) procedures; dash-dot line: ultimate factored load demand (ULS) = V_u .

*T2I1 test was terminated at 76 kips.

Figure 5.2. Load-Deflection Curves for Hanger-Deficient Interior Tests.

5.1.2.1 Solution 8 (Clamped Threadbar with Channel)

Solution 8(a) (T8I1) delayed the formation of damage and increased the ultimate capacity of the specimen. At points of damage documentation during the test, the retrofitted specimen had considerably less damage than the reference specimen. At the estimated ULS for testing (68 kips), the reference test had hanger cracks extending the full distance between the bearing pads and a secondary hanger crack. At the same demand in the retrofit test, the hanger crack was present only behind the bearing pads, indicating the effectiveness of the threadbars in restraining crack

formation. The final damage pattern indicates that the AASHTO distribution widths are appropriate when incorporating the threadbars into the capacity calculations, which provide a conservative estimate of the observed capacity. Although the change in ultimate capacity is less than expected, a comparison of initial hanger failure (drop in load and formation of secondary hanger crack in the web) indicates a larger-than-expected increase. The capacity is larger than estimated and the final damage indicates that the AASHTO distribution widths are appropriate when using the retrofit solution.

5.1.2.2 Solution 14 (Load-Balancing PT)

Test T2I1 was conducted on the interior ledges of the hanger-deficient specimen (Specimen 2), which was retrofitted by Solution 14. Similar to the exterior test, the test was terminated prior to failure at a termination load of 105 kips (17 percent larger than the reference measured capacity). Significantly reduced damage at key demands (SLS, ULS) indicates the success of the load-balancing PT in providing a supplement load path that reduces the demand on the ledges and hanger reinforcement.

5.1.2.3 Solution 17 (Concrete Infill with Full-Depth FRP Anchored with Steel Waling)

Solution 17 (T2I2) was installed on the interior ledges of the hanger-deficient specimen after test T2I1. The existing cracks from T2I1 were very thin and ultimately concealed by concrete infill. Therefore, the existing cracks were negligible for test T2I2. Solution 17 improved the hanger capacity of the specimen by 23 percent. This is the highest improvement among the retrofit solutions for the interior ledges of the hanger-deficient specimen tests. However, the capacity increase of 21 kips is less than the 35 kip deficiency of the hanger-deficient reference specimen. However, the solution can be used to strengthen the interior ledges of the inverted-T bent caps with hanger deficiency since it was the most effective one among the retrofit solutions for the interior portion of hanger-deficient bent caps.

5.2 Ledge-Deficient Specimens

Table 5.4 provides a summary of the estimated and observed capacity, deficiency (see Equation [5.1]), and overstrength factor (see Equation [5.2]) for the reference ledge-deficient specimens. The failure mechanism was ledge flexure as designed, but at larger-than-expected loads. Analysis of the test results in Section 4.3 showed that the AASHTO ledge capacity equations

are conservative and that a modified distribution width can be rationally justified; for simplicity, the AASHTO provisions are included in this section for evaluation of the retrofit test results, and analysis focuses on the increase of capacity relative to the reference test, rather than on ability to address the estimated deficiency.

Table 5.4. Comparison of Expected and Observed Deficiency of Ledge-Deficient Reference Specimen.

	Failure Mode	Demand (kips)	Estimated			Observed		
			Capacity (kips)	Deficiency (kips)	Ω	Capacity (kips)	Deficiency (kips)	Ω
Ext.	Ledge shear friction	63.0	144	—	2.06	66	10.3	0.94
	Ledge flexure		48	22	0.69			
	Hanger		81	—	1.16			
	Punching shear		65	5	0.93			
	Bearing		352	—	5.03			
Int.	Ledge shear friction	75.5	162	—	1.93	85	—	1.01
	Ledge flexure		74	10	0.88			
	Hanger		86	—	1.03			
	Punching shear		80	4	0.95			
	Bearing		351	—	4.00			

5.2.1 Analysis of the Exterior Ledges

The exterior portions of the ledge-deficient specimens were strengthened with an end stiffener (Solution 3), clamped threadbar (Solution 8), load-balancing PT (Solution 14), and concrete infill with partial- and full-depth FRP (Solutions 16 and 17). Table 5.5 summarizes the estimated capacity and measured ultimate load for each exterior ledge-deficient test. Retrofit values are normalized by the values for the reference test (T5E1). The load-deflection curves for the ledge-deficient exterior tests are plotted with ULS and estimated capacities in Figure 5.3.

Retrofit solutions improved the capacities at the exterior girders by 21 percent to 82 percent, with most tests failing with a combination of ledge flexure and punching shear. Solutions 3, 8(b), and 17 lowered the initial stiffness of the structure compared to the reference specimen and caused a relatively larger deflection, as shown in Figure 5.3. Solutions 8(a), 16, and 14 did not significantly affect the initial stiffness of the structure. In the following subsections, each solution is discussed in depth.

Table 5.5. Summary of Capacity Analysis and Test Result for Ledge-Deficient Exterior.

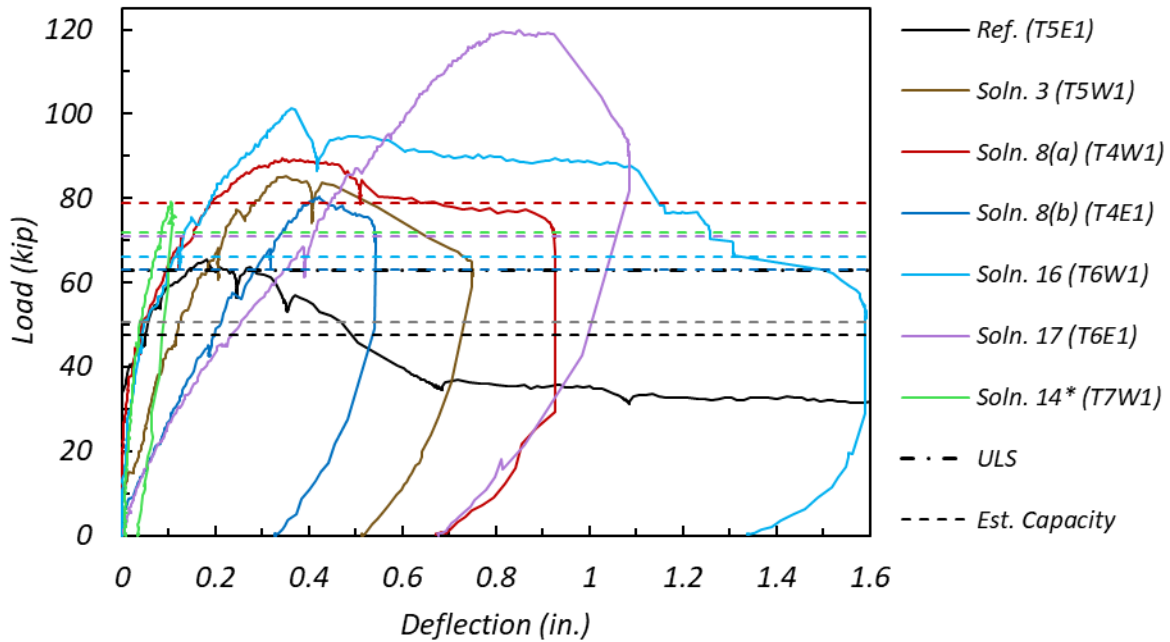
Test ID	Solution No.	Est. Capacity (kips)	Meas. Ult. Load (kips)	Est./Meas.	Est. Ret.**/Ref.	Meas. Ret./Ref.	Obs. Failure Mode
T5E1	Reference	48	66	0.72	1.00	1.00	Ledge flexure
T5W1	3	51	86	0.59	1.06	1.30	Strut-tie
T4W1	8(a)	79	90	0.88	1.66	1.36	Ledge flexure and punching
T4E1	8(b)	63	80	0.79	1.33	1.21	Ledge flexure and punching
T6W1	16	66	102	0.64	1.37	1.55	Ledge flexure and punching
T6E1	17	71	120	0.59	1.48	1.82	Ledge flexure and punching
T7W1	14	72	82*	0.88	1.50	1.24	—
T7W2	3 Post-crack	54	88	0.62	1.14	1.33	Ledge flexure and punching
T7E1	14 Post-crack	72	100*	0.72	1.50	1.52	—
T7E2	8(a) Post-crack	80	101	0.79	1.67	1.53	Ledge flexure and punching

*Test termination load.

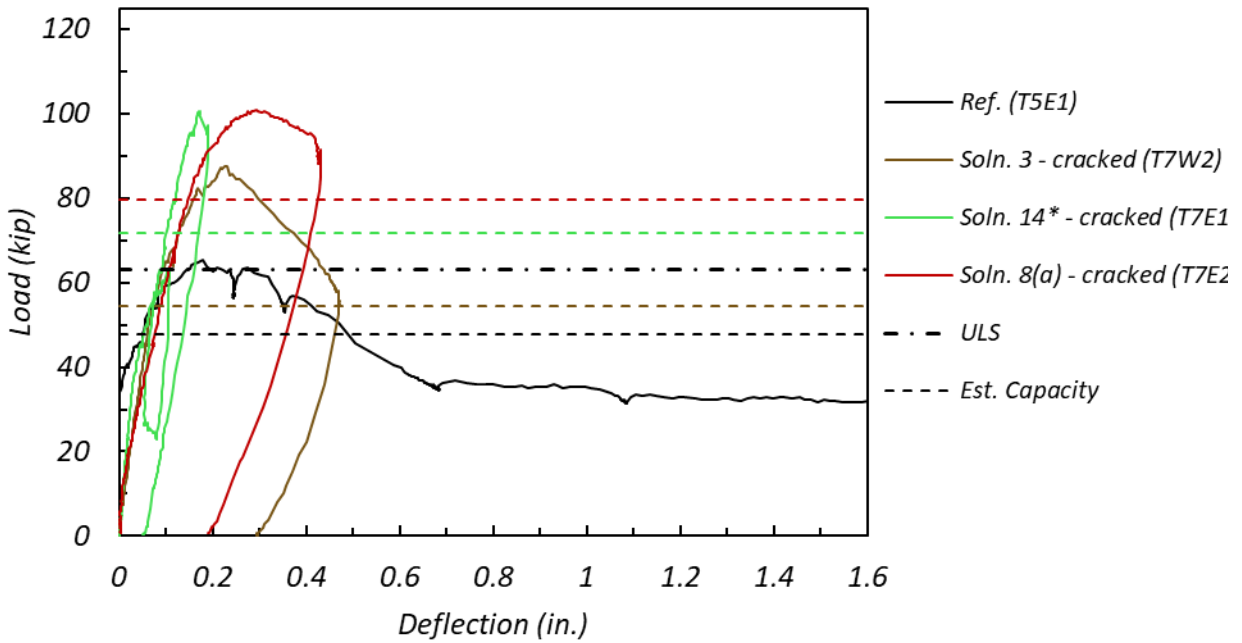
**Ret. = retrofit.

5.2.1.1 Solution 3 (End-Region Stiffener)

Solution 3 was implemented in two ledge-deficient tests (T5W1 and T7W2 [post-crack]), increasing the capacity by 30 percent and 33 percent, respectively. Although this suggests the increase is greater in a cracked bent cap, it should be noted that the test day concrete compressive strength was larger for Specimen 7 (5.2 ksi) than for Specimen 5 (4.5 ksi) and the failure mode was different for the two tests. The uncracked test had failure of the strut-to-node interface similar to the hanger-deficient end plate tests, while the cracked test had a combined ledge-flexure/punching shear failure. The premature failure may be affected by the relatively short embedded length of the anchors (10 in.), and recommendations by Hurlbaeus et al. (2018b) to use increased length may improve capacity further.



(a) Un-cracked specimen



(b) Pre-cracked specimen

Note: Solid lines: experimentally measured capacities; dashed lines: estimated capacities using empirical AASHTO LRFD (2014) procedures; dash-dot line: ultimate factored load demand (ULS) = V_u .
 * T7W1 and T7E1 tests terminated at 79 kips and 100 kips, respectively.

Figure 5.3. Load-Deflection Curves for Ledge-Deficient Exterior Tests.

5.2.1.2 Solution 8 (Clamped Threadbar with Channel)

Solution 8 (threadbars and channels) was installed for three different specimens having different conditions. All three conditions failed in a combination of ledge flexure and punching shear at loads significantly larger than the pure ledge flexure failure of the reference test. For the specimen with a threadbar and channel on the exterior only (T4E1), the capacity is similar to that of the punching shear tests with the same bearing pad size. This is to be expected since there is nothing on the interior side of the girder to strengthen the punching shear capacity. When a threadbar and channel are provided on both sides of the load (T4W1 and T7E2), there is a moderate increase in the punching shear capacity. This increase is not as large as expected since the cracks are shallower (35 degrees) than assumed in the capacity estimate (45 degrees). The larger capacity of T7E2 compared to T4W1 is driven by the larger concrete compressive strength (5.2 ksi and 4.1 ksi, respectively), a major influence on the punching shear capacity. The observed damage indicates that the modified ledge distribution widths proposed in Section 4.3.3 are appropriate for use with the clamped threadbar retrofit solution.

Solution 8(a) with threadbars and channels on both sides of the girders was installed on an undamaged specimen (T4W1) and a specimen with cracks from service loads (T7E2). The widths of cracks at service in T7E2 were smaller after implementation of the retrofit and were similar in size to those of T4W1.

5.2.1.3 Solution 14 (Load-Balancing PT)

The tests of Solution 14 (T7W1 and T7E1) were terminated before failure due to safety concerns in the laboratory. For test T7W1 (no prior damage), the load was increased up to a test termination load of 82 kip. For test T7E1 (with existing cracks), the test was terminated when the preexisting cracks were opened as wide as before installing the PT strands (approximately 100 kip). The test termination loads are 24 percent to 52 percent larger than the reference tests, which, along with the reduced damage at key load states (SLS, ULS), validates the design concept of providing an alternative load path to decrease the demand on the ledges, thereby bypassing the need to provide increased ledge strength.

5.2.1.4 Solution 16 and Solution 17 (Concrete Infill with FRP Anchored with Steel Waling)

To evaluate the retrofit solution using the FRP wrap, both Solution 16 and 17 were tested. Although the most apparent design difference between the retrofits is the depth of the FRP on the interior

side, for purposes of discussing increased ledge flexure capacity, the difference is primarily in the use of a bandage strip to anchor the end-face FRP for Solution 17. This bandage strip allows for the use of a smaller effective strain in calculating the estimated capacity. The experimental results validate this design assumption since the observed ultimate capacity of Solution 16 corresponds with debonding of the FRP at the end face. While a drop in capacity occurred, the bent cap was able to sustain a load of approximately 35 percent larger than the reference test. When the bandage strip was used, the ultimate capacity was larger, with failure occurring due to debonding of the unanchored edge of the FRP on the bottom of the bent cap. Both solutions were able to improve the capacity of the bent cap significantly more than expected, 55 percent and 82 percent for Solution 16 and Solution 17, respectively.

5.2.2 Analysis of the Interior Ledges

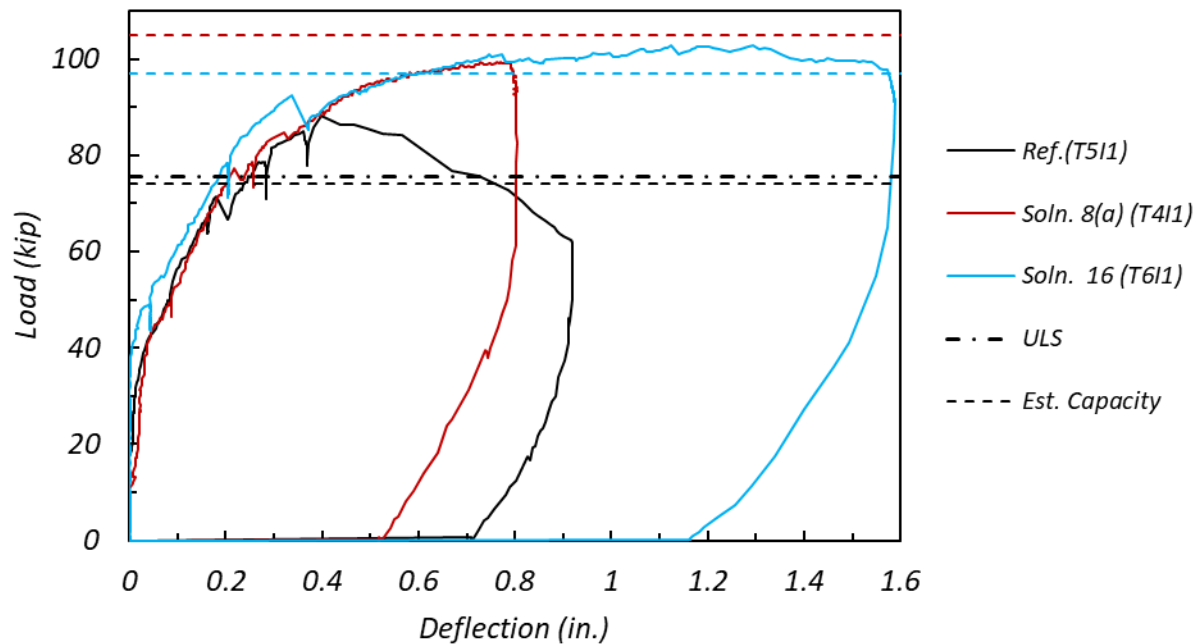
The interior portions of the ledge-deficient specimens were strengthened with two clamped threadbars (Solution 8[a]) and partial-depth FRP (Solution 16). Table 5.6 summarizes the estimated capacity and measured ultimate load for each test. Retrofit values are normalized by the values for the reference test (T5I1). Load-deflection curves are provided in Figure 5.4.

Retrofit solutions improved the capacities at the interior girders by 16 percent to 21 percent. Neither Solution 8(a) nor 16 had a significant impact on the initial stiffness of the specimen (prior to ULS). In the following subsections, the test result for each solution is discussed in depth.

Table 5.6. Summary of Capacity Analysis and Test Result for Ledge-Deficient Interior.

Test ID	Solution No.	Est. Capacity (kips)	Meas. Ult. Load (kips)	Est./Meas.	Est. Ret.*/Ref.	Meas. Ret./Ref.	Obs. Failure Mode
T5I1	Reference	74	85	0.87	1.00	1.00	Ledge flexure
T4I1	8(a)	105	99	1.06	1.43	1.16	Ledge flexure and punching
T6I1	16	97	103	0.94	1.31	1.21	Ledge flexure and punching

*Ret. = retrofit.



Note: Solid lines: experimentally measured capacities; dashed lines: estimated capacities using empirical AASHTO LRFD (2014) procedures; dash-dot line: ultimate factored load demand (ULS) = V_u .

Figure 5.4. Load-Deflection Curves for Ledge-Deficient Interior Tests.

5.2.2.1 Solution 8 (Clamped Threadbar with Channel)

Solution 8(a) increased the ledge-deficient specimen capacity by 14 kips (16 percent). While the reference test failed in ledge flexure, the retrofit test failed in a combination of ledge flexure and punching shear. A clear punching shear cone formed at 95 kips, approximately equal to the punching shear capacity of the ledge-deficient specimens. Prior to testing, it was expected that the punching shear capacity would increase due to the channels providing an alternative load path directly to the threadbars. The observed damage indicates that the placement of the channels did not allow this due to the shallower punching shear crack angle (35 degrees) compared to AASHTO design equations (45 degrees); an improvement in punching capacity may be possible by relocating the channels, but caution should be used since doing so is likely to reduce effectiveness for strengthening ledge and hanger capacity. The observed damage also indicates that the ledge distribution widths are appropriate for use with the clamped threadbar retrofit solution.

5.2.2.2 Solution 16 (Concrete Infill with Partial-Depth FRP Wrap Anchored by Steel Waling)

Test T6I1 was conducted on the ledge flexure specimen retrofitted by partial-depth FRP (Solution 16). The FRP sheets were installed on the infilled concrete blocks for the interior ledges.

This solution improved the ledge flexure capacity by 21 percent. The estimated capacity and the measured ultimate load are considerably close. Although the 21 percent improvement in the ledge flexure capacity is less than the estimated improvement, the solution provided sufficient improvement, 18 kips, in the ledge flexure capacity for the ledge-deficient specimen, which has 10 kips of deficiency. Thus, Solution 16 can be used to strengthen the interior ledge flexure capacity of the inverted-T bent caps. The solution is the most effective solution in terms of capacity increase among the tested retrofit solutions.

CHAPTER 6: SUMMARY AND CONCLUSION

An experimental test program was conducted to investigate the serviceability and strength requirements of six retrofit solutions designed and evaluated in Volume 1 (Hurlebaus et al., 2018a). Two half-scale specimens were designed to reflect the as-built characteristics of IH 35 multi-column bent caps and emphasize hanger deficiencies and ledge deficiencies. Six retrofit solutions, adapted from designs presented in Volume 1 (Hurlebaus et al., 2018a), were implemented on the specimens:

- Solution 3: End-region stiffener.
- Solution 8: Clamped threadbar with channel.
- Solution 14: Load-balancing PT.
- Solution 16: Concrete infill with partial-depth FRP anchored with steel waling.
- Solution 17: Concrete infill with full-depth FRP anchored with steel waling.
- Solution 18: Large bearing pad.

Each specimen provided one interior and two exterior test locations. Some test locations were utilized for multiple tests, resulting in 33 tests on eight specimens. Table 6.1 provides, for each test, the estimated capacity, measured capacity, capacity increase, and failure mode.

Hanger-deficient specimens were strengthened with Solutions 3, 8, 14, and 17 to evaluate the performance of the retrofit methods in improving hanger capacity. The largest exterior hanger capacity increase was provided by Solution 8 (61 percent), and the smallest was provided by Solution 3 (18 percent). The largest interior capacity increase was provided by Solution 17 (23 percent), which resulted in a shift in failure mode from hanger to ledge flexure, although the increase from Solution 8 was nearly as large (21 percent). Solution 14 (interior and exterior) provided substantial reduction in damage at loads expected on in-service bent caps; this retrofit was not tested to failure.

Ledge-deficient specimens were strengthened with Solutions 3, 8, 14, 16, and 17 to assess the effectiveness of the solutions in increasing the ledge flexure capacity. The largest exterior ledge capacity increase was provided by Solution 17 (82 percent), and the smallest was provided by Solution 8 (21 percent for one threadbar, 36 percent for two threadbars) and Solution 3 (33 percent). Solution 14 was implemented on the exterior only and provided a substantial reduction in damage but was not tested to failure. The interior ledge capacity increase was

investigated by two solutions, with Solution 16 (21 percent) providing a greater increase in capacity than Solution 8 (16 percent).

Punching shear tests were conducted on ledge-deficient specimens to assess the effect of bearing pad size (Solution 18) on punching shear capacity. Larger pads increased the exterior capacity by 14 percent, but there was slight or no improvement in the interior capacity. TxDOT (2015) *Bridge Design Manual* adaptations of AASHTO (2014) LRFD provisions for the design of inverted-T bent caps were utilized to calculate the expected capacity of the bent cap specimens. The design equations were found to be overly conservative compared to the measured ultimate loads. Based on the observed damage patterns, modified equations were proposed for the evaluation of in-service bent caps and for the design of retrofit solutions.

The findings of the experimental tests and the evaluation of code equations for calculation of capacity were used to develop design recommendations, as documented in Hurlebaus et al. (2018b).

Table 6.1. Summary of Test Results and Capacity Analyses.

Specimen ID	Test ID	Solution No.	Est. Capacity (kips)	Meas. Ult. Load (kips)	Meas. Ret. **/Ref.	Obs. Failure Mode
HD Ext.	T1W1	Reference	42	66	1.00	Hanger
	T1E1	8(a)	77	106	1.61	Hanger
	T8W1	8(b)	64	88	1.33	Hanger
	T8E1	8(a) Post-crack	82	98	1.48	Hanger
	T2E1	3	74	78	1.18	Strut-tie
	T2W1	14	66	82*	1.24	—
	T2W2	17 Post-crack	73	92	1.39	Ledge flexure and punching
HD Int.	T1I1	Reference	49	90	1.00	Hanger
	T8I1	8(a)	84	109	1.21	Hanger
	T2I1	14	76	105*	1.17	—
	T2I2	17 Post-crack	68	111	1.23	Ledge flexure and punching
LD Ext.	T5E1	Reference	48	66	1.00	Ledge
	T5W1	3	51	86	1.30	Strut-tie
	T4W1	8(a)	79	90	1.36	Ledge flexure and punching
	T4E1	8(b)	63	80	1.21	Ledge flexure and punching
	T6W1	16	66	102	1.55	Ledge flexure and punching
	T6E1	17	71	120	1.82	Ledge flexure and punching
	T7W1	14	72	82*	1.24	—
	T7W2	3 Post-crack	54	88	1.33	Ledge flexure and punching
	T7E1	14 Post-crack	72	100*	1.52	—
	T7E2	8(a) Post-crack	80	101	1.53	Ledge flexure and punching
LD Int.	T5I1	Reference	74	85	1.00	Ledge flexure
	T4I1	8(a)	105	99	1.16	Ledge flexure and punching
	T6I1	16	97	103	1.21	Ledge flexure and punching
Punching Ext. (LD)	T3W1	Reference	51	70	1.00	Punching
	T3E1	18	61	80	1.14	Punching
Punching Int. (LD)	T3I1	Reference	55	104	1.00	Punching
	T3I2	18	75	94	0.90	Punching
	T3I3	18	75	94	0.90	Punching
	T7I1	Reference	64	112	1.00	Punching
	T7I2	18	87	119	1.06	Punching
	T7I3	Reference	64	112	1.00	Punching
	T7I4	18	87	113	1.01	Punching

Note: HD = hanger-deficient and LD = ledge-deficient

* Test termination load.

** Ret. = retrofit.

REFERENCES

- AASHTO. (2014). *LRFD Bridge Design Specifications*, Seventh Edition. American Association of State Highway and Transportation Officials, Washington DC.
- ASTM. (2012). *C143, Standard Test Method for Slump of Hydraulic Cement Concrete*. ASTM, West Conshohocken, Philadelphia.
- ASTM. (2015). *C31/31M, Standard Practice for Making and Curing Concrete Test Specimens in the Field*. ASTM, West Conshohocken, Philadelphia.
- ASTM. (2016). *C192, Standard Practice for Making and Curing Concrete Test Specimens in the Laboratory*. ASTM, West Conshohocken, Philadelphia.
- ASTM. (2017). *C39, Standard Test Method for Compressive Strength of Cylindrical Concrete Specimens*. ASTM, West Conshohocken, Philadelphia.
- ASTM. (2016). *C109, Standard Test Method for Compressive Strength of Hydraulic Cement Mortars*. ASTM, West Conshohocken, Philadelphia.
- Furlong, R.W., and Mirza, S.A. (1974). *Strength and Serviceability of Inverted T-beam Bent-Caps Subject to Combined Flexure, Shear, and Torsion*. TxDOT Report #153-1F, Center for Highway Research, University of Texas at Austin, Austin, TX.
- Hurlebaus, S., Mander, J.B., Birely, A.C., Terzioglu, T., Cui, J., and Park, S.H. (2018a). *Strengthening of Existing Inverted-T Bent Caps—Volume 1: Preliminary Design*. Rep. No. FHWA/TX-18/0-6893-R1-Vol1, Texas A&M Transportation Institute, The Texas A&M University System.
- Hurlebaus, S., Mander, J.B., Birely, A.C., Terzioglu, T., Cui, J., and Park, S.H. (2018b). *Strengthening of Existing Inverted-T Bent Caps: Design Recommendation and Example*. Rep. No. FHWA/TX-18/0-6893-P1, Texas A&M Transportation Institute, The Texas A&M University System.
- TxDOT. (2015). *Bridge Design Manual—LRFD*. Texas Department of Transportation, Center for Highway Research, University of Texas at Austin, Austin, TX. <http://onlinemanuals.txdot.gov/txdotmanuals/lrf/lrf.pdf>.

